Karlsruher Institut für Technologie

Dissipation and Noise in Granular Aluminum Fluxonium Qubits

Zur Erlangung des akademischen Grades eines

Doktors der Naturwissenschaften

von der KIT-Fakultät für Physik des
Karlsruher Instituts für Technologie (KIT)

genehmigte

Dissertation

von

Patrick Paluch

Tag der mündlichen Prüfung:
27. Juni 2025

Referent:	Prof. Dr. Ioan Pop
Korreferent:	Prof. Dr. Wolfgang Wernsdorfer

Abstract

The dream of universal quantum computing promises to revolutionize many fields due to its potential to drastically speed up certain calculations compared to classical computers. This has naturally attracted attention and investment. For example, in 2024, Google unveiled their Willow superconducting quantum processor, achieving a significant milestone by demonstrating quantum error correction below the surface code threshold. Despite these advances, the road to a fully fledged quantum computer is still uncharted, and current technology is not sufficient to get there. Therefore, unconventional materials hold great potential for addressing challenges faced by traditional approaches. This work focuses on fluxonium qubits made from the disordered superconductor granular aluminum (grAl), aiming to gain deeper insights into underlying loss mechanisms and noise sources.

One of the main results of this work is the identification of inductive loss as the dominant decoherence mechanism in grAl fluxonium qubits with frequencies lower than 300 MHz at the half flux bias. The observed inductive loss tangent aligns with previously measured single-photon internal quality factors of grAl resonators, and the energy relaxation profiles are well described by a combination of inductive, dielectric, and Purcell loss. The study endeavors to deepen the understanding of decoherence by refining loss models via the quantum fluctuation-dissipation theorem and proposing an improved framework for Purcell loss. A comparison with other qubit materials underscores the universal nature of inductive loss in grAl fluxoniums, in contrast to well established Josephson junction array (JJA) based fluxoniums which show no such limitation at even lower qubit frequencies.

The second outcome of this thesis is the validation of flexible striplines ('flexlines') for the use in future cryogenic microwave setups. This enables at least an order of magnitude increase in the density of microwave input circuitry without thermally overloading the cryostat, paving the way for increasingly complex superconducting detectors and quantum devices. The study found no significant differences in qubit performance between setups using flexlines and conventional coaxial cables. Passive heat load measurements indicated comparable photon shot noise-induced dephasing for both setups. The introduced heating pulse method demonstrated a faster thermalization time for flexlines compared to coaxial cables, and it can serve as a simple health check for other groups as well. An extended thermal model was developed to better understand the contributions of various attenuators in the input chains to the measured heat loads and to propose improved input chains.

To further exploit the versatility of grAl for fluxonium qubits, the investigation of the microscopic origin of the limiting inductive loss is of interest to develop potential suppression methods. JJA-based fluxoniums could play a crucial role in this context, as particularly long arrays with increased plasma frequencies can emulate the properties of grAl while leveraging their better-understood behavior.

Acknowledgements

I would not be where I am today without the support of so many people who accompanied me on this long journey and to whom I owe great thanks.

First and foremost, I would like to thank my doctoral advisor, Ioan Pop. Thank you for giving me the opportunity almost six years ago to become part of your research group, first as a HiWi and later as a doctoral student. I couldn't imagine a better doctoral advisor, who guides one through the rollercoaster ride of a PhD with such sophistication and wealth of experience, but also with tireless patience and empathy. I have learned so many lessons from you both for my scientific career and for life. The opportunity to build the first lab at Campus North (CN) from scratch filled me with great pride, and you showed me once again that one grows with their tasks. Thank you also for tolerating my interest in cryostats at Qinu in the beginning, when it was not yet clear that it would be mutually beneficial for the group and me. I really appreciated your honest conversation style throughout the years. Thank you also for all the valuable feedback to the manuscript.

Next, I would like to thank my second advisor, Wolfgang Wernsdorfer, from the bottom of my heart. Your passion for cryogenics and your incredible workload impressed me at the beginning of my time at KIT and sparked a great interest in the topic within me. I thank you for countless hours of scientific discussions and detailed technical training, which you seem to share with great joy and self-evidence. Thank you also for always being there when there was a challenge with a cooldown. I especially want to mention the joint trips to CN, which I fondly remember. I am also deeply grateful to you for being able to cheer me up with a certain lightness during the times of greatest mishaps. When 'the drama in five acts', the loss of a load of helium mixture, happened, after some light-hearted banter, you responded with: "Such things always happen. You can't make an omelette without breaking an egg!" (German original: "Wo gehobelt wird, da fallen auch Späne!"). I took these words as an occasion to view such mishaps, as serious as they are in their own right, with a certain humor in retrospect. This also motivated me to process some of these incidents in small comics in this thesis. As I learned from you one day when I came into the Technikumshalle and the Leifors almost tipped over while being lifted with the crane: "Bloody hell! I guess the older you get, the bigger these stupidities become."

I would also like to thank my external examiner, Pol Forn-Díaz, for being willing to attend my examination and read the manuscript. It was a pleasure to visit you in Barcelona. At Qilimanjaro, you welcomed us with great hospitality, making the journey associated with setting up a Qinu cryostat a pleasant experience.

Furthermore, I owe a particularly large part of my thanks to my colleague Martin Spiecker. I don't know how much time we spent in joint discussions, but I am grateful for every minute. I am simply fascinated by your humble genius, with which you enlightened the whole group. Thank you for showing me for the 100th time in a playful way how fascinating physics is. Your broad excitement for various topics in physics always captivated me, and you repeatedly motivated me to tackle the most stubborn topics and understand them in detail. I can say with good conscience that without you, there would hardly be a treatise on open quantum systems and an alternative derivation of Purcell loss in this thesis, which gave the whole work significantly more depth. I can only speak of incredible luck that I had you by my side throughout my PhD, and it was real highlights when we once again pondered an initially absurd solution strategy. I fondly remember heating the chips with an improvised 'vacuum chamber', laser-trimming the resonator, or closing the sample box in an argon atmosphere. And thank you for spending so much time on feedback to the manuscript.

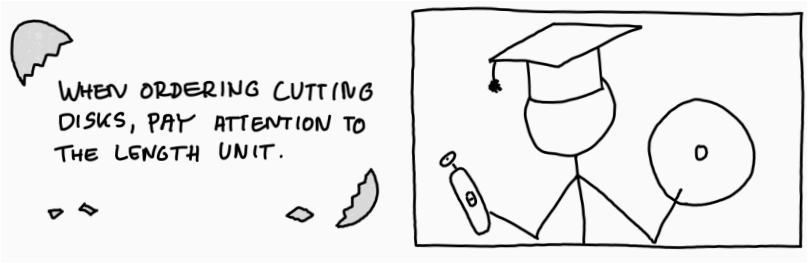

Next, I would like to thank Dennis Rieger and Simon Günzler for the countless uplifting conversations and general willingness to discuss. I could always come to you with my problems, and you always had an open ear for me and could help me, or at least convey a more relaxed approach to stress. I fondly remember the time back in the days when we equipped the Bluefors cryostat in the Technikumshalle and conducted our first experiments in it. Thank you, Dennis, for taking the time back then to explain to me with precise logic how Ramsey and echo experiments work. You were also there when I slowly realized that my to-do list keeps getting longer and longer, and you told me to not despair about it, but accept that I can't do everything at once and have to prioritize. And thank you too, for valuable feedback to parts of the manuscript.

Mahya Khorramshahi, thank you for the many uplifting conversations in which we could simply talk our burdens off our souls. Your fundamentally positive and lively nature always brought a smile to my face :) I fondly remember the festive evening with Iranian food, where we all ended up dancing for hours.

Nicolas Gosling, thank you for your relentless helpfulness. You are always there when needed and have been a great help to me and the entire group from the beginning. It was

always exciting to conduct measurements with you on our MNP barrel, which sometimes extended into the late evening hours and included once a joint burger evening at INT with Martin. Thank you for your feedback on parts of this manuscript.

I would also like to thank the rest of the Black Forest Quantum (BFQ) group for the always encouraging scientific environment. Thomas Reisinger, I could always rely on your help, and I want to thank you especially for your active support in setting up the CN lab, as well as for the countless order requests and help with laser-trimming the resonator, etc. Simon Geisert, tonight's the night to thank you for memorable evenings in the HiQCuing events and at KIT, which is also true for Nicolas Zapata (30). Thank you for repeatedly reminding me months before my birthday: "Maaaaaan… soon you will turn 30. Must be hard." But jokes aside, it is always a pleasure to talk with you, Sir. Speaking of this birthday, I must especially thank Mathieu Féchant, who DJed at my birthday party and kept the audience on their toes until the middle of the night and until it was not only the beat anymore that was dropping in our basement (not looking at anyone). Thank you also for your numerous music and film tips; I am always fascinated by your wealth of experience in this area. I want to thank Ameya Nambisan for bringing a smile to my face with her cheerful nature every time we meet, even if we have to wait a long time for a water pipeline to be installed (but I guess better when it is done professionally...). Denis Bénâtre, thank you for taking over the Phoenix and Peacock fridges. Also, the Papaoutai duet was a real highlight, pas vrai? I also want to thank Paul Kugler for his motivation to set up the new cryostat in CN. It was a pleasure to install the almost-lost DC lines there with you.

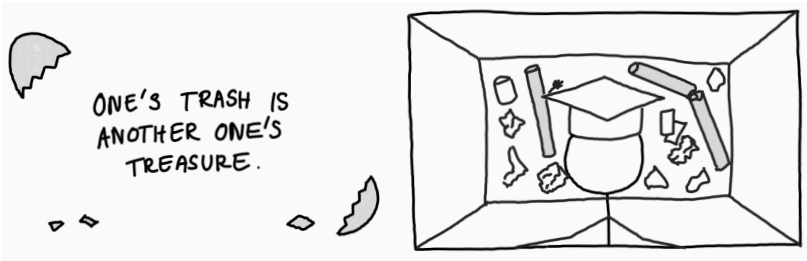

I would also like to remember former members of the BFQ group. Thank you, Francesco Valenti, for adding a touch of aesthetics to my PhD time, whether through your inspiring murals in the new CN lab or the beautiful HiQCuing events in the picturesque villa of your hometown in the Italian Alps. Many thanks also to Anil Murani for the short but wonderful time in Karlsruhe. I would also like to thank Patrick Winkel and Ivan Takmakov, who introduced me to the physics of parametric amplifiers. Patrick, I'm sorry for first shocking you with having annealed your sample, but what a luck, that it actually turned out useful! Although no longer part of our group during the PhD, I would still like to mention Julian Ferrero, who always made me laugh and with whom we celebrated the most legendary parties at PHI. Thanks also to Viktor Adam and Luca Kosche for always interesting conversations. Viktor, I am still fascinated by how our life paths have intersected so far, from MPIK to KIP and now at KIT, and I am grateful for your important help with my first publication.

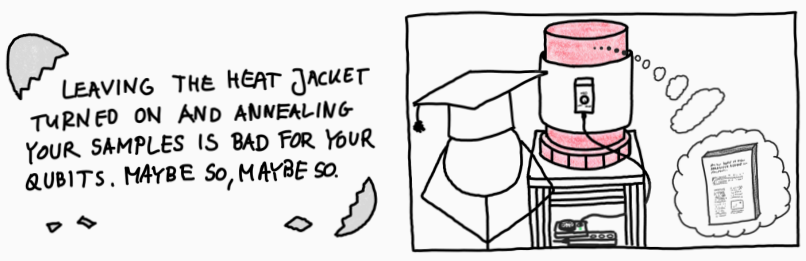

The work at PHI as well as at INT/IQMT would not be possible without the diverse help provided every day by the numerous staff in the secretariats, IT, workshops, and cleanroom team. Many thanks to Claudia Alaya, Steffi Baatz, Carmen Dörflinger, and Dorothea Trautmann for their always quick help with bureaucratic work, and Lars Behrens for valuable IT support. From the workshops, I would like to thank Michael Meyer, Frank Landhäußer, Maik Nothdurft, Melissa Baumgärtner, Jannis Ret, and Patrick Rust, who always processed our sometimes very short-term orders quickly and with great precision. A special thanks goes to Michael Meyer, who always took the time to adapt technical drawings to our individual wishes. From the CFN cleanroom team, I would like to thank two people in particular: Silvia Diewald, who spent countless hours on the electron beam lithography machine and in detailed discussions of various dose tests. Without your very helpful initiative, we would never have fabricated a suitable sample so quickly. Secondly, I would also like to thank Lucas Radtke, who always dedicated himself to our requests with great commitment, whether it was writing a new optical mask, handling the PLASSYS system, or dicing the finished wafers. In this context, I would also like to mention Hannes Rotzinger, who also kept the PLASSYS system running with maintenance and always provided a pleasant encounter with a smile and a good conversation. The same goes for Christoph Sürgers, thank you for your constant helpfulness over the years. At INT, the setup of the new lab would never have gone so smoothly without your active help, Torsten Stehli, for which I am truly very grateful. Many thanks also to Matthias Hettler for various IT support and the permission to use the KIT internal transport vehicle, and Martin Limbach for the introduction to the INT workshop.

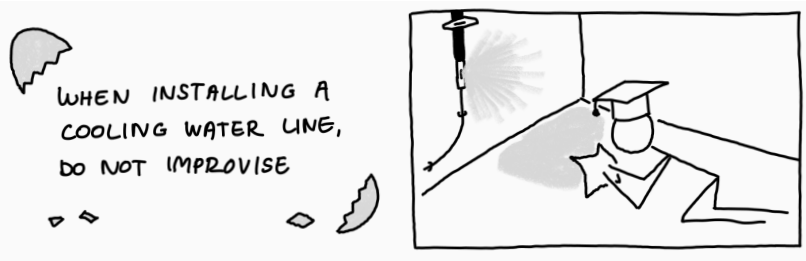

Apart from the PhD, I would also like to thank Marcel Schrodin, who gave me the opportunity to pursue my interest in Sionludi cryostats professionally and be part of such a dynamic and interesting company as Qinu. My personal highlight so far was our joint trip to Barcelona for the installation of the cryostat at Qilimanjaro. But I'm sure that won't be the last highlight. I would also like to thank Péter Fejes for always being immediately by my side in countless moments when there was something to do with the GHS, and my

colleagues Alex, Eugen and Aaron, it is always a great pleasure to chat with you in the Technikumshalle.

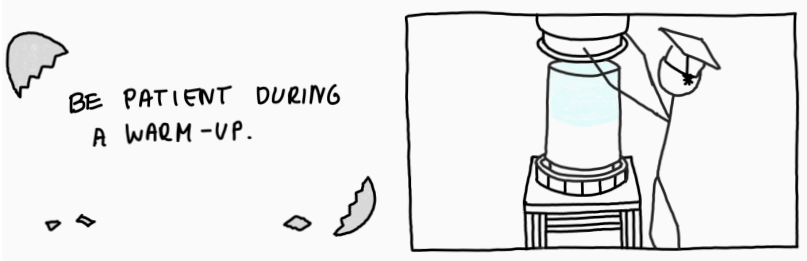

Good teachers are essential for a student's career, it is said. So I also owe it to a number of teachers that I ended up in physics and discovered a true passion for it. The first necessary condition for this was created by Brigitta Schönle, who brought me back on the right track after a school exclusion, and for her commitment, I am infinitely grateful. I am sorry that I could not fulfill your wish to inspire me for chemistry, but you also awakened my interest in physics at the same time. That this ignited flame then became a blazing fire, I owe to our NwT and physics teacher Gerhard Dangelmaier. Again, I can only speak of luck that I had you as a teacher for so many years. The interactive excursions in NwT to the interior of the Maustobelviadukt, to the Widderstall testing facility for solar power systems, or to the Nördlinger Ries, as well as the delicious samples of your home-made apple cider, remain vivid memories. Also, that you gave us a message for life at the end of the physics advanced course with the metaphor of the three-legged chair shows once again how valuable you were as a teacher for certainly a large number of people. Thank you for the many valuable lessons and also for the Jackson - Classical Electrodynamics book from your wife's studies in the early 70s, which you handed over to me at the end. I am also deeply grateful to Horst Bittner, who supported and accompanied me in dealing with physics outside of school. Thanks to your mediation, I ended up at the student research center (SFZ) in Bad Saulgau and ultimately at an international physics competition in Iran. For allowing me to have such an overwhelming experience, I am deeply grateful to you and Rudolf Lehn from SFZ. On this note, I would also like to thank my classmate Nicolas Staudenmaier, with whom I spent at the SFZ many hours outside in the cold, measuring the polarization of the sky with tourmaline crystals. It is a pleasure to see that you have taken a similar path as I have and now hold a PhD title as a dedicated quantum enthusiast. Finally, I would like to thank Mr. "Daniel Düsentrieb" Göhlert for always standing by my side with great enthusiasm and clarity in various physics problems. I still remember well when I wanted to know one day how a $\lambda/4$ filter works, and you simply took me to the physics preparation and handed me various polarization filters to experience and understand it firsthand.

Finally, I would also like to thank my friends from my studies in Heidelberg, Falk, Patrick, Mattis, Ekaterina, Caro, Eva, and Katja, for the many evenings in recent years and the shared experiences in academia. I am very glad that you have stayed with me!

Not to forget are my longest friends from school, Kaan, Nicki, Aylin, and Johanna. You were always four stable pillars for me and you were there for me even in difficult phases.

What incredible luck that I have you! For the necessary distraction and an open ear, I could also count on my friends Basti, Dany, Eva, and Holger from the Dossenheim times, as well as Pascal, Matthias, Maik, Mingjie and Daniel from my new home Karlsruhe. I thank you from the bottom of my heart for the moral support over the past years - I don't know what I would have done without you. A special thanks goes to you, dear Frank, from whom I have learned so much craftsmanship and practical knowledge (from time to time maybe also some "unnützes Wissen") that I can draw on for the rest of my life. Soon I will have more time for the hall again.

Schließlich möchte ich auch noch meiner Familie danken, allen voran meinen Eltern, die immer an mich geglaubt haben und mich zu dem Mensch erzogen haben, der ich heute bin. Unendlicher Dank gilt aber auch meiner Oma Karin, die mir schon von klein auf vermittelt hat, wie ernst ich die Schule nehmen sollte und mein Interesse am Lösen sämtlicher Rätsel seit jeher gefördert hat, und so meiner Neugierde freien Lauf gelassen hat. Ohne dich hätte mein Leben einen gänzlich anderen Weg gehen können. Ich möchte auch meinen Großeltern aus Olbernhau danken. Ihr habt mir mit eurer Liebe ein zweites Zuhause gegeben und die jährlichen Sommerferien bei euch haben mir eine unglaublich schöne Kindheit beschert. Danke auch an dich, liebe Naddi, für die zahlreichen Kraftzusprüche und für dein immerzu großes Herz.

亲爱的Hang，我想衷心地感谢你陪伴了我整个博士生涯。你一直在我身边并坚定地支持着我，即使有时候要忍受我挑灯夜战的工作。感谢你和我一起经历了这一切挑战，尤其是在博士论文的最后阶段，你总是在家为疲惫的我准备好如此美味的饭菜。你的爱和关心是我读博路上的坚强后盾。

Figure 1: Black Forest Quantum (BFQ) Group in 2022. From the upper right, the spiral hallway down: Dennis Rieger, Ioan M. Pop, Thomas Reisinger, Denis Bénâtre, Nicolas Zapata, Markus Weßbecher, Simon Günzler, Ritika Dhundhwal, Fabian Zwiehoff, Martin Spiecker, Immanuel Speitelsbach, Simon Geisert, Sören Ihssen, Ameya Nambisan, Mathieu Féchant, Mahya Khorramshahi, Patrick Paluch and Nicolas Gosling

Figure 2: Black Forest Quantum (BFQ) Group in 2024. From top left to bottom down: Ioan M. Pop, Soroush Arabi, Mathieu Féchant, Dénis Bénâtre, Nicolas Gosling, Nicolas Zapata, Mahya Khorramshahi, Ameya Nambisan, Martin Spiecker, Mitchell Field, Simon Günzler, Patrick Paluch, Paul Kugler, Simon Geisert, Philipp Lenhard, Naomi Remmlinger, Janic Beck, Ritika Dhundhwal, Sören Ihssen, Thomas Reisinger

Contents

List of Publications

Authors marked with † have contributed equally.

[1] F. Valenti†, A. Murani†, **P. Paluch**, R. Gartmann, L. Scheller, R. Weller, R. Kruk, T. Reisinger, L. Ardila-Perez, and I. M. Pop, "Seismometry of radiation-induced quasiparticle bursts in superconducting devices", Phys. Rev. B **113**, 174504 (2026).

[2] D. Bénâtre, M. Féchant, N. Zapata, N. Gosling, **P. Paluch**, T. Reisinger, and I. M. Pop, "Simultaneous sweet-spot locking of gradiometric fluxonium qubits", Phys. Rev. Appl. **24**, 054031 (2025) (cit. on pp. 65, 66).

[3] M. Khorramshahi, M. Spiecker, **P. Paluch**, S. Geisert, N. Gosling, N. Zapata, L. Brauch, C. Kübel, S. Dehm, R. Krupke, W. Wernsdorfer, I. M. Pop, and T. Reisinger, "High-impedance granular-aluminum ring resonators", Phys. Rev. Appl. **24**, 024066 (2025) (cit. on p. 47).

[4] S. Ihssen†, S. Geisert†, G. Jauma, P. Winkel, M. Spiecker, N. Zapata, N. Gosling, **P. Paluch**, M. Pino, T. Reisinger, W. Wernsdorfer, J. J. Garcia-Ripoll, and I. M. Pop, "Low crosstalk modular flip-chip architecture for coupled superconducting qubits", Appl. Phys. Lett. **126**, `10.1063/5.0245667` (2025) (cit. on p. 48).

[5] **P. Paluch**, M. Spiecker, N. Gosling, V. Adam, J. Kammhuber, K. Vermeulen, D. Bouman, W. Wernsdorfer, and I. M. Pop, "Thermalization of a flexible microwave stripline measured by a superconducting qubit", Appl. Phys. Lett. **126**, `10.1063/5.0243116` (2025) (cit. on pp. 67, 74).

[6] S. Geisert†, S. Ihssen†, P. Winkel, M. Spiecker, M. Fechant, **P. Paluch**, N. Gosling, N. Zapata, S. Günzler, D. Rieger, D. Bénâtre, T. Reisinger, W. Wernsdorfer, and I. M. Pop, "Pure kinetic inductance coupling for cQED with flux qubits", Appl. Phys. Lett. **125**, 064002 (2024) (cit. on pp. 45, 64, 65).

[7] D. Willsch†, D. Rieger†, P. Winkel, M. Willsch, C. Dickel, J. Krause, Y. Ando, R. Lescanne, Z. Leghtas, N. T. Bronn, P. Deb, O. Lanes, Z. K. Minev, B. Dennig, S. Geisert, S. Günzler, S. Ihssen, **P. Paluch**, T. Reisinger, R. Hanna, J. H. Bae, P. Schüffelgen, D. Grützmacher, L. Buimaga-Iarinca, C. Morari, W. Wernsdorfer, D. P. DiVincenzo, K. Michielsen, G. Catelani, and I. M. Pop, "Observation of Josephson harmonics in tunnel junctions", Nat. Phys. **20**, 815–821 (2024).

[8] M. Spiecker, **P. Paluch**, N. Gosling, N. Drucker, S. Matityahu, D. Gusenkova, S. Günzler, D. Rieger, I. Takmakov, F. Valenti, P. Winkel, R. Gebauer, O. Sander, G. Catelani, A. Shnirman, A. V. Ustinov, W. Wernsdorfer, Y. Cohen, and I. M. Pop, "Two-level system hyperpolarization using a quantum Szilard engine", Nat. Phys. **19**, 1–6 (2023) (cit. on pp. 45, 46, 75, 93, 96).

[9] D. Rieger†, S. Günzler†, M. Spiecker, **P. Paluch**, P. Winkel, L. Hahn, J. K. Hohmann, A. Bacher, W. Wernsdorfer, and I. M. Pop, "Granular aluminium nanojunction fluxonium qubit", Nat. Mater. **22**, 194–199 (2023) (cit. on pp. 16, 42, 45, 64, 65, 68, 75, 78, 94).

[10] D. Gusenkova, F. Valenti, M. Spiecker, S. Günzler, **P. Paluch**, D. Rieger, L.-M. Pioraş-Ţimbolmaş, L. P. Zârbo, N. Casali, I. Colantoni, A. Cruciani, S. Pirro, L. Cardani, A. Petrescu, W. Wernsdorfer, P. Winkel, and I. M. Pop, "Operating in a deep underground facility improves the locking of gradiometric fluxonium qubits at the sweet spots", Appl. Phys. Lett. **120**, 054001 (2022) (cit. on p. 45).

List of Figures

List of Tables

1 Introduction

This introductory chapter starts by weaving the current work into the broader context of existing research on the topic, and by giving a brief overview of the present thesis. The following section focuses on key concepts relevant for the subject matter, such as of superconducting quantum circuits, including a presentation of the chosen qubit platform and material. In the last two sections, the reader finds an overview of different sources for qubit dissipation and dephasing, respectively.

1.1 Motivation & Manuscript Overview

Curiosity–a trait inherent to humankind–has always helped us to extend our knowledge about the world. This natural driving force led ancient philosophers to reflect on natural phenomena and fundamental questions of life, and with the emergence of the scientific method distinct disciplines such as physics gradually evolved.

The groundbreaking work in the early days of physics, when Galilei disputed the geocentric theory of the universe with his observations and Newton formulated classical mechanics [11], led to a fundamental shift of our understanding, nurturing us for more than two centuries. The 19^{th} century brought a deeper understanding of thermodynamics and electrodynamics, which, together with classical mechanics, would later be summarized as classical physics. At the brink of the turn of the 19^{th} century, it appeared that essentially all physics had been understood, except for a few puzzling challenges.

One of these challenges was that the microscopic derivation of thermodynamics by Boltzmann [12], as well as the explanation of observable blackbody radiation[1] by Planck [13], was based on the hypothesis - peculiar in terms of classical physics - that an electromagnetic oscillator can only absorb or emit energy in discrete packets, the so-called quanta.[2] In 1905, Einstein concluded, while investigating the photoelectric effect, that the quanta hypothesized by Planck and Boltzmann must be real in the form of photons [14]. With this, the puzzling seed started to grow into a whole new branch of physics.

[1] The classical theory of thermodynamics predicted that an ideal blackbody would emit an unlimited amount of energy for decreasing wavelengths, known as ultraviolet catastrophe, which was in stark contrast to experimental observations.

[2] Today, we refer to the moment when Max Planck gave a lecture titled 'On the Theory of the Law of Energy Distribution in the Normal Spectrum' at a meeting of the German Physical Society in 1900 as the birth of quantum physics.

The full theory of quantum mechanics was developed in the 1920s by de Broglie, Schrödinger, Heisenberg, Born and others, revealing a perspective on nature that rather evades human intuition, which is accustomed to large objects. Part of this peculiar quantum behavior originates from the fact that now only the probability for a future state of a system can be predicted via its wavefunction $|\Psi\rangle$, throwing away the familiar determinism in classical physics.[3]

However, accepting the laws of the quantum realm also presents opportunities, one of which was first envisioned by Feynman in a keynote speech in 1981 [15]: "Can we [simulate quantum mechanics] with a new kind of computer–a quantum computer?" In fact, this question started an on-going research avalanche on quantum computing, promoted by the promise to revolutionize many fields like quantum chemistry [16], cryptography [17], quantum simulation [18] and optimization [19] due to a computational speed-up compared to classical computers for certain calculations.

For this reason, quantum computing understandably attracts a lot of attention, constantly fueling both the funding for numerous dissertations in fundamental research every year and the willingness of big companies like Google and IBM to invest a significant amount into the fabrication of quantum hardware. At the end of 2024, Google presented their newest generation of superconducting quantum processor, named Willow, with which they demonstrated for the first time quantum error correction below the surface code threshold, i.e., an exponential suppression of the logical qubit error rate when increasing the code distance [20].

Despite this progress, there still lie many necessary milestones ahead, making a large-scale fault-tolerant quantum computer remain somewhat elusive. Therefore, to better understand why the realization is challenging on the one hand and why there is a theoretical speed-up on the other hand, a few important concepts will be introduced in the following.

The core element of quantum information technology is the quantum bit, or short qubit. Similar to a classical bit that can have one of the two values 0 or 1, the qubit are ascribed two eigenstates, $|0\rangle$ and $|1\rangle$. The qubit, however, appears with the distinct feature that its state can be any superposition of the two eigenstates,

$$|\Psi\rangle = c_0|0\rangle + c_1|1\rangle, \tag{1.1}$$

with the normalization $|c_0|^2 + |c_1|^2 = 1$ to account for the fact that the probability to measure any of the states is equal to one. However, such a superposition is not yet unique to qubits, as it is also possible to realize these properties classically [21]. What truly provides an advantage of a quantum computer is the concept of entanglement, extending the superposition to all elements of a system. For a system with N qubits, the most general wavefunction can be written as

$$|\Psi\rangle = c_0|00\ldots00\rangle + c_1|00\ldots01\rangle + \cdots + c_{2^N-1}|11\ldots11\rangle, \tag{1.2}$$

[3] Actually, as has been pointed out by Feynman in his famous lecture series [15], classical physics is also indeterminate from a practical point of view.

with corresponding normalization, $\sum_i |c_i|^2 = 1$. It is this exponential scaling of the 2^N-dimensional state space that is desired to be employed with quantum computing.

Due to their clarity, Eqs. (1.1) and (1.2) offer a pathway to address some of the challenges in realizing a full-scale quantum computer, which were specified already 25 years ago in the DiVincenzo criteria [22]:

- a scalable physical system with well characterized qubits,
- the ability to initialize the state of the qubits,
- long decoherence times of physical qubits,
- a universal set of quantum gates,
- the measurability of the final qubit states.

While the first point mainly tackles the exponential scaling from Eq. (1.2), the other four points focus on a proper control and readout of individual qubit states, as in Eq. (1.1). The conflicting pathways of up-scaling, interconnectivity and good individual qubit performance render the realization of a scalable quantum computer, and connected with that, which qubit platform would be best-suited, a difficult endeavor.[4]

Despite the presence of other natural choices to base qubits for a future full-fledged quantum processor on, such as trapped atomic ions [24, 25], neutral atoms [26–28], nitrogen-vacancy centers in diamond [29], and spins in semiconductors [30], superconductors emerged as one of the most promising candidates [31].

The success story of superconducting qubits has gone a long way, starting from the seminal paper in 1999 by Nakamura *et.al.* on the Cooper-pair box [32], to several recent demonstrations of quantum error correction [20, 33, 34]. Superconducting qubits, individually fabricated using nanostructuring, are macroscopic in size. This makes them more prone to potential sources of decoherence but also allows for extensive design flexibility. In this way, we naturally became quantum engineers [35], investigating a wide-ranging parameter space, that allows us to study different loss mechanisms and continuously improve the performance of our qubits. Along this road, some quantum engineers became very creative and developed various new types of qubits, such as the flux qubit [36], the transmon [37], the fluxonium [38], or the $0-\pi$ qubit [39]. For all major types of superconducting qubits, universal high-fidelity single- and two-qubit gates have been achieved [40]. Furthermore, the combination of well-established methods like the dispersive readout scheme (see also Section 1.3.4) and the development of nearly quantum-limited amplifiers [41–43] endowed us with fast and efficient single-shot readout.

In this work, various loss mechanisms and noise channels of superconducting fluxonium qubits are investigated, addressing the third of the above DiVincenzo criteria. Despite continuous improvements in qubit coherence [44–46], it is beneficial to explore alternative

[4] DiVincenzo ended his publication with leaving open the question, which qubit platform might be the 'winning' one, and that it might be even counterproductive to ask this question [23].

qubit platforms and materials. By utilizing the rather unconventional fluxonium qubit and granular aluminum material, a rather niche area of research is delved into. Eager to gain new insights from this, we leverage the collective knowledge and experience of our diverse community along the way. Or, to say it humbly in the words of Newton, we stand on the shoulders of giants [47].

The manuscript is organized as follows: In this chapter, key concepts underlying the research on superconducting quantum circuits are introduced. This includes a refinement of existing loss models via the quantum fluctuation-dissipation theorem and the proposal of an improved framework for Purcell loss. The first main result on granular aluminum fluxonium qubits, with emphasis on the measured energy relaxation versus qubit frequency and a discussion of possible loss mechanisms, is presented in Chapter 2. The second main result is then shown in Chapter 3: proving that flexible microwave striplines are well-suited for integration in cryogenic microwave setups, enabling a significant increase in density of microwave input circuitry, by using a superconducting qubit as a sensor for thermal photon shot noise. Finally, Chapter 4 encapsulates the key findings and offers a forward-looking perspective on each result.

1.2 Superconductivity in a Nutshell

1.2.1 Experimental Observations

The low-temperature laboratory of H.K. Onnes, who is today considered as "the father of low-temperature physics" [48], at the University of Leiden dominated low-temperature physics in the beginning of the 20^{th} century for more than two decades with multiple pioneering discoveries. Certainly as a glowing example stands out the discovery of superconductivity in 1911 [49], by observing that "the resistivity of mercury apparently disappears just above 4 K" [50]. In fact, even refined long-time measurements of persistent currents in superconducting rings can only set a lower bound on their decay time of $\sim 10^5$ years and, thus, show no sign of a nonzero resistivity [51]. This perfect conductivity is the first main feature of superconductors.

The second characteristic was revealed by the experiment from Meissner and Ochsenfeld in 1933 [52]: When field-cooling a superconductor through its critical temperature T_c, the magnetic field gets expelled and, thus, the probe behaves as a perfect diamagnet ($\chi_\mathrm{m} = -1$). This behavior differs from that of a perfect conductor which obeys Lenz's law and opposes any change of the magnetic field in the sample. The existence of this Meissner effect implies that superconductivity will be destroyed by magnetic fields larger than a critical magnetic field strength B_c, which is empirically well-described by Tuyn's formula [53],

$$B_\mathrm{c}(T) \approx B_\mathrm{c}(0)\left[1 - \left(\frac{T}{T_\mathrm{c}}\right)^2\right] \tag{1.3}$$

Depending on their behavior outside this Meissner phase, in magnetic fields $B > B_\mathrm{c}$, there are two types of superconductors: Type I superconductors abruptly switch into

the normal conducting state and lose their perfect diamagnetism when B surpasses B_c. This is contrasted by type II superconductors, which, though also expelling the field perfectly up to a lower critical field B_{c1}, their diamagnetic behavior gradually weakens ($-1 < \chi_m < 0$) for fields $B_{c1} < B < B_{c2}$, until they also become fully normal conducting for $B > B_{c2}$. While most elemental superconductors are of type I (with the exceptions of Nb, V and Tc), metal alloys and compounds as well as high-T_c superconductors are all of type II. Regarding the most featured materials in this work, Al in bulk is type I, but the typically very thin films in use (cf. Section 1.2.3 and Ref. [54]), and especially disordered granular aluminum (grAl) become type II. The intermediate state in type II superconductors, referred to as Shubnikov phase, is microscopically explained by the formation of normal conducting islands, in which magnetic field can locally penetrate the material, usually called vortices [55]. Each of these vortices carries one flux quantum $\Phi_0 = h/2e$, and in two dimensions they will organize into a hexagonal lattice, the Abrikosov lattice, to minimize the total free enthalpy [50], with a distance

$$d_v = \sqrt{\frac{2\Phi_0}{\sqrt{3}B}} \approx 49\,\mathrm{nm} \times (B\,/\,\mathrm{T})^{-1/2} \tag{1.4}$$

between the vortices–an important metric in superconducting circuit design when flux trapping should be avoided.[5] In the case of our fluxonium qubit with a loop area of $140 \times 25\,\mu m^2$ (see Section 2.1.2), a magnetic field of 300 nT is needed to achieve a magnetic flux of $\Phi_0/2$ through the loop, resulting in a distance $d_v = 90\,\mu m$ between the vortices. In order to avoid flux trapping in close-by superconducting films, ideally at least one dimension of the structure is chosen to stay well below this value.

1.2.2 BCS Theory

Almost half a century had to pass until a satisfactory microscopic theory of superconductivity was published by Bardeen, Cooper and Schrieffer (BCS) in 1955 [56]. The observation of the isotope effect [57–60], as shown in Fig. 1.1A, revealed that the critical temperature T_c is inversely proportional to the square-root of the atomic mass M. This result provided the first hint that the lattice plays an important role in the underlying mechanism. Soon after, a promising idea emerged for a phonon-mediated, attractive interaction between electrons to overcome their strong Coulomb repulsion [61–64]. Building upon this, Cooper demonstrated that two electrons on the Fermi surface with opposite spin and momentum minimize their energy by forming a bound pair [65], which now bears his name.

The BCS theory shows that it is energetically favorable for $T < T_c$ to form a new quantum ground state in which electrons are virtually excited in Cooper pairs [56], creating an energy gap

$$\Delta_0 \approx 2\hbar\omega_D e^{-2/V_0 D(E_F)} \tag{1.5}$$

[5] As a good rule of thumb, a typical value for the total magnetic field strength in central Europe of $B = 49\,\mu T$ yields the easy-to-calculate distance $d_v = 7\,\mu m$.

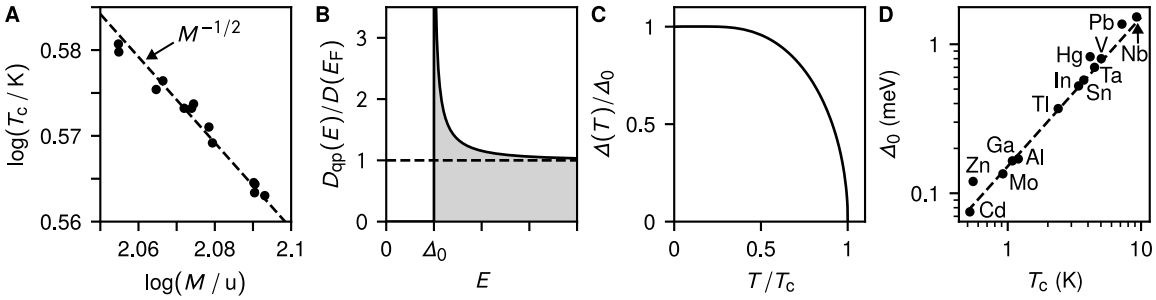

Figure 1.1: Plots related to BCS theory. **(A)** Critical temperature T_c of measured tin samples with varying atomic mass M [58–60], found to follow a $M^{-1/2}$ dependence (dashed line), which became known as isotope effect. The plot is adapted from Ref. [55]. **(B)** Quasiparticle density of states $D_{qp}(E)$, normalized to the density of states of the free-electron gas at the Fermi energy, $D(E_F)$, as a function of the quasiparticle energy E. The solid line was calculated with Eq. (1.7), showcasing the opening of an energy gap Δ_0 for quasiparticle excitations. The dashed line shows the density of states of electrons or holes in the normal conducting state. **(C)** Normalized energy gap $\Delta(T)/\Delta_0$ versus normalized temperature T/T_c, obtained by solving Eq. (1.8). **(D)** Energy gap Δ_0 at zero temperature versus critical temperature T_c for some typical elemental superconductors. The dashed line visualizes the BCS ratio prediction of Eq. (1.10).

for individual particle excitations, ω_D representing the Debye frequency. The approximation in Eq. (1.5) was made under two assumptions: The first assumption is a momentum-independent interaction potential V_0 across a spherical Fermi surface with constant density of states $D(E_F)$ around the Fermi energy E_F. Second, it is assumed that the Cooper pairs are only weakly coupled, $V_0 D(E_F) \ll 1$.

The necessary energy ΔW to break up a Cooper pair is given by

$$\Delta W = 2E = 2\sqrt{(E_{kin} - E_F)^2 + \Delta_0^2}, \tag{1.6}$$

illustrating that a minimum energy of $2\Delta_0$ is needed for such an excitation from the ground state, which are generally referred to as (Bogoliubov) quasiparticles. When their kinetic energy with respect to the Fermi energy, $E_{kin} - E_F$, is positive (negative), they possess electron-like (hole-like) character. From the conservation of states, it is found for the density of states $D_{qp}(E)$ of quasiparticles,

$$D_{qp}(E) = \begin{cases} D(E_F)/\sqrt{1 - (\Delta_0/E)^2} & \text{for } E > \Delta_0 \\ 0 & \text{for } E < \Delta_0, \end{cases} \tag{1.7}$$

which is also illustrated in Fig. 1.1B. For energies much larger than the Fermi energy, $E \gg E_F$, the quasiparticles essentially behave like free electrons in the normal metal.

For finite temperatures below the critical temperature, $0 < T < T_c$, thermally excited quasiparticles reduce the number of states available for electrons to exchange phonons [55], causing a reduction of the energy gap, $\Delta < \Delta_0$. The temperature-dependence of the energy gap, $\Delta = \Delta(T)$, can be extracted by numerically solving

$$\frac{2}{V_0 D(E_F)} = \int_0^{\hbar\omega_D} \frac{d\epsilon}{\sqrt{\epsilon^2 + \Delta^2}} \tanh\left(\frac{\sqrt{\epsilon^2 + \Delta^2}}{2k_B T}\right), \tag{1.8}$$

leading to the normalized gap $\Delta(T)/\Delta_0$ depicted in Fig. 1.1C. The special case that the energy gap disappears when reaching the critical temperature, $\Delta(T = T_c) = 0$, yields

$$k_B T_c = \frac{2e^{\gamma_E}}{\pi} \hbar \omega_D e^{-2/V_0 D(E_F)}, \tag{1.9}$$

with the Euler-Mascheroni constant $\gamma_E \approx 0.577$, explaining also the isotope effect, since $\omega_D \propto M^{-1/2}$. Combining Eq. (1.5) and Eq. (1.9) results in the familiar BCS ratio

$$\frac{\Delta_0}{k_B T_c} \approx 1.76. \tag{1.10}$$

Note that Eq. (1.10) is valid as long as all of the above assumptions hold, which is not necessarily the case for real superconductors [55]. For many elements such as Al, In or Nb, however, it is in good agreement (Fig. 1.1D). However, for grAl used extensively in this thesis, significant deviations are visible in the regime of large resistivity [66]. In conclusion, it is truly remarkable that the BCS theory with its very limited number of variables is able to explain most experimental findings, including the Meissner effect, the electrodynamic behavior, the critical field, the critical temperature as well as thermodynamic properties [50].

1.2.3 Surface Impedance

Despite having zero DC resistance below the critical temperature $T < T_c$, superconductors still exhibit non-zero surface impedance for RF signals at frequency ω,

$$Z_s = R_s + i\omega L_s, \tag{1.11}$$

where R_s and L_s describe the surface resistance and inductance, respectively. The surface inductance $L_s = L_m + L_{kin}$ consists of the ordinary magnetic or geometric inductance L_m and a so-called kinetic inductance L_{kin}. Microscopically, all charge carriers in a superconductor will be accelerated by high-frequency electric fields. Due to their inertia, the kinetic energy that is temporarily saved in the motion through the superconductor, can only be regained when the charges are decelerated by an oppositely signed electric field. Since this process involves a temporal delay between energy absorption and release, one can ascribe the charge carriers a kinetic inductance L_{kin}, which is however dominated by Cooper pairs, that can travel through the superconductor without any ohmic loss. Quasiparticles, on the other hand, underlie the same scattering processes as normal metal electrons. In consequence, they will lose kinetic energy during their motion, leading to a significantly smaller contribution to L_{kin} and a finite amount of ohmic loss, which is captured in R_s.

For a profound analysis of Eq. (1.11), based on the concept of a complex conductivity of a superconductor [67] within the Mattis-Bardeen theory [68], the reader is referred to the dissertation of Gao [69]. Here, it is focused on temperatures well below the critical temperature, $T \ll T_c$, where the resistive part is negligible, since quasiparticles exponentially die out, and the surface impedance is dominated by the inductive part, given by

$$Z_s \approx i\omega L_s = i\omega \mu_0 \lambda. \tag{1.12}$$

The magnetic penetration depth λ characterizes the length scale in which screening currents extend into the volume of a superconductor to shield from external magnetic fields, and it is one of three characteristic length scales, that characterize the electrodynamical properties of a superconductor. The other two quantities are, first, the coherence length $\xi_0 = \hbar v_\mathrm{F}/\pi\Delta_0$ (v_F is the Fermi velocity), which quantifies the length scale on which the Cooper pair density rises from zero at a normal metal interface[6] towards the bulk value in a superconductor [55], and second, the mean free path l of electrons in the normal state. Based on the relative sizes of these three quantities, the following limits are distinguished:

1. **London limit ($\lambda, l \gg \xi_0$)**
   In this regime, non-local effects can still be neglected and the magnetic field is constant over the extent of a Cooper pair. The magnetic penetration depth is identical to the London penetration depth which is defined within the phenomenological London theory [70] as
   $$\lambda = \lambda_\mathrm{L} = \sqrt{\frac{m_\mathrm{s}}{\mu_0 n_\mathrm{s} q_\mathrm{s}}}, \tag{1.13}$$
   where m_s, n_s and q_s represent the mass, density and charge of a Cooper pair, respectively. Superconductors in this regime are labeled 'pure' since electron scattering does not play a role ($l \gg \xi_0$), and they are typically of type II.

2. **Pippard limit ($l \gg \xi_0 \gg \lambda$)**
   Non-local effects are not anymore negligible, because the magnetic field varies strongly within the size of a Cooper pair and therefore, it has to be replaced by a suitably averaged field expression [71]. The magnetic penetration depth in this regime is given by
   $$\lambda \approx (0.28\lambda_\mathrm{L}^2 \xi_0)^{1/3}. \tag{1.14}$$
   Superconductors in this limit are still termed 'pure', but usually of type I. For example, many classical superconductors such as pure aluminum ($\lambda = 50\,\mathrm{nm}$ and $\xi_0 = 1600\,\mathrm{nm}$) belong to this regime.

3. **Dirty limit ($\lambda, \xi_0 \gg l$)**
   According to Pippard's nonlocal theory in Ref. [71], a reduction in the mean-free path increases the magnetic penetration depth as
   $$\lambda = \lambda_\mathrm{L}\sqrt{1 + \xi_0/l}. \tag{1.15}$$
   Superconductors in this limit can be realized for example by alloying a superconductor. They are labeled 'dirty' and are always of type II [50]. Granular aluminum (see Section 1.3.3), which is used to realize superinductors in the quantum circuits of this work, usually falls into this category. For typical normal state resistivities ($\rho_\mathrm{dc} > 100\,\mu\Omega\mathrm{cm}$), λ reaches a few micrometers [72], ξ_0 is expected to decrease only slightly ($\propto T_\mathrm{c}$), and $l \propto 1/\rho_\mathrm{dc}$ drops rapidly to below 1 nm [73, 74].

[6] Take as an example the normal metal cores in the Abrikosov lattice in type II superconductors (Section 1.2.1). Here, ξ_0 gives a characteristic length scale of their diameter.

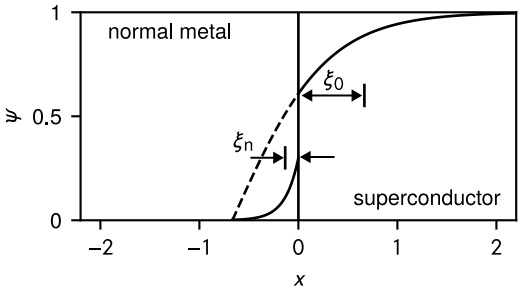

Figure 1.2: Proximity effect on a normal metal-superconductor interface. Order parameter ψ (solid line) versus distance x from the interface between normal metal ($x < 0$) and superconductor ($x > 0$). Included are the two characteristic length scales ξ_n and ξ_0, respectively. The dashed line shows the continuation of the tanh-shaped curve in the superconductor.

For thin films with thickness d, the expressions for the magnetic penetration depth, similar to the dirty limit, need to be equipped with a correction factor, $\lambda \rightarrow \lambda \coth(d/\lambda)$ [75]. Interestingly, this influence of the film thickness on the magnetic penetration depth can also change the behavior of a typical type I superconductor to behave as a type II superconductor for sufficiently thin films [54]. Lastly, at non-zero temperatures, λ is empirically found to obey $\lambda(T) = \lambda(0)\,(1 - T/T_c)^{-1/4}$ [75].

1.2.4 Proximity Effect

The proximity effect or Holm-Meissner effect [76] describes a phenomenon that occurs on the interface between a superconductor and a normal metal. The effect can be described microscopically by Andreev reflections [77, 78] at the interface, in which an electron in the normal metal transforms into a Cooper pair in the superconductor, and a reflected hole in the normal metal.

A more intuitive access to this effect can be given within the phenomenological Ginzburg-Landau theory [79], reducing the problem to the simple insight that the order parameter ψ, a local measure for the density of superconducting electrons, can not change infinitely quickly at the interface between two materials, in which the charge carriers are ordered very differently. As a consequence, it is possible for Cooper pairs to enter the normal metal within a characteristic length scale ξ_n. On the one hand, this extends the superconductor by a thin layer into the normal metal, and, on the other hand, this slightly depletes the number of Cooper pairs in the superconductor within the coherence length ξ_0 as a characteristic length scale [80], weakening the superconductivity in this layer. In Fig. 1.2, it is illustrated how the order parameter ψ would change near the interface between a normal metal and a superconductor according to the Ginzburg-Landau theory. A more rigorous calculation based on BCS theory [81], results in a coherence length

$$\xi_n = \frac{\hbar v_{F,n}}{2\pi k_B T}, \tag{1.16}$$

if it is dealt with a pure normal metal, in which the electron mean free path l_n is much smaller than ξ_n. $v_{F,n}$ is the Fermi velocity of the electrons in the normal metal. In case of a dirty normal metal ($l_n \gg \xi_n$), Eq. (1.16) needs to be adapted, $\xi_n \rightarrow \sqrt{\xi_n l_n/3}$. Values for ξ_n are typically ranging from 0.1 to 1 µm [80].

1.2.5 Josephson Effects

From the microscopic BCS theory, presented in Section 1.2.2, follows that "superconductivity is an inherently quantum phenomenon, which manifests itself on a macroscopic scale" [82]. For this reason, the whole ensemble of superconducting electrons can be described with a single macroscopic wavefunction

$$\psi(\vec{r}) = \sqrt{n_\mathrm{s}}\, e^{i\theta(\vec{r})}, \tag{1.17}$$

in which n_s describes the Cooper pair density, and $\theta(\vec{r})$ is the phase of the wavefunction.

The Josephson effects[7] result from the overlapping evanescent parts of the wavefunctions $\psi_1 = \sqrt{n_{\mathrm{s},1}}\, e^{i\theta_1}$ and $\psi_2 = \sqrt{n_{\mathrm{s},2}}\, e^{i\theta_2}$ of two superconductors, that are interrupted by either a thin insulating barrier (SIS), by a normal metal layer (SNS), by a geometric constriction in the superconductor (SCS or 'weak link') or by a ferromagnetic layer (SFS) [50]. All of these cases are summarized under the term 'Josephson junction' (JJ), but throughout the rest of the manuscript, the focus will be restricted to SIS junctions, as this is by far the most commonly used type of JJ in superconducting quantum circuits, thanks to its low intrinsic AC dissipation, and therefore the only relevant for the purpose.

Along with the wavefunction overlap comes coherent tunneling of Cooper pairs across the junction, allowing for a lossless transport in the form of a supercurrent, even if there is no potential difference between the two superconducting islands [50]. In the weak coupling limit, the following relation, also known as Josephson's first equation, holds for the supercurrent I_s across the junction [83, 85],

$$I_\mathrm{s} = I_\mathrm{c} \sin(\varphi). \tag{1.18}$$

Here, I_c is the critical current, which corresponds to the maximum current that can flow through the junction without the appearance of any voltage. Any current smaller than I_c that is injected through the junction will only lead to a phase difference $\varphi = \theta_2 - \theta_1$ between the two superconductors, known as the DC Josephson effect. I_c depends on parameters like the junction area, the junction thickness, as well as the Cooper pair densities $n_{\mathrm{s},1}$ and $n_{\mathrm{s},2}$ in the superconductors. When both superconductors are identical, Ambegaokar and Baratoff [86] showed that the BCS theory provides a relation between the normal state resistance R_n of a SIS junction and its critical current I_c,

$$R_\mathrm{n} I_\mathrm{c}(T) = \frac{\pi \Delta(T)}{2e} \tanh\left(\frac{\Delta(T)}{2k_\mathrm{B}T}\right), \tag{1.19}$$

where $\Delta(T)$ is the energy gap of both superconducting electrodes. For $T \longrightarrow 0$, Eq. (1.19) yields a handy way of estimating the critical current $I_\mathrm{c}(0)$ from the measurable R_n,

$$I_\mathrm{c}(0) = \frac{\pi \Delta_0}{2eR_\mathrm{n}}. \tag{1.20}$$

[7] First predicted in 1962 by Josephson [83] and experimentally observed three years later by Giaever [84].

Besides from Eq. (1.18), Ref. [83] provides a second prediction, namely that a voltage drop V across the junction is associated with the temporal evolution of the phase across the junction,

$$\dot{\varphi} = \frac{2\pi}{\Phi_0} V, \tag{1.21}$$

which is also known as Josephson's second equation. If a current larger than I_c is forced through the junction, Eq. (1.18) dictates that the current can not only be carried by a supercurrent. Instead, a quasiparticle current will also flow across the junction, inheriting the voltage drop V. Integrating Eq. (1.21) and inserting it in Eq. (1.18) yields a high-frequency supercurrent,

$$I_s(t) = I_c \sin(2\pi f_J t + \varphi_0), \tag{1.22}$$

with $f_J/V = 1/\Phi_0 \approx 0.483\,\mathrm{GHz}/\mu\mathrm{V}$, also known as AC Josephson effect. Together with the fact that frequencies are nowadays the most accurately measurable physical quantity [87, 88], this effect provides an excellent way to create a voltage standard [89].

Another way of combining the two Josephson equations is the following. According to Eq. (1.18), a varying supercurrent over time results in a similarly varying phase difference across the junction over time, which is connected to a voltage drop, as prescribed by Eq. (1.21). In this sense, the JJ behaves in exactly the same way as an inductor would, and the JJ can be ascribed a non-linear inductance $L(\varphi) = L_J/\cos(\varphi)$, with the Josephson inductance $L_J = (\Phi_0/2\pi)/I_c$. This can also be noted as an energy phase relationship in the form

$$E(\varphi) = -E_J \cos(\varphi), \tag{1.23}$$

with $E_J = (\Phi_0/2\pi)^2/L_J = \hbar I_c/(2e)$. This non-linear dependence is what quantum engineers would like to exploit, making the JJ essentially the basic building block for superconducting quantum bits, which will be addressed in more detail in the next chapter.

The applicability of the Josephson effects, however, does by far not end at this point. In fact, one of the most common application is probably superconducting interference devices (SQUIDs), which can measure magnetic fields with unprecedented precision, making them suitable as sensors in biomagnetic systems such as magnetoencephalography, to detect neuronal electrical currents, or magnetocardiography, to measure the local magnetic activity of the heart muscle [90, 91]. SQUIDs can also be used as in-situ cooled gradiometric sensors in geophysical explorations to deduce the presence of mineral ores or oil from local anomalities, or as primary thermometers in the temperature range from 10 mK to 10 K [92].

1.3 Superconducting Quantum Circuits

As pointed out in Section 1.1, the success story of superconducting qubits, with the Josephson junction (Section 1.2.5) as its working horse, has gone a long way since the first demonstration of the Cooper pair box in 1999 [32], and it resulted in various circuit designs like the transmon [37] or fluxonium qubit [38].

In this section, the concept of circuit quantization for describing superconducting circuits quantum mechanically is briefly introduced. After that, the focus lies on the qubit of choice, the fluxonium, together with the material of choice, granular aluminum, to realize the necessary superinductor. The section is concluded by introducing the framework of circuit quantum electrodynamics (cQED), which provides the dispersive readout scheme.

1.3.1 Circuit Quantization

Superconducting circuits can be treated as quantum mechanical systems that obey the time-dependent Schrödinger equation,

$$\hat{H}|\psi(t)\rangle = i\hbar\frac{\partial}{\partial t}|\psi(t)\rangle, \tag{1.24}$$

in which the Hamilton operator $\hat{H}$ represents the total energy of the system and determines the temporal evolution of the system's quantum state $|\psi(t)\rangle$. The technique of circuit quantization [93, 94] offers a practical yet systematic way of using the classical lumped element electrical circuit diagram of a system to deduce its quantum Hamiltonian. A good starting point is the most basic superconducting quantum circuit, the quantum harmonic oscillator (QHO), which is the quantum analog of a classical LC oscillator with inductance L and capacitance C, as illustrated in Fig. 1.3A. Following the formalism of circuit quantization yields the QHO Hamiltonian

$$\hat{H} = \frac{1}{2C}\hat{Q}^2 + \frac{1}{2L}\hat{\Phi}^2, \tag{1.25}$$

in which the charge operator $\hat{Q}$ and flux operator $\hat{\Phi}$ act as conjugate variables, obeying the commutation relation $[\hat{Q}, \hat{\Phi}] = \hat{Q}\hat{\Phi} - \hat{\Phi}\hat{Q} = -i\hbar$. By defining the operators $\hat{n} = \hat{Q}/(2e)$ and $\hat{\varphi} = (2\pi/\Phi_0)\hat{\Phi}$ for the reduced charge (or excess number of Cooper pairs on the capacitor) and the reduced flux (or gauge-invariant phase along the inductor), respectively, the Hamiltonian in Eq. (1.25) can be rewritten in the form

$$\hat{H} = \frac{1}{2}E_\mathrm{C}\hat{n}^2 + \frac{1}{2}E_\mathrm{L}\hat{\varphi}^2, \tag{1.26}$$

with the capacitive energy $E_\mathrm{C} = (2e)^2/C$ and the inductive energy $E_\mathrm{L} = (\Phi_0/2\pi)^2/L$. Note that this definition of the capacitive energy differs from the more common form $E'_\mathrm{C} = e^2/2C$ by a factor of 8. As elaborated in Ref. [95], the latter definition is, however, a historical remnant from single electron transistors, leading to an inconsistency with the definition of inductive energy that will be avoided throughout this work. Eq. (1.26) can be further simplified with the formalism of second quantization [96], resulting in

$$\hat{H} = \hbar\omega_\mathrm{r}\left(\hat{a}^\dagger\hat{a} + \frac{1}{2}\right), \tag{1.27}$$

where the resonance frequency $\omega_\mathrm{r} = \sqrt{E_\mathrm{L}E_\mathrm{C}}/\hbar$ and the creation (annihilation) operator $\hat{a}^\dagger$ ($\hat{a}$) were introduced. The latter are related to the original operators $\hat{n}$ and $\hat{\varphi}$ via

$$\hat{n} = n_\mathrm{zpf}\, i(\hat{a} - \hat{a}^\dagger) \quad \text{and} \quad \hat{\varphi} = \varphi_\mathrm{zpf}\,(\hat{a} + \hat{a}^\dagger). \tag{1.28}$$

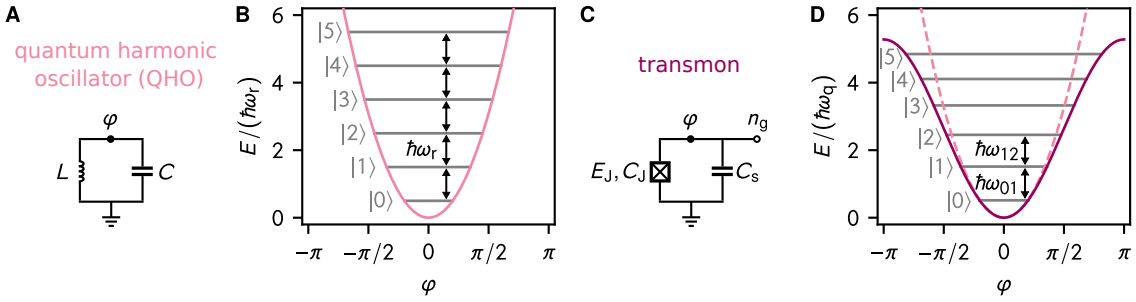

Figure 1.3: Two basic quantum circuits. **(A)** Electrical circuit diagram of the quantum harmonic oscillator (QHO), equal to the classical LC oscillator. According to the rules of circuit quantization, there is only a single node, with superconducting phase φ, besides the connection to ground. **(B)** Energy potential of the QHO (pink), in units of $\hbar\omega_\mathrm{r}$, versus phase φ. Values of $E_\mathrm{C}/h = 0.8\,\mathrm{GHz}$ and $E_\mathrm{L}/h = 5\,\mathrm{GHz}$ were chosen. The resulting energy levels (horizontal gray lines) are equidistantly spaced. **(C)** Electrical circuit diagram of the transmon, implementing the non-linearity of the Josephson junction. **(D)** Energy potential of the transmon (magenta), in units of $\hbar\omega_\mathrm{q}$, versus phase φ. Values of $E_\mathrm{C}/h = 0.8\,\mathrm{GHz}$ and $E_\mathrm{J}/h = 5\,\mathrm{GHz}$ were chosen, such that the transmon Hamiltonian Eq. (1.30) coincides with the Hamiltonian of the QHO from panel B for small φ (pink, dashed). The resulting energy levels of the transmon (horizontal gray lines) now inherit an anharmonicity α, as described in the text, allowing to separate two energy levels, typically the two lowest, $|0\rangle$ and $|1\rangle$, constituting the computational subspace.

Herein, n_zpf and φ_zpf describe the zero-point fluctuations of the reduced charge and flux, respectively, that are present even in the quantum mechanical ground state. They can also be written in the form

$$n_\mathrm{zpf} = \left(\frac{E_\mathrm{L}}{4E_\mathrm{C}}\right)^{1/4} = \frac{1}{2\sqrt{\pi z}} \quad \text{and} \quad \varphi_\mathrm{zpf} = \left(\frac{E_\mathrm{C}}{4E_\mathrm{L}}\right)^{1/4} = \sqrt{\pi z}, \tag{1.29}$$

where $z = Z/R_\mathrm{Q}$ is the resonator's impedance $Z = \sqrt{L/C}$ normalized to the resistance quantum $R_\mathrm{Q} = h/(2e)^2$ of a Cooper pair. By means of Eq. (1.29), it becomes evident that the choice of z determines whether the QHO is dominated by zero-point fluctuations in the reduced charge ($2\pi z \ll 1$) or the reduced flux ($2\pi z \gg 1$).

Solving the eigenvalue problem imposed by the Hamiltonian in Eq. (1.27), $\hat{H}|\psi\rangle = E|\psi\rangle$, results in an infinite series of eigenstates $|k\rangle$, ($k = 0, 1, 2, \dots$), with corresponding eigenenergies $E_k = \hbar\omega_\mathrm{r}(k + 1/2)$, that are all equivalently spaced, as can also be seen in Fig. 1.3B. This linearity of the energy levels renders the QHO impractical to use it as a qubit, for which a computational subspace of only two quantum states is needed, as control pulses of frequency ω_r (or higher harmonics of it) would always drive multiple transitions at the same time. Still, the QHO proves to be a useful circuit for the readout of a qubit, as shown in Section 1.3.4.

In order to introduce non-linearity to the energy spectrum, the linear inductor of the QHO is replaced with the Josephson junction (JJ) introduced in Section 1.2.5, as visualized in Fig. 1.3C. With the inherent non-linear inductance and energy-phase relationship in Eq. (1.23) of the junction, the Hamiltonian now reads

$$\hat{H} = \frac{1}{2}E_\mathrm{C}(\hat{n} - n_\mathrm{g})^2 - E_\mathrm{J}\cos(\hat{\varphi}), \tag{1.30}$$

in which a possible offset charge n_g has been included. This offset charge originates from external electric fields or quasiparticles, effectively leading to a charge dispersion of the resulting eigenstates and energies, and it can be controlled via a gate voltage from a nearby charge bias line. The total capacitance $C = (2e)^2/E_C = C_J + C_s$ is composed of the junction capacitance C_J and a shunt capacitance C_s in parallel to the junction.

Similar to the above discussion of the effect of the normalized impedance z onto the dominating zero point fluctuations in the QHO, the ratio E_J/E_C determines here whether it is dominated by charge noise ($E_J \ll E_C$) or flux noise ($E_J \gg E_C$). Gradually, the community has moved away from circuit designs with $E_J \leq E_C$, in which the dominating charge noise is found to be hard to suppress, towards ones for which $E_J \gg E_C$ is fulfilled [35]. The latter case is typically referred to as the transmon regime, and it is realized in practice by implementing a large shunting capacitance $C_s \gg C_J$. A ratio of $E_J/E_C \simeq 6$ is often chosen, since it represents a balance between an adequate suppression of charge noise and a sufficiently large anharmonicity $\alpha = (\omega_2 - \omega_1) - (\omega_1 - \omega_0) \approx -E_C/8$ on the order of a few hundred megahertz in the correct qubit frequency regime, $\omega_q = \omega_1 - \omega_0 \approx (\sqrt{E_L E_C} - E_C/8)/\hbar \simeq 3 - 6\,\mathrm{GHz}$ [35, 37]. The charge dispersion of the energy levels scales $\propto \exp(-8\sqrt{E_J/E_C})$, and therefore it is well-suppressed in the transmon regime. The energy spectrum of such a typical transmon is illustrated in Fig. 1.3D.

The transmon qubit clearly caught on as the favored basic building block for state-of-the-art quantum processors [20, 97–99], in a large part owing to its simple and reliable fabrication process, compared to other superconducting qubits, and the large improvement in coherence time and in quality of readout fidelity and control techniques over the past two decades. Despite this success story, many more challenges are ahead. Maybe, taking a step back and thinking outside the transmon box helps in wringing out one or another improvement.

1.3.2 Qubit of Choice: Fluxonium

The broader class of flux qubits conceptually build up on the transmon circuit, but with the clear distinction in that an inductive element is connected in parallel. One member of this group is the fluxonium circuit [38] that is illustrated in Fig. 1.4A, for which the impedance of the inductor exceeds the resistance quantum R_Q, which is usually labeled as a so-called superinductance. The fluxonium Hamiltonian reads

$$\hat{H} = \frac{1}{2}E_C\hat{n}^2 + \frac{1}{2}E_L\left(\hat{\varphi} - \varphi_{ext}\right)^2 - E_J\cos(\hat{\varphi}). \tag{1.31}$$

In Eq. (1.31), the influence of an offset charge has been omitted, since it is strongly suppressed by the superinductance. Conventionally, this superinductance is realized in the form of Josephson junction arrays [38, 100, 101], with innovative alternative approaches such as disordered superconductors, as in the present work granular aluminum (Section 1.3.3), emerging during the last decade.

At the same time, the inductor and the JJ form a closed loop, through which an external magnetic flux $\Phi_{ext} = (\Phi_0/2\pi)\varphi_{ext}$ can thread, which acts as a new control variable, similar

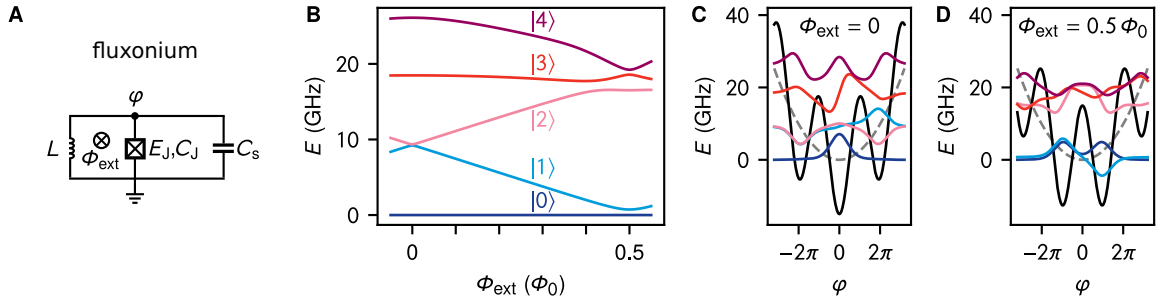

Figure 1.4: Fluxonium quantum circuit. **(A)** Electrical circuit diagram of the fluxonium, essentially consisting of a transmon circuit, that is shunted by a superinductor L, introducing a closed loop that encloses an external magnetic flux Φ_{ext}. Similar to the transmon, there is only a single node with superconducting phase φ. **(B)** Fluxonium energy spectrum, according to Eq. (1.31), of a fluxonium with parameters $E_C/h = 40\,\text{GHz}$, $E_L/h = 0.5\,\text{GHz}$ and $E_J/h = 15\,\text{GHz}$, illustrating the energies of the lowest five eigenstates with respect to the ground state, as a function of the external magnetic flux Φ_{ext}. At half-flux bias ($\Phi_{\text{ext}} = 0.5\,\Phi_0$), the fluxonium usually exhibits a particularly large anharmonicity, rendering the computational subspace of the two lowest energy levels $|0\rangle$ and $|1\rangle$ a well-controllable qubit here. **(C)** Energy potential (black) and wavefunctions (colored) versus phase φ for zero-flux bias, $\Phi_{\text{ext}} = 0$, and **(D)** for half-flux bias. The dashed gray line symbolizes the energy potential of a QHO with the same capacitive and inductive energy values, respectively. The colored lines represent the resulting wavefunctions of the lowest five eigenstates.

to the offset charge in the transmon. Its strong influence onto the energy levels is depicted in Fig. 1.4B.

In Fig. 1.4C and D, it can be seen that quite different energy potentials are possible by tuning Φ_{ext}, reaching from a single-well-like structure (Φ_{ext}=0) to a double-well-like one at lowest energies ($\Phi_{\text{ext}} = 0.5\,\Phi_0$), which results in very distinct sets of wavefunctions there. In general, much larger anharmonicities than for the transmon are achieved, which is an important prerequisite for fast and high-fidelity control gates.

Record-breaking coherence times up to 1.5 ms were observed with this qubit topology [44, 102], fueling its further investigation which includes first proposals for a high-performance quantum processor based on fluxonium qubits [103]

1.3.3 Material of Choice: Granular Aluminum

As discussed in the previous section, the fabrication of fluxonium qubits necessitates the realization of superinductors to suppress the sensibility to charge noise. Since the fabrication process of superconducting qubits usually already includes the integration of a Josephson junction (JJ), it is straightforward to utilize their inherent inductive behavior also for the realization of a superinductor. For this reason, the most commonly used platform are arrays with a large number ($\sim 10^2$) of JJs in the regime of $E_J/E_C \gg 1$, in which they possess a much larger critical current and are much more linear than the JJ that implements the non-linear qubit element [100].

An alternative approach to realize superinductors is achieved by harnessing the high kinetic inductance of disordered superconductors, most often in the form of nitrides such

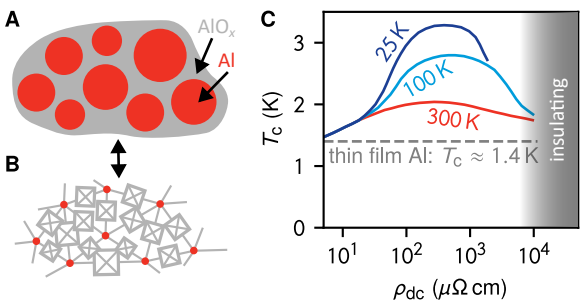

Figure 1.5: Granular aluminum. **(A)** Microscopically, grAl consists of pure Al grains interrupted by thin insulating AlO_x barriers, which can be modeled as **(B)** a network of JJs [120]. **(C)** Critical temperature T_c versus resistivity ρ_{dc} of grAl thin films, exhibiting the superconducting dome. Substrate cooling during grAl deposition allows for even larger values of T_c (data taken from Ref. [121]). For resistivities $\rho_{dc} \gtrsim 10^4\,\mu\Omega\,\text{cm}$, grAl becomes insulating.

as NbN [104–107], NbTiN [108–111] or TiN [112–115], but there exist also oxygen-based ones like InO [116, 117]. In this work, another disordered, oxygen-based superconductor named granular aluminum (grAl) is investigated. As shown in Fig. 1.5A and B, grAl is a nano-composite of quite uniform aluminum (Al) grains (diameter $2-4\,\text{nm}$) in an amorphous aluminum oxide (AlO_x) matrix [118, 119] that can be modeled as a network of JJs [95, 120]. A rather peculiar feature of grAl, illustrated in Fig. 1.5C, is that the added oxygen enhances the superconducting gap compared to pure Al, surpassing critical temperatures of 2 K with a dome-shaped dependence on the room-temperature direct-current (DC) resistivity ρ_{dc} [66], which becomes even more pronounced in cold-deposited grAl films [121]. This behavior is in stark contrast to other superconductors, such as Nb, that are weakened by the presence of impurities. For resistivities $\rho_{dc} \gtrsim 10^4\,\mu\Omega\,\text{cm}$, grAl undergoes a superconductor-to-insulator transition (SIT).

GrAl can be conveniently fabricated by providing an oxygen atmosphere during the standard evaporation of Al, in which the oxygen pressure determines the resistivity of the deposited thin film. In direct relationship with the resistivity, which is proportional to the normal state sheet resistance $R_\square = \rho_{dc} t$ of a film with thickness t, stands according to Eqs. (1.19) and (1.23) the superconductor's kinetic inductance, which can reach up to a few nH per square for thin films of grAl. A small element of volume V_{grAl}, structured from such a thin film, possesses an intrinsic non-linearity, which is quantified by the self-Kerr coefficient [120]

$$K_{11} \propto \frac{\omega_1^2}{j_c V_{grAl}}, \tag{1.32}$$

where ω_1 is the fundamental frequency of the element, and j_c is the critical current density of the grAl film, which is proportional to $1/\rho_{dc}$ [72]. By varying the fabrication parameters, one can achieve very different values for K_{11}, spanning a wide range from a few Hz to some MHz, rendering grAl as a versatile material for superconducting circuits. As such, grAl was demonstrated to be used as a low-loss and high-kinetic inductance material for superconducting resonators [122–124]. This promising development pushed forward its integration into circuits in need of a larger non-linearity such as a fluxonium qubit with a grAl-based superinductor [125], or parametric amplifiers [43]. Other important milestones, along with an even further increasing non-linearity, were reached in the realization of a transmon with a grAl JJ [126], and an all-grAl fluxonium (gralmonium) with an SCS JJ fabricated in a single deposition step [9].

Besides these rather specialized applications, grAl also receives much attention on a more fundamental level, due to its rich physics involving the Kondo effect and Kubo spins, for which the interested reader is referred to an excellent review in Ref. [127].

1.3.4 Circuit Quantum Electrodynamics

As one of the DiVincenzo criteria, which were briefly recited in Section 1.1, the measurement of the qubit state poses a challenge since the state readout should ideally happen with zero uncertainty. For this reason, the concept of quantum non-demolishing (QND) measurements has been put forward. The essential ingredient of QND measurements is that the quantum system does not evolve in time under the action of the measurement apparatus once it got projected [128]. The Hamiltonian of a system allowing for a QND measurement would commute with the measurement operator $\hat{O}_{\mathrm{M}}$, and it can be realized by a longitudinal interaction between the qubit and the readout.

The neighboring field of cavity quantum electrodynamics, in which the interaction between matter (atoms) and light (photons) is studied, has already put large effort into the study and realization of QND measurements. Its huge success [129–131] led to a knowledge transfer to the world of superconducting circuits, which got known as circuit quantum electrodynamics (cQED) [132]. In cQED, a superconducting qubit, such as the two lowest energy levels of a fluxonium circuit, is coupled to the bosonic modes of a readout resonator or a cavity.

The quantum Rabi model provides a framework in which the longitudinal interaction between light and matter is approximated by a transversal one, which results in the following Hamiltonian [133]:

$$\hat{H} = \hbar\omega_{\mathrm{r}}\left(\hat{a}^{\dagger}\hat{a} + \frac{1}{2}\right) + \frac{\hbar\omega_{\mathrm{q}}}{2}\hat{\sigma}_z + \hbar g(\hat{a}^{\dagger} + \hat{a})(\hat{\sigma}^{-} + \hat{\sigma}^{+}), \tag{1.33}$$

where ω_{r} and ω_{q} are the resonator and qubit frequencies, respectively, and g represents the interaction strength between the resonator and the qubit. $\hat{a}$ and $\hat{a}^{\dagger}$ describe the annihilation and creation operators for the resonator mode, $\hat{\sigma}^{-}$ and $\hat{\sigma}^{+}$ similarly for the qubit mode.[8] Generally, all terms in Eq. (1.33) should be considered [134–136], in order to properly capture the interaction strength, which can be significantly larger in cQED than in cavity QED [93]. For now, however, the discussion continues with the Jaynes-Cummings formalism [137], which omits counter-rotating terms in the quantum Rabi Hamiltonian in Eq. (1.33), such as $\hat{a}^{\dagger}\hat{\sigma}^{+}$, since they play a minor role in the time evolution of the quantum states [138]. This so-called rotating-wave approximation (RWA) leads to the Jaynes-Cummings Hamiltonian

$$\hat{H} = \hbar\omega_{\mathrm{r}}\left(\hat{a}^{\dagger}\hat{a} + \frac{1}{2}\right) + \frac{\hbar\omega_{\mathrm{q}}}{2}\hat{\sigma}_z + \hbar g(\hat{a}^{\dagger}\hat{\sigma}^{-} + \hat{a}\hat{\sigma}^{+}), \tag{1.34}$$

[8] These operators can also be written as $\hat{\sigma}^{\pm} = \hat{\sigma}_x \pm i\hat{\sigma}_y$, and they are therefore based on the Pauli spin matrices $(\hat{\sigma}_x, \hat{\sigma}_y, \hat{\sigma}_z)$ that are introduced in Section 1.4.1.

In this case, it is possible to diagonalize the Hamiltonian to find the eigenenergies of the resonator-qubit system,

$$\begin{aligned} E_{|n_\mathrm{r},0_\mathrm{q}\rangle} &= \hbar\omega_\mathrm{r} n_\mathrm{r} + \frac{\hbar\Delta}{2}\sqrt{1+(2g/\Delta)^2 n_\mathrm{r}}, \\ E_{|n_\mathrm{r},1_\mathrm{q}\rangle} &= \hbar\omega_\mathrm{r}(n_\mathrm{r}+1) - \frac{\hbar\Delta}{2}\sqrt{1+(2g/\Delta)^2 (n_\mathrm{r}+1)}, \end{aligned} \tag{1.35}$$

where $n_\mathrm{r} = \langle \hat{a}^\dagger \hat{a} \rangle$ signifies the number of photons in the resonator, and $\Delta = \omega_\mathrm{q} - \omega_\mathrm{r}$ is the detuning between qubit and resonator mode. Particularly of interest is the dispersive coupling regime [139], for which the detuning is much larger than the coupling strength, $\Delta \gg g$, such that Eq. (1.35) simplifies to

$$\hat{H} = \hbar\left(\omega_\mathrm{r} + \frac{g^2}{\Delta}\hat{\sigma}_z\right)\hat{a}^\dagger\hat{a} + \frac{\hbar}{2}\left(\omega_\mathrm{q} + \frac{g^2}{\Delta}\right)\hat{\sigma}_z. \tag{1.36}$$

Here, two observations about the mutual influence between resonator and qubit can be made: First, the resonator mode acquires a dispersive shift $\chi = \pm g^2/\Delta$ depending on the qubit state, and second, the qubit now inherits a constant offset g^2/Δ, the Lamb shift, only because of the presence of the readout. The terms in Eq. (1.36) can, however, also be sorted in a different way,

$$\hat{H} = \hbar\omega_\mathrm{r}\hat{a}^\dagger\hat{a} + \frac{\hbar}{2}\left(\omega_\mathrm{q} + \frac{g^2}{\Delta}(1+2\hat{a}^\dagger\hat{a})\right)\hat{\sigma}_z. \tag{1.37}$$

This representation facilitates to see that the interaction between qubit and resonator can also be interpreted as a $2\chi n_\mathrm{r}$ shift of the qubit mode, that depends on the number of photons n_r in the resonator. This effect is also known as the AC Stark effect, and it can be used to calibrate the resonator photon number, if the dispersive shift has been independently measured from IQ distributions (as described in Section 3.2.2).

The dispersive readout scheme has become the standard method to read out superconducting qubits. Fig. 1.6A and B illustrate how this scheme is realized by coupling the readout mode either inductively or capacitively to the fluxonium, respectively. The Hamiltonian of the coupled resonator-fluxonium system can be written in the natural basis of $\hat{\vec{n}} = (\hat{n}_\mathrm{r}, \hat{n}_\mathrm{q})^T$ and $\hat{\vec{\varphi}} = (\hat{\varphi}_\mathrm{r}, \hat{\varphi}_\mathrm{q} - \hat{\varphi}_\mathrm{ext})^T$ as

$$\begin{aligned} \hat{H} &= \frac{1}{2}\hat{\vec{n}}^T\mathbf{E}_\mathrm{C}\hat{\vec{n}} + \frac{1}{2}\hat{\vec{\varphi}}^T\mathbf{E}_\mathrm{L}\hat{\vec{\varphi}} - E_\mathrm{J}\cos(\hat{\varphi}_\mathrm{q} - \varphi_\mathrm{ext}) \quad \text{with} \\ \mathbf{E}_\mathrm{C} &= \begin{pmatrix} E_{C_\mathrm{r}} & 0 \\ 0 & E_{C_\mathrm{q}} \end{pmatrix} \quad \text{and} \quad \mathbf{E}_\mathrm{L} = \begin{pmatrix} E_{L'_\mathrm{r}} & E_{L'_\mathrm{s}} \\ E_{L'_\mathrm{s}} & E_{L'_\mathrm{q}} \end{pmatrix} \quad \text{for inductive,} \\ \mathbf{E}_\mathrm{C} &= \begin{pmatrix} E_{C'_\mathrm{r}} & -E_{C'_\mathrm{s}} \\ -E_{C'_\mathrm{s}} & E_{C'_\mathrm{q}} \end{pmatrix} \quad \text{and} \quad \mathbf{E}_\mathrm{L} = \begin{pmatrix} E_{L_\mathrm{r}} & 0 \\ 0 & E_{L_\mathrm{q}} \end{pmatrix} \quad \text{for capacitive} \end{aligned} \tag{1.38}$$

coupling, respectively. Herein, the reduced capacitances $C'_\mathrm{r} = C_\mathrm{r} - C_\mathrm{s}^2/C_\mathrm{q}$, $C'_\mathrm{q} = C_\mathrm{q} - C_\mathrm{s}^2/C_\mathrm{r}$, $C'_\mathrm{s} = C_\mathrm{s} - C_\mathrm{r}C_\mathrm{q}/C_\mathrm{s}$ and similar expressions for the inductances were introduced. The reader is referred to Ref. [95] for a thorough derivation of Eq. (1.38), as well as a discussion of strategies for its numerical diagonalization. There, it is also shown that the inductive

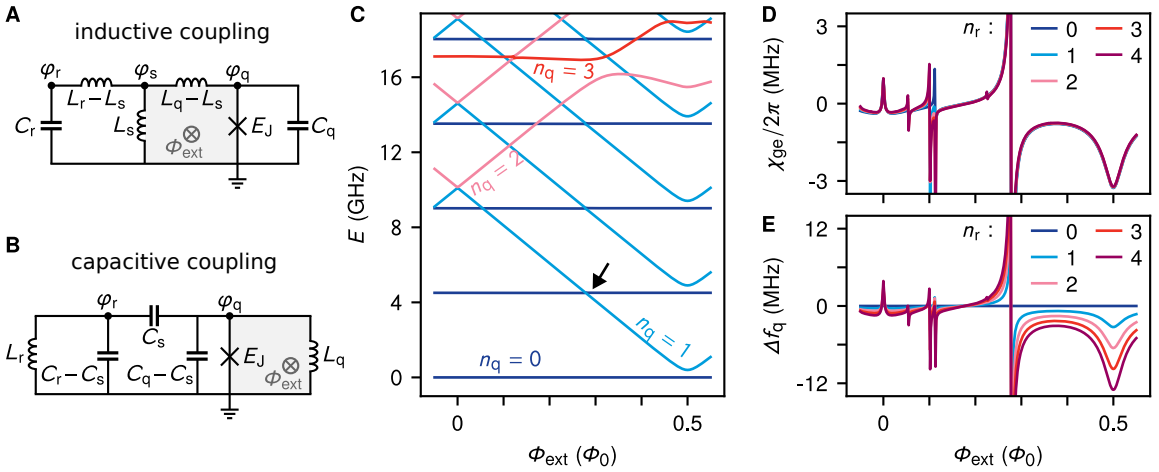

Figure 1.6: Dispersive fluxonium readout. Electrical circuit diagrams of an **(A)** inductively and **(B)** capacitively coupled resonator-fluxonium system. The fluxonium is threaded by an external magnetic flux Φ_{ext} and couples to the readout resonator with total inductance L_r (total capacitance C_r) by sharing an inductance L_s (capacitance C_s) of its total inductance L_q (total capacitance C_q). Out of the three nodes with phases φ_r, φ_q and φ_s in panel A only two are independent. **(C)** Sorted energy spectrum of an inductively coupled fluxonium with the parameters $L_r = 25$ nH, $C_r = 50$ fF, $L_q = 300$ nH, $C_q = 5$ fF, $E_J = 15$ GHz, $L_s = 5$ nH, as a function of Φ_{ext}. Lines of the same color correspond to dressed eigenstates $|\overline{n_q, n_r}\rangle$ with maximum overlap with a product state $|n_q, n_r\rangle = |n_q\rangle \otimes |n_r\rangle$ with the same number of photons in the qubit, n_q, and only differ by the amount of photons in the resonator, n_r. In the vicinity of an avoided level crossing, as indicated by the arrow, the correspondence between dressed eigenstates and product states becomes useless and n_q and n_r lose their property of being a good quantum number. **(D)** Dispersive shift χ_{ge} and **(E)** AC Stark shift Δf_q of the lowest qubit transition for different n_r. Generally, the amount of features appearing in both these quantities tends to increase with larger n_r.

and capacitive coupling can be mapped onto each other, and thus, they can result in the same energy spectrum. The caveat, however, is that the charge and flux matrix elements, relevant for qubit decoherence (see Section 1.5), generally differ.

Ref. [95] also presents a robust sorting algorithm for the numerically calculated eigenstates of the rich energy spectrum, made available in the *bfqcircuits* library [140]. An example for such a sorted energy spectrum for a typical set of resonator, fluxonium and coupling parameters is shown in Fig. 1.6C. The sorted energy spectrum also allows for the calculation of the dispersive shifts χ_{jk} as a function of the external magnetic flux bias φ_{ext}, which are defined by

$$\begin{aligned} h\chi_{jk}(n_r) &= (E_{|n_r,k\rangle} - E_{|0,k\rangle}) - (E_{|n_r,j\rangle} - E_{|0,j\rangle}) \\ &= (E_{|n_r,k\rangle} - E_{|n_r,j\rangle}) - (E_{|n_r-1,k\rangle} - E_{|n_r-1,j\rangle}). \end{aligned} \tag{1.39}$$

The two representation methods highlight once more the fact that the influence between resonator and qubit is of mutual nature. Fig. 1.6D shows the most relevant dispersive shift $\chi_{ge} = \chi_{01}(n_r)$ within the computational subspace of the fluxonium qubit, while Fig. 1.6E shows the associated AC Stark shift $\Delta f_q(n_r)$ of the bare qubit frequency for different resonator photon numbers n_r. The latter is given by

$$h\Delta f_q(n_r) = (E_{|n_r,1\rangle} - E_{|n_r,0\rangle}) - (E_{|0,1\rangle} - E_{|0,0\rangle}). \tag{1.40}$$

Nowadays, a point has been reached at which cQED proved to be a worthy successor of cavity QED, repeatedly showing fast QND-like readout on a timescale of $\sim 100\,\mathrm{ns}$ with fidelities surpassing 99 % [141–148]. However, the continuous improvements in qubit readout have also unveiled limits for many of the above approximations for the dispersive coupling regime, and the tiny remaining amount of infidelity is what is of most importance, in fact. On the one hand, it represents the processes that are not yet fully understood, and on the other hand, it is a limiting factor towards the realization of a fully-fledged quantum processor. The assumption of a superconducting artificial atom being a perfect two-level system was questioned since the early days of cQED, especially in case of the transmon with its low anharmonicity [149]. The ongoing study of measurement-induced state transitions, mostly in transmons [134–136, 150, 151], but nowadays also in fluxoniums [152], sheds more and more light into this exciting field of research. Recent developments stress that the readout infidelity should not be the only measure to quantify the readout quality, but readout-induced leakage should also be characterized independently [153, 154].

1.4 Open Quantum Systems

In this section, a closer look is taken at open quantum systems, which are a common framework to describe qubit decoherence (see Section 1.5). Section 1.4.1 starts by introducing the concept of a density matrix, before presenting the Lindblad master equation, both from a phenomenological (Section 1.4.2) as well as a microscopical (Section 1.4.3) point-of-view.

1.4.1 Density Matrix

The concept of a density matrix ρ, or density operator, is equivalent to the state vector $|\psi\rangle$, or wavefunction, formalism in an isolated quantum system, that can only be in a pure state, over which all information is known. However, in situations when a system's interaction with its environment is investigated, or when it is entangled with another system, the system is said to be in a mixed state, since it exchanges information with the environment or the other system. In this case, the density matrix approach offers a suitable representation of the system,

$$\rho = \sum_j \lambda_j |\psi_j\rangle\langle\psi_j|. \tag{1.41}$$

The density matrix inherits three important properties: First, it is Hermitian, $\rho = \rho^\dagger$, ensuring that all of its eigenvalues are real. Second, its trace is one, $\mathrm{Tr}\{\rho\} = 1$, which normalizes the probabilities, and third, it is always positive semi-definite, $\langle\psi|\rho|\psi\rangle \geq 0$, $\forall\,|\psi\rangle$, asserting that all probabilities λ_j are non-negative. The time evolution of the density matrix is governed by the von-Neumann equation,

$$\dot{\rho} = -\frac{i}{\hbar}\left[\hat{H}, \rho\right]. \tag{1.42}$$

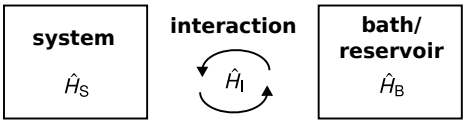

Figure 1.7: Open quantum system. A system with Hamiltonian $\hat{H}_S$ (e.g. a resonator-fluxonium) that couples via the interaction Hamiltonian $\hat{H}_I$ to a bath or reservoir with Hamiltonian $\hat{H}_B$.

For N quantum systems prepared in states ρ_i, their joint state can be written as $\rho = \rho_1 \otimes \rho_2 \otimes \cdots \otimes \rho_N$. One of the subsystems ρ_i can be removed from the joint state by tracing it out, $\rho_1 \otimes \rho_2 \otimes \cdots \otimes \rho_{i-1} \otimes \rho_{i+1} \otimes \cdots \otimes \rho_N = \mathrm{Tr}_i\{\rho\}$, via the partial trace Tr_i.

The density matrix of a qubit with basis states $|0\rangle$ and $|1\rangle$ has the general form,

$$\rho = \begin{pmatrix} \rho_{00} & \rho_{01} \\ \rho_{10} & \rho_{11} \end{pmatrix}. \tag{1.43}$$

The diagonal terms ρ_{00} and ρ_{11} (populations) represent the probabilities of measuring the qubit in $|0\rangle$ and $|1\rangle$, respectively. To fulfill the above criteria, they need to be non-negative and add up to one. The off-diagonal entries $\rho_{01} = \rho_{10}^{\dagger}$ (coherences) are a measure of the statistical mixture or entanglement with the environment. This qubit density matrix can also be expressed in terms of the Pauli spin matrices[9],

$$\rho = \frac{1}{2}\left(\mathbb{1} + \vec{r} \cdot \vec{\sigma}\right), \tag{1.44}$$

in which $\vec{r}$ is the Bloch vector for the quantum state ρ. All possible states set up the Bloch sphere, which is an intuitive way to visualize the qubit state. While all pure states ($\mathrm{Tr}\{\rho^2\} = 1$) lie on the surface of the sphere ($|\vec{r}| = 1$), any mixed state lies within it ($|\vec{r}| < 1$). The maximally mixed state $\rho = \mathbb{1}/2$ is located in the center of the sphere.

1.4.2 Lindblad Master Equation

Fig. 1.7 depicts an open quantum system with Hamiltonian $\hat{H}_S$ (e.g. a superconducting qubit) that is coupled to a bath or reservoir with Hamiltonian $\hat{H}_B$ via an interaction Hamiltonian $\hat{H}_I$, resulting in the total Hamiltonian

$$\hat{H} = \hat{H}_S \otimes \mathbb{1} + \mathbb{1} \otimes \hat{H}_B + \hat{H}_I. \tag{1.45}$$

The interaction Hamiltonian can usually be written as a sum of tensor products of Hermitian bath operators $\hat{B}_\alpha = \hat{B}_\alpha^{\dagger}$ acting on the system via the Hermitian operators $\hat{A}_\alpha = \hat{A}_\alpha^{\dagger}$, thus $\hat{H}_I = \sum_\alpha \hat{A}_\alpha \otimes \hat{B}_\alpha$. In principle, the evolution of the total density matrix ρ is governed by Eq. (1.42), but usually only the evolution of the system density matrix ρ_S is of interest, so the bath can be traced out,

$$\dot{\rho_S} = -\frac{i}{\hbar}\mathrm{Tr}_B\left\{\left[\hat{H}, \rho\right]\right\}. \tag{1.46}$$

[9] $\vec{\sigma} = (\hat{\sigma}_x, \hat{\sigma}_y, \hat{\sigma}_z)^T$, with $\hat{\sigma}_x = \left(\begin{smallmatrix} 0 & 1 \\ 1 & 0 \end{smallmatrix}\right)$, $\hat{\sigma}_y = \left(\begin{smallmatrix} 0 & -i \\ i & 0 \end{smallmatrix}\right)$ and $\hat{\sigma}_z = \left(\begin{smallmatrix} 1 & 0 \\ 0 & -1 \end{smallmatrix}\right)$

This integro-differential equation, known as Nakajima-Zwanzig equation [155, 156], is generally hard to calculate as it contains unnecessarily many details. The sheer amount of subsystems in the reservoir leads to a vast number of degrees of freedom, which is even worse when looking at the exponential scaling of the Hilbert space. An alternative, bottom-up route lies in in the axiomatic approach of Kraus maps which preserve the fundamental properties of a density matrix, see Section 1.4.1. Within the Markov approximation, the reservoir is assumed to retain no information about the system on longer timescales, and therefore it can be considered memoryless. With this assumption, one arrives at the Markovian master equation, $\partial_t \rho_\mathrm{S} = \mathcal{L}\rho_\mathrm{S}(t)$, with the Liouville superoperator $\mathcal{L}$. The Lindblad form of this master equation,

$$\frac{\partial \rho}{\partial t} = -\frac{i}{\hbar}[\hat{H}, \rho] + \sum_\alpha \mathcal{D}[\hat{L}_\alpha]\rho \qquad \text{with} \qquad \mathcal{D}[\hat{L}_\alpha]\rho = \hat{L}_\alpha \rho \hat{L}_\alpha^\dagger - \frac{1}{2}\left\{\hat{L}_\alpha^\dagger \hat{L}_\alpha, \rho\right\}, \tag{1.47}$$

is shown to be the most general Markovian solution for the evolution of a density matrix [157].[10] The Lindblad superoperators $\mathcal{D}[\hat{L}_\alpha]\rho$ capture the system's interaction with the bath and therefore account for its decoherence [158–160]. For example, the Lindblad operators $\hat{L}_\downarrow = \sqrt{\Gamma_\downarrow}\,\hat{\sigma}_-$, $\hat{L}_\uparrow = \sqrt{\Gamma_\uparrow}\,\hat{\sigma}_+$, $\hat{L}_\varphi = \sqrt{\Gamma_\varphi/2}\,\hat{\sigma}_z$ describe relaxation, excitation and pure dephasing, respectively, of a qubit system, as introduced in Section 1.5. However, this introduction of qubit decoherence has been purely phenomenological and lacks a microscopic description so far, which will be addressed in the next section.

1.4.3 Microscopic Derivation of the BSM Master Equation

The following derivation is based on Refs. [159] and [160], and it starts by transforming the von-Neumann equation in Eq. (1.46) into the interaction picture (in which operators and density matrices will be indicated with bold font). Re-inserting the formally integrated equation back into itself yields

$$\dot{\boldsymbol{\rho}}_\mathrm{S}(t) = -\frac{i}{\hbar}\mathrm{Tr}_\mathrm{B}\left\{\left[\hat{\boldsymbol{H}}_\mathbf{I}(t), \rho_0\right]\right\} - \frac{1}{\hbar^2}\int_0^t \mathrm{d}t'\,\mathrm{Tr}_\mathrm{B}\left\{\left[\hat{\boldsymbol{H}}_\mathbf{I}(t), \left[\hat{\boldsymbol{H}}_\mathbf{I}(t'), \boldsymbol{\rho}(t')\right]\right]\right\} \tag{1.48}$$

This integro-differential equation is still exact but not closed, as the integral on the r.h.s. depends on the full density matrix at all previous times. The Born approximation, though crude, is the next step in moving forward and assumes the system and bath are uncorrelated, i.e. $\boldsymbol{\rho}(t) = \boldsymbol{\rho}_\mathrm{S}(t) \otimes \boldsymbol{\rho}_\mathbf{B}(t)$.[11] This assumption would however fail over time as system and bath become entangled. To maintain validity at least for a statistical ensemble, the system is subject to the condition of being constantly reinitialized in a product state, with the bath state chosen randomly. The bath is assumed to be in equilibrium and its density matrix diagonal, known as the random phase assumption [161]. For this, the interaction of the

[10] For two operators A and B, $\{A, B\} = AB + BA$ represents the anti-commutator.
[11] For more information on this step, the reader is referred to Ref. [95].

system with the bath should be weak to ensure the bath state $\boldsymbol{\rho}_{\mathbf{B}}(t) = \bar{\rho}_{\mathrm{B}}$ remains largely unchanged. In total, the Born approximation alters Eq. (1.48) to

$$\dot{\boldsymbol{\rho}}_{\mathrm{S}}(t) = -\frac{1}{\hbar^2}\int_0^t \mathrm{d}t'\,\mathrm{Tr}_{\mathrm{B}}\left\{\left[\hat{\boldsymbol{H}}_{\mathbf{I}}(t),\left[\hat{\boldsymbol{H}}_{\mathbf{I}}(t'),\boldsymbol{\rho}_{\mathrm{S}}(t')\otimes\bar{\rho}_{\mathrm{B}}\right]\right]\right\}, \tag{1.49}$$

in which the first term on the r.h.s. of Eq. (1.48) was removed because of the diagonality of $\bar{\rho}_{\mathrm{B}}$. By using the diagonal decomposition of the interaction Hamiltonian that was introduced in Section 1.4.2, one arrives at

$$\begin{aligned}\dot{\boldsymbol{\rho}}_{\mathrm{S}}(t) = -\frac{1}{\hbar^2}\int_0^t \mathrm{d}t' \sum_{\alpha\beta}\Big(& C_{\alpha\beta}(t,t')\left[\hat{A}_\alpha(t)\hat{A}_\beta(t')\boldsymbol{\rho}_{\mathrm{S}}(t') - \hat{A}_\beta(t')\boldsymbol{\rho}_{\mathrm{S}}(t')\hat{A}_\alpha(t)\right] \\ & + C_{\beta\alpha}(t',t)\left[\boldsymbol{\rho}_{\mathrm{S}}(t')\hat{A}_\beta(t')\hat{A}_\alpha(t) - \hat{A}_\alpha(t)\boldsymbol{\rho}_{\mathrm{S}}(t')\hat{A}_\beta(t')\right]\Big),\end{aligned} \tag{1.50}$$

with the bath self-correlation functions

$$C_{\alpha\beta}(t,t') = \mathrm{Tr}_{\mathrm{B}}\left\{\hat{B}_\alpha(t)\hat{B}_\beta(t')\bar{\rho}_{\mathrm{B}}\right\} = \langle\hat{B}_\alpha(t)\hat{B}_\beta(t')\rangle_{\bar{\rho}_{\mathrm{B}}}, \tag{1.51}$$

which quantify the extent to which the bath preserves information about its interactions with the system over time [160]. The master equation in Eq. (1.50) is time-local, but not yet Markovian. For this, the Markovian approximations will be imposed: first, the retarded-time density operator is replaced by the current-time one, $\boldsymbol{\rho}_{\mathrm{S}}(t') \approx \boldsymbol{\rho}_{\mathrm{S}}(t)$, and second, the integral limit is extended to infinity, which is justified by the typically rapidly decaying self-correlation function. Transforming the resulting equation back to the Schrödinger picture yields the time-local Redfield equation [161],

$$\begin{aligned}\dot{\rho}_{\mathrm{S}}(t) = -\frac{i}{\hbar}\left[\hat{H}_{\mathrm{S}},\rho_{\mathrm{S}}(t)\right] - \frac{1}{\hbar^2}\int_0^\infty \mathrm{d}\tau \sum_{\alpha\beta}\Big(& C_{\alpha\beta}(\tau)\left[\hat{A}_\alpha,\hat{\boldsymbol{A}}_{\boldsymbol{\beta}}(-\tau)\rho_{\mathrm{S}}(t)\right] \\ & + C_{\beta\alpha}(-\tau)\left[\rho_{\mathrm{S}}(t)\hat{\boldsymbol{A}}_{\boldsymbol{\beta}}(-\tau),\hat{A}_\alpha\right]\Big),\end{aligned} \tag{1.52}$$

Unfortunately, this master equation is not of Lindblad form, as it does not necessarily maintain positivity of $\rho_{\mathrm{S}}(t)$. To overcome this last challenge, the system energy eigenbasis, $\hat{H}_{\mathrm{S}}|k\rangle = \hbar\omega_{\mathrm{k}}|k\rangle$, is introduced and used to make the time-dependence of the coupling operators in the interaction picture explicit [159]. Now, before transforming back to the Schrödinger picture, the so-called secular approximation is applied, in which fast-oscillating terms are neglected. Some more transformations finally lead to the Born-Markov-Secular (BMS) master equation, which takes on the form [159]

$$\begin{aligned}&\dot{\rho}_{\mathrm{S}}(t) = -\frac{i}{\hbar}\left[\hat{H}_{\mathrm{S}} + \sum_{lk}\sigma_{lk}L_{lk},\rho_{\mathrm{S}}(t)\right] + \frac{1}{\hbar^2}\sum_{lknm}\gamma_{lk,nm}\left[L_{lk}\rho_{\mathrm{S}}(t)L_{nm}^\dagger - \frac{1}{2}\left\{L_{nm}^\dagger L_{lk},\rho_{\mathrm{S}}(t)\right\}\right], \\ &\quad\text{with}\qquad \gamma_{lk,nm} = \sum_{\alpha\beta}\gamma_{\alpha\beta}(\omega_{lk})\delta_{\omega_{lk},\omega_{mn}}\langle k|A_\beta|l\rangle\langle n|A_\alpha|m\rangle^* \\ &\quad\text{and}\qquad \sigma_{lk} = \sum_{\alpha\beta}\sum_n\frac{1}{2i}\sigma_{\alpha\beta}(\omega_{ln})\delta_{\omega_l,\omega_k}\langle n|A_\beta|l\rangle\langle n|A_\alpha|k\rangle^*.\end{aligned} \tag{1.53}$$

Herein, $\hat{L}_{lk} = |l\rangle\langle k|$ signifies the Lindblad jump operator and $\omega_{lk} = \omega_l - \omega_k$ the transition frequency between two eigenstates $|k\rangle$ and $|l\rangle$, respectively. As seen from the first part of the BMS master equation, the odd Fourier transforms $\sigma_{\alpha\beta}(\omega) = \int_{-\infty}^{\infty} \mathrm{d}\tau\, C_{\alpha\beta}(\tau)\mathrm{sgn}(\tau)e^{+i\omega\tau}$ of the bath correlation functions $C_{\alpha\beta}(\tau)$ renormalize the system eigenenergies by the Lamb shift. In contrast, the even Fourier transforms $\gamma_{\alpha\beta}(\omega) = \int_{-\infty}^{\infty} \mathrm{d}\tau\, C_{\alpha\beta}(\tau)e^{+i\omega\tau}$ describe the system decoherence induced by the bath, as will be shown in the following section. Since the coupling operators A_α and B_α are Hermitian, it follows that the bath correlation functions fulfill $C_{\alpha\beta}(\tau) = C^*_{\beta\alpha}(-\tau)$, that is, $\gamma_{\alpha\beta}(\omega) = \gamma_{\alpha\beta}(-\omega)$ is always real and $\sigma_{\alpha\beta}(\omega) = -\sigma_{\alpha\beta}(-\omega)$ is always imaginary.

1.5 Qubit Decoherence

The previous section made evident that the interaction of a quantum system with its environment induces additional terms in the evolution of the density matrix. The presence of the environment can be regarded as an ubiquitous observer of the qubit, continuously extracting information about the qubit state. If an external observer could keep track of the full qubit environment, the spreading entanglement could in principle be measured, and the qubit with its environment could be treated as another closed quantum system [162]. However, tracing the plethora of individual quantum systems connected to a (not to mention macroscopic superconducting) qubit is simply infeasible. Anyways, most times only the dynamics of an isolated qubit are of interest, in which case the situation can be seen as a loss of information about the qubit state, which is commonly referred to as qubit decoherence.

Qubit decoherence comes in two distinct forms. First, there is qubit depolarization or dissipation, which arises from environmental noise sources that couple transversely to the qubit. Qubit depolarization occurs with a rate $\Gamma_1 = \Gamma_\uparrow + \Gamma_\downarrow$, which indicates the average speed at which the qubit returns to its equilibrium state after being excited. It is composed of an excitation rate $\Gamma_\uparrow$ and a relaxation rate $\Gamma_\downarrow$, which fulfill detailed balance, $\Gamma_\uparrow/\Gamma_\downarrow = \exp(-\hbar\omega_\mathrm{q}/k_\mathrm{B}T)$, in thermal equilibrium. Second, environmental noise sources that couple longitudinally to the qubit, entail pure dephasing with a rate Γ_φ, which quantifies how fast information about the phase of a prepared superposition state is lost. Both processes are combined in the decoherence rate[12]

$$\Gamma_2 = \frac{\Gamma_1}{2} + \Gamma_\varphi. \tag{1.54}$$

Building up on the BMS master equation in Eq. (1.53), for a non-degenerate system spectrum, a simple rate equation is found for the populations $\rho_{kk} = \langle k|\rho_\mathrm{S}|k\rangle$, also known as Pauli master equation,

$$\dot{\rho}_{kk} = \frac{1}{\hbar^2}\sum_l \left[\gamma_{kl,kl}\rho_{ll} - \gamma_{lk,lk}\rho_{kk}\right]. \tag{1.55}$$

[12] Oftentimes, it is customary to talk about timescales instead of rates, which are simply defined as the inverse of the rates in Eq. (1.54), e.g. $T_2 = 1/\Gamma_2$ is the decoherence time.

Here, the transition rates $\Gamma_{k\to l} \equiv \gamma_{lk,lk}/\hbar^2$ from state $|k\rangle$ to state $|l\rangle$ are given by [159]

$$\Gamma_{k\to l} = \frac{1}{\hbar^2}\sum_{\alpha\beta}\gamma_{\alpha\beta}(\omega_{lk})\langle l|\hat{A}_\beta|k\rangle\langle l|\hat{A}_\alpha|k\rangle^* \geq 0. \tag{1.56}$$

Focusing on a single noise source with interaction Hamiltonian $\hat{H}_\mathrm{I} = \hat{A}\otimes\hat{B}$, Eq. (1.56) reduces to

$$\Gamma_{k\to l} = \frac{1}{\hbar^2}|\langle l|\hat{A}|k\rangle|^2 \underbrace{\int_{-\infty}^{\infty}\mathrm{d}\tau\,\langle\hat{B}(\tau)\hat{B}(0)\rangle_{\bar{\rho}_\mathrm{B}}\,e^{i\omega_{lk}\tau}}_{\equiv\mathcal{S}_B(\omega_{lk})}, \tag{1.57}$$

where the noise spectral density $\mathcal{S}_B(\omega)$ associated with the operator $\hat{B}$ is introduced. As described above, the qubit depolarization rate or thermalization rate between two states, $\Gamma_{1,k\to l}$ is the sum of emission and absorption rates, resulting in

$$\begin{aligned}\Gamma_{1,k\to l} &= \Gamma_{k\to l} + \Gamma_{l\to k}\\ &= \frac{1}{\hbar^2}|\langle l|\hat{A}|k\rangle|^2\left[\mathcal{S}_B(\omega_{lk}) + \mathcal{S}_B(-\omega_{lk})\right],\end{aligned} \tag{1.58}$$

which is an alternative form of Fermi's Golden Rule [159]. The result of Eq. (1.58) provides a typical framework in literature [44, 93, 102, 125, 163–165] to estimate qubit depolarization due to different noise channels, like dielectric or inductive loss. For instance, a lossy capacitor can be modeled as an infinite number of bosonic modes using the so-called Caldeira-Leggett model [166]. The resulting voltage (or current) fluctuations in a lossy shunting impedance $Z(\omega)$ (or admittance $Y(\omega)$) are then proportional to $\mathrm{Re}[Z(\omega)]$ (or $\mathrm{Re}[Y(\omega)]$). Here, I would like to avoid using the Caldeira-Leggett model for two reasons:

1. Even though the assumption of summarizing all couplings to an infinite amount of oscillators to a single macroscopic lossy shunting impedance (or admittance) proves to be a valid and handy way to calculate the corresponding losses, it skips the step of providing intuition about the microscopical origin of the loss mechanisms.
2. The Caldeira-Leggett description is based on a bosonic bath of infinitely many oscillators. It is not immediately clear, how this model can be extended to a TLS bath.

Thus, a slightly different–and to my notion more satisfying–path is going to be taken, which consists in applying the quantum fluctuation-dissipation theorem (QFDT) [167]. For this, the linear response function or susceptibility χ_{AB} between the two operators $\hat{A}$ and $\hat{B}$ in the above interaction Hamiltonian is introduced, which is defined via

$$\hat{B}(t) = \int_{-\infty}^{t}\chi_{AB}(t-\tau)\hat{A}(\tau)\mathrm{d}\tau. \tag{1.59}$$

In Appendix A, it is shown how the Fourier transform $\chi_{AB}(\omega)$ of the susceptibility is connected to the symmetric noise spectral density $S_B(\omega) + S_B(-\omega)$ for both a bosonic and a TLS bath. With Eq. (A11), the following expression for the qubit depolarization rate is obtained,

$$\Gamma_{1,k\to l} = \frac{2}{\hbar}|\langle l|\hat{A}|k\rangle|^2\,\mathrm{Im}[\chi_{AB}(\omega_{lk})]\times\begin{cases}\coth\left(\hbar\omega_{lk}/2k_\mathrm{B}T\right) & \text{for a bosonic,}\\ 1 & \text{for a TLS}\end{cases} \tag{1.60}$$

bath. As will be seen in the following sections, Eq. (1.60) serves as a powerful tool to address several sources for qubit depolarization. For this, however, further assumptions about their microscopic origin still need to be made.

In the following subsections, mainly qubit dissipation due to dielectric loss in the capacitor (Section 1.5.1), resistive loss in the superinductor (Section 1.5.2), and Purcell loss to the transmission line via the dispersively coupled resonator (Section 1.5.3) is considered. Regarding Purcell loss, two different derivations are examined in detail. Section 1.5.4 briefly comments on other decay channels such as flux coupling to a control line, $1/f$ flux noise, and quasiparticle noise. Several noise sources leading to pure dephasing are presented in Section 1.5.5, including photon shot noise, which is relevant for the main results in Chapter 3. Finally, Section 1.5.6 explains the origins of excess thermal photon shot noise.

1.5.1 Dielectric Loss

Dielectric loss originates from the qubit capacitance C in the presence of a lossy medium. Microscopically, the polarization of atoms or molecules in a dielectric medium due to an external electric field can have two possible origins [168]:

1. induced dipole moments, which form vibrational states and can be modeled as harmonically bound electrons (= bosonic bath)
2. alignment of randomly oriented permanent dipole moments, e.g. in intrinsically polar media (H_2O, HF, ...) or dielectric two level systems (TLSs) in residues [169]

The interaction Hamiltonian between a bath of dipole moments $\hat{\vec{p}}_n$ inside the electric field $\hat{\vec{E}}(\vec{x})$ generated by the charged qubit capacitor is given by

$$\hat{H}_\mathrm{I} = -\sum_n \hat{\vec{p}}_n \otimes \hat{\vec{E}}(\vec{x}_n) = -\sum_n \hat{\vec{P}}_\mathrm{e}(\vec{x}_n) \otimes \hat{\vec{E}}(\vec{x}_n). \tag{1.61}$$

For the last equality, the electric polarization per volume $\hat{\vec{P}}_\mathrm{e}(\vec{x}) = \sum_n \hat{\vec{p}}_n \delta(\vec{x} - \vec{x}_n)$, with the Dirac delta function $\delta(x)$, for a finite number of dipole moments is introduced. Both coupling operators in Eq. (1.61) fulfill the condition of being Hermitian: First $\hat{\vec{p}}_n = e\hat{\vec{r}}_n \propto (\hat{b}_n + \hat{b}_n^\dagger)$, where $\hat{\vec{r}}_n$ represents the displacement of the n-th dipole from its equilibrium, and $\hat{b}_n$ ($\hat{b}_n^\dagger$) is its annihilation (creation) operator. Second, the electric field operator can be written as $\hat{\vec{E}}(\vec{x}) = \vec{\mathcal{E}}(\vec{x})\,\hat{n}$, where $\vec{\mathcal{E}}(\vec{x})$ describes the spatial mode profile of the capacitor field. In electrostatics, the polarization density is generally defined as $\vec{P}_\mathrm{e} = \epsilon_0(\epsilon_\mathrm{r} - 1)\vec{E} = \epsilon_0\chi_\mathrm{e}\vec{E}$, where $\epsilon_\mathrm{r} = \epsilon_\mathrm{r}' - i\epsilon_\mathrm{r}''$ is the complex relative permittivity and χ_e is the electric susceptibility [170]. A conveniently used quantity is the dielectric loss tangent $\tan(\delta_\mathrm{c}) = \epsilon_\mathrm{r}''/\epsilon_\mathrm{r}'$ ($\approx \epsilon_\mathrm{r}''/\epsilon_\mathrm{r}$ for its typically small values).[13] A more general approach

[13] In sapphire empirically found to obey a scaling law, $\tan(\delta_\mathrm{C}(\omega)) \propto \omega^\epsilon$, with the exponent varying from $\epsilon = 0.15$ [102] to $\epsilon = 0.7$ [125, 163].

involving time-varying electric fields, shows that the polarization of a medium can not immediately follow a changing external electric field. This can be expressed in the linear-response equation

$$\hat{\vec{P}}_{\mathrm{e}}(\vec{x},t) = \epsilon_0 \int_{-\infty}^{t} \chi_{\mathrm{e}}(t-\tau)\hat{\vec{E}}(\vec{x},\tau)\,\mathrm{d}\tau, \tag{1.62}$$

where the spatial independence of the susceptibility χ_{e} followed from the assumption of a homogeneous, lossy medium. Note that Eq. (1.62) resembles strongly Eq. (1.59) for the operators in the interaction Hamiltonian, such that Eq. (1.60) now provides a direct way of calculating the qubit depolarization rate from an initial qubit state $|k\rangle$ to a final state $|l\rangle$ due to a single dipole moment,

$$\Gamma^{n}_{1,k\to l} = \frac{2}{\hbar}|\langle l|\hat{\vec{E}}(\vec{x}_n)|k\rangle|^2\,\epsilon_0 \mathrm{Im}[\chi_{\mathrm{e}}(\omega_{lk})]\,f(T). \tag{1.63}$$

Here, the temperature dependent factor, which already appears in Eq. (1.60), is $f(T) = \coth(\hbar\omega_{lk}/2k_{\mathrm{B}}T)$ for a bosonic bath mode and $f(T) = 1$ for a bath TLS. It is further simplistically assumed that cross-relaxation terms with $\alpha \neq \beta$ in Eq. (1.56) are negligible, and therefore the summed rates $\Gamma^{n}_{1,k\to l}$ due to the individual dipole moments result in the total depolarization rate

$$\begin{aligned}\Gamma^{\mathrm{diel}}_{1,k\to l} = \sum_n \Gamma^{n}_{1,k\to l} &= \frac{2}{\hbar}\left(\sum_n |\langle l|\hat{\vec{E}}(\vec{x}_n)|k\rangle|^2\right)\epsilon_0 \mathrm{Im}[\chi_{\mathrm{e}}(\omega_{lk})]\,f(T).\\ &= \frac{2}{\hbar}\left(\int |\langle l|\hat{\vec{E}}(\vec{x})|k\rangle|^2\,\mathrm{d}^3x\right)\epsilon_0\epsilon_{\mathrm{r}}\tan(\delta_{\mathrm{C}}(\omega_{lk}))\,f(T),\end{aligned} \tag{1.64}$$

assuming a homogeneous distribution of dipoles and neglecting spatial correlations. The total electrostatic potential energy W_{e} can be expressed either as the volume integral of the fields, or in terms of the total charge $\hat{Q} = 2e\hat{n}$ on the capacitor,

$$W_{\mathrm{e}} = \frac{1}{2}\epsilon_0\epsilon_{\mathrm{r}}\int |\hat{\vec{E}}(\vec{x})|^2\mathrm{d}^3x = \frac{\hat{Q}^2}{2C} = \frac{1}{2}E_{\mathrm{C}}\hat{n}^2, \tag{1.65}$$

assuming that the electric field distribution entering the interaction Hamiltonian coincides with that defining the capacitor energy. Combining Eq. (1.65) and Eq. (1.64) yields

$$\Gamma^{\mathrm{diel}}_{1,k\to l} = \frac{2E_{\mathrm{C}}}{\hbar}|\langle l|\hat{n}|k\rangle|^2\tan(\delta_{\mathrm{c}}(\omega))\,f(T). \tag{1.66}$$

Lastly, the matrix elements of both degrees of freedom in the fluxonium Hamiltonian $\hat{H}$ of Eq. (1.31) can be converted into each other, $\langle l|[\hat{\varphi},\hat{H}]|k\rangle = \hbar\omega_{lk}\langle l|\hat{\varphi}|k\rangle = i(8E_{\mathrm{C}})\langle l|\hat{n}|k\rangle$, for arbitrary eigenstates $|k\rangle$, $|l\rangle$ of $\hat{H}$ [171]. This leads to the expression

$$\Gamma^{\mathrm{diel}}_{1,k\to l} = \frac{2\hbar\omega^2_{lk}}{E_{\mathrm{C}}}|\langle l|\hat{\varphi}|k\rangle|^2\tan(\delta_{\mathrm{c}}(\omega_{lk}))\times\begin{cases}\coth(\hbar\omega_{lk}/2k_{\mathrm{B}}T) & \text{for a bosonic,}\\ 1 & \text{for a TLS}\end{cases} \tag{1.67}$$

bath. Note that this result is in accordance with literature and with the formulas derived there for a bosonic bath within the Caldeira-Leggett formalism [163, 164, 171], as well as for a TLS bath of charge TLSs [165, 172]. The derivation in Ref. [165], based on Fermi's Golden Rule and an interaction Hamiltonian similar to the one used here, considers dipole moments interacting with an electric field, with the notable detail of accounting for the spatial and energetic distribution of the dipole moments.

1.5.2 Inductive Loss

Inductive loss arises from Johnson-Nyquist current noise in the lossy superinductance L of the qubit. Microscopically, the magnetic polarization in materials due to an external magnetic field can have the following origins:

1. paramagnetic surface impurities and defects are usually present in low concentrations of less than parts in a million in single crystal substrates [173], and they have shown to impact the decoherence of superconducting qubits based on disordered superconductors [174, 175]
2. quasiparticles.

Similar to the derivation of dielectric loss in Section 1.5.1, the derivation of inductive loss starts in stating the interaction Hamiltonian $\hat{H}_\mathrm{I}$. In this case, the interaction between a bath of magnetic moments $\hat{\vec{m}}_n$ inside the magnetic field $\hat{\vec{B}}(\vec{x})$ generated by the superinductor is governed by

$$\hat{H}_\mathrm{I} = -\sum_n \hat{\vec{m}}_n \otimes \hat{\vec{B}}(\vec{x}_n) = -\sum_n \hat{\vec{P}}_\mathrm{m}(\vec{x}_n) \otimes \hat{\vec{B}}(\vec{x}_n). \tag{1.68}$$

For the last equality, the magnetic polarization per volume $\hat{\vec{P}}_\mathrm{m}(\vec{x}) = \sum_n \hat{\vec{m}}_n \delta(\vec{x} - \vec{x}_n)$ for a finite number of magnetic moments is introduced. In magnetostatics, the magnetic polarization per volume is given by $\vec{P}_\mathrm{m} = (\mu_\mathrm{r} - 1)\vec{B}/(\mu_0\mu_\mathrm{r}) = \chi_\mathrm{m}\vec{B}/(\mu_0\mu_\mathrm{r})$, where $\mu_\mathrm{r} = \mu_\mathrm{r}' - i\mu_\mathrm{r}''$ denotes the relative magnetic permeability and χ_m is the magnetic susceptibility χ_m [170]. The term $\tan(\delta_\mathrm{L}) = \mu_\mathrm{r}''/\mu_\mathrm{r}' \approx \mu_\mathrm{r}''/\mu_\mathrm{r}$ is known as the inductive loss tangent, and it is assumed here to be independent of frequency.[14] Again, for time-varying electric fields, the magnetic polarization of a medium can not immediately follow a changing external magnetic field, which is expressed in the linear response equation

$$\hat{\vec{P}}_\mathrm{m}(\vec{x}, t) = \frac{1}{\mu_0\mu_\mathrm{r}} \int_{-\infty}^{t} \chi_\mathrm{m}(t - \tau)\hat{\vec{B}}(\vec{x}, \tau)\,\mathrm{d}\tau. \tag{1.69}$$

The spatial independence of the susceptibility χ_m follows from the assumption of a homogeneous, lossy medium. Similar to Eq. (1.62) for the electric polarization, Eq. (1.69) resembles strongly the relation in Eq. (1.59) for the operators in the interaction Hamiltonian. Thus, Eq. (1.60) provides the basis for calculating the qubit depolarization rate due to a single magnetic moment,

$$\Gamma^n_{1,k\to l} = \frac{2}{\hbar}|\langle l|\hat{\vec{B}}(\vec{x}_n)|k\rangle|^2 \frac{\mathrm{Im}[\chi_\mathrm{m}(\omega_{lk})]}{\mu_0\mu_\mathrm{r}} f(T). \tag{1.70}$$

The same assumption that led to the expression Eq. (1.64) for the total depolarization rate can be applied in the magnetic case here, yielding

$$\Gamma^\mathrm{ind}_{1,k\to l} = \frac{2}{\hbar}\left(\int |\langle l|\hat{\vec{B}}(\vec{x})|k\rangle|^2\,\mathrm{d}^3x\right)\frac{\tan(\delta_\mathrm{L}(\omega_{lk}))}{\mu_0} f(T). \tag{1.71}$$

[14] This assumption is made for simplicity in the case of grAl-based inductors. For JJA-based inductors, a frequency dependence $\tan\delta_\mathrm{L}(\omega) \propto K_0(\hbar\omega/2k_\mathrm{B}T)\cdot\sinh(\hbar\omega/2k_\mathrm{B}T)$ is expected if inductive loss arises from quasiparticle tunneling in the JJs [164] ($K_0(x)$ is the modified Bessel function of 2$^{\mathrm{nd}}$ kind and order 0.

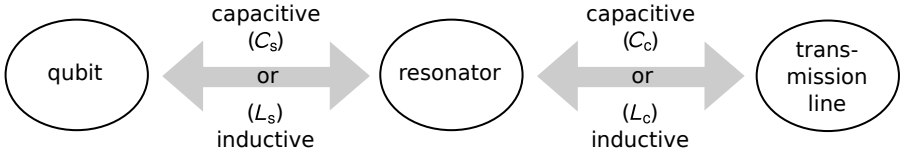

Figure 1.8: Modeling Purcell loss. The qubit is coupled to the resonator either capacitively by sharing a capacitance C_s or inductively by sharing an inductance L_s. The resonator, in turn, is coupled either capacitively via a coupling capacitance C_c or inductively via a coupling inductance L_c to the transmission line, which is usually modeled as a (real) termination impedance Z_0.

The total magnetic energy W_m can be expressed either as the volume integral of the fields, or in terms of the total flux $\hat{\Phi} = (\Phi_0/2\pi)\hat{\varphi}$ from the superinductor,

$$W_m = \frac{1}{2}\mu_0\mu_r \int |\hat{\vec{B}}(\vec{x})|^2 d^3x = \frac{\hat{\Phi}^2}{2L} = \frac{1}{2}E_L\hat{\varphi}^2. \tag{1.72}$$

Finally, the combination of Eq. (1.72) and Eq. (1.71) results in

$$\Gamma^{ind}_{1,k\to l} = \frac{2E_L}{\hbar}|\langle l|\hat{\varphi}|k\rangle|^2 \tan(\delta_L) \times \begin{cases} \coth(\hbar\omega_{lk}/2k_BT) & \text{for a bosonic,} \\ 1 & \text{for a TLS} \end{cases} \tag{1.73}$$

bath, respectively.[15] This equation is equivalent to what is found in the pertinent superconducting qubit literature [163, 164, 171].

1.5.3 Purcell Loss

Spontaneous emission of the qubit via the coupled readout resonator or cavity is known as Purcell effect [176]. In the present context, this so-called Purcell loss arises from a capacitive or inductive coupling of the superconducting qubit to the resonator, which itself is coupled capacitively or inductively to a lossy transmission line, as illustrated in Fig. 1.8. Traditionally, to account for Purcell loss, the qubit is regarded to couple to a single-mode resonator with linewidth κ [132]. The energy relaxation rate due to Purcell loss is then related to the coupling strength g and detuning $\Delta = \omega_q - \omega_r$ between resonator and qubit in the following way,

$$\Gamma_1^P = 2g^2 \frac{\kappa/2}{(\kappa/2)^2 + \Delta^2} \approx \kappa\left(\frac{g}{\Delta}\right)^2 \tag{1.74}$$

The last approximation in Eq. (1.74) is valid in the dispersive limit $\Delta \gg \kappa$. Later research found that far-off resonant modes of the resonator also strongly affect Γ_1^P [177], which can be accounted for in a semi-classical multi-mode model. To find all relevant modes in the circuit, this calculation can be complemented with a full 3D electromagnetic simulation of

[15] As a minor remark, the approximation $\mu_r \approx 1$ was used for the final result of Eq. (1.73). This is justified since only non-ferromagnetic materials are in the vicinity of the qubit, so $\mu_r - 1$ is on the order of 10^{-5} (positive for paramagnetic substances, negative for diamagnetic) [168].

the circuit, e.g. the black-box quantization technique [178, 179], which is also applicable to couplings to other control lines.

An alternative approach to derive loss due to the Purcell effect comes from Koch *et al.* [37]. The idea is to regard qubit and resonator as a joint quantum system, as presented in Section 1.3.4, which is then coupled via the resonator to the transmission line. The energy relaxation rate is then estimated using Fermi's golden rule by treating the interaction Hamiltonian between resonator and transmission line as a small perturbation to the joint quantum system. Starting from the original formulation in Ref. [37] until recent derivations [171, 180], however, there are always two questionable underlying assumptions, which will be addressed in the following on the basis of a semi-classical model.

1. The first assumption consists in the loss of information about the coupling scheme between resonator and transmission line due to the chosen interaction Hamiltonian.
2. The second idea relates to the assumption of a constant linewidth $\kappa = \kappa(\omega_\mathrm{r})$, independent of the qubit frequency. The frequency-dependence must play a role, however, as the transition occurs at the qubit frequency, which is generally different from the resonator frequency, $\omega_\mathrm{q} \neq \omega_\mathrm{r}$, such that the resonator linewidth should be evaluated at ω_q.

After this discussion, an analogous derivation to Refs. [37, 171, 180] is traced out step by step, including alternative approaches to the questionable assumptions. Finally, this section concludes with a comparison of the predictions of both models for various coupling scenarios.

Semi-Classical (SC) Model

The starting point of the semi-classical model is to suppose that the resonator in its ground state is weakly coupled to the fluxonium in a superposition between an initial and final state, that is, the resonator-fluxonium system can be described via the wavefunction $|\psi(t)\rangle = (|\psi_\mathrm{f}(t)\rangle + |\psi_\mathrm{i}(t)\rangle)/\sqrt{2} = (|\overline{0, n_{\mathrm{q},f}}\rangle e^{-i\omega_\mathrm{f} t} + |\overline{0, n_{\mathrm{q},i}}\rangle e^{-i\omega_\mathrm{i} t})/\sqrt{2}$. This means, half a photon with energy $\hbar\omega_\mathrm{fi}$ circulates in the system, where $\omega_\mathrm{fi} = \omega_\mathrm{f} - \omega_\mathrm{i}$ is the transition frequency. Due to the weak coupling, the system remains in the linear-response regime and the resonator behaves as if it were weakly displaced, exhibiting a small coherent oscillation in its expectation values at frequency ω_fi. Then, the expectation value of the oscillating charge $\langle\hat{Q}_\mathrm{r}(t)\rangle = 2en_{\mathrm{zpf,r}}\langle\psi(t)|i(\hat{a}_\mathrm{r} - \hat{a}_\mathrm{r}^\dagger)|\psi(t)\rangle \equiv \tilde{Q}_\mathrm{r}\cos(\omega_\mathrm{fi}t)$ (for capacitive coupling (Fig. 1.9A)) as well as the flux $\langle\hat{\Phi}_\mathrm{r}(t)\rangle = (\Phi_0/2\pi)\varphi_{\mathrm{zpf,r}}\langle\psi(t)|\hat{a}_\mathrm{r} + \hat{a}_\mathrm{r}^\dagger|\psi(t)\rangle \equiv \tilde{\Phi}_\mathrm{r}\sin(\omega_\mathrm{fi}t)$ (for inductive coupling (Fig. 1.9B)) in the resonator are calculated. The matrix elements appearing in the amplitudes $\tilde{Q}_\mathrm{r} = 2en_{\mathrm{zpf,r}}\langle\psi_\mathrm{f}|i(\hat{a}_\mathrm{r} - \hat{a}_\mathrm{r}^\dagger)|\psi_\mathrm{i}\rangle$ and $\tilde{\Phi}_\mathrm{r} = (\Phi_0/2\pi)\varphi_{\mathrm{zpf,r}}\langle\psi_\mathrm{f}|\hat{a}_\mathrm{r} + \hat{a}_\mathrm{r}^\dagger|\psi_\mathrm{i}\rangle$ of charge and flux, respectively, are obtained numerically after diagonalization of the coupled resonator-fluxonium Hamiltonian, as described in Section 1.3.4. Constant (DC) contributions to the expectation values, arising from diagonal matrix elements, do not contribute to dissipation and were therefore omitted. $\hat{a}_\mathrm{r}^\dagger$ ($\hat{a}_\mathrm{r}$) is the creation (annihilation) operator of the bare resonator. The matrix elements are evaluated between the dressed

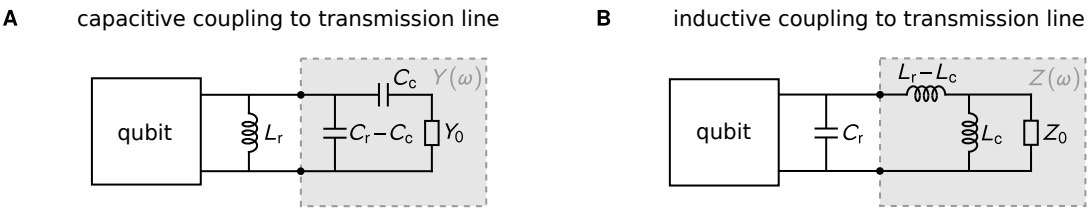

Figure 1.9: Semi-classical model. Electrical circuit diagram of the qubit-resonator system with the resonator coupled **(A)** capacitively and **(B)** inductively to the transmission line.

eigenstates of the coupled resonator–fluxonium system. The zero-point fluctuations $n_{\mathrm{zpf,r}}$ and $\varphi_{\mathrm{zpf,r}}$ are given by Eq. (1.29), involving the resonator impedance $Z_\mathrm{r} = \sqrt{L_\mathrm{r}/C_\mathrm{r}}$.

The dissipation can now be computed by evaluating the time-averaged active power $\bar{P} = \mathrm{Re}[\tilde{V}_\mathrm{r}\tilde{I}_\mathrm{r}]/2$ from the voltage amplitude $\tilde{V}_\mathrm{r} = \tilde{Q}_\mathrm{r}/C_\mathrm{r}$ (or current amplitude $\tilde{I}_\mathrm{r} = \tilde{\Phi}_\mathrm{r}/L_\mathrm{r}$) and the termination admittance $Y(\omega_\mathrm{fi})$ (or impedance $Z(\omega_\mathrm{fi})$) evaluated at the transition frequency. Finally, the transition rate $\Gamma^\mathrm{P}_{\mathrm{i}\to\mathrm{f}} = \bar{P}/(\hbar\omega_\mathrm{fi}/2)$ due to Purcell loss is determined for both capacitive and inductive coupling scenarios, which are presented in the following side by side due to their analogy.

capacitive coupling	inductive coupling
$Y(\omega) = j\omega(C_\mathrm{r} - C_\mathrm{c}) + \left(\frac{1}{j\omega C_\mathrm{c}} + \frac{1}{Y_0}\right)^{-1}$	$Z(\omega) = j\omega(L_\mathrm{r} - L_\mathrm{c}) + \left(\frac{1}{j\omega L_\mathrm{c}} + \frac{1}{Z_0}\right)^{-1}$ (1.75)
$\bar{P} = \tilde{V}_\mathrm{r}^2\,\mathrm{Re}\left[Y(\omega_\mathrm{fi})\right]/2 = \frac{\tilde{Q}_\mathrm{r}^2}{2C_\mathrm{r}^2}\frac{Y_0}{1 + Y_0^2/\omega_\mathrm{fi}^2 C_\mathrm{c}^2}$	$\bar{P} = \tilde{I}_\mathrm{r}^2\,\mathrm{Re}\left[Z(\omega_\mathrm{fi})\right]/2 = \frac{\tilde{\Phi}_\mathrm{r}^2}{2L_\mathrm{r}^2}\frac{Z_0}{1 + Z_0^2/\omega_\mathrm{fi}^2 L_\mathrm{c}^2}$ (1.76)
$\Gamma^\mathrm{P}_{\mathrm{i}\to\mathrm{f}} = \lvert\langle\psi_\mathrm{f}\rvert a_\mathrm{r} - a_\mathrm{r}^\dagger\rvert\psi_\mathrm{i}\rangle\rvert^2 \times \underbrace{\frac{\omega_\mathrm{fi}}{2}\frac{Z_0}{Z_\mathrm{r}}\left(\frac{C_\mathrm{c}}{C_\mathrm{r}}\right)^2\left(1 + \omega_\mathrm{fi}^2 C_\mathrm{c}^2 Z_0^2\right)^{-1}}_{\kappa(\omega_\mathrm{fi})}$	$\Gamma^\mathrm{P}_{\mathrm{i}\to\mathrm{f}} = \lvert\langle\psi_\mathrm{f}\rvert a_\mathrm{r} + a_\mathrm{r}^\dagger\rvert\psi_\mathrm{i}\rangle\rvert^2 \times \underbrace{\frac{\omega_\mathrm{fi}}{2}\frac{Z_\mathrm{r}}{Z_0}\left(\frac{L_\mathrm{c}}{L_\mathrm{r}}\right)^2\left(1 + \frac{\omega_\mathrm{fi}^2 L_\mathrm{c}^2}{Z_0^2}\right)^{-1}}_{\kappa(\omega_\mathrm{fi})}$ (1.77)
for weak coupling ($\omega_\mathrm{fi} C_\mathrm{c} \ll 1/Z_0$): $\kappa(\omega_\mathrm{fi}) \approx \frac{\omega_\mathrm{fi}}{2}\frac{Z_0}{Z_r}\left(\frac{C_\mathrm{c}}{C_\mathrm{r}}\right)^2$	for weak coupling ($\omega_\mathrm{fi} L_\mathrm{c} \ll Z_0$): $\kappa(\omega_\mathrm{fi}) \approx \frac{\omega_\mathrm{fi}}{2}\frac{Z_\mathrm{r}}{Z_0}\left(\frac{L_\mathrm{c}}{L_\mathrm{r}}\right)^2$ (1.78)

Both, for capacitive and inductive coupling between the resonator and the transmission line, Eq. (1.77) applies only to a bath at zero temperature, $T = 0$, where only spontaneous emission is present. At finite temperatures, $T > 0$, since the environment is bosonic, photon

absorption and stimulated emission by the system have to be added. These processes are accounted for by multiplying the relaxation rates in Eq. (1.77) with the familiar factor $\coth(\hbar\omega/2k_\mathrm{B}T)$, that was already encountered for dielectric and inductive loss in the previous sections. In contrast, for a lossy TLS bath no temperature dependence has to be added, since spontaneous, stimulated emission and absorption counterbalance.

Fermi's Golden Rule / Open Quantum System (OQS) Model

This part retraces the historical derivation of Purcell loss from Refs. [37, 171, 180] step by step and provides two proposals for improvement, based on the results of the SC model discussed in the previous part. The derivation starts with the full Hamiltonian $\hat{H}$ of the resonator-qubit system (S) that is coupled via the resonator to the transmission line modeled as an infinite set of bosonic modes,

$$\hat{H} = \underbrace{\sum_k E_k^\mathrm{S} |\psi_k^\mathrm{S}\rangle\langle\psi_k^\mathrm{S}|}_{\hat{H}_\mathrm{S}} + \underbrace{\sum_k \hbar\omega_k \hat{b}_k^\dagger \hat{b}_k}_{\hat{H}_\mathrm{B}} + \underbrace{\sum_k \hbar\lambda_k \left[\hat{a}_\mathrm{r}\hat{b}_k^\dagger + \hat{a}_\mathrm{r}^\dagger \hat{b}_k\right]}_{\hat{H}_\mathrm{I}}, \tag{1.79}$$

where $\hat{a}_\mathrm{r}^\dagger$ ($\hat{a}_\mathrm{r}$) is the creation (annihilation) operator of the bare resonator, and $\hat{b}_k^\dagger$ ($\hat{b}_k$) is the creation (annihilation) operator of the k-th bosonic mode. $|\psi_k^\mathrm{S}\rangle$ and E_k^S represent the eigenstates and corresponding eigenenergies of the resonator-qubit system, respectively. As indicated by the braces, the full Hamiltonian in Eq. (1.79) is conceptually equal to the Hamiltonian of an open quantum system, see Eq. (1.45) for reference, which consists of a system part $\hat{H}_\mathrm{S}$, a bath part $\hat{H}_\mathrm{B}$ and an interaction Hamiltonian $\hat{H}_\mathrm{I}$ describing the coupling between the two. In principle, the microscopic derivation of the BMS master equation, as introduced in Section 1.4.3, could be continued at this point, and the energy relaxation rate subsequently determined according to Eq. (1.58). For completeness, however, it is followed the historical derivation of Refs. [37, 171, 180], which directly relies on the use of Fermi's golden rule.

But before proceeding, the interaction Hamiltonian $\hat{H}_\mathrm{I}$ in Eq. (1.79) is examined closer to address the first questionable assumption. It can be observed that while $\hat{H}_\mathrm{I} = \hat{H}_\mathrm{I}^\dagger$ is Hermitian as a whole, it cannot be diagonally decomposed into system operators $\hat{A}_\alpha = \hat{A}_\alpha^\dagger$ and bath operators $\hat{B}_\alpha = \hat{B}_\alpha^\dagger$, each of which are Hermitian individually. This, however, was one of the fundamental assumptions for the Lindblad master equation in Section 1.4.2. Furthermore, it is not immediately clear, whether $\hat{H}_\mathrm{I}$ represents an inductive or a capacitive coupling between the resonator and the transmission line. For this reason, a more generalized treatment of the coupling is proposed in the following. The proposal is that the coupling is rather provided by the charge number operators $\hat{n}_\mathrm{r} \propto i(\hat{a}_\mathrm{r} - \hat{a}_\mathrm{r}^\dagger)$ (and $\hat{n}_k \propto i(\hat{b}_k - \hat{b}_k^\dagger)$) or the phase operators $\hat{\varphi}_\mathrm{r} \propto \hat{a}_\mathrm{r} + \hat{a}_\mathrm{r}^\dagger$ (and $\hat{\varphi}_k \propto \hat{b}_k + \hat{b}_k^\dagger$) for the resonator (and the k-th bath mode), since they fulfill the condition of being Hermitian, and they give an intuitive understanding of the coupling scheme. Starting from this premise, the interaction Hamiltonian in Eq. (1.79) would then become

$$\hat{H}_\mathrm{I} = \sum_k \hbar\lambda_k (\hat{a}_\mathrm{r}^\dagger \pm \hat{a}_\mathrm{r})(\hat{b}_k^\dagger \pm \hat{b}_k), \tag{1.80}$$

where positive (negative) signs in the interaction Hamiltonian correspond to inductive (capacitive) coupling between the resonator-qubit system and the transmission line.

Continuing at this point with the historical derivation of Refs. [37, 171, 180], the reader is referred to Appendix B, since the complete derivation of Purcell loss is rather lengthy and contains many mathematical details in its individual steps. Instead, only the main ideas are briefly sketched in the following. The derivation starts by treating the interaction Hamiltonian as a perturbation to the unperturbed Hamiltonian of system plus bath. Fermi's golden rule then provides an expression for the transition rate $\gamma_{\mathrm{i}\to\mathrm{f}}$ from an initial eigenstate $|\psi_\mathrm{i}\rangle$ to a final eigenstate $|\psi_\mathrm{f}\rangle$ of the unperturbed Hamiltonian $\hat{H}_\mathrm{S} + \hat{H}_\mathrm{B}$ (with eigenenergies E_i and E_f, respectively), given by

$$\gamma_{\mathrm{i}\to\mathrm{f}} = \frac{2\pi}{\hbar}\delta(E_\mathrm{i} - E_\mathrm{f})|\langle\psi_\mathrm{f}|\hat{H}_\mathrm{I}|\psi_\mathrm{i}\rangle|^2. \tag{1.81}$$

Subsequent tracing out of the bath and weighing of initial states by their probability of being thermally populated, yields the total transition rate $\Gamma_{\mathrm{i}\to\mathrm{f}}$. Now follows the significant step that is potentially an oversimplification of the situation. By taking the continuum limit, the bath density of states and the coupling strength is reduced to a resonator linewidth κ. As a result of the first Markov approximation [181], the linewidth is then assumed to be independent of frequency, which is a valid approximation when a sole resonator is coupled to a transmission line, since the bath modes interact with the system only weakly and in the close vicinity of the resonance frequency (typically $\kappa \ll \omega_\mathrm{r}$). However, as was argued in the previous part, the frequency-dependence must play a role, as the transition occurs at the qubit frequency $\omega_\mathrm{q} \neq \omega_\mathrm{r}$.

For now, however, the above derivation assuming a constant linewidth κ is continued, in order to present a comparison between the two models later on. The remaining steps are carried out in Appendix B and focus on a detailed treatment of the dressed eigenstates $|\overline{n_\mathrm{r}, n_\mathrm{q}}\rangle$ of the resonator-qubit system, as introduced in Section 1.3.4. Here, simply the final result for the total relaxation rate from initially having $n_{\mathrm{q,i}}$ photons in the qubit to finally $n_{\mathrm{q,f}}$ photons due to Purcell loss is stated,

$$\Gamma^\mathrm{P}_{1,n_{\mathrm{q,i}}\to n_{\mathrm{q,f}}} = \sum_{n_{\mathrm{r,f}}} \kappa|\langle\overline{n_{\mathrm{r,f}}, n_{\mathrm{q,f}}}|\hat{a}_\mathrm{r}^\dagger \pm \hat{a}_\mathrm{r}|\overline{0, n_{\mathrm{q,i}}}\rangle|^2 \coth\left(\frac{\hbar\omega_{\mathrm{fi}}}{2k_\mathrm{B}T}\right). \tag{1.82}$$

At this point, it is important to note that κ should–as was semi-classically motivated in the previous section–actually be evaluated at the qubit transition frequency ω_{fi}, which depends on the quantum numbers appearing in Eq. (1.82), rather than at the resonator frequency, as done in the historical derivation [37, 171, 180]. In principle, Eq. (1.82) represents a powerful equation, which also takes into account crossings with other levels, such as the case when the first excited qubit state $n_\mathrm{q} = 1$ has an avoided level crossing with the second excited resonator state $n_\mathrm{r} = 2$ (as for sample 3 in Chapter 2).

Comparison of the Two Models

In this section, both the semi-classical (SC) and the open quantum system (OQS) models are applied to all four coupling combinations in Fig. 1.8 due to the two types of couplings

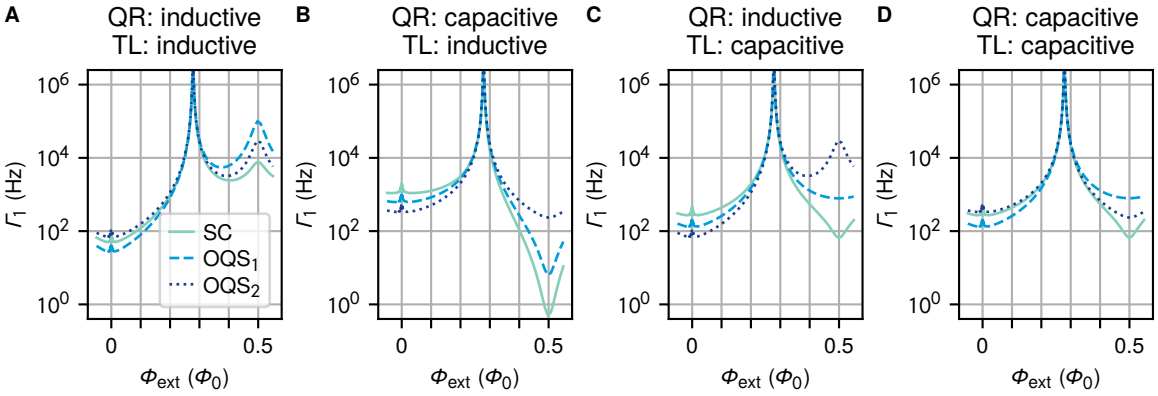

Figure 1.10: Purcell model comparison. Purcell loss following Eq. (1.82) for the open quantum system (OQS) model and Eq. (1.77) for the semi-classical (SC) model, calculated for the four different combinations of qubit-resonator (QR) coupling and resonator-to-transmission line (TL) coupling. For the OQS model two versions are shown, as explained in the text.

(inductive and capacitive) at two different locations (qubit-resonator coupling (QR) and resonator coupling to transmission line (TL)):

- QR: inductive, TL: inductive (Fig. 1.10A),
- QR: capacitive, TL: inductive (Fig. 1.10B),
- QR: inductive, TL: capacitive (Fig. 1.10C),
- QR: capacitive, TL: capacitive (Fig. 1.10D).

In Fig. 1.10, in total three different ways of calculating Purcell loss are shown as a function of the external magnetic flux bias in the fluxonium:

- SC: the prediction of the semi-classical model according to Eq. (1.77),
- OQS_1: the prediction of the open quantum system model according to Eq. (1.82), which assumes a constant $\kappa = \kappa(\omega_r)$, and which is based on the charge or flux operators as coupling operators,
- OQS_2: the prediction of the open quantum system model based on the historical derivation in Refs. [37, 171, 180], i.e., without adaptation of the interaction Hamiltonian, and with constant $\kappa = \kappa(\omega_r)$.

For the inductively coupled resonator-qubit systems in Fig. 1.10A and C, the same parameters as in Fig. 1.6 are chosen. For the capacitively coupled resonator-qubit systems in Fig. 1.10B and D, the shared capacitance $C_s = 0.83\,\mathrm{fF}$ is chosen such that the dispersive shift (Eq. (1.39)) matches the one of the inductively coupled resonator-qubit system. In this way, the energy spectra of all four systems coincide. For the OQS models, the constant resonator linewidth κ is chosen to be of similar value as experimentally measured (cf. Section 2.5). For the SC model, a coupling inductance $L_c = 0.20\,\mathrm{nH}$ in Fig. 1.10A and B and a coupling capacitance $C_c = 6.5\,\mathrm{fF}$ in Fig. 1.10C and D, respectively, are chosen such that the Purcell loss coincides with the OQS models in the vicinity of the avoided level crossing between the first resonator and fluxonium transition at $\Phi_{ext} \approx 0.28\Phi_0$ for both

resonator coupling types to the transmission line. For all four coupling combinations, a bosonic bath at zero temperature, $T = 0$, is assumed, such that the shown rates in Fig. 1.10 correspond only to spontaneous emission.

The following observations can be made:

- The choice of the interaction Hamiltonian in the OCS models results in a difference of the predicted Purcell loss for all four combinations. This fact has implications on a recent work on a grAl fluxonium [125] with inductive QR-coupling and capacitive TL-coupling. There, a slight increase in Γ_1 around half-flux was attributed to Purcell loss, that was estimated with the original OQS_2 Purcell loss model. The OQS_1 or SC model would, however, predict more than an order of magnitude smaller Γ_1 values at the lowest frequencies around half-flux, similar to Fig. 1.10C. An alternative way to explain the measured energy relaxation in Ref. [125] would consist in assigning the observed peak in Γ_1 to inductive losses, as for the resonator-fluxonium devices in Section 2.5.
- The main difference between the SC and OCS_1 models is for all four combinations that the SC model predicts a factor $\omega_\mathrm{q}/\omega_\mathrm{r}$ smaller (larger) energy relaxation rates when the qubit frequency ω_q is below (above) the resonator frequency ω_r. This behavior is expected when comparing the frequency-dependent linewidths $\kappa(\omega)$ in Eq. (1.78) with a constant linewidth $\kappa = \kappa(\omega_\mathrm{r})$. The difference becomes the largest for the present resonator-fluxonium parameters at the low qubit frequencies around the half-flux sweet spot $\Phi_\mathrm{ext} = 0.5\Phi_0$. For the three low-frequency fluxoniums investigated in Chapter 2, however, Purcell loss is not a limiting factor, even when applying the OQS model together with the temperature-dependent coth-factor. Studying samples in the future that are intentionally Purcell-limited at low frequencies would be interesting to clarify which model for Purcell loss is applicable.
- Another very interesting feature is that the type of coupling to the transmission line seems to play a crucial role for the Purcell loss of the fluxonium qubit. While basically no difference between inductively and capacitively coupled resonator-fluxoniums is observed when the resonator is coupled capacitively to the transmission line (Fig. 1.10C and D), there is a huge impact when the resonator is coupled inductively to the transmission line (Fig. 1.10A and B), where it leads to a striking difference in Purcell loss of about five orders of magnitude at $\Phi_\mathrm{ext} = 0.5\Phi_0$ for the semi-classical model! Fluxonium qubits that might be Purcell-limited in the future due to specific coupling choices could benefit from implementing a capacitive qubit-resonator coupling in combination with an inductive coupling of the resonator to the transmission line. This approach could represent an alternative pathway to the current efforts in Purcell filtering.

1.5.4 Other Loss Mechanisms

In this section, a few other loss mechanisms known to lead to qubit dissipation are briefly presented. For the fluxonium qubits investigated in this thesis, however, these are not found to be the limiting factor.

Flux Noise from a Coupled Control Line

The qubit can also dissipate energy due to the coupling to its control lines. Relevant for the present work is the fast-flux line (see Section 2.1) which is inductively coupled to the fluxonium loop via a mutual inductance M. In this way, current noise with a spectral density $S_I(\omega)$ will be translated into flux noise in the fluxonium loop with a spectral density $S_\Phi(\omega) = M^2 S_I(\omega)$. In the following, simply the result of Refs. [37, 182] is restated,

$$\Gamma^{\mathrm{M}}_{1,k\to l} = \frac{\omega_{lk}}{\pi}\left(\frac{R_\mathrm{Q}}{R}\right)\left(\frac{M}{L}\right)^2 |\langle l|\hat{\varphi}|k\rangle|^2 \coth\left(\frac{\hbar\omega_{lk}}{2k_\mathrm{B}T}\right), \tag{1.83}$$

with the resistance quantum R_Q, as introduced in Section 1.3.1. For Eq. (1.83), the simplest case of an ohmic termination with resistance R of the closest attenuator in an unfiltered control line was considered.[16] In contrast to Ref. [182], Eq. (1.83) contains a slight adaptation of the temperature factor, since the relaxation rate Γ_1 is expected to be proportional to the symmetric noise spectral density $\mathcal{S}_\Phi(\omega) + \mathcal{S}_\Phi(-\omega)$, which in turn is proportional to $\coth(\hbar\omega_{lk}/2k_\mathrm{B}T)$ for a bosonic noise source, as discussed in the previous sections.

$1/f$ Flux Noise

Another source for decoherence inherent to solid-state devices is $1/f$ flux noise which is attributed to emerge from surface defects on the substrate [174, 183–186]. $1/f$ flux noise possesses a flux noise spectral density of $\mathcal{S}_\Phi(\omega) = \mathcal{A}_\Phi^2/|\omega|$. The flux noise amplitude $\mathcal{A}_\Phi$ is typically found in a range from 1 to $40\,\mu\Phi_0$ in flux-sensitive devices over a broad range of frequencies from millihertz to gigahertz [174, 187–192]. At finite temperatures, the positive and negative frequency components of spectral densities are related by detailed balance, $\mathcal{S}_\Phi(-\omega)/\mathcal{S}_\Phi(+\omega) = \exp(-\hbar\omega/k_\mathrm{B}T)$. With Eq. (1.58) and the corresponding matrix element one then finds for the relaxation rate associated with $1/f$ flux noise [165, 175]

$$\Gamma^{1/f}_{1,k\to l} = (2\pi)^4 (E_\mathrm{L}/h)^2 \frac{(\mathcal{A}_\Phi/\Phi_0)^2}{\omega_{lk}} |\langle l|\hat{\varphi}|k\rangle|^2 \left(1 + e^{-\hbar\omega_{lk}/k_\mathrm{B}T}\right). \tag{1.84}$$

A side-by-side comparison of the prefactors for inductive loss in Eq. (1.73) and loss due to $1/f$ flux noise in Eq. (1.84) with a flux noise amplitude $\mathcal{A}_\Phi = 40\,\mu\Phi_0$ extracted from the echo experiments in Section 3.2.1 yields for sample 3, which also has the largest value of E_L (cf. Table 3.1), that loss due to $1/f$ flux noise is approximately a factor 10 smaller than inductive loss, such that it can safely be neglected.

[16] Qubit dissipation caused by control lines can also be suppressed by adding elements such as low-pass filters [182], leading to a more complex expression for the termination admittance.

Non-Equilibrium Quasiparticles

Another loss channel for superconducting qubits is tunneling of non-equilibrium quasiparticles through a resistive Josephson junction [193, 194]. The relaxation rate due to quasiparticle tunneling is then given by

$$\Gamma_{1,k\to l}^{\mathrm{qp}} = 16 x_{\mathrm{qp}} (E_{\mathrm{L}}/h) \sqrt{\frac{2\Delta_0}{\hbar\omega_{lk}}} \left| \left\langle l \right| \sin\left(\frac{\hat{\varphi}}{2}\right) \left| k \right\rangle \right|^2 \coth\left(\frac{\hbar\omega_{lk}}{2k_{\mathrm{B}}T}\right). \tag{1.85}$$

This equation is valid under the assumption that the characteristic quasiparticle energy is small compared to the gap energy Δ_0 and the transition energy, $\hbar\omega_{lk}$, respectively [163, 194]. The quasiparticle density is denoted with x_{qp}. For a commonly used superconductor, such as aluminum with a superconducting gap of $\Delta_0 = 1.76 k_{\mathrm{B}} T_{\mathrm{c}} \approx 210\,\mu\mathrm{eV}$ (Eq. (1.10)), a negligibly small quasiparticle density of $x_{\mathrm{qp}}^{\mathrm{th}} = \sqrt{2\pi k_{\mathrm{B}} T/\Delta_0} \exp\left(-\Delta_0/k_{\mathrm{B}}T\right) \sim 10^{-54}$ would be expected in thermal equilibrium at a typical dilution stage temperature of $T = 20\,\mathrm{mK}$ [195]. However, even at these very low temperatures, unexpectedly high levels of $x_{\mathrm{qp}} \sim 10^{-6}$ are observed in a large variety of devices [123, 163, 193, 196–204], which is attributed to non-equilibrium quasiparticles generated in rare events. Such events happen when cosmic rays or local radioactivity penetrate the qubit chip and potentially generate a phonon shockwave, which is able to break Cooper pairs in the superconductor [202, 205–207].

Abatement strategies to protect from non-equilibrium quasiparticles exist in shielding from the incoming radiation in a deep-underground lead-shielded cryostat [206], adding normal metal sinks in galvanic contact to the superconducting circuits, that act as quasiparticle traps [208], or integrating phonon traps on the sample chip [205]. Phonon traps can be realized either in the form of neighboring superconducting islands with a lower spectral gap than of the superconductor used in the circuit [202, 209, 210], or via a neighboring normal metal plane, as theoretically described in [207]. The latter was also one of the reasons for the integration of a normal metal ground plane in the sample design presented in Section 2.1.

1.5.5 Pure Dephasing

Longitudinal noise sources lead to random fluctuations of the qubit frequency. Such fluctuations result over time in a random phase accumulation of a qubit's superposition state, which is commonly referred to as pure dephasing. There are multiple possible sources in the environment of a qubit that can lead to qubit dephasing. In contrast to energy relaxation, pure dephasing is reversible by dynamically decoupling the qubit from its environment with coherent pulse sequences [189]. Notable examples for such sequences typically originate from the neighboring field of nuclear magnetic resonance, such as the Hahn spin-echo [211] or the Carr-Purcell-Meiboom-Gill (CPMG) [212, 213] pulse sequence. Empirically, most noise channels leading to pure dephasing possess a noise spectral density with a $1/f$ dependence, given by $\mathcal{S}_B(\omega) = \mathcal{A}_B^2/|\omega|$, where $\mathcal{A}_B$ describes

the noise amplitude associated with the noisy variable $\hat{B}$ of the bath. Since the $1/f$ noise spectral density falls off much faster compared to typical inverse measurement times $1/t$, the phase decay function has a Gaussian envelope $e^{-(\Gamma_\varphi t)^2}$ with a pure dephasing rate given by [214, 215]

$$\Gamma_\varphi = \mathcal{A}_B \eta \left| \frac{\partial \omega_\mathrm{q}}{\partial B} \right|, \tag{1.86}$$

in which η denotes a numerical factor due to the filtering of the applied pulse sequence. In the case of free induction (Ramsey experiment), one finds $\eta_\mathrm{R} = \sqrt{1/\ln(\omega_\mathrm{ir} t)}$, where ω_ir defines an infrared cut-off frequency. For an echo sequence, it is $\eta_\mathrm{E} = \sqrt{\ln 2}$ [192].

Common $1/f$ noise channels are flux noise, critical current noise and charge noise, which will all be presented briefly in the following. In the end, with photon shot noise one notable exception from $1/f$-like noise is presented, which is of particular interest for the experiments presented in Chapter 3.

Flux Noise

The same flux noise that led to dissipation in Section 1.5.4 can also cause pure dephasing of the qubit. The origin of this type of noise is still somewhat debated, but research hints more and more to surface spins [174, 183–186]. The flux noise amplitude $\mathcal{A}_\Phi$ is typically found in a range from 1 to 40 $\mu\Phi_0$ in flux-sensitive devices over a broad range of frequencies from millihertz to gigahertz [174, 187–192]. For the fluxonium qubits in the present work, this is the dominating source of dephasing except for in vicinity of the flux sweet spots, where it is to first-order suppressed.

Critical Current Noise

Fluctuations of the Josephson energy $E_\mathrm{J} = \hbar I_\mathrm{c}/(2e)$ of superconducting qubits stem from critical current noise in the integrated Josephson junctions. The predominant microscopic model for the origin of this noise are trapped charges that inhibit tunneling through a section of the junction due to Coulomb repulsion, thereby effectively altering the junction area [216]. The critical current noise amplitude is empirically found to follow $\mathcal{A}_{I_\mathrm{c}} \approx 12\,\mathrm{pA} \times (I_\mathrm{c}/\mu\mathrm{A})/(A/\mu\mathrm{m}^2) \times (T/4.2\mathrm{K})$ which reduces for typical junction areas in this work and at a temperature $T = 20\,\mathrm{mK}$ to $\mathcal{A}_{I_\mathrm{c}} \approx 2 \times 10^{-7}\, I_\mathrm{c}$. Away from the flux sweet spots, this leads to at least an order of magnitude smaller dephasing rates than flux noise. At the flux sweet spots, however, it could play a minor role for the dephasing rate, besides the photon shot noise-induced dephasing. For an order of magnitude estimate, the following is assumed: A crude approximation for the qubit frequency at half-flux is given by the phase slip rate [217], $f_{01}(\Phi = \Phi_0/2) = 4/\sqrt{\pi}(E_\mathrm{J}^3 E_\mathrm{C})^{1/4} \exp(-8\sqrt{E_\mathrm{J}/E_\mathrm{C}})$. Nonetheless, for sufficiently large $E_\mathrm{J}/E_\mathrm{C}$ ratios, it can be assumed that the exponential factor is dominating the behavior of f_{01}, such that its sensitivity with respect to E_J is $|\partial f_{01}/\partial E_\mathrm{J}| \approx 4 f_{01}/E_\mathrm{J}\sqrt{E_\mathrm{J}/E_\mathrm{C}}$.

Thus, Eq. (1.86) yields the following expression for pure dephasing rate due to critical current noise

$$\Gamma_\varphi = \eta \mathcal{A}_{I_\mathrm{c}} \left| \frac{\partial \omega_{01}}{\partial I_\mathrm{c}} \right| = (\mathcal{A}_{I_\mathrm{c}}/I_\mathrm{c}) \times 4\eta\, \omega_{01} \sqrt{\frac{E_\mathrm{J}}{E_\mathrm{C}}}. \tag{1.87}$$

For the low-frequency fluxonium qubits investigated in Section 2.5, this value would be on the order of 1 kHz or less. It is therefore negligible compared to the dephasing rates found experimentally in Section 3.3, rendering their attribution to photon shot noise a valid hypothesis.

Charge Noise

Another noise source with $1/f$-like spectral density is due to fluctuations of the offset charge on the superconducting islands of a circuit, called charge noise, originating from fluctuating electrical potentials in the vicinity of the superconducting qubit. As already the transmon qubit was described to have a reduced sensitivity to charge noise [218], compared to the Cooper-pair box, it should not be of importance for the fluxonium at all, which is protected against charge fluctuations due to the large superinductor connecting the island node to ground.

Photon Shot Noise-Induced Dephasing

The discussion in Section 1.3.4 showed that the dispersive coupling of the qubit to a readout resonator or a cavity leads to a dispersive shift of the qubit frequency, depending on the number n_r of photons in the resonator (cf. Eq. (1.37)),

$$\omega_{\mathrm{q},n_\mathrm{r}} = \omega_{\mathrm{q},0} + 2\chi n_\mathrm{r} = \omega_{\mathrm{q},0} + \chi_\mathrm{ge} n_\mathrm{r}, \tag{1.88}$$

which is known as the AC Stark shift. In practice, however, preparing a resonator in a pure Fock state $|n_\mathrm{r}\rangle$ is difficult [219]. Usually the resonator is situated in a coherent state $|\alpha\rangle$, which implies that the Fock states $|n\rangle$ are Poisson distributed, $P(n) = |\langle n|\alpha\rangle|^2 = (\bar{n}_\alpha^n/n!)\exp(-\bar{n}_\alpha)$, where $\bar{n}_\alpha$ is the average photon number of this coherent state. The standard deviation of its photon number is found to be $\sigma_n = \sqrt{\bar{n}_\alpha}$. The distributions of qubit frequencies for different values of $\bar{n}_\alpha$ are depicted in Fig. 1.11. In the case that individual photon numbers can not be resolved, that is the dispersive shift is much smaller than the qubit decoherence time, $\chi_\mathrm{ge} \ll \Gamma_2$, the distribution has a Gaussian line shape [220] with standard deviation $\sigma \propto \sqrt{\bar{n}_\alpha}$ for large $\bar{n}_\alpha$, essentially corresponding to a classical state.[17] In this context, one can also speak of *coherent state photon shot noise* [192], since all the noise is due to a coherent quantum state of the resonator. However, even in the absence of a readout drive, the distribution of measured qubit frequencies possesses a finite linewidth of almost Lorentzian shape. The Lorentzian part is due to the resonator's

[17] In the opposite case, $\chi_\mathrm{ge} \gg \Gamma_2$, individual qubit transitions are observed for each occupied Fock state, which is also known as 'number splitting' [220, 221].

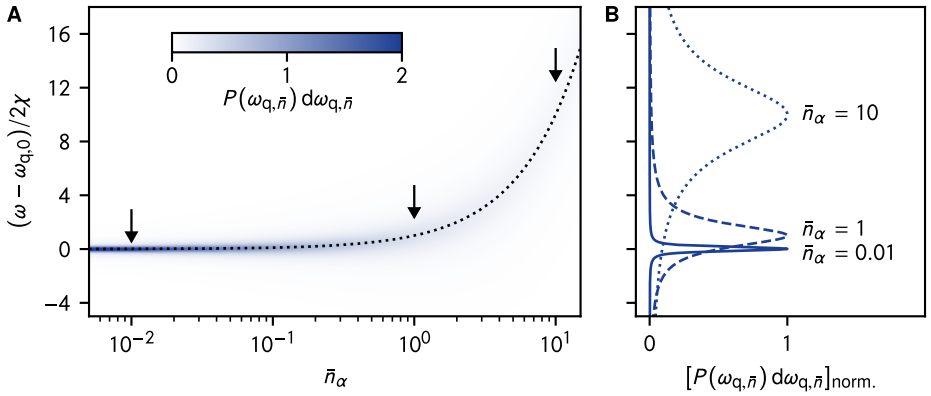

Figure 1.11: Broadening of qubit frequency. **(A)** Probability $P(\omega_{q,\bar{n}})\,d\omega_{q,\bar{n}}$ to detect the qubit frequency $\omega_{q,\bar{n}}$ within a frequency interval $d\omega_{q,\bar{n}}$ as a function of the average photon number $\bar{n}_\alpha$, which comes from the dispersively coupled resonator being prepared in a coherent state $|\alpha\rangle$, and the normalized frequency ω. This representation of the AC Stark effect is similar to typical experiments, where the probability density is encoded in measurable quantities like the resonator phase shift [220]. The expectation value for $\omega_{q,\bar{n}}$ follows the prediction of Eq. (1.88) with $n_r = \bar{n}_\alpha$ (dotted line). **(B)** Vertical line cuts of panel A (indicated by the arrows) for average photon numbers $\bar{n}_\alpha = 0.01$, 1, and 10, normalized such that the distribution peaks at a value of 1. The distribution of qubit frequencies approaches a Lorentzian line shape for $\bar{n}_\alpha \to 0$, limited mostly by the resonator's natural linewidth, and transforms into a Gaussian line shape with standard deviation $\sigma \propto \sqrt{\bar{n}_\alpha}$ for large $\bar{n}_\alpha$.

natural linewidth κ. In practice, however, there is always a small Gaussian contribution due to an unavoidable residual resonator photon population n_{th}. For the latter, the term *thermal photon shot noise* is used to differentiate from the above quantum version due to a coherent state. For arbitrarily strong readout drives, the distribution of qubit frequencies generally follows the line shape of a Voigt profile, which is a convolution of a Lorentzian and a Gaussian line distribution. To account for both types of photon shot noise, the total average photon number in a resonator can be written as the sum of the thermal photon number and the additional photon number due to a coherent drive,

$$\bar{n} = \bar{n}_{th} + \bar{n}_\alpha. \tag{1.89}$$

As pointed out in the beginning of Section 1.5.5, fluctuations in the qubit frequency directly translate into pure dephasing of the qubit. Pure dephasing that arises due to a fluctuating photon number of the resonator is coined under the term *photon shot noise-induced dephasing*. If the fluctuating photon number is due to a coherent drive of the resonator, the term *measurement-induced dephasing* is used.

Photon shot noise can also be described with a Lorentzian noise spectral density, $\mathcal{S}(\omega) \propto 2\kappa/(\omega^2 + \kappa^2)$, which falls off much faster than the typical inverse measurement time $1/t = O(\Gamma_{\bar{n}})$ that is on the order of the photon shot noise induced dephasing rate $\Gamma_{\bar{n}}$. In this limiting case, the phase decay function has an exponential envelope, $e^{-\Gamma_{\bar{n}} t}$ [214, 215]. However, deriving $\Gamma_{\bar{n}}$ for an arbitrary photon number $\bar{n}$ proves to be somewhat more complicated. For this reason, simply the results of the derivation in Refs. [222, 223] are

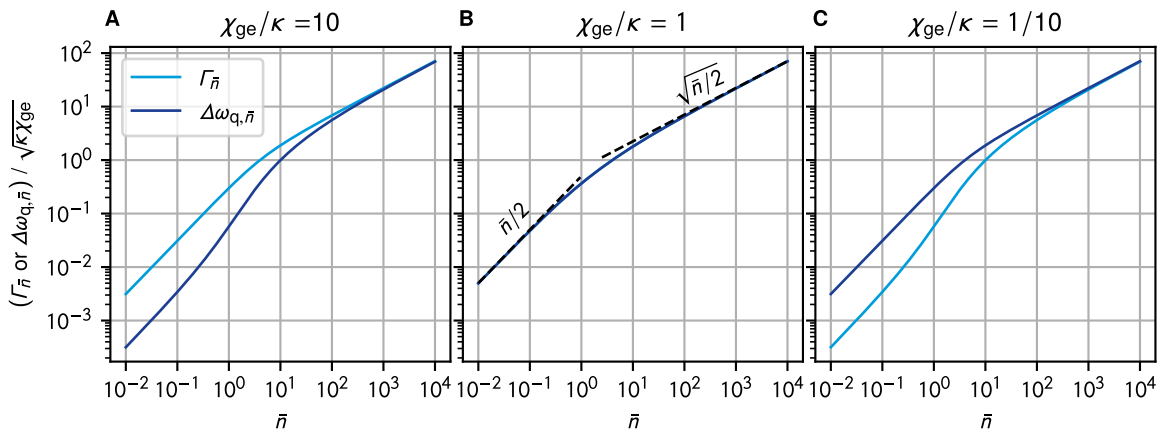

Figure 1.12: Photon shot noise in the resonator affects the qubit. Eq. (1.90) is used to calculate the photon shot noise-induced dephasing rate $\Gamma_{\bar{n}}$ (light-blue) and qubit frequency shift $\Delta\omega_{q,\bar{n}}$ (dark-blue), normalized to the harmonic mean $\sqrt{\kappa\chi_{ge}}$ of resonator linewidth and dispersive shift, for **(A)** $\chi_{ge}/\kappa = 10$ **(B)** $\chi_{ge}/\kappa = 1$ **(C)** $\chi_{ge}/\kappa = 1/10$. In panel B, the dashed lines represent the predictions Eq. (1.91) for small photon numbers, and Eq. (1.92) for large photon numbers, respectively.

recited, which yield a common expression for $\Gamma_{\bar{n}}$ and also a qubit frequency shift $\Delta\omega_q$ as follows,

$$\Gamma_{\bar{n}} + i\Delta\omega_q = \frac{\kappa}{2}\left(\sqrt{\left(1 + \frac{i\chi_{ge}}{\kappa}\right)^2 + \frac{4i\chi_{ge}}{\kappa}\bar{n}} - 1\right). \tag{1.90}$$

The frequency shift $\Delta\omega_q = \Delta\omega_{q,\bar{n}} + \Delta\omega_{q,0}$ consists of a photon number-dependent AC Stark shift $\Delta\omega_{q,\bar{n}}$ and the Lamb shift $\Delta\omega_{q,0} = \chi_{ge}/2$. In the regime of small photon numbers $\bar{n} \ll 0.1$ holds the approximation

$$\Gamma_{\bar{n}} + i\Delta\omega_{q,\bar{n}} = \frac{\kappa\chi_{ge}}{\kappa^2 + \chi_{ge}^2}(\chi_{ge} + i\kappa)\bar{n}. \tag{1.91}$$

In the case $\chi_{ge} = \kappa$, the even more compact expression $\Gamma_{\bar{n}} = \Delta\omega_{q,\bar{n}} = \kappa\bar{n}/2$ is found. Conversely, in the limit of large photon numbers, $\bar{n} \gg \max(\chi_{ge}/\kappa, \kappa/\chi_{ge})$, one can approximate

$$\Gamma_{\bar{n}} = \Delta\omega_{q,\bar{n}} = \sqrt{\frac{\kappa\chi_{ge}\bar{n}}{2}}. \tag{1.92}$$

In Fig. 1.12, Eq. (1.90) is evaluated for three different ratios χ_{ge}/κ. In the case when resonator linewidth and dispersive shift are balanced, $\chi_{ge} = \kappa$, Eq. (1.90) predicts that rate and shift are equal for an arbitrary photon number, $\Gamma_{\bar{n}} = \Delta\omega_{q,\bar{n}} = (\kappa/2)(\sqrt{1 + 2\bar{n}} - 1)$ (Fig. 1.12B). In the unbalanced case $\chi_{ge} > \kappa$ (or $\chi_{ge} < \kappa$) shown in Fig. 1.12A (C), the normalized rates $\Gamma_{\bar{n}}/\sqrt{\kappa\chi_{ge}}$ and shifts $\Delta\omega_{q,\bar{n}}/\sqrt{\kappa\chi_{ge}}$ are equal to the balanced case in the high photon number limit, and they differ from it for small photon numbers. As predicted from Eq. (1.91), both the dephasing rate and the frequency shift are linearly proportional to $\bar{n}$, and they differ only in a ratio χ_{ge}/κ.

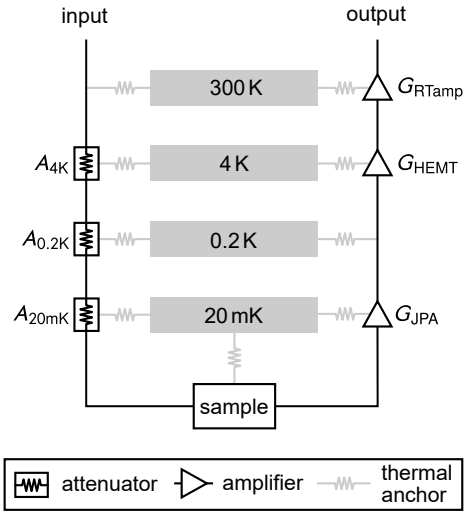

Figure 1.13: Microwave readout chain. Samples are typically cooled within a dilution refrigerator, which consists of several temperature stages to subsequently shield from hot thermal radiation. In order to drive a resonator-qubit sample, anchored at the 20 mK dilution stage, a microwave input and output chain from 300 K down to 20 mK are installed inside the cryostat. Attenuators with attenuations A_i, typically thermally anchored at the three lowest temperature stages (20 mK, 0.2 K and 4 K), are inserted into the input chain to sufficiently reduce the photon shot noise coming from room temperature, as discussed in the text. In order to create an at room temperature measurable signal level, a readout signal traveling along the output chain is amplified by a series of amplifiers.

1.5.6 Excess Photon Shot Noise from Microwave Chains

According to the Bose-Einstein statistic, $n_{\mathrm{B}}(f,T) = (\exp(hf/k_{\mathrm{B}}T)-1)^{-1}$, and in the absence of a readout drive, a residual photon population of $\bar{n} = \bar{n}_{\mathrm{th}} \sim 10^{-8}$ would be expected for an 8 GHz resonator in thermal equilibrium at 20 mK. However, in experiments with resonators in the gigahertz (GHz) regime, the residual $\bar{n}_{\mathrm{th}}$ is observed to be between 2×10^{-4} and 2×10^{-1} [9, 192, 223–229], orders of magnitude larger than the expected value. Research over the past decade found evidence, that the excess thermal photons in the resonator originate from heat loaded in attenuators or filters anchored at higher temperature stages, transmitted via the microwave chains in form of blackbody radiation [225]. It is thus crucial to ensure that new microwave input chains do not degrade qubit performance by causing excessive thermal photon shot noise-induced dephasing.

In order to illustrate the concept of excessive thermal photon shot noise, a simplified sketch of a typical microwave readout chain for a resonator-qubit sample is shown in Fig. 1.13, containing only attenuators on the input side and amplifiers on the output side. The attenuators in the input chain are necessary for reducing the blackbody radiation coming from room temperature. An attenuator with attenuation $A_i > 0$ effectively works as a beamsplitter in the sense that it attenuates incoming noise by a factor $a_i = 10^{-A_i/10\,\mathrm{dB}}$ and adds a $1-a_i$ fraction of blackbody radiation according to its temperature (cf. Fig. 3.12D and Eq. (3.13)). In typical setups, the thermal excess photon shot noise reaching the sample is wished to be below 10^{-3}. For a resonator at 6 GHz, room-temperature blackbody radiation reaching the resonator would result in photon shot noise on the order of 10^3 if no attenuation were to be inserted. To bridge the six orders of magnitude, 60 dB of attenuation are therefore needed, optimally at the dilution stage for minimum added noise. Unfortunately, practice throws a wrench into this plan. In order to control a single qubit, Ref. [230] estimates an average power of −78 dBm, for which quantities such as

the duty cycle or the shape of control pulses were factored in.[18] To realize this signal level at the sample with 60 dB of attenuation in the input chain, signals need to start at room temperature on average with −18 dBm power, out of which essentially everything ($1 - 10^{-6} = 99.9999\%$) would be dissipated in the attenuator anchored on the dilution stage in the above scenario. This corresponds to an average heating power of 16 µW, which basically equals the available cooling power on the dilution stage of a customary dilution refrigerator [231]. To keep the impact of the heating power at a minimal level, it should be negligibly small compared to the available cooling power. This condition becomes even more stringent when operating more than one qubit at the same time. Thus, in order to reduce the heating power on the dilution stage, the total 60 dB of attenuation need to be distributed onto different temperature stages. In Ref. [230], the authors provide an in-depth analysis of various such distributions of the attenuators, and they conclude in what corresponds in our case to $A_{20\mathrm{mK}} = A_{0.2\mathrm{K}} = A_{4\mathrm{K}} = 20\,\mathrm{dB}$. This choice is motivated by the following considerations: At GHz frequencies, blackbody radiation remains in the linear regime for temperatures $T > 1\,\mathrm{K}$, such that $n_\mathrm{B} \propto T$. Therefore, the attenuation should be chosen according to the temperature ratios between the different stages. Accordingly, an attenuation of 20 dB on the 4 K stage is appropriate, as it reflects the temperature ratio 300 K/4 K. The decision to prefer $A_{20\mathrm{mK/0.2K/4K}} = 20/20/20\,\mathrm{dB}$ over $30/10/20\,\mathrm{dB}$ was justified by reducing the heating power at the dilution stage by approximately a factor of 10, which might become relevant when targeting the control over systems with up to 100 qubits. Since in the present work only a handful of qubits are of interest at the same time, the above constraint can be released a little bit, such that a total attenuation of 30 dB or even 40 dB becomes feasible at 20 mK. Any additional attenuation due to cable sections in-between the temperature stages then only complies with a reduction of blackbody radiation from higher temperature stages, without leading to harmfully hot input chains. For completeness, it is mentioned that there are also other types of microwave chains, such as flux lines, pump lines or output lines. For a critical discussion of their design considerations, the reader is referred again to Ref. [230].

So far, only the ubiquitous photon shot noise in the absence of input signals, which is typically referred to as *passive heat load*, has been discussed. However, the heating power due to the attenuation of input signals in principle also results in a temperature increase of the attenuators, accompanied by an increase of photon shot noise. This additional amount is commonly called *active heat load*, which will be discussed extensively in Chapter 3.

In the end, the other half of the microwave chain, the output side, as depicted in Fig. 1.13, shall be briefly discussed. After their interaction with the sample, readout signals used to infer the qubit state via the dispersive interaction with a readout resonator, typically have an equivalent power of −135 dBm in the single-photon regime. In order to make such weak signals detectable by the measurement apparatus at room temperature, they need to be amplified by $\sim 100\,\mathrm{dB}$. This essentially requires several amplifiers in the output chain. Typically used are a nearly quantum-limited amplifier at the dilution stage, a low

[18] Therein, it is also argued that resonator readout pulses typically result in a more than an order of magnitude smaller average power, such that their relevance for this estimate can be neglected.

noise amplifier (LNA) based on high-electron mobility transistors (HEMT) at 4 K as well as a standard room temperature amplifier (RT amp) outside the cryostat. The amplifier at the 20 mK stage is conventionally realized in form of a resonant Josephson parametric amplifier (resonant-JPA) or a traveling-wave parametric amplifier (TWPA) [42]. The latter category also includes in-house developed amplifiers such as the dimer Josephson junction array amplifier (DJJAA) [41] or the granular aluminum parametric amplifier (grAlPA) [43]. Photon shot noise coming from the output line is usually sufficiently well suppressed in the setup due to the integration of multiple isolators or circulators.

2 Dissipation in Granular Aluminum Fluxonium Qubits

This chapter presents the first main result of this work: the observation that inductive loss is the limiting factor for several low-frequency granular aluminum (grAl) fluxonium qubits. For this, grAl fluxoniums were for the first time combined with a coplanar waveguide (CPW) architecture and with a normal metal ground plane. A comparison with other fluxonium qubits based on grAl and other high kinetic inductance materials hints at the universal nature of inductive loss in grAl, in agreement with previously measured internal losses of grAl-based resonators. This project was carried out in close collaboration with Martin Spiecker, who documented the design considerations and the initial work in Ref. [95].

As discussed in Section 1.3.3, the nano-composite grAl is a promising material when it comes to realizing superinductors with a small footprint due to its high kinetic inductance and–compared to Josephson junction (JJ) arrays–a high plasma frequency [120]. Furthermore, internal quality factors of grAl resonators were found to be on the order of $10^5 - 10^6$ in the single photon regime [123, 232], rendering grAl attractive for quantum circuits. For this reason, grAl becomes particularly interesting for fluxonium qubits which feature a large inductance in parallel to the non-linear JJ. While the research on fluxoniums based on grAl superinductors is continuously increasing [6, 8–10, 125, 145, 233], a general understanding of their underlying loss mechanisms has been put forward only very recently [125]. The present work attempts to tackle this task.

This chapter is organized as follows: In Section 2.1, the different sample design generations are presented, followed by an introduction of sample holder as well as magnetic and thermal radiation shielding in use in Section 2.2. Section 2.3 provides an overview of the microwave setup that was used throughout the work. Section 2.4 then focuses on two challenges that were encountered in flux biasing the fluxonium qubits. Finally, Section 2.5 contains the main results of the measured energy relaxation versus magnetic flux bias for three grAl fluxonium qubit samples, which are compared with other fluxonium samples in the literature in Section 2.6.

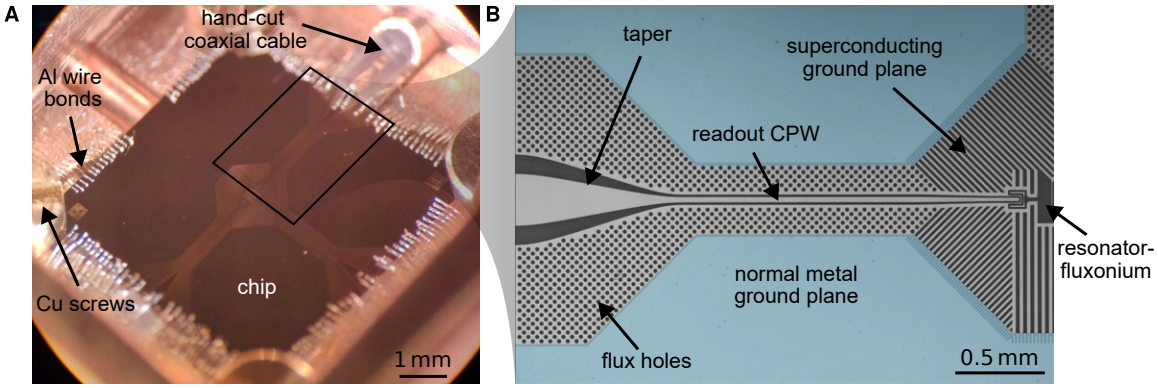

Figure 2.1: Generation 1 sample design. Optical images of **(A)** the sample chip installed in the copper (Cu) sample holder, and **(B)** a zoom-in into one of the three coplanar waveguides (CPW) on a chip. The chip is mechanically anchored via Cu screws on all four corners. Electrical and thermal contact is established with aluminum (Al) or gold (Au) wire bonds. The CPW in panel B, used for resonator readout, is made of (superconducting) Al, and its inner and outer conductors have a width of 30 µm and 170 µm, respectively, which grow in a tapered way towards the chip edge for a facilitated placement of wire bonds. The outer conductor is filled with a grid of "flux holes", 22 µm in diameter. In the close vicinity of the resonator-fluxonium, the superconducting ground plane merges into a stripe-like structure with a maximum 20 µm stripe width. More details on the resonator-fluxonium will be presented with the generation 2 sample design in Section 2.1.2.

2.1 Sample Design

At the start of this project, fluxonium qubits were commonly designed for a 3D microwave waveguide or cavity [102, 163, 233, 234]. Notable exceptions to this approach are represented by Refs. [38, 110], in which the resonator-fluxonium devices are coupled to an on-chip transmission line to read out quantum information. This strategy of placing the fluxonium in a 2D coplanar waveguide (CPW) architecture was regarded as attractive for the present work as well, as it potentially allows for the integration of on-chip qubit control lines in the close vicinity of the fluxonium loop. With this emerges the tantalizing possibility of fast-flux control over qubit and coupler circuits [171, 235], which may enhance computational speed in future flux-qubit-based quantum processors. It also opens up interesting experimental possibilities, such as Floquet engineering of the of the spectrum [236] and quantum Szilard engine [8] spectroscopy based on fast-flux reset. In the following, different generations of the sample design are presented, together with a short discussion on which observations made the development of a second generation necessary.

2.1.1 Generation 1: Design with Flux Holes

Fig. 2.1 provides an overview of the first generation sample design of grAl fluxoniums in 2D CPW architecture. As illustrated in Fig. 2.1A, a chip containing two grAl fluxoniums is placed inside the Cu sample holder that is presented in more detail in Section 2.2. For now, only the motivation and the design of the CPW architecture will be presented without

diving into the detailed fabrication. For the latter, the reader is trusted to stay patient for the upcoming discussion of the second generation of sample design in Section 2.1.2. Therein, also a detailed discussion of the fluxonium design is going to be presented.

Dedicated CPWs are used for resonator readout and qubit control (Fig. 2.1B). Superconducting Al is implemented near the fluxonium, resonators, and CPWs, where most electromagnetic fields are stored, to reduce microwave losses. The outer conductors of the CPWs are perforated with 'flux holes' to prevent flux trapping and pinning in the large superconducting metal sheet. Similarly, simply-connected shapes with stripe widths well below the threshold for vortex penetration in superconducting thin films are used near the resonator-fluxoniums. In Eq. (1.4), this threshold was estimated for the comparably large and sensitive fluxonium loop of size $(140 \times 25)\mu m^2$ to be 90 µm. In future miniaturized designs, for example obtained by meandering the fluxonium loop [3], stronger magnetic fields would be required, resulting in a lower threshold on the maximum stripe width. Terminating the superconducting structure at a normal metal ground plane avoids low-frequency modes of the long stripes. The normal metal ground plane also helps in efficiently thermalizing the sample, especially when combined with gold (Au) wire bonds, which were tested for some samples. Most of the time, however, Al wire bonds were chosen, as shown in Fig. 2.1A. In this case, efficient chip thermalization is still achieved via four Cu screws that mechanically fix the chip to the sample holder at its corners.[1] The wire bonds also electrically connect the ground plane to the sample holder and the CPW inner conductors to the inner pins of hand-cut coaxial cables.

The normal metal ground plane was originally also intended to act as a phonon trap, which could reduce the number of excess quasiparticles circling on the qubit chip [205, 210], which might become a limitation of future quantum processors based on superconducting qubits [207, 237]. High-energy particles can generate a phonon shockwave that is able to partially break superconductivity in multiple superconducting circuits on the same chip at the same time. This poses a serious threat to quantum computation because error-correction schemes cannot correct for such large and correlated errors. Possible solutions to this problem include shielding from the incoming radiation by going to a deep-underground facility with a lead-shielded cryostat [206], by keeping the quasiparticles away from active elements of the circuit by implementing either quasiparticle traps in the form of normal metal sinks in galvanic contact to the superconducting circuit [208], or by shielding the circuit from the generated phonon shockwave with the help of phonon traps. There are two major routes two realize phonon traps for superconducting circuits. The first one consists in placing a superconducting material with a lower spectral gap on the qubit chip [202, 205, 238], to down-convert the high-energy phonons that would otherwise continue breaking the circuit's Cooper pairs into quasiparticles. A second possibility represents the use of a neighboring normal metal ground plane [207, 210], such that a large amount of the phonons' initial energy is channeled to the normal metal electrons, away from the superconductor.

[1] Ultrasonically cleaned Cu screws were used instead of brass screws to avoid potential magnetizable impurities near the qubits.

Samples fabricated within this first generation yielded fluxonium qubits with promising, but strongly fluctuating energy decay times exceeding 20 µs and decoherence times of more than 6 µs, respectively (cf. Tables 5 and 6). In contrast to the samples of the second generation presented in Section 2.5, note that the qubit frequencies at half-flux bias were consistently above 1.2 GHz. However, during the flux-biasing of fluxoniums in this generation, the issue of sudden flux jumps was encountered, as discussed in Section 2.4.1, leading to the development of a second design generation without flux holes.

2.1.2 Generation 2: Flux Hole-Free Design

In Fig. 2.2, one of the grAl fluxoniums of the second design generation is presented. The CPW architecture resembles in many respects the one of the first generation, but it differs strongly in the design of the superconducting outer conductors of the CPWs, which has now only a width of 28 µm on each side and no flux holes anymore. Despite the close proximity of the normal conducting ground plane, electromagnetic field simulations with the high-frequency structure simulation software (HFSS) from Ansys [239] ensured that the losses in the CPW are still negligible [95].

For the superconducting ground plane, the use of niobium (Nb) over Al was preferred, as it helped avoiding problems with ripped off CPWs during the dicing process of the wafer, plus Nb has shown to possess low losses on sapphire substrates [240]. Additionally, in this first optical lithography step a 5 nm thick Al layer on top of the 45 nm thick Nb film was used to be able to keep using the calibrated argon milling process to connect to the normal metal ground plane out of silver (Ag) in a second step. Before the deposition of the 100 nm thick Ag ground plane, a 4 nm thick sticking layer of Nb was evaporated onto the wafer. The thickness of the sticking layer is chosen such that it does not proximitize the Ag (cf. Section 1.2.4), as this would allow again for flux pinning (cf. Section 1.2.1). The readout CPWs terminate in a capacitive coupling to the readout resonator via its capacitor shoe, and the qubit control CPW terminates in a fast-flux coil (Fig. 2.2B), designed to have a mutual inductance with the fluxonium loop of $M \sim 1\,\mathrm{pH}$ [95]. In this way, a current of 1 mA tunes the fluxonium by one flux quantum. Both HFSS simulations and experimental results have shown a crosstalk between the two readout CPWs is approximately −40 dB. If this already promising crosstalk for CPWs on the same chip needs to be lowered even further, a modular approach as in Ref. [4] could be considered.

Prior to the optical lithography steps described in the previous paragraph, the fluxonium, the resonator and in later versions a Purcell filter are deposited in a single electron beam lithography step. First, the Josephson junction (JJ) in Fig. 2.2D is realized by a combination of the Dolan-bridge technique [241] and undercuts (more details in Ref. [95]) and a deposition of 20 nm and 30 nm thick Al layers under two tilt angles ±31°, with an intermediate 4 min long static oxidation at 20 mbar of the first layer. Then, all inductances are patterned within a third deposition step of grAl with zero tilt. This includes the fluxonium and resonator inductances with a width of 170 nm, as well as the shared inductance and also the inductance of the potential Purcell filter with a width of 250 nm. The shared inductance thereby realizes the inductive coupling between the fluxonium qubit and the readout

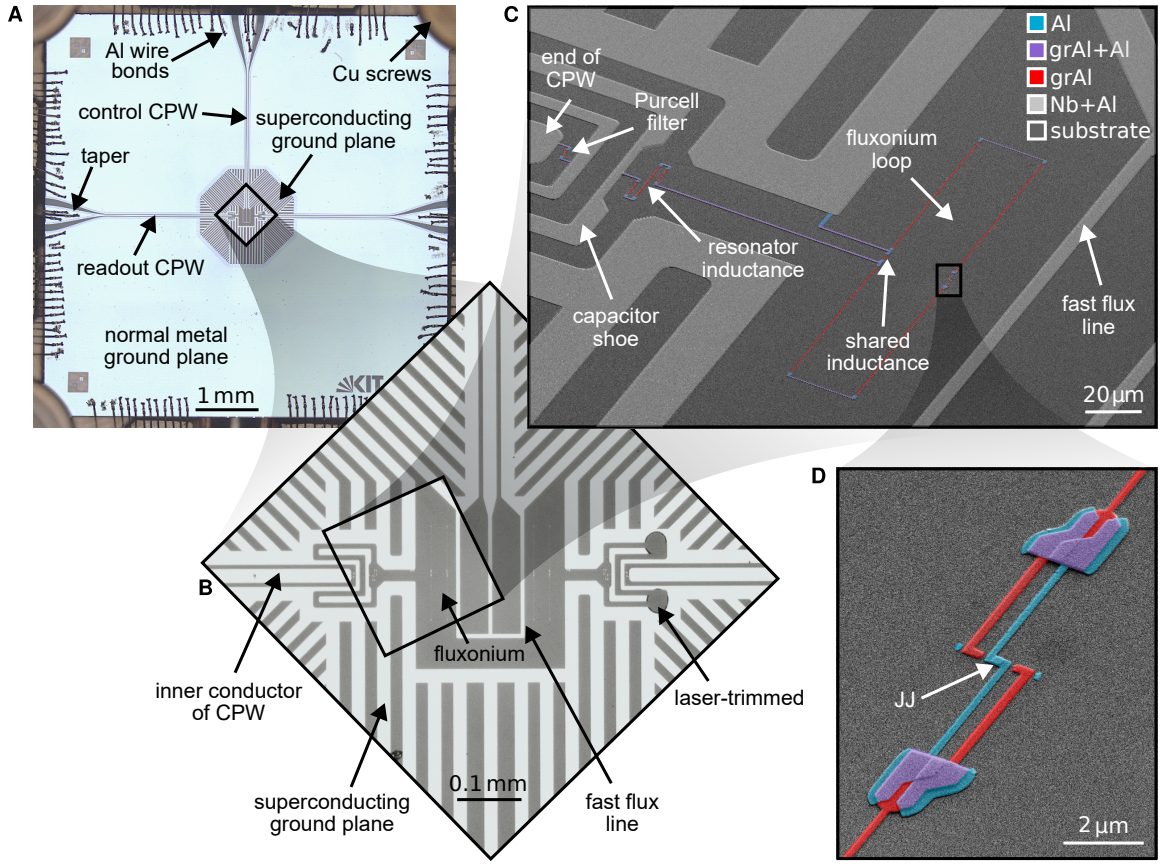

Figure 2.2: Generation 2 sample design. Optical images of **(A)** the full chip and **(B)** a zoom-in of its central area. There are three coplanar waveguides (CPW) per chip, one each for reading out the two fluxonium qubits, and one for the fast-flux line for qubit control. Close to the CPWs as well as in the vicinity of the fluxonium qubits, a superconducting structure out of Nb and Al is implemented, which terminates in a normal metal ground plane out of Ag. Al wire bonds are used to connect the ground plane to the sample holder and the inner conductor of the tapered CPWs to the inner pins of the hand-cut coaxial cables (more details in Section 2.2). The two resonator-fluxoniums on this chip correspond to samples 1 (left) and 2 (right) in Section 2.5. False-colored scanning electron micrographs of **(C)** a resonator-fluxonium device and **(D)** its Josephson junction (JJ). The fluxonium is inductively coupled to the readout resonator via a 250 nm wide shared inductance. The resonator terminates on the one side in the ground plane and on the other side in a capacitor shoe for capacitive coupling to the CPW. As depicted in panel B, the capacitor shoe of the right-hand resonator was laser-trimmed post-fabrication, to increase the separation of both readout resonator modes on the chip. At the end of the CPW, a small inductance was implemented to realize a Purcell filter in later samples. All inductive elements, including also the resonator and fluxonium superinductances with a width of 170 nm, are made out of a 50 nm thick grAl layer. The resonator-fluxonium device is realized within a three-angle shadow evaporation (Appendix C). The JJ has an area of $A_{\mathrm{JJ}} = (0.24 \times 0.33)\,\mu\mathrm{m}^2$.

resonator. Due to the large kinetic inductance of grAl, the resonator has a smaller footprint compared to conventional CPW resonators.

Details on the fabrication process of the two optical lithography steps as well as the preceding e-beam-lithography step can be found in Appendix C. A selection of fabricated wafers with details on their design and fabrication parameters is presented in Appendix D. An overview of some of the measured samples can be found in Appendix E. Details regarding the design process of the grAl fluxoniums are summarized in Ref. [95].

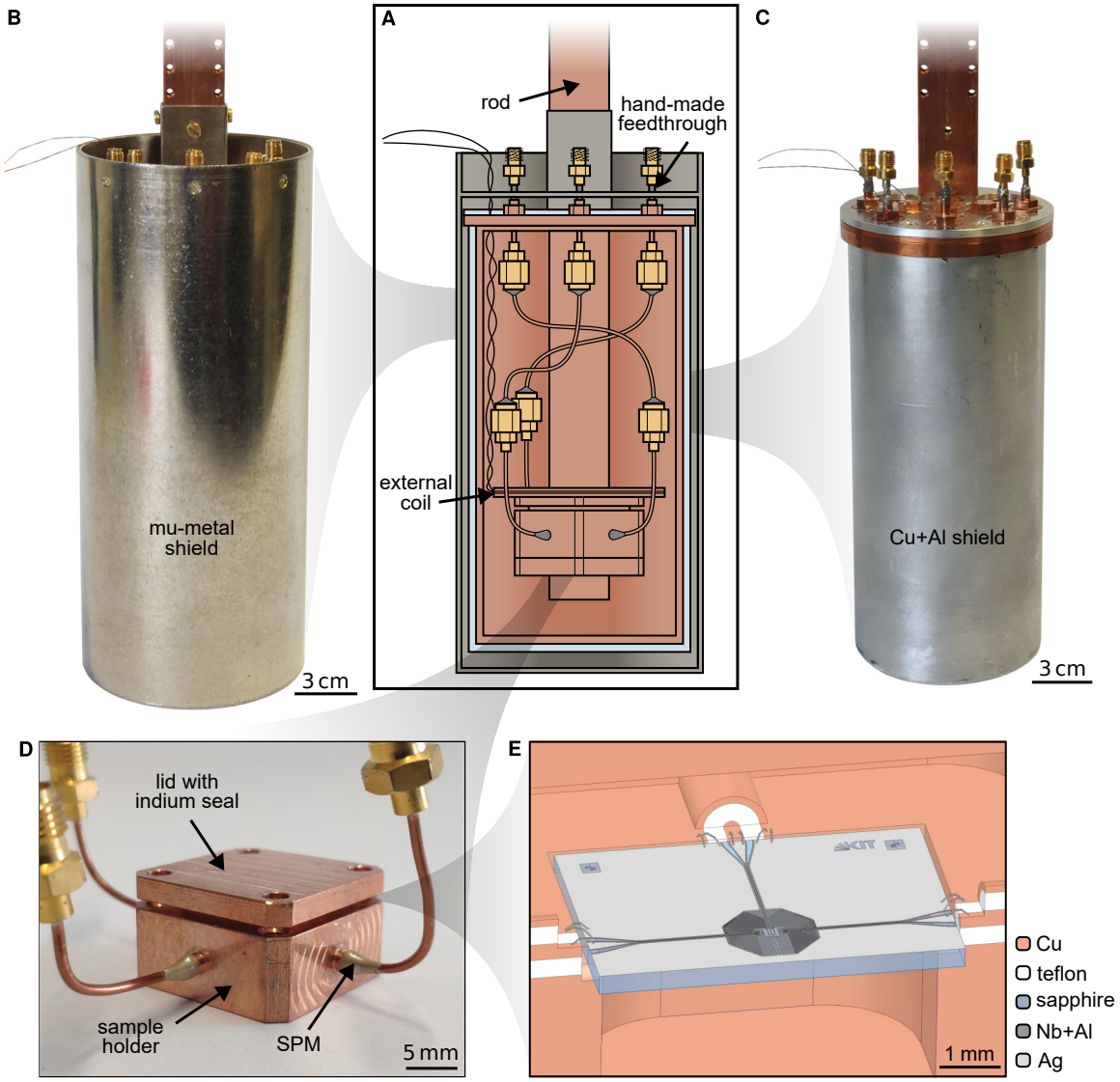

Figure 2.3: Sample holder and shields. **(A)** Side-view sketch of the half-open magnetic and thermal radiation shields. A look into the interior reveals that the sample holder is fixed mechanically onto the thick Cu rod, onto which also all shields are screwed. Microwave signals reach the sample box via hand-made SMA feedthroughs and cables with non-magnetic SMA connectors. An external coil with superconducting wire is supplied by a twisted pair of wires, which passes the shields via minimum-sized holes to minimize excess thermal radiation into the interior. Optical images of **(B)** the outer mu-metal shield, **(C)** the inner Cu+Al shield, and **(D)** the Cu sample holder including lid. **(E)** Side-view sketch of the half-cut sample holder, revealing that the chip is suspended in air to avoid low-frequency modes in the substrate. The photographs in panels B, C and D as well as the half-cut 3D model in panel E were adapted from Ref. [95]. ©2024 by Martin Spiecker. Reprinted with permission.

2.2 Sample Holder and Shielding

Fig. 2.3 provides an overview of the sample holder as well as the surrounding magnetic and thermal radiation shields that were first introduced in Ref. [123]. In the schematic drawing of Fig. 2.3A, the interior of a full constellation is shown. The sample holder is

equipped with an external magnetic coil with superconducting wire for flux-biasing the fluxonium qubits. For mechanical stability as well as proper thermalization, the sampler holder is mounted via a small Cu piece onto a $(2 \times 1)\,\mathrm{cm}^2$ thick Cu rod, which is used to attach the whole setup on the dilution stage of a cryostat.[2] In principle, the shields can host up to two sample holders at the same time. All components inside the Cu+Al shield are aimed to be non-magnetic, which includes especially the SMA connectors of the coaxial cables, the hand-made feedthroughs on the upper base of the inner shield, and the screws for mounting the chip inside the sample holder (cf. Fig. 2.1A). For magnetic and thermal radiation shielding, a combination of an outer 1 mm thick mu-metal shield (Fig. 2.3B) and an inner shield, which consists of a thin Al cylinder being shrinked onto a Cu cylinder (Fig. 2.3C), is used [123]. As mu-metal possesses a relative permeability of $\mu_\mathrm{r} \sim 10^5$, its purpose lies in attenuating the external magnetic field by up to five orders of magnitude. The intention of the Cu+Al shield is two-fold: First, the remaining magnetic fields inside the mu-metal shield will be further shielded and pinned as soon as Al becomes superconducting ($T < 1.2\,\mathrm{K}$), and second, it provides an efficient radiation shield that is thermalized on the dilution stage, as all holes are sought to be tightly closed.

The sample holder is illustrated in Fig. 2.3D. For resonator readout and qubit control signal delivery, three coaxial cables were slid through the side walls of the holder. The cables were hand-cut with a sharp scalpel beforehand to create a flat surface, which allows for a reliable placement of bonds onto the inner conductor. After correct positioning, the cables are fixed with a silver-polymer mixture (SPM), as used in Section 3.1.3.[3] Once the sample holder has been prepared in such a way, a sample chip is placed inside (Fig. 2.3E) and mechanically fixed via Cu screws on all four corners of the chip (as shown in Fig. 2.1A). All CPWs and the ground plane are then electrically and thermally contacted via ultrasonically-welded Al or Au wire bonds to the inner pins of the coaxial cable and the Cu sample holder, respectively. Afterwards, the sample holder is closed with a lid, between which a thin line of indium is placed to provide another seal to suppress the intrusion of thermal radiation.

2.3 Microwave Setup

An overview of the employed microwave setup is shown in Fig. 2.4. The setup consists of two main parts: First, in order to extract quantum information from the resonator-fluxonium sample, there is a microwave input chain that leads directly to the CPW that is coupled capacitively to the readout resonator. A circulator with 20 dB in-band ($4 - 8\,\mathrm{GHz}$) isolation in backward direction helps in providing directionality of the signal flow, needed to extract information from the resonator in single-port reflection measurements. After their reflection/interaction with the resonator, input signals are routed towards the output line, where they get amplified in an amplifier chain of at least a low noise amplifier (LNA)

[2] In the rare case that such an coil-equipped sample holder is not fixed to a rod or similar, the interested reader may catch a glimpse of their motion in Ref. [242].

[3] Even though soldering was also a valid and mechanically more stable option, it sometimes led to squeezing out the teflon dielectric due to the higher temperatures involved in the process.

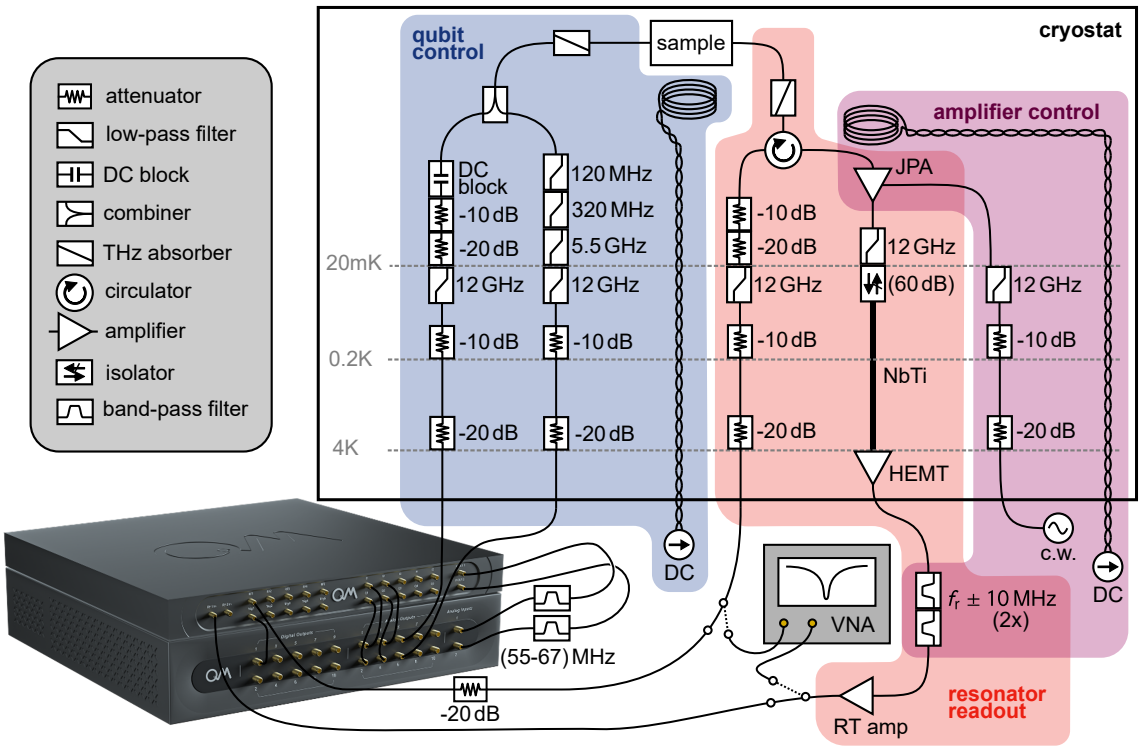

Figure 2.4: Microwave setup. Resonator readout (red) to infer information about the qubit state is performed either with a vector network analyzer (VNA) or Quantum Machines (QM) measurement setup (OPX+ and Octave). Optionally, a flux-tunable Josephson parametric amplifier (JPA) can be added into the readout chain (purple). For qubit control (blue), two input chains were combined at 20 mK. The first qubit control line is built to transmit only radio frequency (RF) microwave signals. The second line is used for transmitting DC fast flux changes to the qubit flux line. The decoupling of the DC and RF lines is due to different attenuation and filtering requirements for each regime. The QM setup can also provide qubit control pulses for most of the relevant qubit frequency range.

consisting of high-electron mobility transistors (HEMT) anchored at the 4 K stage and a room-temperature amplifier (RT amp). In order to keep the added noise from the amplifier chain as low as possible, it is important to insert the least attenuation as possible. Therefore, a superconducting NbTi coaxial cable is implemented between the dilution stage and the HEMT, and a CuNi coaxial cable with a silver-coated inner conductor is used from the HEMT to room-temperature. An isolator with an in-band isolation of 60 dB is placed in the output chain at the dilution stage to prevent reflected signals–caused by potential impedance mismatches in the chain–from reaching the sample.

Optionally, a flux-tunable Josephson parametric amplifier (JPA) in form of a home-made dimer Josephson junction array amplifier (DJJAA), as introduced in Ref. [41], can be added to the amplifier chain. This amplifier serves as a near-quantum limited amplifier with $\sim$ 20 dB amplification at the dilution stage, providing a valuable resource to realize rapid high-fidelity single-shot readout. The only additional obstacle that needs to be overcome when using such an amplifier is that the comparably strong pump pulse, which is needed for its internal frequency conversion and thus amplification, also travels along the output line, resulting in a saturation of the RT amp if no further measures are taken. For this

reason, one or–as in this case–sometimes even two consecutive band-pass filters are typically integrated into the output chain at room temperature, before the RT amp. These 3D cavity-based band-pass filters [243] are tunable in frequency such that a suppression of several orders of magnitude of the pump tone compared to the readout pulse can be achieved.

The second part of the setup consists in qubit control. Apart from magnetic flux biasing of the fluxonium qubit with the external coil presented in the previous section, two distinct microwave chains were combined, one for radio frequency (RF) control pulses and one for slow direct current (DC) like pulses, at the dilution stage to a single line that is connected to the fast-flux coil-terminated CPW. The control line for DC pulses consists of three consecutive low-pass filters having a minimum cut-off frequency of $\sim$ 120 MHz, instead of the otherwise used 30 dB attenuation, on the dilution stage. In the microwave chain for RF pulses, a DC block was inserted to prevent low-frequency signals that are sent via the DC line from propagating back out of the cryostat via the RF line.

All microwave lines connected directly to the sample possess in total 60 dB of attenuation distributed on the different temperature stages (for a discussion of their distribution, the reader is referred to Section 1.5.6) or an equivalent low-pass filtering. Additionally, there is in each of these lines a home-made Eccosorb®-based THz absorber positioned as close as possible to the qubit,[4] which acts as an infrared filter with an attenuation of more than 10 dB for frequencies larger than 60 GHz. Furthermore, all lines, including the output line and the optional pump line, contain a low-pass filter (model: either TFWL-K-12G20G-SfSm from TElePur or 3L250-12240/T20000-O from K&L) with a $\sim$12 GHz cut-off frequency.

Experiments were performed in either one of the two following modes: The first consists in continuous wave (c.w.) readout and control signals. In this mode, a vector network analyzer (VNA) provides c.w. microwave signals for the readout and, in turn, is also able to evaluate the scattering parameter S_{21} between the sent and the received signal. This parameter contains information about the device under test, in this case the readout resonator inheriting information about the qubit state. Such a measurement can be combined with the usage of another c.w. microwave source (not shown in Fig. 2.4) to play a second microwave tone to saturate the qubit, which is usually sufficient to extract the qubit spectrum in a so-called two-tone spectroscopy.

The second mode is commonly referred to as 'time-domain', which relates to the fact that pulses with a certain temporal length and their position relative to each other can be defined. To realize time-domain measurements, the quantum orchestration platform provided by Quantum Machines was used, which consists of an FPGA-based OPX+ instrument [244], allowing to program complex quantum operations, and the Octave instrument [245] that allows for a seamless up- and down-conversion of the OPX+-provided baseband pulses to microwave frequencies needed to readout the resonator or control the qubit.

[4] The THz absorbers were usually attached directly on top of the feedthroughs of the shielding (cf. Section 2.2), since putting them in the interior of the shielding was avoided.

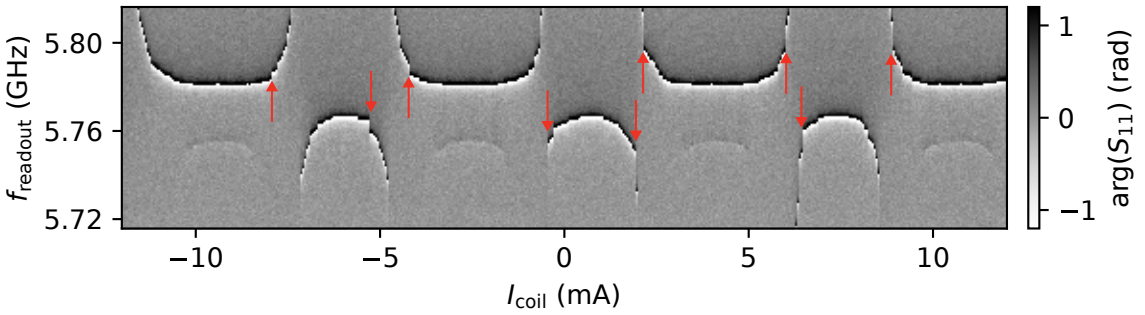

Figure 2.5: Flux jumps. Single-port reflection phase response arg(S_{11}) of the readout resonator versus current I_{coil} in the external coil. The response deviates from being periodic in I_{coil} and instead shows sudden 'flux jumps', as indicated by the red arrows.

2.4 Challenges with Flux Control

2.4.1 Flux Jumps

As introduced in Section 1.3.4, normally a dispersive shift of the readout resonator that is periodic in external magnetic flux Φ_{ext} would be expected, which, in turn, is ideally linearly proportional to the current I_{coil} in the external coil. Within first c.w. measurements with samples of the first generation, however, sudden jumps in the flux bias of the fluxonium qubits were observed, as indicated by the arrows in Fig. 2.5. This behavior is suspected to originate from the flux holes in the outer conductors of the CPWs, leading to the evolved design of the second generation.

2.4.2 Flux Delay

In this section, the phenomenon of flux delay is introduced, which was observed in samples of the second generation[5] when performing adiabatic flux ramps using the fast-flux coil. All of the following results were received with the resonator-fluxonium of sample 3 in Section 2.5.

The initial observation of flux delay occurred when performing an energy relaxation spectroscopy, i.e., measuring the energy relaxation as a function of the external magnetic flux through the fluxonium loop. The idea was to speed up the experimental workflow by taking advantage of the fast-flux line, which would allow for calibrating the qubit control pulses and readout of the qubit state only at a single flux point, e.g. the half-flux sweet spot, and intermediately ramp the flux quickly to a different magnetic flux to let the qubit decay there. The encountered problem was that the duration of free energy decay at a certain flux position seemed to affect the flux position. In order to get a clearer understanding of the phenomenon, the plainer experiment illustrated in Fig. 2.6B was devised.

[5] It has not been tested on samples of the first generation.

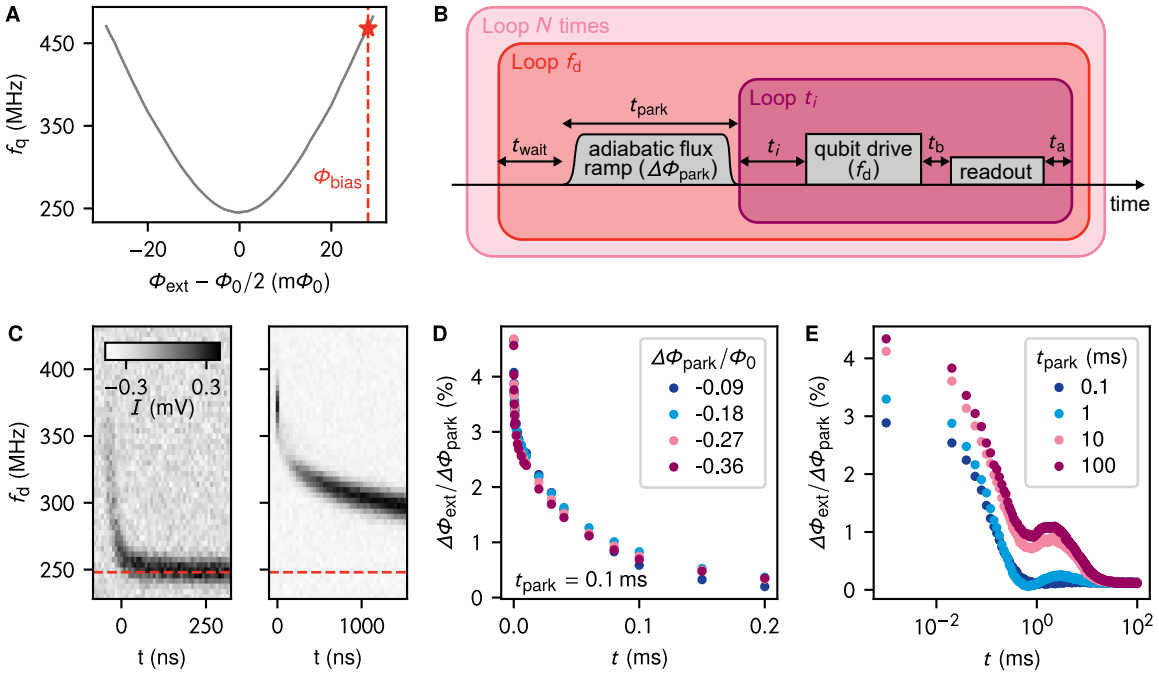

Figure 2.6: Observation of flux delay. **(A)** Qubit frequency f_q around the half-flux sweet spot versus magnetic flux Φ_{ext}. The flux bias Φ_{bias} of the long-timescale experiments is shown as well. **(B)** Pulse sequence for the experiments performed to explore the flux delay, using three nested loops. With the inner-most loop, effectively a stroboscopic measurement of the resonator with a preceding qubit drive pulse of frequency f_d is realized. The drive pulse was for the long-timescale experiments a few-µs long saturation pulse and for the short-timescale experiments in panel C a calibrated π pulse. Before such a loop, the magnetic flux is adiabatically changed by $\Delta\Phi_{park}$ to 'park' the qubit at a different flux spot for a time t_{park}. Additional waiting times t_b and t_a before and after the readout pulse, respectively, were inserted to optimize the timing of pulses on the different lines, and another waiting time t_{wait} before each flux ramp was used to suppress the influence among repetitions. **(C)** Results of a measurement similar to panel B, with the distinction that the adiabatic flux ramp was included in the inner-most loop to allow for arbitrary sampling of the waiting times t_i after the flux ramp (but with the cost of longer total measurement time). The color scale represents the averaged I quadrature of single-port reflection measurements, which contains information about the qubit state: Small values on the shown scale of I correspond to the qubit being thermally populated, $p_{th} \sim 0.4$, while for larger values of I, the population is inverted to ~ 0.6. The qubit was biased at the half-flux sweet spot, $\Phi = \Phi_0/2$ and parked at the next zero-flux sweet spot ($\Delta\Phi_{park} = \Phi_0/2$) for either 400 ns (left panel) or 40 µs (right panel). **(D)** The observed flux delay amplitude $\Delta\Phi_{ext}$, obtained by converting the extracted qubit frequency with panel A into an external flux, scales linearly with $\Delta\Phi_{park}$. Note that the flux bias point was moved away from the first-order flux-insensitive sweet spot to $\Phi_{bias} = 28\,m\Phi_0$ to obtain a better sensitivity. The parking time was $t_{park} = 0.1$ ms and the flux delay decays on a similar timescale of ~ 0.1 ms. **(E)** For even longer parking times, non-monotonic features appear in the decay. The slowest decay happens on a timescale of ~ 3.5 ms.

Here, just an adiabatic flux ramp to and back from a parking flux position, at a flux difference of $\Delta\Phi_{park}$ for a duration t_{park}, is performed and the qubit frequency is stroboscopically observed after the flux ramp. The first results of this experiment are depicted in Fig. 2.6C, showing that a short parking duration (left panel) leads to a rather quick return to the flux bias point, whereas a longer parking duration (right panel) entails a much slower relaxation to the set flux bias point. Further investigations revealed that the flux delay amplitude $\Delta\Phi_{ext}$ (the difference between set and actual flux value) is linearly dependent

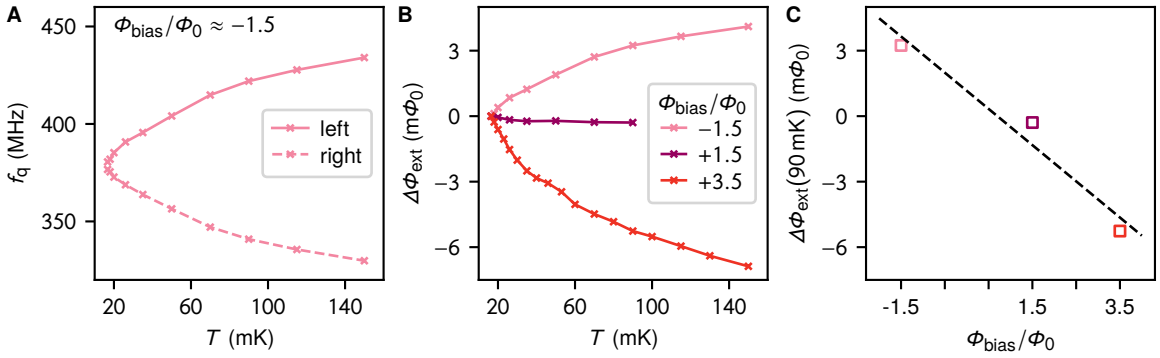

Figure 2.7: Flux shift versus temperature. **(A)** Observation of qubit frequency shift with increasing dilution stage temperature. The qubit is initially biased at base temperature with the external magnetic coil to the $-1.5\,\Phi_0$ sweet spot. For the measurements, an additional flux is generated via the fast-flux line, such that the qubit is consecutively at two symmetric flux points with respect to the sweet spot (left and right of it) corresponding to the same qubit frequency. For each temperature, the qubit frequency is then detected via two tone spectroscopy for the same flux biases. **(B)** Similar result as in panel A for different sweet spots, but the qubit frequency was converted with Fig. 2.6A into a shift of the magnetic flux. Both the left- and right-hand frequencies fall onto similar values for the flux shift, but for better visibility, only the left-hand frequencies are illustrated. **(C)** Flux shift at $T = 90\,\mathrm{mK}$ versus magnetic field bias Φ_{bias}. An approximately linear dependence is observed (dashed line).

on $\Delta\Phi_{park}$ (Fig. 2.6D), and the rather peculiar behavior of a non-monotonic and very slow decay of $\Delta\Phi_{ext}$ as the parking duration is increased to values of 1 ms or more (Fig. 2.6E).

As strange as this observation may be, it also raises the question of its microscopic origin. The just described linearity shows that the effect is not due to a heating effect (with power P_{heat}) in the supply microwave chains, as the amplitude then would need to scale as $\Delta\Phi_{ext} \propto P_{heat} \propto I^2 \propto \Delta\Phi^2_{park}$, where I is the current flowing through the fast-flux coil. One of the first hypotheses was an ensemble of spins, which might slowly depolarize after the flux ramp, and which is commonly observed as a source of $1/f$ flux noise in flux-sensitive devices [174, 185, 186].

The presence of a spin ensemble can indeed be witnessed in the simpler, yet distinct experiment presented in Fig. 2.7. The qubit frequency was observed using two-tone spectroscopy for an increasing dilution stage temperature T. As shown in Fig. 2.7A, the fluxonium was biased symmetrically to the left and right of the $-1.5\,\Phi_0$ half-flux sweet spot at base temperature, thus at the same qubit frequency. By simultaneously observing the qubit frequency change to the left and right of the sweet spot, potential temperature dependencies of the fluxonium parameters can be distinguished from flux shifts. However, as both frequency shifts translate into the same flux shift using the spectrum shown in Fig. 2.6A, it is revealed that no such changes in the spectrum occur. The measurement was repeated for two other half-flux sweet spots, as shown in Fig. 2.6B, where different temperature sensitivities can be observed. Since a much flatter temperature dependence is observed near the $+1.5\,\Phi_0$ sweet spot, it is likely that the "true" zero-flux point after the initial cooldown is near this sweet spot, i.e., the point at which no shielding currents are present in the fluxonium loop. Finally, Fig. 2.6C shows that the flux shift has an approximately linear dependence on the external magnetic field bias Φ_{bias}, as exemplified

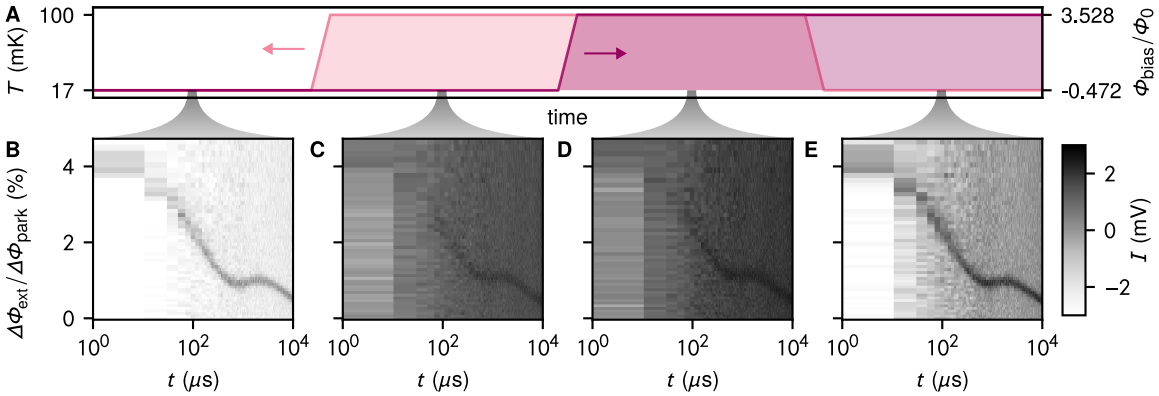

Figure 2.8: Flux delay for varying temperature and flux bias. **(A)** To test the hypothesis of a spin ensemble responsible for flux delay, the temperature T of the dilution stage as well as the flux bias point Φ_{bias} were varied and the same experiment (panels B to E) was repeated under these different conditions. The two values of Φ_{bias} were chosen such that they possess the same difference of $28\,\text{m}\Phi_0$ relative to the closest half-flux sweet spot, respectively. Averaged I quadrature of single-port reflection measurements, similar to the results of Fig. 2.6E, for **(B)** $T = 17\,\text{mK}$ and $\Phi_{\text{bias}} = -0.472\,\Phi_0$, **(C)** $T = 100\,\text{mK}$ and $\Phi_{\text{bias}} = -0.472\,\Phi_0$, **(D)** $T = 100\,\text{mK}$ and $\Phi_{\text{bias}} = 3.528\,\Phi_0$, **(E)** $T = 17\,\text{mK}$ and $\Phi_{\text{bias}} = 3.528\,\Phi_0$, respectively. Among all four conditions, no difference in the non-monotonic decay of the flux delay is observed within the measurement accuracy. The lower contrast in panels C and D is owed to the increased temperature, which increases p_{th}. For all four cases, the parameters $\Delta\Phi_{\text{park}} = -0.36\,\Phi_0$ and $t_{\text{park}} = 10\,\text{ms}$ were used.

by the shift at $T = 90\,\text{mK}$. This observation is consistent with the measurements conducted in Ref. [186] and suggests that the observed flux shift is due to an ensemble of magnetically active surface spins. Note that these could correspond to the same paramagnetic spin ensemble with negligible zero-field splitting found in Ref. [174].

To test whether such a spin ensemble is also responsible for the observed flux delay in Fig. 2.6, the experiments illustrated in Fig. 2.8 were performed. The idea was to repeat the same flux delay measurement at different temperatures T of the dilution stage, and for flux-bias points with the same relative position to their closest half-flux sweet spot, but offset by multiple flux quanta. Both parameters should affect the average population of such a spin ensemble. However, as shown in Fig. 2.8B-E, the variation of these parameters had no effect on the decay of the flux delay amplitude,[6] rendering the spin ensemble hypothesis as unlikely.

At the current time, the question of the microscopic origin has not yet been definitively clarified, but a specific detail in the design of the second generation is considered to be most likely responsible. In Fig. 2.9A, a part of the two optically defined metal layers of such a chip design is shown. As can be seen in the left zoom-in, the fast-flux line is geometrically separated from the lower part of the superconducting ground plane to allow the entry of the external magnetic field. However, this design choice results in two separate superconducting structures being connected via a very low ohmic resistance in the normal metal ground plane (right zoom-in). In this way, leaking currents could arise through the flux ramp, which decay after the ramp with a comparatively long time constant, since on

[6] This also includes experiments at $\Phi_{\text{bias}} = 10.528\,\Phi_0$, which are not shown in Fig. 2.8.

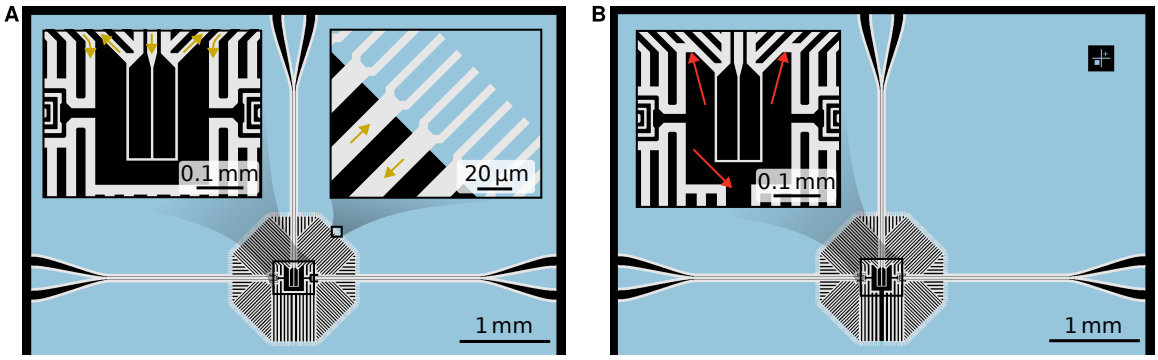

Figure 2.9: Ground plane design of generations 2 and 3. (A) Due to the openings that allow an external flux to enter the central area, the fast flux coil is not connected to the bottom part of the superconducting ground plane (light gray) via a superconducting connection, but only via a short section in the normal metal (light blue), allowing potentially for leakage currents (symbolized by the yellow arrows). The order of the two metal layers was inverted for visualizing the fork-like structure in the contact area. **(B)** New design generation, in which the two upper openings were closed and replaced by a single opening at the bottom, as indicated by the red arrows. In both panels, resonator-fluxoniums are not shown for clarity.

long timescales the current has to minimize its resistance by flowing through the other superconducting CPWs connected to the normal metal copper box. To counteract this, a third design generation was developed, which is depicted in Fig. 2.9B. The difference is to open the central area for the external magnetic flux bias at only one point at the lower end and to close the two upper openings (see red arrows in the zoom-in). However, since no samples incorporating this latest design have been tested yet, the effectiveness of this measure cannot be definitively assessed at this time. Nevertheless, the use of simply-connected superconducting structures is already regarded as a sound design choice.

Finally, Fig. 2.10 demonstrates that the flux delay can be largely eliminated through appropriate counter flux pulses. However, there is a certain difficulty in applying this method in experiments such as the aforementioned energy relaxation spectroscopy or a quantum Szilard engine [140] spectroscopy, as the counter flux pulse would theoretically need to be individually calibrated for the long history of the magnetic flux. On a related note, an end-to-end framework was recently presented, which is able to characterize and

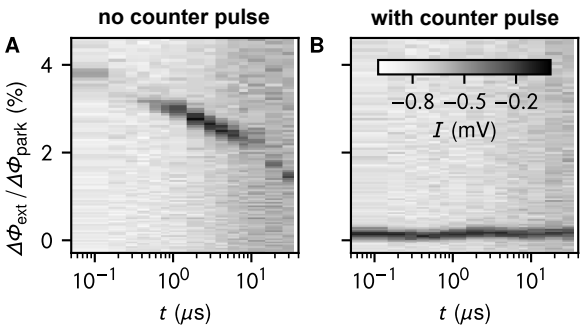

Figure 2.10: Countering flux delay. (A) The parking parameters $\Delta\Phi_{\text{park}} = -0.36\,\Phi_0$ and $t_{\text{park}} = 0.1\,\text{ms}$ result in a slowly decaying flux delay. **(B)** Repetition of the experiment in panel A, but with a double-exponential counter flux pulse of the form $\Delta\Phi_{\text{park}}(t) = A_1 \exp(-t/\tau_1) + A_2 \exp(-t/\tau_2)$ immediately after the flux ramp (cf. Fig. 2.6B). Empirical parameters $A_1 = 5.4\,\text{m}\Phi_0$, $\tau_1 = 45\,\mu\text{s}$, $A_2 = 2.2\,\text{m}\Phi_0$ and $\tau_2 = 0.9\,\mu\text{s}$ were used.

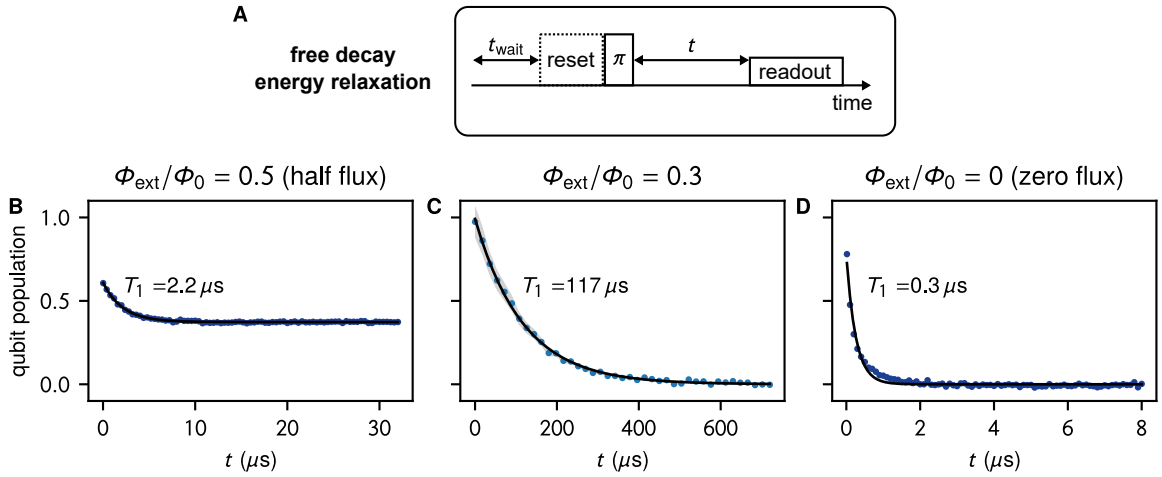

Figure 2.11: Energy relaxation measurement at different flux biases. **(A)** Pulse sequence of one repetition in a free decay energy relaxation measurement, consisting of a preceding waiting time t_{wait} to provide sufficient spacing between each repetition, a reset of the qubit state to its ground state $|g\rangle$, a π pulse for initializing the qubit in its excited state $|e\rangle$ (or no additional pulse for initialization in $|g\rangle$), a free decay waiting time t and a final readout of the resonator, which inherits information about the qubit state. **(B)** Measured energy relaxation of sample 3 at half-flux bias ($\Phi_{ext}/\Phi_0 = 0.5$), **(C)** at $\Phi_{ext}/\Phi_0 = 0.3$, and **(D)** at zero-flux bias ($\Phi_{ext}/\Phi_0 = 0$). The black lines in panels B to D show an exponential fit to the data points (blue).

compensate for general flux pulse distortions on timescales ranging from nanoseconds up to milliseconds, as long as the flux control line is approximately linear [246]. If the design change does not bring an improvement in flux delay, this framework could also be a potential solution. Furthermore, ramping in both positive and negative directions in the same manner is advisable to prevent long-term accumulation of flux distortion.

2.5 Energy Relaxation of GrAl Fluxoniums versus Flux Bias

In characterizing generation 2 resonator-fluxonium samples with comparably low qubit frequencies $f_q < 300$ MHz at their half-flux sweet spot, surprisingly low energy relaxation times T_1 on the order of just a few microseconds were measured. In order to get a better understanding of the underlying loss mechanisms, for three samples an energy relaxation spectroscopy was performed, i.e., measuring the energy relaxation versus the external magnetic flux bias. Before presenting these results, the basic experiments that are typically used to characterize the decoherence in superconducting qubits are presented.

The general idea for measuring qubit energy relaxation is illustrated in Fig. 2.11A. To prepare the qubit in either its ground state $|g\rangle$ or excited state $|e\rangle$, typically one of the following possibilities is chosen. The qubit can be actively reset either with a preceding measurement and a conditional π pulse, or with a fast-flux reset. In the latter, the qubit is adiabatically flux ramped to the avoided level crossing with the resonator, such that a potential qubit excitation is quickly 'dumped' in the resonator, leaving the qubit in its ground state. If the qubit should be initialized in $|e\rangle$, this can be achieved with a

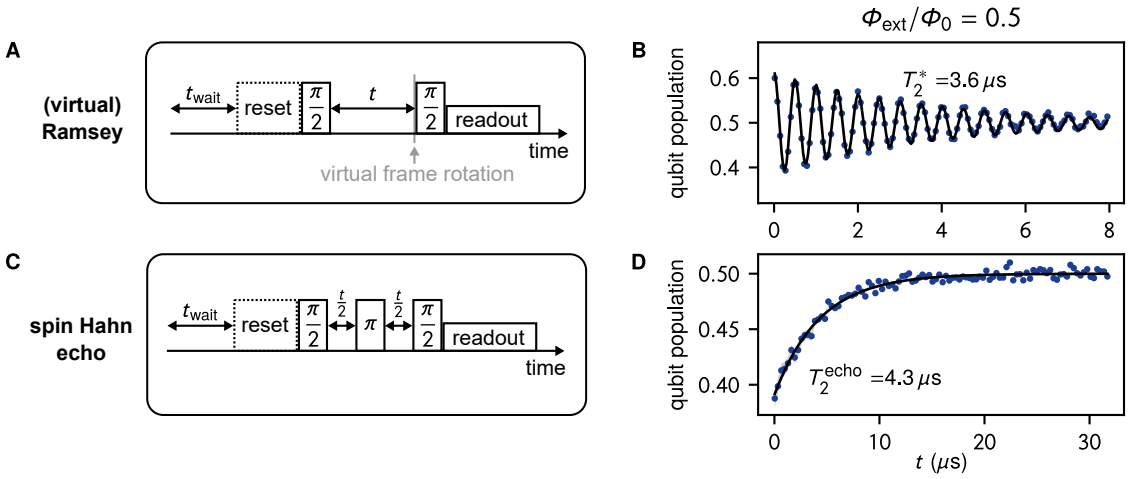

Figure 2.12: Decoherence measurements at half-flux bias. **(A)** Pulse sequence of one repetition in a Ramsey experiment that resembles in most parts the free energy decay measurement in Fig. 2.11A. The difference exists in that the qubit is instead brought in a superposition state with a $\pi/2$ qubit control pulse before the free precession time t, after which a second $\pi/2$ pulse is played. As explained in the text, optimized $\pi/2$ pulses without frequency detuning were used and the qubit frame was rotated virtually in the OPX+ instrument. **(B)** Measured Ramsey oscillations of sample 3 at half-flux bias ($\Phi_{ext}/\Phi_0 = 0.5$). The black line is a fit to the measured data (blue) of a cosine function with an exponentially decaying envelope. **(C)** Pulse sequence of one repetition in a spin Hahn echo experiment that consists of the same pulses as the Ramsey sequence in panel A, except for an intermediate, refocusing π qubit control pulse (and without the virtual frame rotation). **(D)** Measured echo decoherence of sample 3 at $\Phi_{ext}/\Phi_0 = 0.5$. The black line represents an exponential fit to the data points (blue).

subsequent π pulse, as in the pulse sequence of Fig. 2.11A. If none of these two active reset possibilities is available, an energy relaxation experiment can still be performed though. The initial π pulse then just inverts on average the thermal population of the statistical ensemble. The three datasets in Fig. 2.11B-D, which were measured with sample 3 presented later in this section, in fact, used this simple implementation of the free decay energy relaxation without a preceding reset of the qubit state. Fig. 2.11B shows the surprisingly fast relaxation with an energy relaxation time $T_1 = 2.2\,\mu s$ at the low-frequency ($f_q = 284\,MHz$) half-flux sweet spot ($\Phi_{ext}/\Phi_0 = 0.5$). Moving away from the half-flux bias results in a significant increase of the energy relaxation time, as shown in Fig. 2.11C, with $T_1 = 117\,\mu s$ at $\Phi_{ext}/\Phi_0 = 0.3$. At the zero-flux sweet spot ($\Phi_{ext}/\Phi_0 = 0$), the energy relaxation time collapses once again to values well below a microsecond. Interestingly, this sample experienced a strong impact of aging: Three years before these measurements, the sample has already been characterized soon after its fabrication. At that time, the sample possessed a significantly larger energy relaxation time $T_1 = 38\,\mu s$ as well as decoherence time $T_2^* = 10\,\mu s$ along with a much larger qubit frequency at half-flux of $f_q = 0.88\,GHz$.

Before analyzing the underlying loss mechanisms that explain the strong dependence on the magnetic flux bias, two other conventional experiments used to characterize qubit decoherence, are briefly introduced on the basis of Fig. 2.12. The first one of these experiments is the Ramsey measurement, which is illustrated in Fig. 2.12A. For this, the qubit is, similar to the free decay energy relaxation experiment above, reset in one of its eigenstates, before it is brought with a $\pi/2$ qubit control pulse in a superposition state to the equator

of the Bloch sphere. Conventionally, this $\pi/2$ qubit control pulse is slightly detuned from the qubit transition frequency to achieve a more precise creation of the superposition state under optimal conditions. However, since the idea is to simply calibrate the π pulse and transfer these values to the $\pi/2$ pulse by appropriately scaling the pulse amplitude or duration, such a detuned $\pi/2$ pulse would also have a small $\hat{\sigma}_z$ component. This would cause the qubit to precess not perfectly on the equator, but slightly off-center. To eliminate this small component, one can also apply $\pi/2$ pulses without detuning, thereby preparing the qubit in a perfect superposition state on the equator [247]. To emulate the necessary frequency detuning during the free evolution, the qubit frame is now instead virtually rotated within the software of the OPX+ instrument. In both versions of the Ramsey experiment, since the qubit frequency fluctuates in real experiments ($\sigma_{\omega_q} \neq 0$), the ensemble-averaged phase of the superposition state smears out during the free evolution with the pure dephasing rate Γ_φ. Together with the simultaneous energy decay, the qubit population measured after a second $\pi/2$ pulse in a Ramsey experiment possesses an envelope that is decaying on the characteristic timescale $T_2^* \approx T_2 = 1/\Gamma_2$, where Γ_2 is the decoherence rate given by Eq. (1.54). The measured data from the Ramsey experiment using $\pi/2$ pulses without detuning, performed on sample 3 at its half-flux sweet spot, is presented in Fig. 2.12B. The second experiment is known as spin Hahn echo (Fig. 2.12C), and it resembles to a large extent the Ramsey sequence. The main difference consists in an intermediate π pulse, which refocuses the qubit during its free evolution, i.e. phase drifts due to fluctuations of the qubit frequency on timescales equal or larger to the total free evolution time t cancel each other out. The reduced amount of dephasing results in a decoherence time T_2^{echo} that is larger than the one observed in the Ramsey experiment, as observed in Fig. 2.12D for sample 3 at its half-flux sweet spot.

The discussion now turns back to the detailed investigations of the underlying loss mechanisms for the surprisingly low values of the observed energy relaxation time at half-flux. In the following, three samples of the second design generation are considered, for which the energy relaxation was measured at a comparably large set of external magnetic flux biases. Samples 1 and 2 are two resonator-fluxoniums that are located on the same chip shown in Fig. 2.9. They were produced in a rather later batch, in which Purcell filters were already integrated, and they were electrically contacted using Al bonds. In contrast, sample 3 belongs to an older batch without Purcell filters, and Au bonds were used. An overview of the fitted qubit spectra for all three samples is shown in Fig. 2.13A. Extracted values for the qubit parameters L_q (and E_L), C_q (and E_C) and E_J from fitting these spectra, together with the frequency f_r of the fundamental resonator mode, are presented in Table 2.1.

The measured energy relaxation rates Γ_1 over a broad range of external magnetic flux biases Φ_{ext} in the fluxonium loops are illustrated in Fig. 2.13B for all three samples. The data points were obtained with the pulse sequence described in Fig. 2.11A. For all three data sets, dielectric, inductive and Purcell loss were fit on the basis of Eq. (1.67), Eq. (1.73) and Eq. (1.77), respectively. Since dielectric loss is by many orders of magnitude not the limiting loss mechanism in the vicinity of half-flux, where qubit frequencies are the lowest, it is not possible to distinguish between a bosonic bath (with increased relaxation rate due to the temperature dependent coth factor) or a TLS bath. For simplicity, a TLS bath is assumed, as observed in Ref. [165] as the limiting factor for the measured energy relaxation.

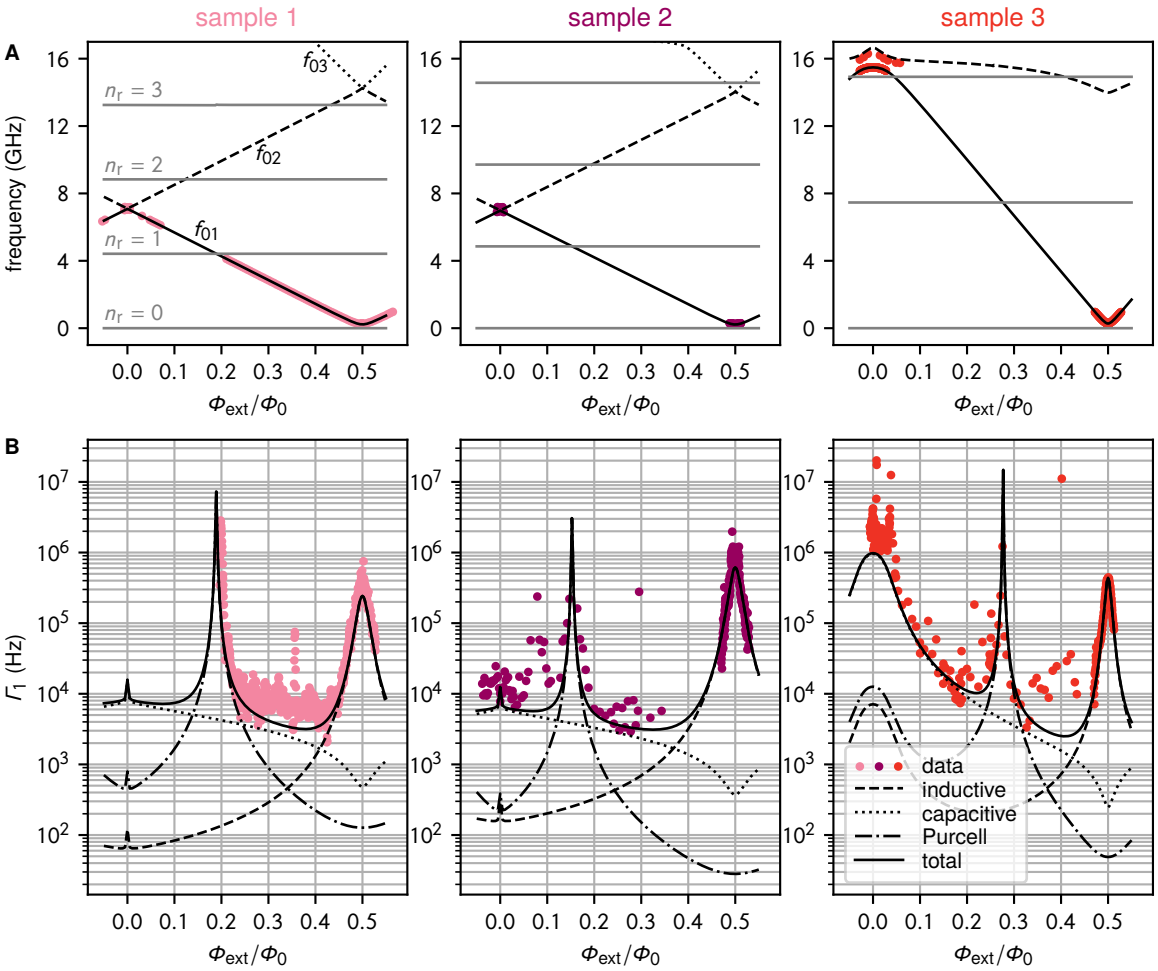

Figure 2.13: Spectroscopy and losses. **(A)** Measured and calculated energy spectra of three grAl fluxoniums, as a function of the external magnetic flux Φ_{ext}. Samples 1 (pink) and 2 (magenta) are located on the same chip, but were measured in distinct cooldowns. Sample 3 (red) belongs to an older batch with Au wire bonds and without a Purcell filter. The black lines correspond to the first (f_{01}, solid), second (f_{02}, dashed) and third (f_{01}, dotted) qubit transition, and the gray lines display the lowest resonator transitions. **(B)** Measured energy relaxation rates Γ_1 and fitted rates (black lines) due to different loss mechanisms, for all three samples. Inductive loss rates (dashed) were calculated using Eq. (1.73), while capacitive loss rates (dotted) were obtained from Eq. (1.67). The semi-classical model for Purcell loss (dash-dotted), introduced in Section 1.5.3, was employed for its estimation.

However, a difference from Ref. [165] lies in the assumption of a free exponent $\epsilon = 0.7$ for the frequency dependence of the dielectric loss tangent, $\tan\delta_C \propto \omega^\epsilon$, as is the case for other fluxonium qubits partially limited by dielectric loss [125, 163]. The necessity for this choice is particularly evident from the strong increase in Γ_1 for sample 3 with rising qubit frequencies (towards zero-flux), but this assumption also plays a significant role for the other two samples. In the case of inductive loss, a better agreement with the measured values was achieved with a bosonic bath in thermal equilibrium at $T = 30\,\mathrm{mK}$ than with a TLS bath. It should be noted, that the coth temperature dependence from Eq. (1.73), assumed here for simplicity, might still be just an approximation of a more complicated temperature dependency [69]. Table 2.1 contains the used values for the inductive loss

	L_q (nH)	E_L (GHz)	C_q (fF)	E_C (GHz)	E_J (GHz)	f_r (GHz)	L_s (nH)	C_c (fF)	$\tan(\delta_L)$ $\times 10^{-6}$	$\tan(\delta_C)$ $\times 10^{-6}$
1	440	0.371	5.19	29.8	17.4	4.403	11.5	6.0	1.0	24.3
2	446	0.366	5.42	28.6	16.6	4.843	10.6	3.0	2.5	19.4
3	176	0.931	6.48	23.9	14.6	7.455	2.51	6.0	1.0	6.48

Table 2.1: Parameters of the resonator-fluxonium devices and the estimated losses. Resonator frequency f_r and qubit parameters L_q, C_q and E_J were extracted from fits of the measured spectroscopy data shown in Fig. 2.13A. The stated values for L_s, C_c, $\tan(\delta_L)$, and $\tan(\delta_C)$ were used as fit parameters for Purcell, inductive, and capacitive loss, respectively. The value of $\tan(\delta_C)$ refers to the value at 6 GHz.

tangent $\tan(\delta_L)$ and for the dielectric loss tangent $\tan(\delta_C)$ (at 6 GHz). Furthermore, the values of the shared inductance L_s between fluxonium and resonator and the coupling capacitance C_c between resonator and transmission line, which were needed to estimate Purcell loss according to the semi-classical model, are listed there. The third major loss mechanism considered here is Purcell loss, for which a bosonic bath has been assumed, as is commonly done in the literature. However, based on the available datasets, distinguishing between a bosonic and a TLS bath is not possible, since the qubit is limited by inductive loss at the lowest qubit frequencies. Finally, loss due to non-equilibrium quasiparticles, $1/f$ flux noise and the coupling to the fast flux line are not limiting the energy relaxation and were therefore neglected in the following analysis.

In fitting the individual loss mechanisms to the three data sets, the following three observations can be made. First, inductive loss is responsible for the large increase in energy relaxation rate in the vicinity of the half-flux bias point for all three samples. In fact, if these fluxonium qubits would not be limited by inductive loss there, their energy relaxation rate could be by more than two orders of magnitude smaller (corresponding to energy relaxation times T_1 of a few hundred microseconds), if limited by dielectric loss then. The reason, why inductive loss plays a major role in this regime is because of their comparably low transition frequencies lower than 300 MHz for all three samples. To better understand why a low qubit frequency f_q becomes a major factor, the following estimation can be made: The fluxonium qubits studied here lie in a parameter regime, in which the reduced flux matrix element close to half-flux possesses approximately a dependence $|\langle 0|\hat{\varphi}|1\rangle|^2 \propto 1/f_q^2$. Provided that $\tan(\delta_L)$ has no drastic frequency dependence, inductive loss, according to Eq. (1.73), is then expected to follow a $1/f_q^2$ dependence in the case of a TLS bath, and a $1/f_q^3$ dependence in the case of a bosonic bath for sufficiently low qubit frequencies $hf_q \ll k_B T$. The last condition starts being fulfilled for qubits at only a few hundred megahertz transition frequency and bath temperatures of around 30 mK. Furthermore, the fitted inductive loss tangents $\tan(\delta_L)$ are in accordance with the quality factors $Q_i \sim 10^5 - 10^6$ that were measured on thin-film grAl resonators [123, 232]. Thus, the magnitude of the estimated inductive loss in all three samples can be trusted.

Second, while not being the dominant loss mechanism around half-flux, dielectric loss is limiting the energy relaxation of all three fluxonium qubits for frequencies above ~ 2 GHz (except in the vicinity of the avoided level crossing with the resonator). By assuming a frequency dependence $\tan(\delta_C) \propto f_q^\epsilon$ with an exponent $\epsilon = 0.7$ of the dielectric loss

tangent, which is a usual value in literature [125, 163], dielectric loss according to Eq. (1.67) describes the measured energy relaxation well up to largest qubit frequencies of $\sim 16\,\mathrm{GHz}$, and therefore, it even provides an explanation why the energy relaxation time for sample 3 at zero-flux is well below 1 µs. In contrast to inductive loss, for dielectric loss the strong dependence on f_q around half-flux is at least partly suppressed, as another factor $\propto f_\mathrm{q}^2$ is incorporated into Eq. (1.67).[7]

Third, Purcell loss is limiting qubit energy relaxation only in the vicinity of the avoided level crossing. Especially, in the vicinity of half-flux, Purcell loss is negligible compared to the expected inductive loss, such that a discrimination between the open quantum system (OQS) or semi-classical (SC) Purcell models, which were presented in Section 1.5.3, could not be carried out with the present experimental data.

2.6 Comparison with Other Fluxonium Qubits

In this last section, the measured data from the energy relaxation spectroscopy is compared with other implementations of fluxonium qubits in literature. For this, the measured relaxation rate Γ_1 of a multitude of fluxonium qubits from Refs. [6, 9, 102, 125, 171, 175], rescaled by the squared reduced flux matrix element, $|\langle 0|\hat{\varphi}|1\rangle|^2$, the temperature-dependent factor $\coth(hf_\mathrm{q}/(2k_\mathrm{B}T))$ and the fluxonium's capacitive energy E_C/h, and a constant numerical factor is plotted in Fig. 2.14. This at first glance peculiar choice of representation is motivated by the following considerations: To compare various qubit implementations with generally different qubit parameters in terms of their loss mechanisms, a parameter-independent quantity should be considered. In the case of dielectric loss, this quantity is represented by the dielectric loss tangent $\tan(\delta_\mathrm{C})$. Transforming Eq. (1.67) leads to

$$\tan(\delta_\mathrm{C}) = \Gamma_1^\mathrm{diel} \times \left[4\pi |\langle 0|\hat{\varphi}|1\rangle|^2 \coth\left(\frac{hf_\mathrm{q}}{2k_\mathrm{B}T}\right) \frac{f_\mathrm{q}^2}{E_\mathrm{C}/h} \right]^{-1}, \tag{2.1}$$

which corresponds exactly to the quantity shown in Fig. 2.14 times f_q^{-2}, if the energy relaxation of a fluxonium qubit is limited by dielectric loss.[8] The illustrated quantity should therefore scale as $\propto f_\mathrm{q}^{2+\epsilon}$, because $\tan(\delta_\mathrm{C}) \propto f_\mathrm{q}^\epsilon$ possesses itself an empirical frequency-dependence (cf. Section 1.5.1). If, one the other hand, this quantity is limited by inductive loss, Eq. (1.73) yields

$$\Gamma_1^\mathrm{ind} \times \left[4\pi |\langle 0|\hat{\varphi}|1\rangle|^2 \coth\left(\frac{hf_\mathrm{q}}{2k_\mathrm{B}T}\right) \frac{1}{E_\mathrm{C}/h} \right]^{-1} = \tan(\delta_\mathrm{L}) \times \frac{E_\mathrm{C}E_\mathrm{L}}{h^2}, \tag{2.2}$$

which is independent of f_q. Among the illustrated energy relaxation data, fluxoniums with a JJ array based superinductor [102, 171] clearly stand out, as they follow the trend of being

[7] A minor caveat is noted by the frequency dependence of the dielectric loss tangent, which reduces the suppression $\propto f_\mathrm{q}^\epsilon$.

[8] The case of a TLS bath is recovered in Eq. (2.1) by setting $T \to \infty$.

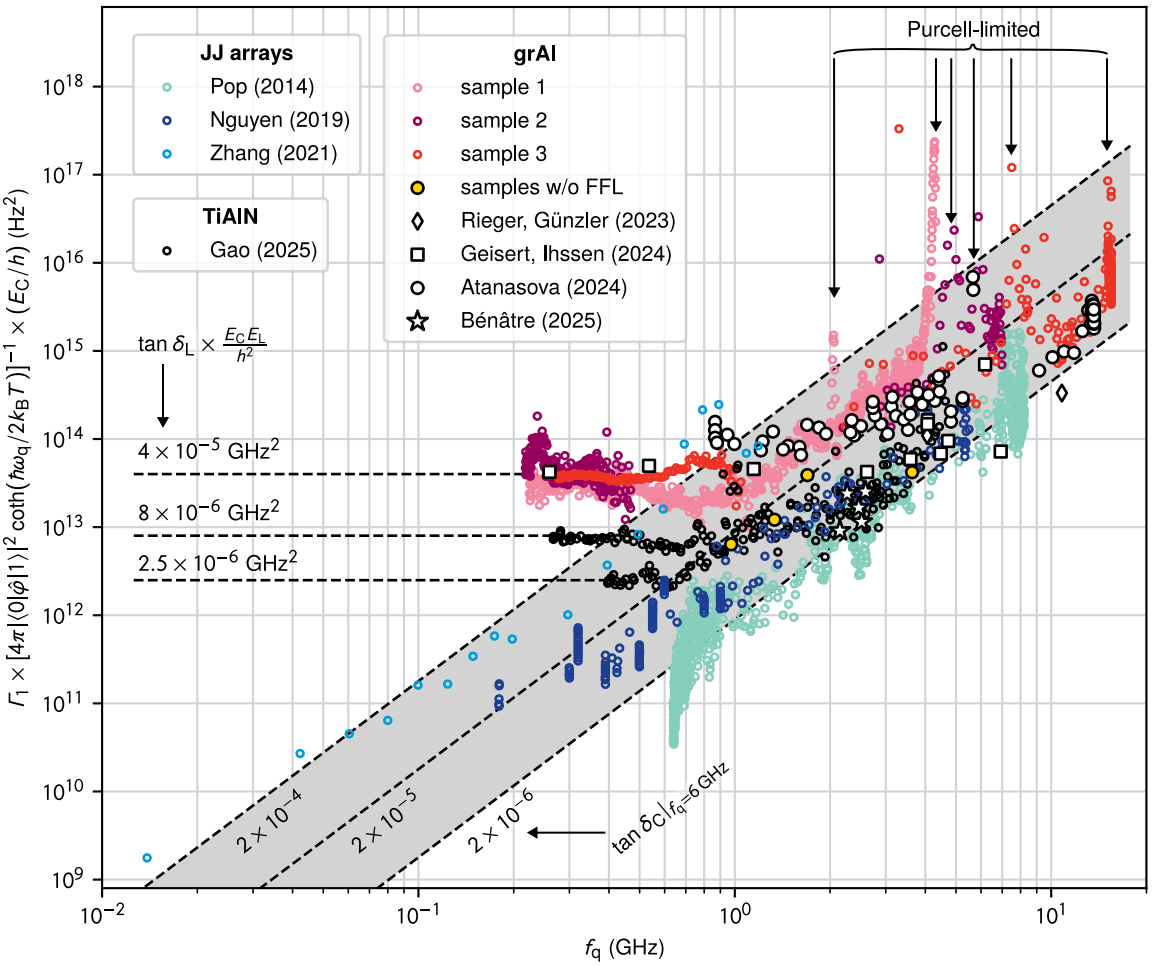

Figure 2.14: Comparison of energy relaxation rates for different fluxonium implementations. Energy relaxation rate Γ_1, rescaled by the squared reduced flux matrix element, $|\langle 0|\hat{\varphi}|1\rangle|^2$, the temperature-dependent factor $\coth(hf_q/2k_BT)$ and the fluxonium capacitive energy E_C/h, as well as a numerical factor. According to Eqs. (2.1) and (2.2), this rescaled relaxation rate is expected to be equal to $\tan\delta_C \cdot f_q^2$, if limited by capacitive loss, or frequency-independent and equal to $\tan\delta_L \cdot E_C E_L/h^2$, if limited by inductive loss. The dataset comprises the three samples shown in Fig. 2.13B, along with similar samples lacking a fast-flux line (FFL) on the chip (cf. Tables 5 and 6). Additional grAl fluxonium devices from the literature are referenced in Refs. [**Benatre2025May**, 6, 9, 125]. For comparison, data from fluxoniums employing a superinductor based on Josephson junction arrays (Refs. [102, 163, 171]) and from devices using the disordered superconductor TiAlN (Ref. [175]) are also considered.

limited by capacitive loss ($\propto f_q^{2.7}$) and showing no signature of being limited by inductive loss, down to qubit frequencies as low as $\sim$ 10 MHz. In contrast, the dominating loss of the grAl fluxonium samples studied in this work is inductive loss for qubit frequencies around 1 GHz and below, which is reflected in the approximately constant value towards lower frequencies. Furthermore, there are no fluxoniums based on a grAl superinductor, which deviate from this trend, except for potentially some additional samples from both the first and second design generations without a fast flux line (FFL) on the chip, as well as the samples from Ref. [2]. These seem to follow the trend further and appear to have a lower capacitive loss tangent. However, due to limited statistics of the FFL samples (four samples

measured only once at their half-flux spot, with significant temporal fluctuations in T_1) and Ref. [2] containing only a minimum qubit frequency at half-flux of $\sim 2.2\,\mathrm{GHz}$, this statement cannot be definitively confirmed and requires further measurements. Fluxoniums with a superinductor based on the spinodal material and disordered superconductor TiAlN [175] are also added for reference. For these, comparably low dielectric loss was observed, and the measured energy relaxation rates also saturate towards lower qubit frequencies. If this loss could be associated with inductive loss, it would correspond to 5 to 15 times smaller inductive loss tangents for equal qubit parameters E_C and E_L. The authors, however, argue that the underlying loss mechanism of their fluxonium qubits is $1/f$ flux noise, such that the inductive loss tangents are likely to be even smaller.

Returning to grAl-based fluxoniums, a conclusion can be drawn that, unless inductive losses are reduced in the future, this platform will remain limited to T_1 times of a few hundred microseconds for qubit frequencies around ~ 1–$2\,\mathrm{GHz}$, depending on the dielectric loss tangent.

3 Thermalization of a Flexible Stripline Measured by a Superconducting Qubit

In this chapter, the second main result of the manuscript is presented: when using a flexible stripline assembly to connect a qubit readout input chain from room temperature to the dilution stage of a cryostat, a residual population of the readout resonator of $(2.2 \pm 0.9) \times 10^{-3}$ photons, a 0.28 ms thermalization time of the flexible stripline attenuators, and an effective qubit temperature of 26.4 mK, close to the temperature of the dilution stage is observed. Furthermore, there are no significant differences in qubit performance when using flexible striplines or conventional coaxial cables. The heating pulse methodology presented here can serve as a simple health check for other groups to test the thermalization of their input chains. These results encourage the use of flexible striplines in future cryogenic microwave setups, enabling at least an order of magnitude increase in the density of microwave input circuitry, paving the way for increasingly complex superconducting detectors and quantum devices. Finally, an extended thermal model of the input chains is presented to gain insight into the origins of the measured shot noise and propose improved versions of both input chains. This chapter is adapted to large extent from Paluch et al., Appl. Phys. Lett. 126, 034003, 2025 (Ref. [5]).

The growing size of cryogenic quantum processors [33, 97–99, 248] and detector arrays [249–252] requires an increasing microwave circuitry density for readout and control. Possible strategies to cope with this challenge consist in frequency or time-division multiplexing [253–257], which are, however, limited by the available bandwidth and the finite lifetime of the measured states. This motivates the demand for increasingly denser cryogenic microwave circuitry compatible with high-coherence devices [230], for which new platforms based on photonic links [258–260] or flexible microwave striplines [261–267] have recently been developed.

Flexible striplines with integrated microwave attenuators and filters promise to increase the cabling density by at least one order of magnitude compared to conventional coaxial setups. In Section 3.1, the cryogenic microwave setup is presented with a focus on the implementation of the coaxial cable and flexible stripline input chains. Section 3.2 proceeds with the superconducting fluxonium qubit in a circuit quantum electrodynamics (cQED) readout architecture that was used to measure the *in-situ* thermalization time and contribution to photon shot noise-induced dephasing of both input chains. The main results,

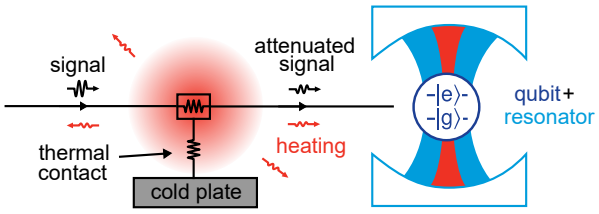

Figure 3.1: Principle of measuring the thermalization of the input chains. Microwave power dissipated in the attenuators generates local heating which radiates towards the resonator-qubit device, deteriorating its performance.

that the flexible stripline thermalizes with a time constant of 0.28 ms, almost a factor of two faster than cryogenic coaxial attenuators in a similar setup, and the observation of residual photon populations of $(2.2 \pm 0.9) \times 10^{-3}$, are shown in Section 3.3. An extended thermal model of the input chains is proposed in Section 3.4, which is used to understand the contributions of different temperature stages to the measured photon shot noise, and to propose improved versions of the two input chains.

3.1 Cryogenic Microwave Circuitry

In the last two decades, superconducting qubits have emerged as one of the most promising candidates for future large-scale quantum processors [33, 97–99, 248]. One reason for this development is the steadily increasing qubit coherence time, nowadays exceeding a few hundred microseconds [44–46]. This improvement also results in a higher sensitivity to dephasing, a measure for fluctuations of the qubit frequency (see Section 1.5.5), that originates from a multitude of different noise sources [187, 216, 268]. As explained in Section 1.3.4, the standard tool to read out quantum information in circuit QED is the dispersive coupling of the qubit to a readout resonator or cavity [269], which, however, adds another noise source for dephasing. This so-called photon shot noise arises from the fact that each photon in the resonator changes the qubit frequency by the dispersive shift $\chi_{\mathrm{ge}}/2\pi$ [220, 270–272]. In this way, fluctuations in the average resonator photon number $\bar{n}$ directly translate into qubit dephasing.

The discussion in Section 1.5.6 showed that, even in the absence of a readout drive, excess photons in the resonator originate from heat loaded in attenuators or filters anchored at higher temperature stages, transmitted via the microwave lines in form of blackbody radiation [225] (Fig. 3.1). In experiments with resonators in the gigahertz (GHz) regime, the residual $\bar{n}$ is observed to be between 2×10^{-4} and 2×10^{-1} [9, 192, 223–229], orders of magnitude larger than the expected $\sim 10^{-8}$ when in thermal equilibrium at 20 mK. While the lower observed limit corresponds to dephasing rates that are on the edge of measurability with state-of-the-art superconducting qubits [224], coherence times are usually dominated by photon shot noise in the upper limit. It is thus crucial to ensure that new microwave input chains do not degrade qubit performance by causing excessive thermal photon shot noise-induced dephasing.

Photon shot noise, as introduced in Section 1.5.5, is employed here to quantify the thermalization of different microwave input chains. In addition to the passive heat load from higher temperature stages, the attenuators in the input chains are also heated by readout

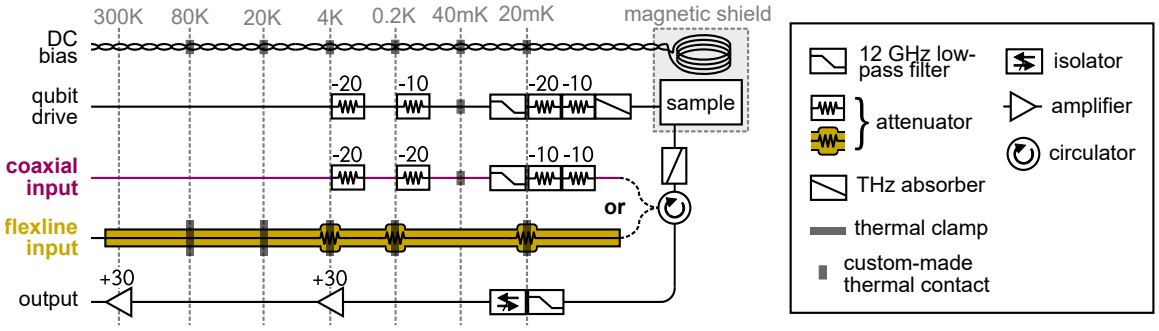

Figure 3.2: Cryogenic microwave setup. Microwave setup with a direct current (DC) line for magnetic flux biasing of the fluxonium, and three microwave lines for qubit control, readout signal input and output. The input chain is implemented either as a a coaxial cable with *SubMiniature A* (SMA) connectorized attenuators or as a flexible coplanar stripline ("flexline") with integrated attenuators (model *Cri/oFlex*® 3, see Section 3.1.2 and Ref. [274]). Both readout assemblies contain a total of 60 dB attenuation, distributed at various temperature stages. The coaxial attenuators at 20 mK were additionally thermalized via a copper braid (see Section 3.1.1). The coaxial lines are thermalized to the 40 mK intermediate stage using Ag-plated Cu wires and contain a 12 GHz low-pass filter anchored at 20 mK. To thermalize the flexline, custom-designed thermal clamps were used at 80 K, 20 K, 4 K, 200 mK and 20 mK, as detailed in Section 3.1.3. In the output chain, signals are amplified by 60 dB using a low noise amplifier (LNA) at 4 K and a room-temperature amplifier. The sample is surrounded by a Cu+Al and a mu-metal shield, as used in Ref. [123].

and control pulses. This active heat load generates additional photon shot noise-induced dephasing [224, 225], which is used to quantify the thermal contact between the attenuator and the cold plate. In separate cooldowns in a dilution refrigerator (model *Sionludi XL*, see Ref. [273]), the performance of two microwave input chains, a conventional coaxial cable and a flexible stripline, is compared (Fig. 3.2). The microwave setup following the input chains remains unchanged in both cases. Furthermore, separate drive and DC lines are employed for qubit manipulation and for magnetic flux biasing, respectively.

3.1.1 Details on Coaxial Cable Input Chain

In order to perform comparative experiments between a conventional coaxial cable setup and a flexible stripline setup, the SMA connectorized attenuators are distributed on the different temperature stages in the same way as the integrated attenuators of the flexible stripline (20 dB at 4 K, 200 mK and 20 mK each). At 4 K and 200 mK, attenuators with a stainless steel casing from *XMA Corporation* are used. As depicted in Fig. 3.3A, the attenuation at 20 mK is split into two 10 dB attenuators with an oxygen-free high thermal conductivity (OFHC) copper outer casing from *Quantum Microwave*. Additional copper braids from their outer casing to the dilution stage improve the thermal contact. For the cables interconnecting the temperature stages, coaxial cables from *Coax Co.* (part number: SC-119/50-CN-CN [275]) with an outer conductor diameter of 1.19 mm, an inner conductor diameter of 0.287 mm, and with lengths of 0.7 m between the 300 K and 4 K, 0.3 m between the 4 K and 0.2 K, and 0.4 m between the 0.2 K and 20 mK stages were used, respectively.

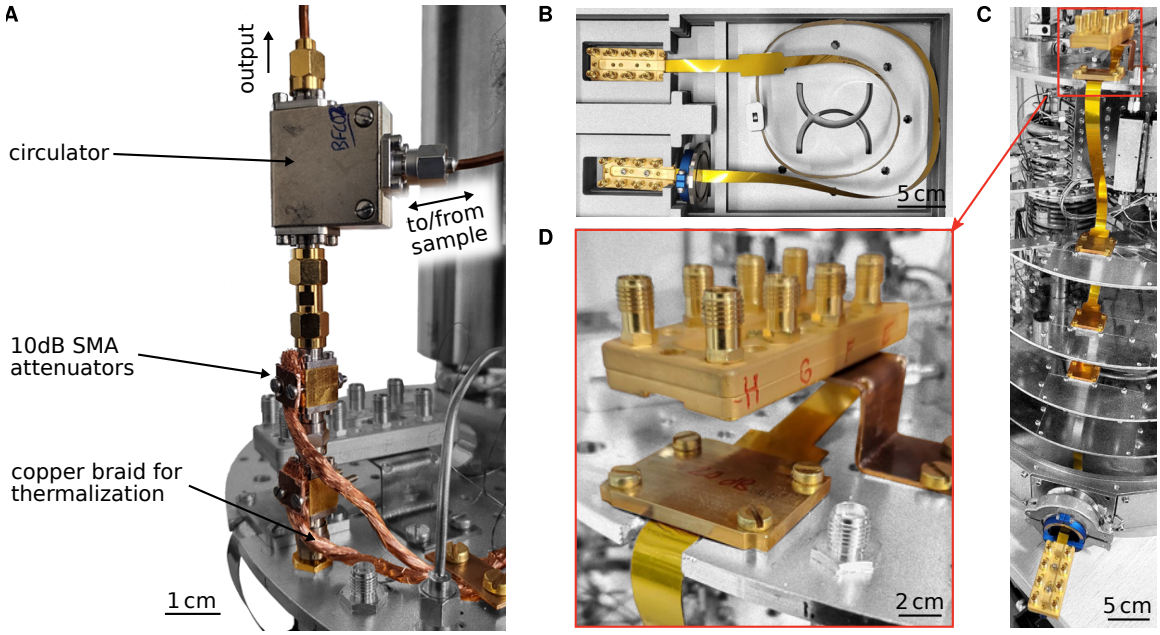

Figure 3.3: Photographs of the installation of both input chains. **(A)** Dilution stage part of the coaxial input chain (cf. 'coaxial input' in Fig. 3.2). Copper braids are clamped onto the outer casing of the two 10 dB attenuators to improve the thermal contact between them and the dilution stage. Input signals are routed first to reflect on the sample and then towards the output chain, using a *Quinstar* circulator with 20 dB in-band (4 – 8 GHz) isolation. As indicated in Fig. 3.2, all microwave parts on top of the attenuators were also used for the flexline setup. **(B)** Flexible stripline assembly as delivered from *Delft Circuits*. **(C)** Fully-installed flexline (cf. 'flexline input' in Fig. 3.2). **(D)** Zoom-in of the flexible stripline thermalized at the dilution stage (red box). The thermal clamp is directly at the position of the integrated 20 dB attenuator.

3.1.2 Details on Flexible Stripline Input Chain

The results of Section 3.1.3 show that the design of the clamp and the use of an additional thermal contact layer play a role when thermalizing the flexible stripline, especially at mK temperatures. The flexible stripline assembly from *Delft Circuits* (Fig. 3.3B) was clamped within a length of 26 mm and with an additional layer of *Apiezon® N* grease on both sides at the 20 mK, 200 mK, 4 K, 20 K as well as 80 K temperature stages (Fig. 3.3C). Choosing only an intermediate clamp length compared to the suggestion from Section 3.1.3 results from a compromise between maximizing the clamp length and a facilitated integration into the cryostat. At the 4 K, 200 mK and 20 mK stages the thermal clamp is directly at the position of the integrated 20 dB attenuators (Fig. 3.3D), which are composed of four 5 dB unit cells in order to reduce the noise temperature [225, 267]. Lengths of the cable sections are 0.32 m between the 300 K and 4 K, 0.14 m between the 4 K and 0.2 K, and 0.2 m between the 0.2 K and 20 mK stages, respectively.

3.1.3 Flexible Stripline Thermalization Experiments

Before the installation of the flexible microwave stripline (see Section 3.1.2), the quality of different thermal contacts was investigated, which is presented in the following.

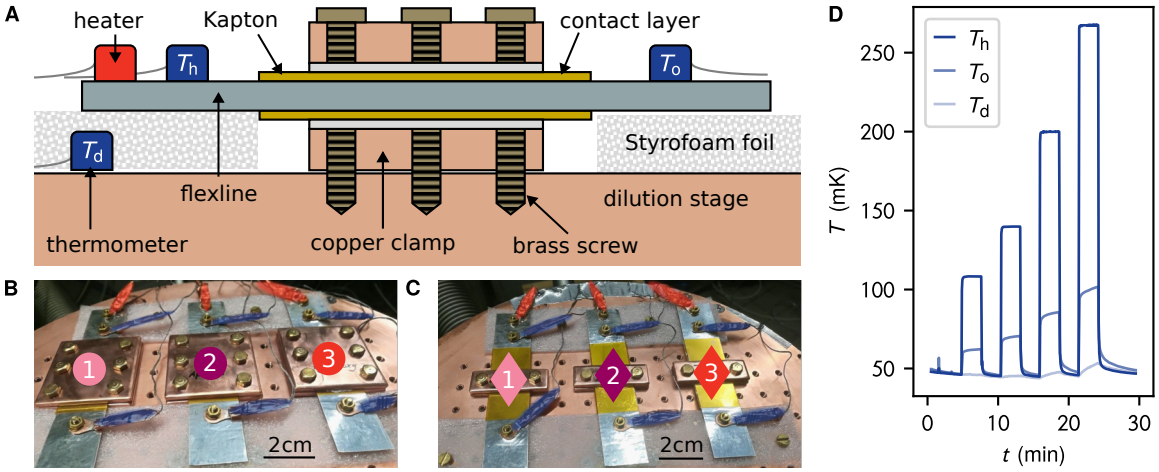

Figure 3.4: Setup for thermalization experiments of flexible stripline samples. **(A)** Side-view sketch of the experiment: The central section of a flexible stripline is clamped inbetween two copper plates and attached to the dilution stage of the cryostat via brass screws. Between the copper clamps and the flexline is the factory-made *Kapton*® isolation and possibly an additional thermal contact layer. A heater is attached close to one end of the stripline and three thermometers on the heater side (T_h), opposite to the heater side (T_o) as well as on the dilution stage (T_d). In order to minimize the thermal contact between the thermometers and the dilution stage, a Styrofoam foil is placed between the ends and the dilution stage. The physical implementation of this experiment is shown in **(B)** with a larger contact area (circle markers) and in **(C)** with a smaller contact area (diamond markers) between each side of the strip and the clamps. For each clamp, three different thermal contact layers are investigated: 1. no additional layer (pink), 2. grease (magenta) and 3. SPM (red). Thermometers (highlighted in blue) and heaters (in red) were fixed to the test cables with brass nuts, brass washers and a brass screw passing through the cables. Thermometers measuring T_d are not visible here. **(D)** Example of monitored temperatures while injecting sequentially increasing powers P_{heat} into the heater.

Experimental Setup

Test stripes of a flexline are thermalized in their central part with a copper clamp and possibly an additional thermal contact layer to the dilution stage. Then, heat is applied at one side of the cable (Fig. 3.4A), and the temperatures are measured on the heater side (T_h), opposite to the heater side (T_o) as well as on the dilution stage (T_d). In total, three different thermal contact configurations are investigated:

1. no thermal contact layer
2. *Apiezon*® *N* grease
3. silver-polymer mixture (SPM)

In distinct cooldowns, comprising stabilized dilution stage temperatures T_d from 20 mK up to 20 K, two different clamp sizes are used: first, as shown in Fig. 3.4B, a longer clamp with a length of $L_c^{(long)} = 45\,\text{mm}$ and a minimum distance between thermometer and the clamp of $d_{hc}^{(long)} = 25\,\text{mm}$, and second, as shown in Fig. 3.4C, a shorter clamp with $L_c^{(short)} = 15\,\text{mm}$ and $d_{hc}^{(short)} = 40\,\text{mm}$. The width of the stripline is always $W = 22\,\text{mm}$. An example for the monitored temperatures for setup 1 with a larger clamp is depicted in

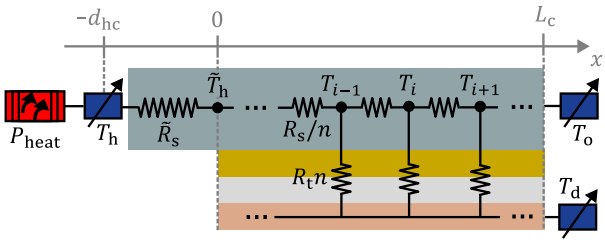

Figure 3.5: Simplified lumped-element model of the setup. A horizontal x-axis along the stripline with origin at the boundary between the heater side and the clamp is introduced. Background colors refer to the color scheme used in Fig. 3.4A.

Fig. 3.4D, where the dilution stage was stabilized at ~ 50 mK and the stripline was heated subsequently with 1 µW, 2 µW, 5 µW and 10 µW.

Theoretical Model

In order to obtain a quantitative measure for the thermalization of the flexline, the setup is modeled as shown in Fig. 3.5. The clamped section of the stripline is assumed to have a total thermal resistance R_s along the stripline and R_t via the thermal contact layer to the clamp. If the contact is split horizontally into $n = L_c/\Delta x$ sections of equal size, then each site along the strip is connected via a smaller contact resistance R_s/n to its neighbors and a larger contact resistance $R_t n$ to the clamp. The copper clamp is assumed to have a constant temperature $T = T_d$ over the whole length because of its significantly larger heat conductivity compared to the thermal contact layer and its good contact to the dilution stage. For simplicity, a change in thermal conductivities due to temperature gradients along the stripline is neglected. In thermal equilibrium, applying Fourier's law to the i-th site leads to the following heat flow balance:

$$\frac{T_{i-1} - T_i}{R_s/n} = \frac{T_i - T_{i+1}}{R_s/n} + \frac{T_i - T_d}{R_t n} \tag{3.1}$$

In the continuous limit ($n \to \infty$), this equation becomes

$$T''(x) = (T(x) - T_d)\,\frac{R_s}{R_t L_c^2} \tag{3.2}$$

along the clamp ($0 \le x \le L_c$). With the boundary conditions due to the differential version of Fourier's law, $T'(L_c) = 0$ and $T'(0) = -R_s P_{heat}/L_c$, the solution of Eq. (3.2) becomes:

$$\frac{T(x) - T_d}{P_{heat}} = \sqrt{R_s R_t}\,\frac{\cosh\left(\sqrt{R_s/R_t}\left(1 - \frac{x}{L_c}\right)\right)}{\sinh\left(\sqrt{R_s/R_t}\right)} \tag{3.3}$$

The temperatures on both ends of the clamp are $T(L_c) = T_o$ and $T(0) = \tilde{T}_h = T_h - \tilde{R}_s P_{heat}$, with $\tilde{R}_s = (d_{hc}/L_c)R_s$, taking the temperature gradient along the stripline at the heater-side into account. Solving for the measured temperature differences results in:

$$\begin{aligned} \frac{T_o - T_d}{P_{heat}} &= \frac{\sqrt{R_s R_t}}{\sinh\left(\sqrt{R_s/R_t}\right)} \\ \frac{T_h - T_d}{P_{heat}} &= \frac{\sqrt{R_s R_t}}{\tanh\left(\sqrt{R_s/R_t}\right)} + \frac{d_{hc}}{L_c} R_s \end{aligned} \tag{3.4}$$

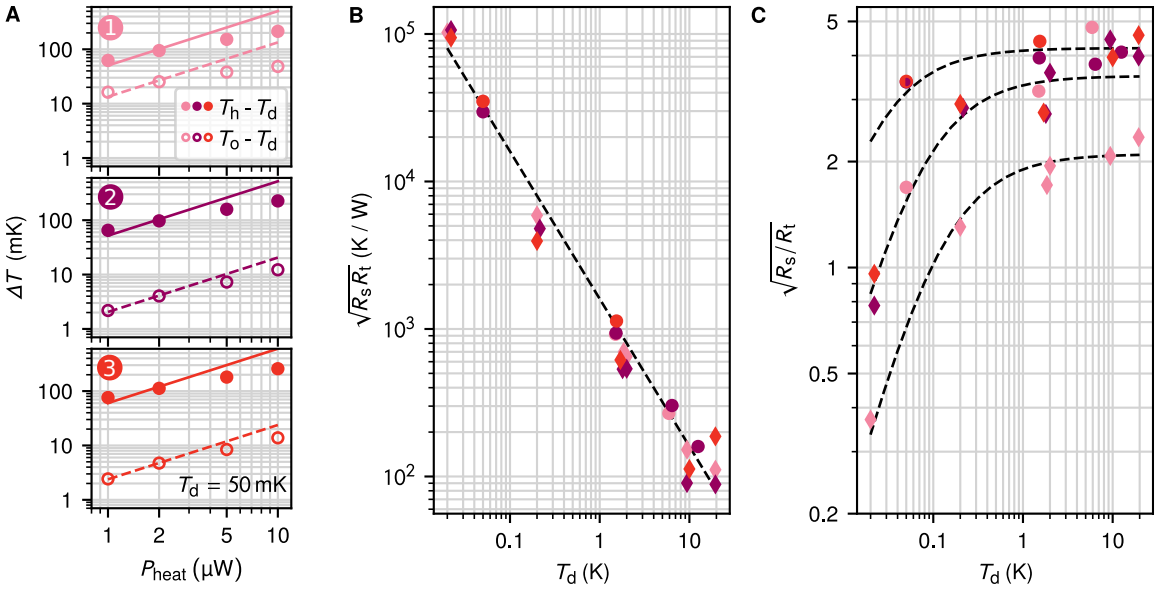

Figure 3.6: Experimental results of thermalization experiments. **(A)** Temperature differences $T_h - T_d$ (filled circles) and $T_o - T_d$ (empty circles) for the three different thermal contacts and the large clamp. Note that both the x- and y-axis have a logarithmic scale. The two lines in each plot are linear fits crossing the origin to the two datasets. Since non-linear effects are observed above a certain power (here approximately 3 μW), only the points below this threshold are used for a fit. **(B)** $\sqrt{R_s R_t}$ and **(C)** $\sqrt{R_s/R_t}$ for all setups and clamp sizes as a function of the dilution stage temperature T_d, extracted via Eq. (3.5) and Eq. (3.4). The dashed line in **(B)** is a $\propto T_d^{-1}$-fit to all data points with a proportionality constant of 1600 K^2/W. The dashed lines in **(C)** are guides to the eye for three different subsets of data points, as explained in the text.

Computation of the ratio of these two equations results in a monotonically increasing function $f = f\left(\sqrt{R_s/R_t}\right)$:

$$\frac{T_h - T_d}{T_o - T_d} = \underbrace{\cosh\left(\sqrt{\frac{R_s}{R_t}}\right) + \frac{d_{hc}}{L_c}\sqrt{\frac{R_s}{R_t}}\sinh\left(\sqrt{\frac{R_s}{R_t}}\right)}_{f=f\left(\sqrt{R_s/R_t}\right)}, \tag{3.5}$$

from which $\sqrt{R_s/R_t}$, a measure for the thermalization of the stripline, can be uniquely extracted from the measured temperature differences. Re-insertion of the extracted $\sqrt{R_s/R_t}$ in Eq. (3.4) then also yields the geometric mean $\sqrt{R_s R_t}$ of the thermal resistances.

Analysis and Results

From the monitored temperatures the points in time are chosen when a thermal equilibrium along the stripe is reached. A deviation from a linear dependence of the temperature differences on P_{heat} is observed, most likely due to a temperature dependence of $R_{s,t}$, which is not covered by the simple model. Therefore, linear fits crossing the origin are performed only with the points at lower powers (Fig. 3.6A).

f_r (GHz)	$\kappa/2\pi$ (MHz)	$\chi_{ge}/2\pi$ (MHz)	L_q (nH)	C_q (fF)	E_J (GHz)
7.458	4.10	-2.70	176	6.48	14.6

Table 3.1: Parameters of the resonator-qubit device. The resonance frequency f_r as well as the parameters L_q, C_q and E_J from a qubit spectrum fit were extracted from the spectroscopy data shown in Fig. 3.7D. The determination of the resonator linewidth $\kappa/2\pi$ and the dispersive shift $\chi_{ge}/2\pi$ is described in Section 3.2.2.

An overview of all extracted values for the parameters $\sqrt{R_s/R_t}$ and $\sqrt{R_sR_t}$ resulting from the above equations Eq. (3.4) and Eq. (3.5) is given in Fig. 3.6B and C for all setups, clamp sizes and dilution stage temperatures. The geometric mean of the thermal resistances, $\sqrt{R_sR_t}$, is observed to be nearly independent of setup and clamp size. All values fall onto the same T_d^{-1}-fit with proportionality constant 1600 K^2/W. In contrast, for $\sqrt{R_s/R_t}$, three categories of points can be identified: The weakest thermalization is indeed reached without a thermal contact layer and with the smaller clamp. A factor of 2 improvement in $\sqrt{R_s/R_t}$ is obtained either with the larger clamp but no additional thermal contact layer, or with the smaller clamp and an additional layer. Lastly, another factor of 2 improvement in $\sqrt{R_s/R_t}$ is reached with the large clamp and an additional thermal contact layer. In general, no significant difference between the grease and the SPM thermal contact layer can be observed.

In conclusion, for temperatures $T_d \leq 50$ mK, a clear improvement is observed when using the larger clamp and adding either grease or SPM as a thermal contact layer. At higher temperatures ($T_d \geq 1$ K), differences between all setups diminish within the measurement accuracy, except for the small clamp without an additional thermal contact layer, which continues to exhibit weaker thermalization. Across all setups, thermalization degrades as the temperature decreases.

3.2 Resonator-Qubit System as Photon Shot Noise Sensor

In order to assess information about photon shot noise, a superconducting quantum circuit was used, which consists of a fluxonium qubit, inductively coupled to a resonator (Fig. 3.7A), implementing the dispersive readout scheme. The circuit corresponds to sample 3 introduced in Section 2.6. As described in Section 3.2.2, the qubit state-dependent response of the readout resonator is fit to extract the resonator linewidth $\kappa/2\pi$ and the dispersive shift $\chi_{ge}/2\pi$, i.e., the resonator frequency difference for the qubit in the ground or excited state. The qubit spectrum is depicted in Fig. 3.7D, while a close-up around its first-order flux-insensitive point $\Phi_{ext}/\Phi_0 = 0.5$ is shown in Fig. 3.7C. Here Φ_{ext} denotes the external magnetic flux threading the fluxonium loop and Φ_0 is the magnetic flux quantum. Relevant parameters of the resonator-qubit system are summarized in Table 3.1.[1]

[1] In Ref. [5], different values for C_q and E_J were stated because the energy levels were wrongly assigned at zero-flux. The values stated in Table 3.1 are now corrected for that.

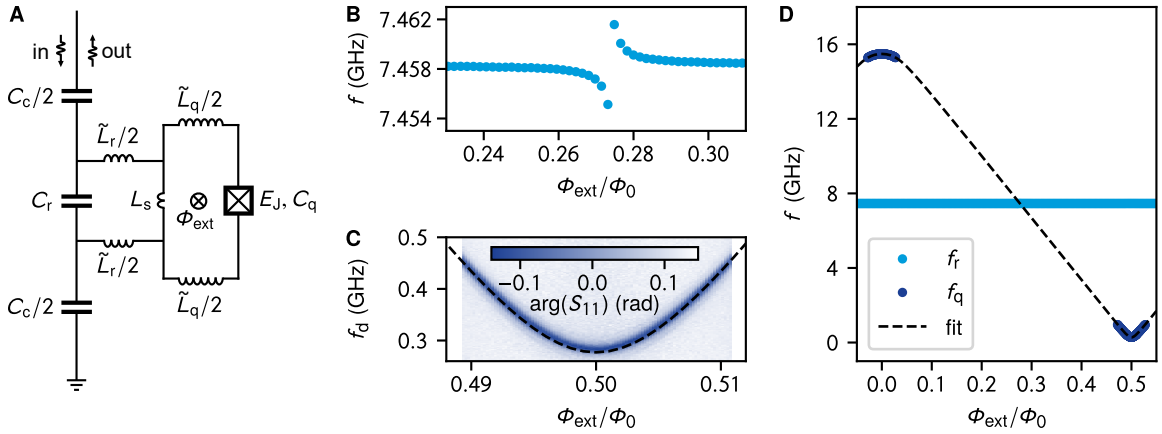

Figure 3.7: Resonator-qubit device. **(A)** Simplified electrical circuit diagram of the fluxonium with inductance $L_q = \tilde{L}_q + L_s$, capacitance C_q, Josephson energy E_J and external flux bias Φ_{ext}. The qubit is coupled inductively to a readout resonator with fundamental mode frequency f_r. The readout resonator is coupled via the capacitance C_c to the microwave lines. **(B)** Avoided level crossing between the qubit and resonator modes. **(C)** Two tone spectroscopy of the qubit around $\Phi_{ext}/\Phi_0 \approx 0.5$. **(D)** Measured resonator and qubit frequencies $f_{r,q}$ as a function of the external flux Φ_{ext}. From the fit (dashed line), the qubit parameters shown in Table 3.1 are extracted.

3.2.1 Qubit Temperature and Performance

Further comparative measurements with the two input chains show no significant differences in qubit performance (Fig. 3.8). This includes an extraction of the qubit temperature T_q from IQ distributions over a range of qubit frequencies $f_q \in [0.285, 1.23]$ GHz, obtained by sweeping Φ_{ext} (Fig. 3.8A). For both setups, T_q is found to be almost constant over the whole range and close to the ≈ 20 mK temperature of the dilution stage; (30.4 ± 1.4) mK for the coaxial cable setup, comparable to (26.4 ± 2.0) mK for the flexline setup. The minor difference in $\bar{T}_q$ is in the range of commonly observed fluctuations between cooldowns. The uptake in T_q for both setups as the qubit frequency decreases below 0.4 GHz or increases beyond 1 GHz could be explained by the fact that the qubit population approaches either 50% or zero, respectively. In both cases, the extracted temperature becomes susceptible to rare out-of-equilibrium excitations, for example from ionizing radiation [203] or readout quantum-demolition effects [145]. Moreover, the dispersive shift for large f_q drops to 1/3 of the value at the lowest f_q, making the readout more challenging. In the literature, typical values for T_q fall in a wide range between 20 and 60 mK [8, 9, 145, 276–278]. Finally, Fig. 3.8B shows that the energy relaxation and decoherence rates of the qubit near $\Phi_{ext}/\Phi_0 = 0.5$ remain unchanged between the two setups within the measurement accuracy. From fits to the measured echo and Ramsey dephasing rates using Eq. (1.86), a flux noise amplitude $\mathcal{A}_\Phi = 40\,\mu\Phi_0$, a ratio $\eta_R/\eta_E = 3.0$ of the numerical filtering factors can be extracted.

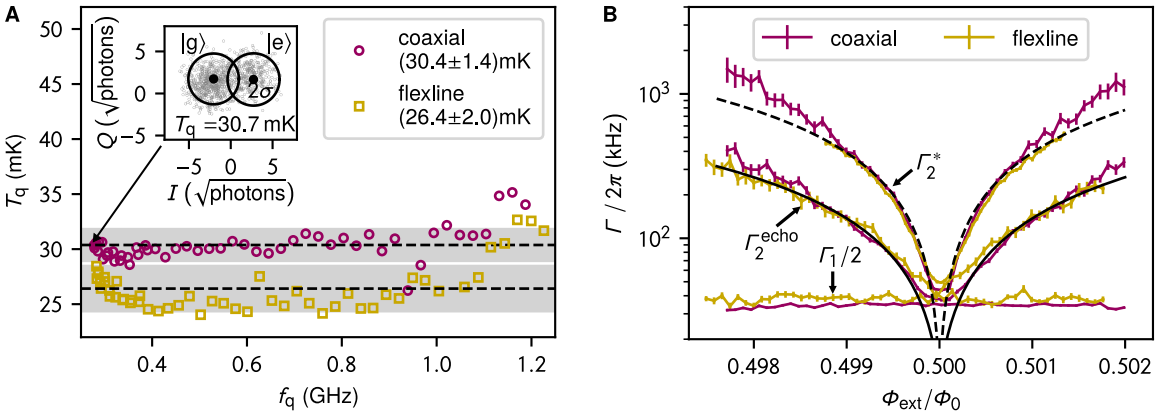

Figure 3.8: Comparison of conventional coaxial cable (magenta) and flexible stripline (yellow) setups. **(A)** Temperature T_q as a function of the qubit frequency f_q, extracted from Gaussian mixture fits of measured IQ distributions. For the fits, 10^5 points are used for the coaxial cable and 5×10^4 points for the flexible stripline. The dashed lines indicate the mean temperature values $\bar{T}_q$ and the horizontally filled areas the $\pm 1\sigma$ range, as stated in the legend. The inset shows a measured IQ distribution using the coaxial cable setup at $\Phi_{ext}/\Phi_0 = 0.5$, as indicated by the arrow. For better visibility, only a subset of 2000 points is shown. The quadratures are normalized to the square-root of the number of measurement photons $n_{meas} \approx \bar{n}\kappa t_{meas}/4$, approximated for negligible internal resonator losses, where $\bar{n}$ is the average number of photons in the resonator and t_{meas} the duration of the readout pulse. The black circles indicate the 2σ regions centered on the pointer states (black markers) corresponding to the qubit in the ground state $|g\rangle$ and the excited state $|e\rangle$, as indicated by the labels. **(B)** Rates (with vertical errorbars from the fit) extracted from energy relaxation, Ramsey as well as echo experiments in the vicinity of $\Phi_{ext}/\Phi_0 = 0.5$, for both the coaxial cable and the flexible stripline setup. Fits according to Eq. (1.86) to measured echo and Ramsey dephasing rates are represented by the solid and dashed black lines, respectively.

3.2.2 Extraction of Resonator Linewidth and Dispersive Shift

Eq. (1.90) and Eq. (1.91) show that knowledge about the dispersive shift $\chi_{ge}/2\pi$ and resonator linewidth $\kappa/2\pi$ is essential for calculating the photon number $\bar{n}$ from a measured value of dephasing rates $\Gamma_{\bar{n}}$. Since there is no additional resonator drive present during the free evolution of the qubit in a Ramsey or echo experiment, the determination of χ_{ge} and κ for the lowest possible photon numbers in the resonator is of interest. For this, I and Q quadratures are measured, as shown in the inset plot of Fig. 3.8A. From these, the qubit state dependent phase response of the readout resonator can be extracted, which is shown as a function of the readout frequency in Fig. 3.9A. The responses are only partly shown because an extraction of two IQ clouds is trusted only within a narrow frequency range around the mean resonance frequency $\bar{f}_r \approx 7.463\,\text{GHz}$. Additionally, when being sufficiently far away from $\bar{f}_r$, the mean value of all $\arg(S_{11})$ is assumed to be valid for both responses. Values for χ_{ge} and κ can be extracted by fitting two distinct phase responses $\arg(S_{11})$ to the measured data. In the fitting procedure, different values κ_g and κ_e of the resonator linewidth for the qubit being in its ground state $|g\rangle$ or excited state $|e\rangle$, respectively, are allowed. This is motivated by the fact that, in principle, the resonator IQ clouds corresponding to $|g\rangle$ or $|e\rangle$ might be squeezed to different degrees, since for one state the grAl resonator's intrinsic nonlinearity cancels out the qubit state-inherited nonlinearity while for another state it might not [279]. This behavior potentially leads

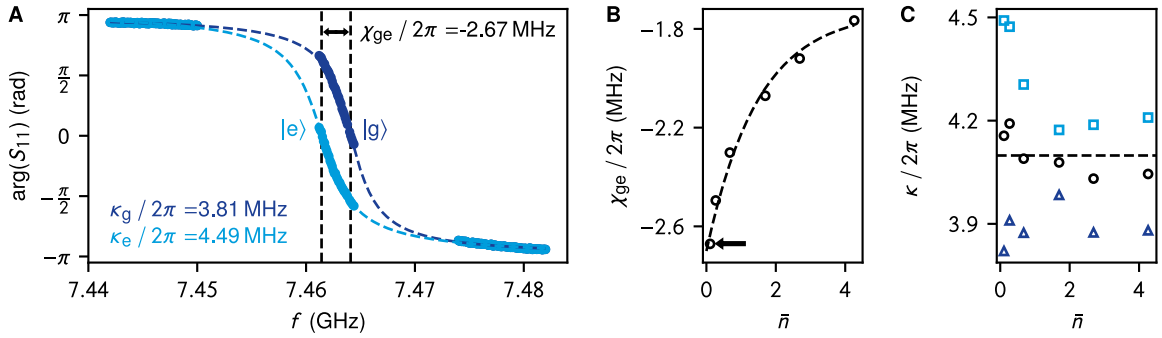

Figure 3.9: Qubit state dependent response of the readout resonator. **(A)** Phase response of the readout resonator coupled to the qubit being in its ground state |g⟩ (dark blue) or its excited state |e⟩ (light blue). For each readout frequency, we performed 10^5 consecutive reflection measurements. Each phase response associated to one of the qubit states is fit separately (dashed lines), from which we extract a dispersive shift between qubit and resonator of $\chi_{ge}/2\pi = -2.67$ MHz and corresponding linewidths $\kappa_g/2\pi = 3.81$ MHz and $\kappa_e/2\pi = 4.48$ MHz. The readout strength corresponds to $\bar{n} \approx 0.11$ photons on average in the resonator, as indicated by the arrow in panel B. **(B)** Dispersive shift $\chi_{ge}/2\pi$ and **(C)** resonator linewidths $\kappa_g/2\pi$ (triangles), $\kappa_e/2\pi$ (squares) and $\kappa/2\pi$ (circles) as a function of the average photon number $\bar{n}$ in the resonator. The black dashed line in panel B is an exponential guide to the eye. The horizontal line in panel C highlights the approximate independence of $\bar{n}$.

to different qubit-state dependent phase roll-offs. In the following, the mean linewidth is estimated by $\kappa = (\kappa_g + \kappa_e)/2$.

This procedure is repeated for different readout strengths to estimate χ_{ge} and κ for $\bar{n} \to 0$. For the dispersive shift, a photon number dependence similar as in Ref. [145] is observed, with an extrapolated value of $\chi_{ge}/2\pi = -2.70$ MHz for lowest photon numbers $\bar{n} \to 0$ (Fig. 3.9B). The mean linewidth $\kappa/2\pi = 4.10$ MHz is found to stay approximately constant over the whole range of $\bar{n}$ (Fig. 3.9C). No significant difference is observed between the coaxial cable and the flexline setup (not shown).

3.3 Measurement of Passive and Active Heat Load

3.3.1 Coaxial Cable Setup

To infer the thermal photon shot noise due to passive heat load in the coaxial cable setup, energy relaxation, Ramsey and echo measurements are performed over a course of 3.5 hours in an interleaved manner (Fig. 3.10A). The measured energy relaxation rates Γ_1 and decoherence rates $\Gamma_2^{*/\mathrm{echo}}$ fluctuate within 2% and the qubit frequency, extracted from the Ramsey fringes, is stable within a few kHz (Fig. 3.10B). Photon shot noise-induced dephasing rates $\Gamma_{\bar{n}} \approx \Gamma_\varphi = \Gamma_2 - \Gamma_1/2$ are estimated by first attributing the total measured dephasing rate Γ_φ entirely to photon shot noise. This approximation is justified by the estimation in Section 1.5.5 that critical current noise is negligible. Next, $\Gamma_2 = \Gamma_2^{\mathrm{echo}}$ is used to extract the fast components of the phase noise that can be associated with photon shot noise. This results in $\Gamma_{\bar{n}}/2\pi = (2.7 \pm 1.1)$ kHz, which is converted with Eq. (1.91) into

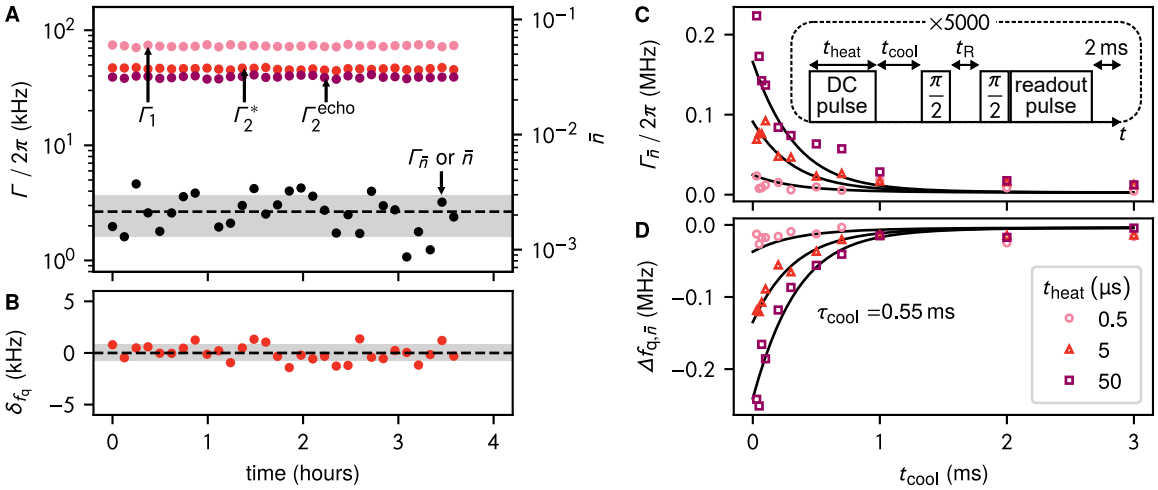

Figure 3.10: Fluxonium qubit measurements using the coaxial cable setup at $\Phi_{\mathrm{ext}}/\Phi_0 = 0.5$. **(A)** Interleaved measurements of Γ_1 relaxation (pink), Γ_2 Ramsey (red) and echo (magenta) dephasing rates over 3.5 hours. Gaussian distribution fits yield values of $\Gamma_1 / 2\pi = (73.1 \pm 1.1)$ kHz, $\Gamma_2^* / 2\pi = (46.2 \pm 0.8)$ kHz and $\Gamma_2^{\mathrm{echo}} / 2\pi = (39.2 \pm 0.9)$ kHz, respectively. Photon shot noise-induced dephasing rates $\Gamma_{\bar{n}}$ (black) are calculated from the extracted Γ_1 and Γ_2^{echo} values as described in the main text and converted into resonator photon numbers $\bar{n}$ according to Eq. (1.91). The dashed line indicates the mean value of $\Gamma_{\bar{n}}$ or $\bar{n}$ and the horizontally filled area their $\pm 1\sigma$ range, as stated in the text. **(B)** The qubit frequency, extracted from Ramsey fringes, fluctuates within a standard deviation of 0.8 kHz around the average qubit frequency $\bar{f}_{\mathrm{q}}$. **(C)** The inset shows the pulse sequence for the measurement of attenuator thermalization time. A DC pulse of duration t_{heat} is sent in the readout line to heat the attenuators, followed by a variable wait time t_{cool} before a standard Ramsey sequence. The markers correspond to photon shot noise-induced dephasing rates $\Gamma_{\bar{n}}$ as well as **(D)** qubit frequency shifts $\Delta f_{\mathrm{q},\bar{n}}$ extracted from Ramsey measurements. The black lines show a fit with common temperature relaxation time $\tau_{\mathrm{cool}} = 0.55$ ms for all heat pulses, following Eqs. (1.90) and (3.6).

residual photon numbers $\bar{n} = (2.1 \pm 0.8) \times 10^{-3}$. This value is in the lower range of what is commonly observed for passive heat load in the community [9, 192, 223–229].

In order to evaluate the thermalization of the coaxial input chain, the pulse sequence illustrated in Fig. 3.10C is employed. At the beginning of each repetition, a DC pulse is coupled into the input chain with a combiner to actively heat the attenuators. This heat pulse is many orders of magnitude larger in amplitude than what is used for the readout pulse. Given the 40 dB of distributed attenuation between room temperature and the dilution stage, approximately 0.25 µW reaches the dilution stage, where nearly all of it is absorbed by the attenuators. Then, a variable time t_{cool} is waited before performing a Ramsey sequence, from which the excess thermal photon shot noise and the temperature of the attenuators can be inferred. Each repetition ends with waiting 2 ms to prevent cumulative heating. To extract $\Gamma_{\bar{n}}$, from all measured decoherence rates Γ_2 the same offset value is subtracted such that, for large t_{cool}, $\Gamma_{\bar{n}}$ corresponds to the average value found in Fig. 3.10A. Extracted values for $\Gamma_{\bar{n}}$ and $\Delta f_{\mathrm{q},\bar{n}}$ as a function of t_{cool} are depicted in Fig. 3.10C and D for three heat pulse durations $t_{\mathrm{heat}} \in [0.5,\ 5,\ 50]$ µs.

The data is modeled on the basis of Eq. (1.90), assuming the input chain is a blackbody radiator with effective temperature T and Bose-Einstein distribution $n_{\mathrm{B}}(f, T)$. The temperature-dependent photon number $\bar{n}(T) = n_{\mathrm{B}}(f_{\mathrm{r}}, T)$ is associated with the blackbody radiation at

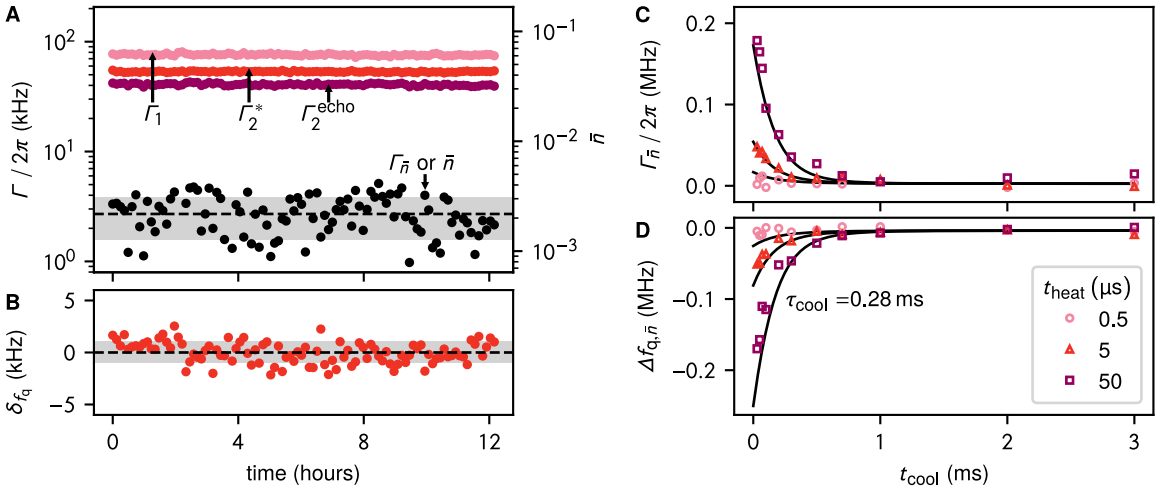

Figure 3.11: Fluxonium qubit measurements using the flexible stripline setup at $\Phi_{ext}/\Phi_0 = 0.5$. **(A)** Interleaved measurements of Γ_1 relaxation (pink), Γ_2 Ramsey (red) and echo (magenta) dephasing rates over 12 hours. Gaussian distribution fits yield values of $\Gamma_1 / 2\pi = (76.0 \pm 1.4)$ kHz, $\Gamma_2^* / 2\pi = (53.3 \pm 0.6)$ kHz and $\Gamma_2^{echo} / 2\pi = (40.7 \pm 0.9)$ kHz, respectively. Photon shot noise-induced dephasing rates $\Gamma_{\bar{n}}$ (black) are calculated from the extracted Γ_1 and Γ_2^{echo} values as described in the main text and converted into resonator photon numbers $\bar{n}$ according to Eq. (1.91). The dashed line indicates the mean value of $\Gamma_{\bar{n}}$ or $\bar{n}$ and the horizontally filled area their $\pm 1\sigma$ range, as stated in the main text. **(B)** The qubit frequency, extracted from Ramsey fringes, fluctuates within a standard deviation of 1.0 kHz around the average qubit frequency $\bar{f}_q$. **(C)** Photon shot noise-induced dephasing rates $\Gamma_{\bar{n}}$ as well as **(D)** qubit frequency shifts $\Delta f_{q,\bar{n}}$ extracted from Ramsey measurements. The black lines show a fit with common temperature relaxation time $\tau_{cool} = 0.28$ ms for all heat pulses, following Eqs. (1.90) and (3.6).

the frequency $f = f_r$. This temperature rises from its thermal equilibrium T_{eq} by ΔT and relaxes exponentially with a time constant τ_{cool} after the heat pulse:

$$\begin{aligned} \bar{n}(t_{cool}) &= \left(\exp\left(\frac{h f_r}{k_B T(t_{cool})} \right) - 1 \right)^{-1} \quad \text{with} \\ T(t_{cool}) &= T_{eq} + \Delta T \exp\left(-\frac{t_{cool}}{\tau_{cool}} \right), \end{aligned} \tag{3.6}$$

where k_B and h are the Boltzmann and the Planck constants, respectively. After a heating pulse, the thermalization of the coaxial cable chain is modeled by a simultaneous fit of the measured relaxation curves $\Gamma_{\bar{n}}$ and $\Delta f_{q,\bar{n}}$ to Eqs. (1.90) and (3.6), yielding a common time constant $\tau_{cool} = 0.55$ ms for all three values of t_{heat} (Fig. 3.10C and D). In Eq. (3.6), the equilibrium temperature $T_{eq} = 58$ mK of the blackbody is fixed to the value corresponding to the mean residual thermal photon population in Fig. 3.10A. The fit yields temperature differences $\Delta T = [33,\ 76,\ 111]$ mK. For the data with the longest heat pulse ($t_{heat} = 50$ µs), a model based on two blackbodies in the input chain decaying with different time constants could possibly describe the data better.

3.3.2 Flexible Stripline Setup

In this subsection, the same experiments as above are repeated with the flexible stripline input chain. Following the procedure described in Section 3.3.1, a passive heat load corresponding to an average photon population in the resonator of $\bar{n} = (2.2 \pm 0.9) \times 10^{-3}$ can be extracted from interleaved energy relaxation and echo measurements over a duration of 12 hours (Fig. 3.11A). This value falls into the same range as the one found with the coaxial setup.

From these considerations, a temperature $T_{\mathrm{eq}} = 58\,\mathrm{mK}$ of the blackbody generating the thermal photon shot noise is obtained. Similar to the coaxial cable case, fitting all three heat pulse scenarios simultaneously requires different values for ΔT while keeping a common τ_{cool} as a fit parameter. The fit yields temperature differences $\Delta T = [24,\ 55,\ 114]\,\mathrm{mK}$ and a time constant of $\tau_{\mathrm{cool}} = 0.28\,\mathrm{ms}$, which is a factor of two faster than for the coaxial cable setup. This behavior indicates that the flexible stripline integrated attenuators are at least as well thermalized as the coaxial cable attenuators. Together with the absence of detrimental effects on the superconducting device observed in Section 3.2.1, these results support the use of flexible striplines at scale in future quantum processor setups and large detector arrays.

Even though the model in Eq. (3.6) fits the data for input chains, this is only a first-order approximation. While all attenuators in both setups are thermalized to temperatures $T < 10\,\mathrm{K}$, in which case both heat capacity and conduction in metals are dominated by electrons [48], so thermalization is independent of temperature, this model ignores two factors. First, the non-linear relationship between T and $\bar{n}_{\mathrm{B}}$ implies that even attenuators that thermalize with the same rate will contribute with different time constants to the thermal photon shot noise decay, depending on their respective temperatures. Second, the hot electron effect [280, 281] and increased Kapitza phonon-phonon boundary resistance [282] decrease heat conduction at temperatures below a few hundred millikelvin. At different times along the temperature relaxation curve, thermal photon shot noise might be dominated by attenuators anchored to different stages of the cryostat. Therefore, the extracted values of T_{eq} and ΔT from the fit of the measured data in Fig. 3.11C and D should be seen as effective parameters characterizing the entire input chain. In Section 3.4, a more realistic and complex input chain thermal model is presented, where the individual contributions of each element in the chain to the total thermal photon shot noise are considered.

Another point worth mentioning is that all t_{heat} used in the experiment are smaller than all values of τ_{cool} that were extracted from the model. This indicates that for all heating scenarios, the steady state under heat load has not been reached yet, but instead the electrons in the attenuators were only partially heated. In a future experiment, it might also be of interest to heat long enough in order to saturate the thermal photon shot noise, and instead vary the input power P_{in}.

3.4 Input Chain Thermal Model

This section introduces a thermal model for input chains that serves as a more comprehensive alternative to the single blackbody model discussed in Section 3.3, enabling a refined estimation of the thermal photon shot noise reaching the resonator–qubit system under thermal load of the chain. The discussion begins in Section 3.4.1 by motivating the approach and illustrating the underlying concept using a simplistic toy model consisting solely of attenuators. Building on this, Section 3.4.2 incorporates cables connecting different temperature stages, resulting in a more realistic representation of both coaxial cable and flexline input chains. Subsequently, Section 3.4.3 applies the extended model to experimental active heat load data from Section 3.3. This allows for identifying the contributions from individual temperature stages to the overall thermal photon shot noise in both types of input chains. Finally, Section 3.4.4 presents improved designs for coaxial and flexline input chains, for which the resulting thermal photon shot noise is evaluated through simulation.

3.4.1 Motivation and Simplistic Toy Model

In Section 3.3, measurements of the passive and active heat load for two different input chains were presented. While modeling each of the input chains as a single blackbody results in a satisfying agreement between experimental data and the fit, the model lacks in giving further insight into contributions from different parts of the input chain to the total photon shot noise due to its simplicity. To overcome this limitation, a more detailed model was created, which is presented in the following.

An input chain consists of a series of attenuators anchored at different temperature stages, and cables interconnecting these stages. To pedagogically illustrate this concept, the following discussion starts with a–still simplistic–toy model, in which the input chain is assumed to consist of three 20 dB attenuators in series, one anchored at each the 20 mK, 0.2 K and 4 K temperature stage.

To estimate the active heat load in an input chain, the first step is to compute the heat input powers $P_{\text{heat}}^{(i)}$ for each attenuator by accounting for all preceding attenuators in the chain:

$$P_{\text{heat}}^{(i)} = (1 - a_i) \prod_{j<i} a_j P_{\text{in}}, \tag{3.7}$$

where $a_i = 10^{-A_i/10\,\text{dB}}$ is the attenuation factor of the i-th attenuator ($A_i > 0$ its attenuation in dB), and P_{in} is the DC power inserted into the cryostat at room temperature.

Then, the heat balance illustrated in Fig. 3.12A is set up for each attenuator in the chain: Within an infinitesimally small time step $\mathrm{d}t$, the energy $P_{\text{heat}}^{(i)}\,\mathrm{d}t$ gets dissipated, out of which the energy $\Lambda_i(T_i)(T_i - T_{\text{eq}}^{(i)})\,\mathrm{d}t$ will be conducted out of the attenuator due to its thermal anchoring. Here, $\Lambda_i(T_i)$ and $T_{\text{eq}}^{(i)}$ are the thermal conductance and equilibrium temperature of the i-th attenuator, respectively. For this, the simplifying assumption

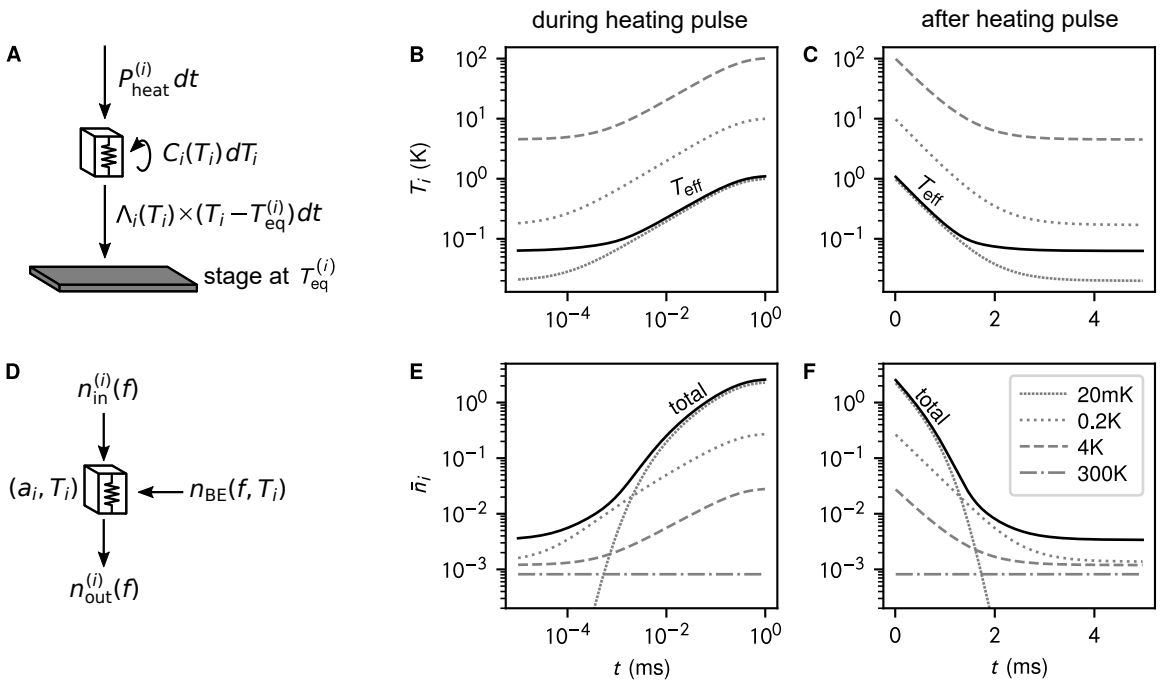

Figure 3.12: Simplistic toy model. **(A)** Illustration of the energy balance of an attenuator in the input chain. An attenuator receives heat input according to Eq. (3.7) and outputs energy due to its thermal anchoring at the stage with constant temperature $T^{(i)}_{\text{eq}}$. The difference must result in changing the internal energy of the attenuator (Eq. (3.8)), from which the temperature change $\mathrm{d}T_i$ within the next time step $\mathrm{d}t$ can be estimated, see Eq. (3.10). Temperatures of all three attenuators in the simplistic toy model chain, as a function of time **(B)** during and **(C)** after a $P_{\text{in}} = 1\,\text{mW}$ strong DC heating pulse. For better visibility, a logarithmic time scale is chosen in panel B. **(D)** An attenuator effectively acts as a beamsplitter [230] by attenuating incoming noise $n^{(i)}_{\text{in}}(f)$ from higher temperature stages with an attenuation factor a_i and adding blackbody radiation $n^{(i)}_{\text{BE}}(f, T_i)$ at the temperature T_i of the attenuator, resulting in the outgoing noise $n^{(i)}_{\text{out}}(f)$, see Eq. (3.13). Contributions $\bar{n}_i$ of all temperature stages (see Eq. (3.14)) to the total photon shot noise $\bar{n}$ (black line), as a function of time **(E)** during and **(F)** after the heating pulse.

is used that the attenuator is in direct contact to an infinitely large bath at $T^{(i)}_{\text{eq}}$. The difference of incoming and outgoing energy must result in change of the attenuator's internal energy,

$$C_i(T_i)\,\mathrm{d}T_i = [P^{(i)}_{\text{heat}} - \Lambda_i(T_i)(T_i - T^{(i)}_{\text{eq}})]\,\mathrm{d}t, \tag{3.8}$$

where $C_i(T_i)$ describes the heat capacity of the i-th attenuator. In all cases considered here, the attenuators are thermalized to temperatures below 10 K, in which case the heat capacity $C(T)$ and thermal conductance $\Lambda(T)$ of metals are electron-dominated and therefore scale linearly with temperature to first order [48]:

$$C_i(T_i) \approx \tilde{C}^{(i)}_{\text{el}} T_i \qquad \text{and} \qquad \Lambda_i(T_i) \approx \tilde{\Lambda}^{(i)}_{\text{el}} T_i \tag{3.9}$$

This condition might start to break down for very large heat pulses when locally temperatures $T > 10\,\text{K}$ are reached and therefore the phononic contributions ($\propto T^3$) are not negligible. However, this effect can still be neglected, because the contribution of the 4 K stage to the total thermal photon shot noise is never significant when the attenuators are hot (cf. the left part of the curves in Fig. 3.14C and F). Also, an additional contribution to

the heat capacity would only counteract an uptake in temperature. Altogether, inserting the approximation Eq. (3.9) into Eq. (3.8) yields

$$\mathrm{d}T_i = \left[\frac{P_{\mathrm{in}}^{(i)}}{\tilde{C}_{\mathrm{el}}^{(i)} T_i} - \frac{\tilde{\Lambda}_{\mathrm{el}}^{(i)}}{\tilde{C}_{\mathrm{el}}^{(i)}} (T_i - T_{\mathrm{eq}}^{(i)}) \right] \mathrm{d}t. \tag{3.10}$$

By repeating this evaluation N times with sufficiently small time steps, the total temperature changes ΔT_i after heating the input chain for the duration $t_{\mathrm{heat}} = N\,\mathrm{d}t$ can be estimated, effectively performing a numerical integration of the heat balance equation Eq. (3.10).

For the simplistic toy model consisting of three attenuators, this yields the dashed curves in Fig. 3.12B. Here, an input power $P_{\mathrm{in}} = 1\,\mathrm{mW}$ and the same proportionality constants $\tilde{C}_{\mathrm{el}}^{(i)} = 50\,\mathrm{pJ/K^2}$ and $\tilde{\Lambda}_{\mathrm{el}}^{(i)} = 100\,\mathrm{nW/K^2}$ were assumed for all three attenuators. The temperatures of the attenuators reach 100 K, 10 K and 1 K after 1 ms of heating in this scenario.

After the heat pulse, Eq. (3.10) is still valid, but now $P_{\mathrm{heat}}^{(i)} = 0$ can be imposed to simplify:

$$\mathrm{d}T_i = -\frac{\tilde{\Lambda}_{\mathrm{el}}^{(i)}}{\tilde{C}_{\mathrm{el}}^{(i)}} (T_i - T_{\mathrm{eq}}^{(i)})\,\mathrm{d}t \equiv -\frac{T_i - T_{\mathrm{eq}}^{(i)}}{\tau_{\mathrm{cool}}^{(i)}}\,\mathrm{d}t, \tag{3.11}$$

which can be easily integrated analytically, leading to an exponential decay towards the thermal equilibrium $T_{\mathrm{eq}}^{(i)}$ with the time constants $\tau_{\mathrm{cool}}^{(i)} = \tilde{C}_{\mathrm{el}}^{(i)} / \tilde{\Lambda}_{\mathrm{el}}^{(i)}$:

$$T_i(t_{\mathrm{cool}}) = T_{\mathrm{eq}}^{(i)} + \Delta T_i \exp\left(-\frac{t_{\mathrm{cool}}}{\tau_{\mathrm{cool}}^{(i)}} \right). \tag{3.12}$$

It should be emphasized that the time constants $\tau_{\mathrm{cool}}^{(i)}$ do not depend on temperature to first order in the $T < 10\,\mathrm{K}$ regime. In Fig. 3.12C, the temperatures of all attenuators in the toy model after the heating pulse are plotted. According to Eq. (3.12), all temperatures decay exponentially with a time constant of $\tau_{\mathrm{cool}}^{(i)} = 0.5\,\mathrm{ms}$.

In order to estimate the total thermal photon shot noise of the input chain during and after the heating event, the fact is used that an attenuator effectively acts as a beamsplitter (Fig. 3.12D), attenuating the incoming photon shot noise $n_{\mathrm{in}}^{(i)}$ by the attenuation factor a_i and adding noise according to its temperature [230]:

$$n_{\mathrm{out}}^{(i)}(f) = a_i n_{\mathrm{in}}^{(i)}(f) + (1 - a_i) n_{\mathrm{BE}}^{(i)}(f, T_i). \tag{3.13}$$

In this way, the total photon shot noise $\bar{n} = n_{\mathrm{out}}^{20\mathrm{mK}}$ reaching the resonator at the frequency $f = f_{\mathrm{r}}$ can be estimated by successively evaluating Eq. (3.13) for all attenuators in the input chain, starting from 300 K down to 20 mK. The 300 K stage is implemented with $a_{300\mathrm{K}} = 0$. Furthermore, the contributions $\bar{n}_i$ of different parts in the input chain to $\bar{n}$ are determined.

For this, the added noise of an attenuator is attenuated by all upcoming attenuation in the chain,

$$\bar{n}_i = (1 - a_i) n_{\mathrm{BE}}^{(i)} \prod_{j>i} a_j. \tag{3.14}$$

In Fig. 3.12E and F, these contributions $\bar{n}_i$ and the total photon shot noise $\bar{n}$ are shown during and after the heating pulse, respectively. Interestingly, three regimes can be distinguished: When the temperatures of all attenuators are elevated the most, the noise contribution $\bar{n}_{20\mathrm{mK}}$ from the attenuator on the 20 mK stage is dominating. When the system is close to its thermal equilibrium with the temperature stages, $\bar{n}_{20\mathrm{mK}}$ is exponentially suppressed while $\bar{n}_{0.2\mathrm{K}}$, $\bar{n}_{4\mathrm{K}}$ and $\bar{n}_{300\mathrm{K}}$ contribute almost equally to the residual photon shot noise of 3.4×10^{-3}. Lastly, there is also an intermediate regime where $\bar{n}_{20\mathrm{mK}}$ is still exponentially suppressed, but $\bar{n}_{0.2\mathrm{K}}$ surpasses $\bar{n}_{4\mathrm{K}}$ by almost an order of magnitude, dominating the thermal photon shot noise there.

Lastly, from the total photon shot noise $\bar{n}$ an effective temperature T_{eff} can be estimated,

$$T_{\mathrm{eff}} = \frac{hf}{k_{\mathrm{B}} \ln\left(1 + 1/\bar{n}\right)}, \tag{3.15}$$

which is also illustrated in Fig. 3.12B and C. It should however be noted that T_{eff} does not per se correspond to the physical temperature of a blackbody, rather it represents the temperature that a blackbody would need to generate the observed photon shot noise at the frequency f of interest. In line with the above, T_{eff} can be approximated by the temperature of the 20 mK stage only in the regime of more elevated temperatures. In contrast, when the system is close to thermal equilibrium with the temperature stages, $T_{\mathrm{eff}} \approx 63\,\mathrm{mK}$ results from the non-negligible contributions of the 0.2 K, 4 K and 300 K stages.

3.4.2 Extended Thermal Model of the Coaxial and Flexline Input Chains

In order to fully describe the coaxial cable and flexible stripline input chains, the extended thermal model will also consider cable sections inbetween temperature stages and split attenuators into individual parts or unit cells. For this, the detailed information about the coaxial and flexline input chains presented in Sections 3.1.1 and 3.1.2 is followed, as shown in Fig. 3.13A.

The DC resistance in all cable sections is assumed to be negligible. Therefore, any heating effect inside of them due to DC pulses is neglected, and they are assumed to stay constant in temperature over time. Another consequence is that cable sections will not participate in attenuating these pulses, leaving Eq. (3.7) unchanged. However, cables still play a role in attenuating blackbody radiation from higher temperature stages. For this reason, Eqs. (3.13) and (3.14) can be extended to cables as well.

A cable is simulated in the following as a series of many small elements with attenuation factors $a_k(T_k)$ $(1 \leq k \leq N)$ that depend on the temperatures T_k of the elements. Eq. (3.13)

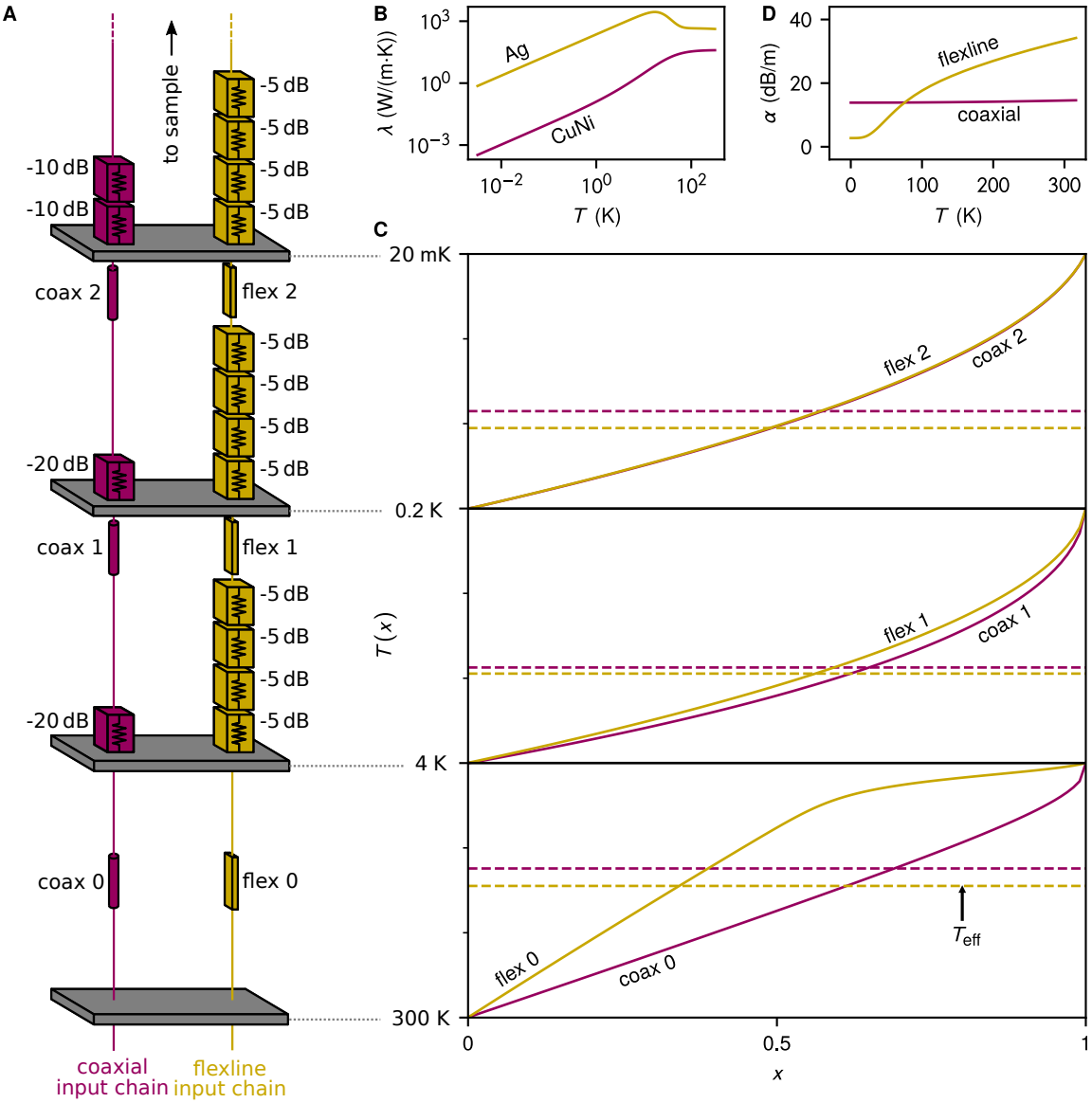

Figure 3.13: Extended input chain thermal models. **(A)** Overview of the full flexible stripline and coaxial cable input chains. Attenuation values stand next to the attenuators, which are directly thermalized on either the 4 K, 0.2 K or 20 mK stage. Different temperature stages are connected via cable sections of either CuNi coaxial cables ("coax") or Ag flexible striplines ("flex"). Details on the cables are summarized in Table 3.2. **(B)** Thermal conductivities λ of the materials used in the cable sections of the input chains as a function of temperature T. The conductor in the coaxial cables is made of CuNi (magenta) and in the flexible stripline it is made of Ag (yellow). Values were taken from Refs. [283–285]. **(C)** Temperature profiles $T(x)$ along the dimensionless length x of all cables in the coaxial (magenta) and flexline (yellow) input chains, respectively. The profiles were calculated using Eq. (3.17), and the horizontal dashed lines correspond to the values of T_{eff} given in Table 3.2. The vertical scale is linear between the temperature stage labels. **(D)** Attenuation per length α for coaxial cables and flexible striplines as a function of temperature T, based on the measured values $\alpha(300\,\text{K})$ at room-temperature and Eq. (3.18).

is successively used for each element in the cable to show that one can assign an effective attenuation a_{eff} and temperature T_{eff} to the cable:

$$\begin{aligned} n_{\text{out}}^{(N)}(f) &= a_N n_{\text{in}}^{(N)}(f) + (1-a_N) n_{\text{BE}}(f, T_N) \\ &= a_N a_{N-1} n_{\text{in}}^{(N-1)}(f) + (1-a_{N-1}) n_{\text{BE}}(f, T_{N-1}) + (1-a_N) n_{\text{BE}}(f, T_N) = \dots \\ &= \prod_{k=1}^{N} a_k n_{\text{in}}^{(1)}(f) + \sum_{j=1}^{N} n_{\text{BE}}(f, T_j)(1-a_j) \prod_{k=j}^{N} a_k \\ &\equiv a_{\text{eff}} n_{\text{in}}^{(1)}(f) + (1-a_{\text{eff}}) n_{\text{BE}}(f, T_{\text{eff}}) \end{aligned} \tag{3.16}$$

However, one can not truly speak of a single blackbody that represents the whole cable: In fact, $T_{\text{eff}} = T_{\text{eff}}(f)$ now depends on the frequency f of interest, similar to the effective temperature defined in Eq. (3.15). In order to calculate a_{eff} and T_{eff}, two ingredients are needed. First, the temperature profile $T(x)$ along the dimensionless length $0 \leq x \leq 1$ of a cable, and second, its temperature-dependent attenuation per length $\alpha(T)$.

To determine the temperature profile, Fourier's law, $\dot{Q} = \frac{\lambda A}{L} \frac{\mathrm{d}T}{\mathrm{d}x}$, can be used. According to this law, $T(x)$ is uniquely defined by the temperature-dependent thermal conductivity $\lambda(T)$ of the conductor material (see Fig. 3.13B) as well as the temperatures $T(0)$ and $T(1)$ at both ends of the cable because of the conservation of heat flow along the cable:

$$\frac{1}{x} \int_{T(0)}^{T(x)} \lambda(T')\, \mathrm{d}T' = \int_{T(0)}^{T(1)} \lambda(T')\, \mathrm{d}T'. \tag{3.17}$$

Both the cross-sectional area A and cable length L do not alter $T(x)$, but they will rescale the heat flow $\dot{Q}$ through the cable. Eq. (3.17) allows to extract the temperature profiles depicted in Fig. 3.13C of all cables in both chains. One can observe that the nearly constant thermal conductivity above 100 K leads to a nearly linear dependence $x \propto T$, and that the nearly linear behavior of $\lambda(T)$ below 10 K yields a nearly quadratic behavior of $x \propto T^2$.

For calculating the temperature-dependent attenuation per length $\alpha(T)$ of the cable, the fact is used that α is proportional to the RF sheet resistance R_{s}, which itself is proportional to the resistivity ρ and inversely proportional to the skin depth δ_{s}. The latter is again proportional to $\sqrt{\rho}$ [170], resulting in

$$\alpha \propto R_{\text{s}} \propto \frac{\rho}{\delta_{\text{s}}} \propto \sqrt{\rho} \qquad \Rightarrow \qquad \alpha(T) = \alpha(300\,\text{K}) \sqrt{\frac{\rho(T)}{\rho(300\,\text{K})}} \tag{3.18}$$

For the flexible stripline, the measured value of $\alpha(300\,\text{K}) = 32.9\,\text{dB/m}$ at $f = f_{\text{r}}$ is inserted and Ref. [285] is used to extract $\rho(T)$. For the coaxial cable, $\alpha(300\,\text{K}) = 14.5\,\text{dB/m}$ at $f = f_{\text{r}}$ is found and Ref. [283] is used to extract $\rho(T)$. The resulting $\alpha(T)$ for both types of cables are shown in Fig. 3.13D. With this, values for the effective attenuations a_{eff} and temperatures T_{eff} for all cable sections in both setups are found, which are summarized in the following Table 3.2:

cable	material	L (m)	A (μm^2)	a_{eff}	A_{eff} (dB)	$T_{\text{eff}}(K)$
coax 0	CuNi (80:20)	0.7	6.5×10^4	0.103	9.88	124
coax 1	CuNi (80:20)	0.3	6.5×10^4	0.384	4.16	2.87
coax 2	CuNi (80:20)	0.4	6.5×10^4	0.279	5.54	0.11
flex 0	Ag ($RRR = 132$)	0.32	$\mathcal{O}(10^3)$	0.329	4.82	144
flex 1	Ag ($RRR = 132$)	0.14	$\mathcal{O}(10^3)$	0.918	0.37	2.98
flex 2	Ag ($RRR = 132$)	0.20	$\mathcal{O}(10^3)$	0.881	0.55	0.12

Table 3.2: Detailed information and extracted parameters of the cables of both input chains.

3.4.3 Application of the Extended Model to Measured Data

In this section, the extended input chain thermal model is applied to the measured data within the active heat load experiments in Sections 3.3.1 and 3.3.2. The model is used to estimate the temperature changes ΔT_i of all attenuators that are generated by the three different heat pulse scenarios, and afterwards calculate the relaxation to thermal equilibrium. For this, there are for each type of attenuator only two free parameters, $\tilde{C}_{\text{el}}^{(i)}$ and $\tilde{\Lambda}_{\text{el}}^{(i)}$ (or equivalently $\tilde{C}_{\text{el}}^{(i)}$ and $\tau_{\text{cool}}^{(i)}$).

In Fig. 3.14A and B, the data points shown in Fig. 3.10C and D for the coaxial input chain are once more plotted. To model the data, the extended input chain model is applied, as described above. In contrast to the flexline, the coaxial input chain consists of two types of attenuators. From a simultaneous fit to all three heat pulse scenarios, the values $\tau_{\text{cool}}^{(1)} = 0.50\,\text{ms}$ and $\tilde{C}_{\text{el}}^{(1)} = 17\,\text{pJ/K}^2$ for the 20 dB attenuators from *XMA* on the 0.2 K and 4 K stages, and $\tau_{\text{cool}}^{(2)} = 0.12\,\text{ms}$ and $\tilde{C}_{\text{el}}^{(2)} = 120\,\text{pJ/K}^2$ for the 10 dB attenuators from *Quantum Microwave* on the 20 mK stage, respectively, are extracted. Additionally, an input power of $P_{\text{in}} = 2.5\,\text{mW}$ and heating durations $t_{\text{heat}}^{\text{model}} \in [0.5,\ 15,\ 50]\,\mu\text{s}$ are used for the extended model. The latter values differ from the real values $t_{\text{heat}} \in [0.5,\ 5,\ 50]\,\mu\text{s}$ slightly, in order to keep $\tilde{C}_{\text{el}}$ and τ_{cool} for all three heat pulse scenarios constant. This difference might arise from the still strong simplification of the attenuators in the model compared to the real world. For instance, by describing the attenuator with a single temperature value T_i, the spatial dependence of the temperature inside the element is neglected. Furthermore, even though the hot electron effect [280, 281] and an increased Kapitza phonon-phonon boundary resistance [282] play a significant role at temperatures below a few hundred millikelvin, their influence has been neglected for the sake of simplicity.

For the data with the longest heat pulse ($t_{\text{heat}} = 50\,\mu\text{s}$), the contributions $\bar{n}_i$ from all temperature stages (20 mK, 0.2 K, 4 K and 300 K) and the cables to the total thermal photon shot noise $\bar{n}$ are shown in Fig. 3.14C, calculated according to Eq. (3.14). Similar to the simplistic toy model in Fig. 3.12, three regimes can be distinguished, each dominated by a different temperature stage. In the beginning, the otherwise exponentially suppressed noise contribution $\bar{n}_{20\text{mK}}$ from the attenuators on the 20 mK stage becomes almost comparable to the contribution $\bar{n}_{0.2\text{K}}$ from the 0.2 K stage. For intermediate timescales, i.e. moderately elevated temperatures, the photon shot noise reaching the resonator is fully dominated by $\bar{n}_{0.2\text{K}}$. When the system approaches thermal equilibrium again, the contribution $\bar{n}_{4\text{K}}$ from

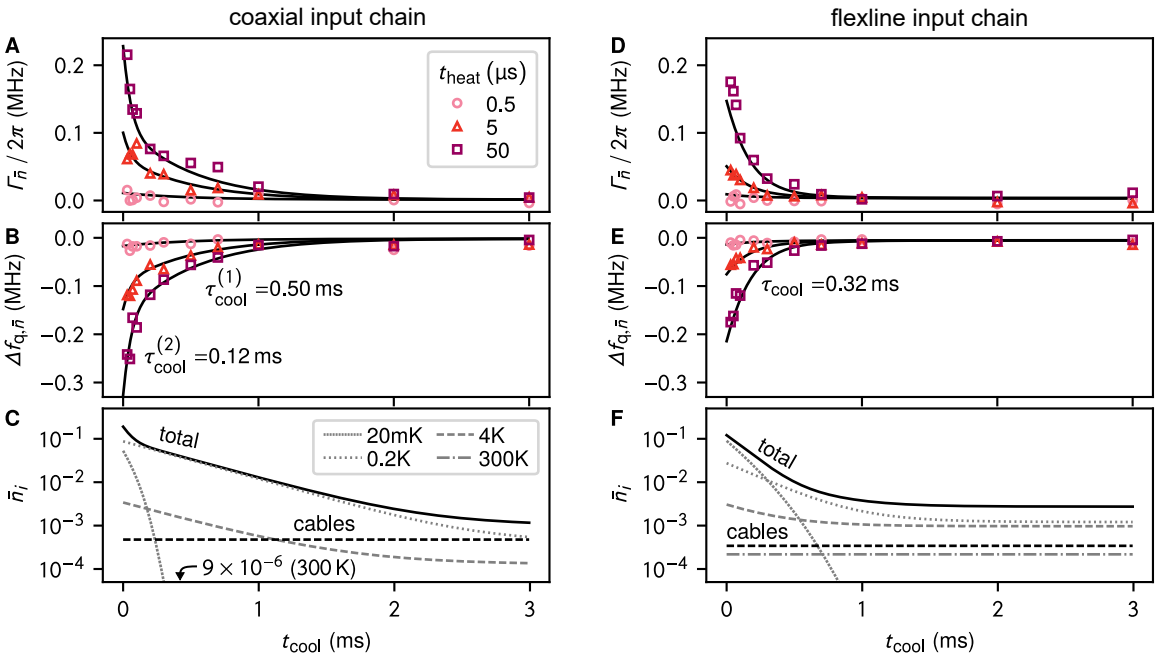

Figure 3.14: Application of the extended input chain thermal model to the active heat load experimental data with both setups. **(A)** Photon shot noise-induced dephasing rates $\Gamma_{\bar{n}}$ as well as **(B)** qubit frequency shifts $\Delta f_{q,\bar{n}}$ extracted from Ramsey measurements with the coaxial input chain, after three different heating scenarios with input power $P_{in} = 2.5\,\mathrm{mW}$ and heating durations t_{heat} as labeled in the legend. The black lines show a simultaneous fit according to the extended thermal model (see previous section) with common relaxation times $\tau_{cool}^{(1)} = 0.50\,\mathrm{ms}$ for the coaxial attenuators on the 0.2 K or 4 K stage and $\tau_{cool}^{(2)} = 0.12\,\mathrm{ms}$ on the 20 mK stage, for all heat pulse scenarios. **(C)** Contributions $\bar{n}_i$ from different temperature stages and the cables (dashed black line) to the total thermal photon shot noise $\bar{n}$ (solid black line), according to Eq. (3.14), for the longest heat pulse ($t_{heat} = 50\,\mu\mathrm{s}$). The contribution of the 300 K stage is as low as 9×10^{-6} and it is therefore not visible on this scale. **(D)** The markers correspond to photon shot noise-induced dephasing rates $\Gamma_{\bar{n}}$ as well as **(E)** qubit frequency shifts $\Delta f_{q,\bar{n}}$ extracted from Ramsey measurements with the flexline input chain, after the same three heating scenarios as for the coaxial input chain. The black lines show a simultaneous fit according to the extended thermal model (see previous section) with common relaxation time $\tau_{cool} = 0.32\,\mathrm{ms}$ for all heat pulse scenarios. **(F)** Contributions $\bar{n}_i$ from different temperature stages and the cables (dashed black line) to the total thermal photon shot noise $\bar{n}$ (solid black line), according to Eq. (3.14), for the longest heat pulse ($t_{heat} = 50\,\mu\mathrm{s}$).

the 4 K stage stays well below $\bar{n}_{0.2K}$. The contribution $\bar{n}_{cables} = 4.8 \times 10^{-4}$ of the coaxial cables is not negligible, but contributes almost equally to the residual thermal photon shot noise of 1.2×10^{-3}, which is on the edge of the experimentally found range in Fig. 3.10A.

In Fig. 3.14D and E, the data points shown in Fig. 3.11C and D for the flexline input chain are plotted once again. Since all 5 dB unit cell attenuators in the flexline are of the same type, from a simultaneous fit of the extended input chain thermal model to the data of all three heat scenarios a common time constant $\tau_{cool} = 0.32\,\mathrm{ms}$ and parameter $\tilde{C}_{el} = 85\,\mathrm{pJ/K^2}$ can be extracted for all attenuators. Additionally, the input power $P_{in} = 2.5\,\mathrm{mW}$ and heating durations $t_{heat}^{model} \in [2,\ 15,\ 50]\,\mu\mathrm{s}$ were used.

As for the coaxial chain, the contributions $\bar{n}_i$ of all temperature stages (20 mK, 0.2 K, 4 K and 300 K) to the total thermal photon shot noise $\bar{n}$ were computed for the case of the

50 µs long heat pulse in the flexline setup (Fig. 3.14F). Similar to the above results, once more three regimes can be distinguished: In the beginning, when the temperatures of all attenuators are elevated the most, the noise contribution $\bar{n}_{20\mathrm{mK}}$ from all attenuators on the 20 mK stage is dominating. There is also an intermediate regime where $\bar{n}_{20\mathrm{mK}}$ is still exponentially suppressed, but $\bar{n}_{0.2\mathrm{K}}$ surpasses $\bar{n}_{4\mathrm{K}}$ by almost an order of magnitude. In the end and in contrast to the coaxial input chain, when the system approaches thermal equilibrium again, $\bar{n}_{20\mathrm{mK}}$ is exponentially suppressed while $\bar{n}_{0.2\mathrm{K}}$ and $\bar{n}_{4\mathrm{K}}$ contribute almost equally to the residual thermal photon shot noise of 2.7×10^{-3}, which is comparable to the experimental value found in Fig. 3.11A. Another difference to the coaxial cable setup is that the contribution arising from all cable sections in the flexible stripline chain sums up to only $n_{\mathrm{cables}} = 3.4 \times 10^{-4}$ and it is therefore negligible for $\bar{n}$.

The direct comparison between the coaxial and flexline input chain thermal models reveals that, depending on the implementation, cables might play a role or even become the limiting factor for the passive heat load reaching the quantum devices. Therefore, a simulation of the passive heat load of a new input chain and the contributions of individual parts to it are recommended.

Apart from the already established superiority of the flexline chain over the coaxial chain in terms of the thermalization of the integrated attenuators, the following section attempts to predict potential improvements for both input chains using the extended thermal model.

3.4.4 Improved Input Chains

Based on the evaluation with the extended thermal model in the previous chapter and assuming the cable sections in both chains (Table 3.2) as well as the integrated attenuators in the flexline as given, the following improved versions of both input chains are proposed:

- **Improved** flexline input chain:
  Due to the use of Ag instead of CuNi, the summed cable attenuation is approximately 15 dB lower for the flexline setup compared to the coaxial setup (cf. Table 3.2). For equalizing the total attenuation between the two input chains, in order to compare them, another 15 dB of attenuation are added to the flexline input chain in Fig. 3.13 at the 20 mK stage. In practice, this can be done either by continuing to use the installed flexline and adding SMA connectorized attenuators on top of it, or by creating a new flexline with another 3×5 dB unit cells of integrated attenuators. For reasons of quick feasibility, the first option is chosen in the upcoming simulation. At the 20 mK temperature stage, there is overall now 35 dB of attenuation, which was argued in Section 1.5.6 to be acceptable for a handful of simultaneously controlled qubits. For all integrated flexline attenuators (SMA attenuators) in the chain, the same parameters $\tilde{C}_{\mathrm{el}}$ and τ_{cool} ($\tilde{C}^{(2)}_{\mathrm{el}}$ and $\tau^{(2)}_{\mathrm{cool}}$) as in Section 3.4.3 are used.[2]

[2] Despite their different attenuation, the same parameters are chosen for the additional 10 dB and 5 dB SMA attenuators.

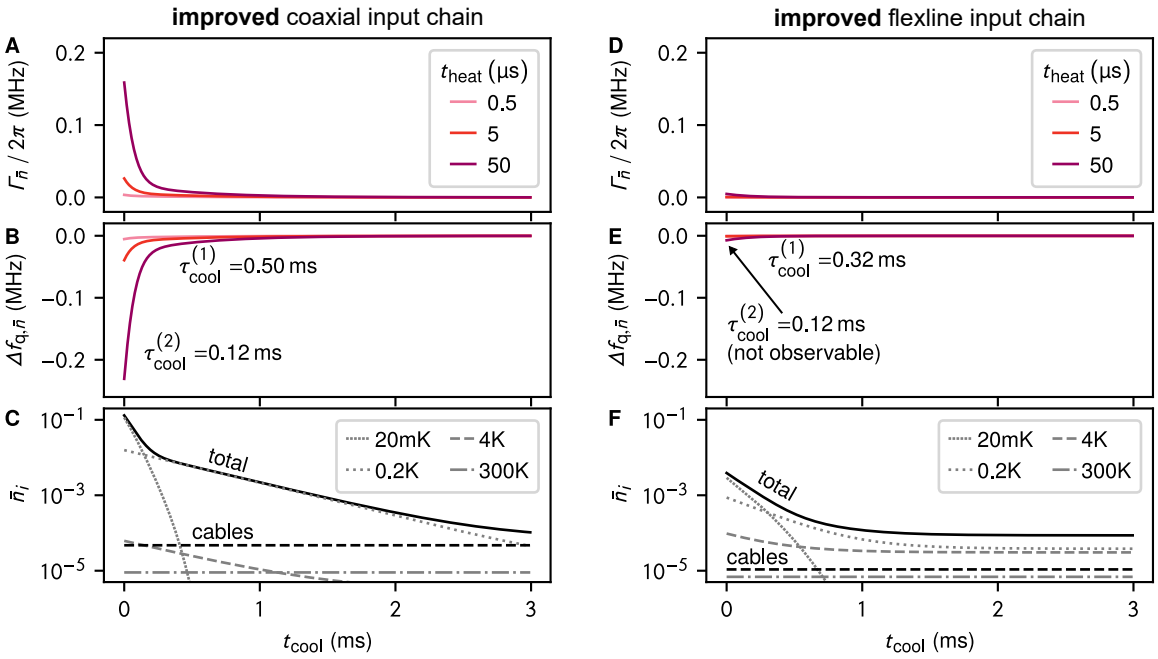

Figure 3.15: Prediction of the extended thermal model for the improved coaxial and flexline input chains. **(A)** Simulated photon shot noise-induced dephasing rates $\Gamma_{\bar{n}}$ as well as **(B)** qubit frequency shifts $\Delta f_{q,\bar{n}}$ for the improved coaxial input chain and for three different heating scenarios with the same input power $P_{in} = 2.5\,\text{mW}$ as in Fig. 3.14, and heating durations t_{heat} as labeled in the legend. All curves used common relaxation times $\tau^{(1)}_{cool} = 0.50\,\text{ms}$ for the coaxial attenuators on the 0.2 K or 4 K stage and $\tau^{(2)}_{cool} = 0.12\,\text{ms}$ on the 20 mK stage, for all heat pulse scenarios. **(C)** Contributions $\bar{n}_i$ from different temperature stages and the cables (dashed black line) to the total thermal photon shot noise $\bar{n}$ (solid black line), according to Eq. (3.14), for the longest heat pulse ($t_{heat} = 50\,\mu\text{s}$). **(D)** Simulated photon shot noise-induced dephasing rates $\Gamma_{\bar{n}}$ as well as **(E)** qubit frequency shifts $\Delta f_{q,\bar{n}}$ for the improved flexline input chain after the same three heating scenarios. All curves used common relaxation times $\tau^{(1)}_{cool} = 0.32\,\text{ms}$ and $\tau^{(2)}_{cool} = 0.12\,\text{ms}$ for all heat pulse scenarios, the latter of which is not yet visible at these powers. **(F)** Contributions $\bar{n}_i$ from different temperature stages and the cables (dashed black line) to the total thermal photon shot noise $\bar{n}$ (solid black line), according to Eq. (3.14), for the longest heat pulse ($t_{heat} = 50\,\mu\text{s}$).

- **Improved** coaxial input chain:
  For a fair comparison between the two improved setups in terms of heat load on the dilution stage, an equal total attenuation on the 20 mK stage is enforced. To achieve this, 15 dB of attenuation are shifted from the 4 K stage to the 20 mK stage. This leaves a 5 dB attenuator at the 4 K stage and results in an additional 10 dB and 5 dB attenuator at the 20 mK stage (the same as for the improved flexline setup).[3]

In Fig. 3.15, the prediction from the extended thermal model for both of these improved input chains is illustrated. The same signal power $P_{in} = 2.5\,\text{mW}$ entering the cryostat to heat up the attenuators in the input chains as in the original cases in Section 3.4.3 is assumed. For both improved input chains, a significant reduction in total passive heat load is observed, down to values of 7.1×10^{-5} and 8.7×10^{-5} photons for the improved coaxial

[3] In practice, 5 dB coaxial attenuators are somewhat rare, such that probably 3 dB or 6 dB attenuators would be used as an approximation.

chain and flexline chain, respectively. Whilst the difference in total thermal photon shot noise in both of the improved setups is only marginal, the contributions from different temperature stages and the cables differ considerably. In case of the improved coaxial input chain, the contribution of the cables is $n_{\text{cables}} = 4.7 \times 10^{-5}$ and constitutes more than half of the total shot noise. The remaining part is mainly due to blackbody radiation from the 0.2 K stage (cf. large t_{cool} in Fig. 3.15C). For the improved flexline input chain, the situation looks significantly different. Here, the contribution of the cables is only $n_{\text{cables}} = 1.1 \times 10^{-5}$, which is almost negligible for the total shot noise. Instead, both the 0.2 K and the 4 K stage are almost equally dominating sources of passive heat load (cf. large t_{cool} in Fig. 3.15F).

Another remarkable difference between the two improved input chains lies in the resulting excess thermal photon shot noise or active heat load. While almost the same levels of active heat load, and with it photon shot noise-induced dephasing rates and qubit frequency shifts, are observed in the case of the coaxial input chain after the improvement (cf. $t_{\text{cool}} \rightarrow 0$ in Fig. 3.15A-C and Fig. 3.4.3A-C), the active heat load is reduced by more than an order of magnitude in case of the improved flexline input chain (cf. $t_{\text{cool}} \rightarrow 0$ in Fig. 3.15D-F and Fig. 3.4.3D-F). In terms of active heat load, the improved flexline input chain shows a clear advantage over the improved coaxial input chain. Finally, it should be noted that, to further reduce the photon shot noise by a factor of 10, an additional 10 dB attenuator would need to be integrated on the 20 mK stage, provided that the existing cooling power of the cryostat permits this. The second-best option would be to implement a 10 dB attenuator on the 0.2 K stage, which would likely lead to only a limited improvement, as the photon shot noise from this stage itself would not be attenuated to the same extent as that from the 4 K stage.

4 Conclusion & Outlook

This chapter summarizes the key findings presented in the manuscript and discusses directions for future research. The focus lies on three main subjects, starting with the analysis of existing Purcell loss models and proposals for follow-up experiments. Then, the first main result is presented, the unveiling of inductive loss as the limiting factor of several grAl fluxoniums at their lowest frequencies, together with an outlook on the possible future of grAl in such circuits. The second key finding, that flexible striplines do not negatively impact qubit performance and exhibit better thermalization properties than coaxial cables, is discussed in the end with prospects of the role that flexible striplines will play for ever-growing quantum processors and detector arrays.

Manuscript Summary

In general, the present work primarily addresses the loss mechanisms and noise sources of fluxonium qubits based on the disordered superconductor granular aluminum (grAl) in a 2D coplanar waveguide (CPW) architecture.

Chapter 1 explores decoherence in fluxonium qubits, offering alternative derivations of dielectric and inductive loss rates using the quantum fluctuation-dissipation theorem (QFDT) instead of the Caldeira-Leggett model. While both yield similar results, QFDT provides deeper microscopic insight via the susceptibility function. The Purcell loss derivation from Refs. [37, 171, 180] is revisited, addressing two key assumptions in prior models: (1) coupling operators should be individually Hermitian, and (2) the resonator linewidth should be frequency-dependent, $\kappa(\omega)$, to reflect the qubit's flux-dependent frequency. A semi-classical model supports this refinement, showing significant differences at low qubit frequencies near the half-flux sweet spot.

In Chapter 2 the first part of the key experimental findings is discussed. For the first time, grAl fluxonium qubits in a 2D CPW architecture were fabricated and characterized. The switch to this architecture was originally motivated by the desire to test relatively rare concepts at the time, such as a fast-flux qubit control line or a normal metal ground plane. The local fast-flux line is appealing because, unlike an external off-chip coil, it allows for rapid ramps of the magnetic flux penetrating the fluxonium loop. This opens up several interesting experimental possibilities, such as active fast-flux reset or quantum Szilard engine [8] spectroscopy. Unfortunately, while testing the implemented fast-flux lines, the problem of flux delays was encountered (Section 2.4.2), which significantly complicated

the use of adiabatic flux pulses in the latest design generation. The normal metal ground plane is motivated by its potential use as a so-called phonon trap to counteract the high values of excess quasiparticle densities commonly observed in superconducting quantum circuits due to high-energy impacts [123, 163, 193, 196–204]. The main result of the qubit characterizations is presented in Section 2.5, where energy relaxation was investigated as a function of the magnetic flux bias for three representative grAl fluxoniums with comparatively low qubit frequencies $f_q < 300\,\mathrm{MHz}$ at their half-flux bias points. It was found that all three qubits near their half-flux sweet spot are limited by inductive loss with an inductive loss tangent consistent with previously measured single-photon internal quality factors $Q_i \sim 10^5 - 10^6$ of grAl resonators [123, 232]. Overall, all three energy relaxation vs. flux profiles can be well described by a combination of inductive, dielectric, and Purcell loss. A comparison of these datasets with other qubit implementations from literature in Section 2.6 indicates that the limitation of grAl by inductive loss at low qubit frequencies is so far of universal nature. This contrasts with fluxonium qubits with Josephson junction array (JJA) based superinductors, which typically do not exhibit inductive loss limitations at frequencies more than an order of magnitude lower [171].

Chapter 3 deals with the thermalization of microwave input chains based on flexible striplines. These microwave lines, also referred to as "flexlines", can be packed significantly denser compared to conventional coaxial cables, without thermally overloading the cryostat. This work focused on the question of how flexlines affect qubit performance and whether quantitative statements about the thermalization of flexlines can be made. To address these questions, one of the samples examined in detail in Chapter 2 was selected. A comparison of the qubit temperature and qubit decoherence between a setup with a flexline input chain and a setup with a coaxial cable input chain showed no significant differences within the typical fluctuations from cooldown to cooldown. Furthermore, to investigate the passive heat load, the photon shot noise-induced dephasing of the qubit was monitored over several hours in a separate measurement. This dephasing is equally large in both setups and can be translated into a residual population of about 2×10^{-3} photons in the resonator, which is in the lower range of what is commonly observed in the literature [9, 192, 223–229]. To investigate the thermalization of the two microwave input chains, a strong heating pulse was coupled into them. This pulse internally heats the built-in attenuators of the chains, causing them to emit more blackbody radiation due to their increased temperature. This active heat load is measurable in a subsequent Ramsey experiment as both additional dephasing and a frequency shift of the qubit. The heating pulse methodology presented here can serve as an easy health check for other groups to test the thermalization of their input chains. For the flexline setup, a thermalization time constant of 0.28 ms was found using a simple blackbody model of the microwave input chain. A comparison measurement with the coaxial setup resulted in a time constant about twice as long, indicating that the flexline integrated attenuators are at least as well thermalized as the SMA connectorized coaxial attenuators. Finally, an extended thermal model was developed to gain a better understanding of how the measured values for passive and active heat load from the various attenuators in the input chains are composed. For this purpose, the attenuation through the built-in cable sections was also considered,

which can contribute a non-negligible share depending on the implementation. The model also helped in proposing improved coaxial and flexline input chains.

Follow-Up Experiments on Purcell Loss Models

In Section 1.5.3, a frequency-dependent resonator linewidth $\kappa(\omega)$ to describe the coupling strength between resonator-fluxonium and the transmission line was motivated with a semi-classical model. As shown in Fig. 1.10, the difference between a constant and a frequency-dependent linewidth becomes more pronounced the further the qubit is detuned from the resonator. Since the qubit frequency ω_q at zero-flux in typical fluxonium implementations only differs from the resonator frequency ω_r by a factor of the order of 1, only the half-flux sweet spot remains as an interesting point to study the difference between the models. In recent years, there has been an increased interest in so-called heavy fluxoniums [171, 286, 287], which have a particularly low frequency at their half-flux sweet spot. Fluxoniums in this parameter regime would be particularly suitable for clarifying the question of which model accurately describes Purcell loss. However, fluxoniums with grAl-based superinductors are only limitedly suitable for this, as they are already limited by the observed inductive loss at low frequencies. Therefore, JJA-based fluxoniums, which show no signs of such limitation even in the case of heavy fluxoniums, present an interesting possibility. Thus, it would be interesting to deliberately produce JJA-based fluxoniums limited by Purcell loss with low qubit frequency at the half-flux sweet spot to determine whether the hypothesis of a frequency-dependent linewidth holds true.

From another perspective, due to the steadily increasing understanding and the associated reductions in dielectric and inductive losses, ever higher energy relaxation times T_1 are to be expected for future fluxonium qubits. At some point, Purcell loss at the half-flux sweet spot will become the limiting factor, so the insights from Section 1.5.3 contribute to further improvement. In this context, it is particularly noteworthy that the various combinations of coupling between fluxonium and resonator and between resonator and transmission line have a strong influence on Purcell loss (Fig. 1.10). For future Purcell loss-limited fluxoniums, a switch to capacitive fluxonium-resonator coupling in combination with inductive coupling of the resonator to the transmission line predicts exceptionally low Purcell loss (Fig. 1.10B) and could represent an alternative pathway to the current efforts in Purcell filtering.

Outlook on Granular Aluminum Fluxonium Qubits

As described in Section 1.3.3, grAl comes on the one hand with several advantages, such as its nonlinearity spanning many orders of magnitude, its intrinsically high plasma frequency [120], and its insensitivity to magnetic fields up to 1 T [288]. This makes grAl an attractive candidate for superconducting quantum circuits. On the other hand, grAl also has inductive losses of yet unknown origin, which are of the same order of magnitude for both grAl resonators [123, 232] and the grAl fluxoniums investigated here (Section 2.5). To use grAl as a material for superinductors in low-frequency qubits in the future, it is

therefore necessary to understand the microscopic cause of the inductive losses in order to potentially eliminate them.

In the recent years, large progress has been made in the investigation of environments which limit the energy relaxation in grAl based fluxonium qubits. This includes on the one hand the heating and cooling of a long-lived two-level system (TLS) environment, that constitutes the main loss mechanism for the fluxonium qubit, within the framework of a quantum Szilard engine [8]. On the other hand, a grAl nanojunction qubit (gralmonium) was shown to be limited by a paramagnetic spin-1/2 ensemble when sweeping the magnetic field such that the spins are in resonance with the qubit [174]. It could very well be that one of these two environments is also responsible for the observed inductive losses in grAl. One interesting follow-up measurement would certainly be a quantum Szilard engine spectroscopy, i.e. the operation of the Szilard engine at various qubit frequencies, which could shed more light onto the frequency distribution of the long-lived TLS environment.

Further insights might also be gained by using the more widespread and better-understood JJA-based fluxoniums found in the literature. One could produce superinductors that emulate the behavior of grAl as closely as possible by, for example, creating particularly long arrays with increased plasma frequencies. Lastly, a comparison with other disordered superconductors could also be helpful.

Perspective on Flexible Striplines in Cryogenic Microwave Setups

The results in Chapter 3 encourage the use of flexible striplines in future cryogenic microwave setups, enabling at least an order of magnitude increase in the density of microwave input circuitry. This paves the way for increasingly complex superconducting detectors and quantum devices from the perspective of microwave input chains.

With ever-increasing qubit coherence, the demands on microwave input chains will also continue to rise. Therefore, models like the extended thermal model presented in Section 3.4.2 or similar analysis software [289] could play a larger role in the future for simulating passive and active heat loads. At some point, it will certainly be helpful to consider low-temperature phenomena that counteract an efficient cooling such as the hot-electron effect [280, 281] or an increased Kapitza phonon-phonon boundary resistance [282], and to address these with optimized attenuator designs.

Appendix

A Quantum Fluctuation Dissipation Theorem

In this section, a relation between the symmetric noise spectral density $\mathcal{S}_B(\omega)+\mathcal{S}_B(-\omega)$, required for the evaluation of the qubit depolarization rate in Eq. (1.58), and the susceptibility $\chi_{AB}(\omega)$ is derived. We consider two typical bath models:

- **Bosonic bath**
  A bosonic bath, such as a collection of harmonic oscillators or the electromagnetic field, is described by
  $$\hat{H}_\mathrm{B} = \sum_k \hbar\omega_k \hat{b}_k^\dagger \hat{b}_k, \tag{A1}$$
  where $\hat{b}_k^\dagger$ ($\hat{b}_k$) are bosonic creation (annihilation) operators. In thermal equilibrium, the bath density matrix is given by $\bar{\rho}_\mathrm{B} = e^{-\beta\hat{H}_\mathrm{B}}/\mathrm{Tr}\{e^{-\beta\hat{H}_\mathrm{B}}\}$, with $\beta = 1/k_\mathrm{B}T$, and the occupation numbers follow the Bose-Einstein distribution $n_\mathrm{B}(\omega_k) = (\exp(\beta\hbar\omega_k) - 1)^{-1}$.
- **TLS bath**
  A bath of two-level systems (TLSs) is described by
  $$\hat{H}_\mathrm{B} = \sum_k \frac{\hbar\omega_k}{2}\hat{\sigma}_{z,k}, \tag{A2}$$
  where $\hat{\sigma}_{z,k}$ is a Pauli operator. In thermal equilibrium, the occupation probabilities are given by the canonical ensemble. In the following, TLSs are treated as independent degrees of freedom.

We assume a general Hermitian bath coupling operator of the form

$$\hat{B} = \sum_k (g_k \hat{b}_k + g_k^* \hat{b}_k^\dagger) \tag{A3}$$

for a bosonic bath, or analogously

$$\hat{B} = \sum_k (g_k \hat{\sigma}_k^- + g_k^* \hat{\sigma}_k^+) \tag{A4}$$

for a TLS bath. This form is sufficient to describe the considered noise channels, since charge- and phase-like operators can be expanded in terms of ladder operators.

The corresponding bath correlation function reads

$$C(\tau) = \langle \hat{B}(\tau)\hat{B}(0)\rangle_{\bar{\rho}_\mathrm{B}} = \sum_k |g_k|^2 \begin{cases} (1+n_\mathrm{B}(\omega_k))e^{-i\omega_k\tau} + n_\mathrm{B}(\omega_k)e^{i\omega_k\tau} & \text{for bosonic,} \\ (1-p_k)e^{-i\omega_k\tau} + p_k e^{i\omega_k\tau} & \text{for TLS} \end{cases} \tag{A5}$$

baths, respectively, where p_k denotes the occupation probability of the excited state of the k-th TLS. In thermal equilibrium, this occupation follows a distribution formally equivalent to the Fermi–Dirac distribution, $p_k = (\exp(\beta\hbar\omega_k) + 1)^{-1}$. The susceptibility is related to the commutator of bath operators via the Kubo formula [290],

$$\chi_{AB}(\tau) = \frac{i}{\hbar}\,\theta(\tau)\,\langle[\hat{B}(\tau), \hat{B}(0)]\rangle_{\bar{\rho}_\mathrm{B}}, \tag{A6}$$

which holds independently of the specific bath statistics. Taking the Fourier transform, the imaginary part of the susceptibility becomes

$$\mathrm{Im}[\chi_{AB}(\omega)] = \frac{1}{2\hbar}\int_{-\infty}^{\infty} [C(\tau) - C(-\tau)]\, e^{i\omega\tau}\, d\tau = \frac{1}{2\hbar}\,[\mathcal{S}_B(\omega) - \mathcal{S}_B(-\omega)]\,. \tag{A7}$$

For a bosonic bath, evaluation of Eq. (A5) yields the detailed balance relation

$$\frac{\mathcal{S}_B(\omega) - \mathcal{S}_B(-\omega)}{\mathcal{S}_B(\omega) + \mathcal{S}_B(-\omega)} = \tanh\!\left(\frac{\beta\hbar\omega}{2}\right), \tag{A8}$$

and correspondingly

$$\mathcal{S}_B(\omega) + \mathcal{S}_B(-\omega) = 2\hbar\,\mathrm{Im}[\chi_{AB}(\omega)]\coth\!\left(\frac{\beta\hbar\omega}{2}\right). \tag{A9}$$

For a TLS bath, assuming an ensemble of independently fluctuating TLSs with a symmetric distribution of occupation probabilities, the symmetric spectral density becomes effectively frequency-dependent but does not acquire an additional thermal factor. In this case,

$$\mathcal{S}_B(\omega) + \mathcal{S}_B(-\omega) = 2\hbar\,\mathrm{Im}[\chi_{AB}(\omega)]. \tag{A10}$$

Combining both cases, one obtains the compact relation

$$\mathcal{S}_B(\omega) + \mathcal{S}_B(-\omega) = 2\hbar\,\mathrm{Im}[\chi_{AB}(\omega)] \times \begin{cases} \coth\!\left(\frac{\beta\hbar\omega}{2}\right) & \text{for bosonic,} \\ 1 & \text{for TLS} \end{cases} \tag{A11}$$

baths, respectively, which is used in Section 1.5 to derive Eq. (1.60).

B Full Derivation of Purcell Loss with the Open Quantum System Model

In this Appendix, the full derivation of Purcell loss on the basis of an open quantum system model, as discussed in Section 1.5.3 and similar to Refs. [37, 171, 180], is presented. With the interaction Hamiltonian in Eq. (1.80), the full Hamiltonian in Eq. (1.79) of the open quantum system consisting of a system (S) and a bath (B) would be rewritten to

$$\hat{H} = \underbrace{\sum_k E_k^{\mathrm{S}} |\psi_k^{\mathrm{S}}\rangle\langle\psi_k^{\mathrm{S}}|}_{\hat{H}_{\mathrm{S}}} + \underbrace{\sum_k \hbar\omega_k \hat{b}_k^\dagger \hat{b}_k}_{\hat{H}_{\mathrm{B}}} + \underbrace{\sum_k \hbar\lambda_k \left[(\hat{a}_{\mathrm{r}}^\dagger \pm \hat{a}_{\mathrm{r}})\hat{b}_k^\dagger \pm (\hat{a}_{\mathrm{r}}^\dagger \pm \hat{a}_{\mathrm{r}})\hat{b}_k \right]}_{\hat{H}_{\mathrm{I}}}, \tag{B1}$$

where $\hat{a}_{\mathrm{r}}^\dagger$ ($\hat{a}_{\mathrm{r}}$) is the system creation (annihilation) operator, and $\hat{b}_k^\dagger$ ($\hat{b}_k$) is the creation (annihilation) operator of the k-th bosonic bath mode. $\lambda_k \in \mathbb{R}$ quantifies the coupling strength. $|\psi_k^{\mathrm{S}}\rangle$ and E_k^{S} represent the eigenstates and corresponding eigenenergies of the resonator-qubit system, respectively. Positive (negative) signs in the interaction Hamiltonian correspond to inductive (capacitive) coupling between the resonator-qubit system and the transmission line. According to Fermi's golden rule, the transition rate $\gamma_{\mathrm{i}\to\mathrm{f}}$ from an initial state $|\psi_{\mathrm{i}}\rangle = |\psi_{\mathrm{i}}^{\mathrm{S}}\rangle \otimes_k |m_k\rangle$ to a final state $|\psi_{\mathrm{f}}\rangle = |\psi_{\mathrm{f}}^{\mathrm{S}}\rangle \otimes_k |m_k'\rangle$, both of which are eigenstates of $\hat{H}_{\mathrm{S}} + \hat{H}_{\mathrm{B}}$ with eigenenergies E_{i} and E_f, respectively, is given by

$$\gamma_{\mathrm{i}\to\mathrm{f}} = \frac{2\pi}{\hbar}\delta(E_{\mathrm{i}} - E_{\mathrm{f}})|\langle\psi_{\mathrm{f}}|\hat{H}_{\mathrm{I}}|\psi_{\mathrm{i}}\rangle|^2. \tag{B2}$$

Insertion of the interaction Hamiltonian $\hat{H}_{\mathrm{I}}$ from Eq. (B1) into Eq. (B2) yields

$$\begin{aligned}\gamma_{\mathrm{i},\{m_k\}\to\mathrm{f},\{m_k'\}} = \frac{2\pi}{\hbar}\delta(E_{\mathrm{i}} - E_{\mathrm{f}}) \sum_k \hbar^2|\lambda_k|^2 |\langle\psi_{\mathrm{f}}^{\mathrm{S}}|\hat{a}_{\mathrm{r}}^\dagger \pm \hat{a}_{\mathrm{r}}|\psi_{\mathrm{i}}^{\mathrm{S}}\rangle|^2 \\ \times \left(m_k\delta_{m_k',m_k-1} + (m_k+1)\delta_{m_k',m_k+1} \right) \prod_{k=k'} \delta_{m_{k'}',m_{k'}}.\end{aligned} \tag{B3}$$

The next step consists in writing the full system's eigenenergies as $E_{\mathrm{i}} = E_{\mathrm{i}}^{\mathrm{S}} + \hbar\sum_{m_k} m_k\omega_k$ and $E_{\mathrm{f}} = E_{\mathrm{f}}^{\mathrm{S}} + \hbar\sum_{m_k'} m_k'\omega_k$, and summing over all initial and final states of the bath, thereby weighing initial states by their probability of occurrence, $P(\{m_k\}) = \exp\left(-\sum_k \beta\hbar m_k\omega_k\right)/Z$, to receive the total transition rate

$$\begin{aligned}\Gamma_{\mathrm{i}\to\mathrm{f}} =& \sum_{\{m_k\},\{m_k'\}} P(\{m_k\})\gamma_{\mathrm{i},\{m_k\}\to\mathrm{f},\{m_k'\}} \\ =& 2\pi\hbar \sum_{\{m_k\},\{m_k'\}} P(\{m_k\})\delta\left(E_{\mathrm{i}}^{\mathrm{S}} - E_{\mathrm{f}}^{\mathrm{S}} + \hbar\sum_l (m_l - m_l')\omega_l\right) \\ & \times \sum_k |\lambda_k|^2 |\langle\psi_{\mathrm{f}}^{\mathrm{S}}|\hat{a}_{\mathrm{r}}^\dagger \pm \hat{a}_{\mathrm{r}}|\psi_{\mathrm{i}}^{\mathrm{S}}\rangle|^2 \left(m_k\delta_{m_k',m_k-1} + (m_k+1)\delta_{m_k',m_k+1} \right) \prod_{k=k'} \delta_{m_{k'}',m_{k'}} \\ =& 2\pi\hbar \sum_k |\lambda_k|^2 |\langle\psi_{\mathrm{f}}^{\mathrm{S}}|\hat{a}_{\mathrm{r}}^\dagger \pm \hat{a}_{\mathrm{r}}|\psi_{\mathrm{i}}^{\mathrm{S}}\rangle|^2 \\ & \times \left[\delta(E_{\mathrm{i}}^{\mathrm{S}} - E_{\mathrm{f}}^{\mathrm{S}} - \hbar\omega_k)(n_{\mathrm{B}}(\omega_k) + 1) + \delta(E_{\mathrm{i}}^{\mathrm{S}} - E_{\mathrm{f}}^{\mathrm{S}} + \hbar\omega_k)n_{\mathrm{B}}(\omega_k) \right],\end{aligned} \tag{B4}$$

where the average thermal population $n_\mathrm{B}(\omega_k) = \sum_{\{m_j\}} P(\{m_j\}) m_k = (\exp(\beta\hbar\omega_k) - 1)^{-1}$ of the k-th bosonic bath mode was introduced. Lastly, the continuum limit is taken by equating the coupling strengths $|\lambda_k|^2$ and density of states $\rho(\omega_k)$ of all bath modes into a frequency-independent linewidth $\kappa = 2\pi\hbar\rho(\omega_k)|\lambda_k|^2$ and introduce $\omega_\mathrm{fi} = (E_\mathrm{f}^\mathrm{S} - E_\mathrm{i}^\mathrm{S})/\hbar$ to obtain

$$\Gamma_{\mathrm{i}\to\mathrm{f}} = \kappa|\langle\psi_\mathrm{f}^\mathrm{S}|\hat{a}_\mathrm{r}^\dagger \pm \hat{a}_\mathrm{r}|\psi_\mathrm{i}^\mathrm{S}\rangle|^2 \left[\theta(-\omega_\mathrm{fi})(n_\mathrm{B}(-\omega_\mathrm{fi}) + 1) + \theta(\omega_\mathrm{fi}) n_\mathrm{B}(\omega_\mathrm{fi})\right], \tag{B5}$$

where $\theta(\omega)$ denotes the Heaviside step function. The first term in square brackets in Eq. (B5) applies only in the case of downward transitions or emission ($E_\mathrm{f}^\mathrm{S} < E_\mathrm{i}^\mathrm{S}$), while the second term applies only in the case of upward transitions or absorption ($E_\mathrm{f}^\mathrm{S} > E_\mathrm{i}^\mathrm{S}$). In principle, both processes can be summarized in the total relaxation rate

$$\Gamma_{1,\mathrm{i}\to\mathrm{f}} = \kappa|\langle\psi_\mathrm{f}^\mathrm{S}|\hat{a}_\mathrm{r}^\dagger \pm \hat{a}_\mathrm{r}|\psi_\mathrm{i}^\mathrm{S}\rangle|^2 (2n_\mathrm{B}(\omega_\mathrm{fi}) + 1) = \kappa|\langle\psi_\mathrm{f}^\mathrm{S}|\hat{a}_\mathrm{r}^\dagger \pm \hat{a}_\mathrm{r}|\psi_\mathrm{i}^\mathrm{S}\rangle|^2 \coth\left(\frac{\beta\hbar\omega_\mathrm{fi}}{2}\right). \tag{B6}$$

As argued in Refs. [171, 180], primarily transitions between fluxonium states are of interest, while exact knowledge about the resonator state is usually missing. Therefore, it makes sense to denote the dressed eigenstates of the resonator-qubit system in the form $|\psi^\mathrm{S}\rangle = |\overline{n_\mathrm{r}, n_\mathrm{q}}\rangle$ with the indices r and q referring to the resonator and qubit state, respectively. As outlined in Section 1.3.4, associating such a dressed eigenstate with quantum numbers n_r and n_q is valid, when the overlap between a dressed eigenstates and a product state $|n_\mathrm{r}, n_\mathrm{q}\rangle = |n_\mathrm{r}\rangle \otimes |n_\mathrm{q}\rangle$ is large, which is always justified, except in the vicinity of an avoided level crossing. For the average total relaxation rate, in which only the fluxonium state n_q changes, all possible initial states $n_\mathrm{r,i}$ and final states $n_\mathrm{r,f}$ of the resonator need to be averaged over, thereby weighting each transition by the probability, that an initial resonator state is thermally occupied, $P(n_\mathrm{r,i}) = [1 - \exp(-\hbar\omega_\mathrm{r}/k_\mathrm{B}T_\mathrm{r})] \exp(-\hbar\omega_\mathrm{r} n_\mathrm{r,i}/k_\mathrm{B}T_\mathrm{r})$. With this, Eq. (B5) yields

$$\Gamma_{1,n_\mathrm{q,i}\to n_\mathrm{q,f}} = \sum_{n_\mathrm{r,i}, n_\mathrm{r,f}} P(n_\mathrm{r,i}) \kappa |\langle\overline{n_\mathrm{r,f}, n_\mathrm{q,f}}|\hat{a}_\mathrm{r}^\dagger \pm \hat{a}_\mathrm{r}|\overline{n_\mathrm{r,i}, n_\mathrm{q,i}}\rangle|^2 \coth\left(\frac{\beta\hbar\omega_\mathrm{fi}}{2}\right). \tag{B7}$$

The evaluation of this sum is a somewhat cumbersome task, but fortunately with resonator frequencies of $\sim 5\,\mathrm{GHz}$, $P(n_\mathrm{r,i})$ falls off very rapidly with $n_\mathrm{r,i}$, such that even $P(n_\mathrm{r,i} = 1)$ is negligibly small for temperatures $T_\mathrm{r} < 200\,\mathrm{mK}$ of the resonator. Thus, the sum over $n_\mathrm{r,i}$ in Eq. (B7) can be removed, yielding

$$\Gamma_{1,n_\mathrm{q,i}\to n_\mathrm{q,f}} = \sum_{n_\mathrm{r,f}} \kappa |\langle\overline{n_\mathrm{r,f}, n_\mathrm{q,f}}|\hat{a}_\mathrm{r}^\dagger \pm \hat{a}_\mathrm{r}|\overline{0, n_\mathrm{q,i}}\rangle|^2 \coth\left(\frac{\beta\hbar\omega_\mathrm{fi}}{2}\right), \tag{B8}$$

which is the relationship shown in Eq. (1.82).

C Detailed Fabrication Steps for grAl Fluxonium Qubits

#	description	parameters
1	EL-13 spin coating	ramp: 1000 rpm/s, speed: 2000 rpm, time: 100 s, baking: 200 °C, 5 min → thickness ~ 950 nm
2	A-4 spin coating	ramp: 1000 rpm/s, speed: 2000 rpm, time: 100 s, baking: 200 °C, 5 min → thickness ~ 200 nm
3	gold sputtering	
4	e-beam writing (JOEL 50 keV)	
5	gold removal	Lugol solution 15 %, 10 s
6	development	IPA / H_2O 3:1 @ 6 °C, 90 s, slightly move wafer
7	e-beam evaporation (PLASSYS)	
	1. plasma descum	O_2/Ar: 10/5 sccm, 2 min, voltage: 200 V, current: 10 mA
	2. getter pumping	titanium evap. with shutter closed, 0.2 nm/s, 2 min
	3. Al evaporation	1.0 nm/s, tilt: −31°, 20 nm
	4. junction oxidation	20 mbar, 4 min (~ 40 s needed to reach pressure)
	5. Al evaporation	1.0 nm/s, tilt: 31°, 30 nm
	6. argon milling	Ar 4 sccm, 1 min, voltage: 400 V, current: 15 mA
	7. grAl evaporation	1.0 nm/s, O_2 4.9-5.0 sccm, tilt: 0°, 35-40 nm
8	lift-off	N-Ethyl-2-pyrrolidone (NEP) @ 90 °C, 90 min additional 3 min in ultrasonic bath rinsing in IPA and ethanol

Table 1: Fabrication steps for electron-beam lithography (EBL) of grAl fluxonium qubits. The process includes resist spinning, e-beam writing, plasma cleaning, and three-angle Al/Al/grAl deposition. Some parameters were varied over different samples, for details see Table 3.

#	description	parameters
1	AZ 5214E coating	ramp: 2000 rpm/s, speed: 4000 rpm, time: 60 s, baking: 110 °C, 50 s → thickness ~ 1.4 µm
2	UV exposure	hard mask exposure: 2.0 mW/cm^2 for 12 s reverse baking: 120 °C for 60 s flood exposure: 2.0 mW/cm^2 for 30 s
3	development	AZ developer / H_2O 3:2 for 60 s rinsing in deionized water
4	e-beam evaporation (PLASSYS)	
	1. plasma descum	O_2/Ar: 10/5 sccm, 2 min, voltage: 200 V, current: 10 mA
	2. getter pumping	titanium evap. with shutter closed, 0.2 nm/s, 2 min
	3. argon milling	Ar 4 sccm, 3 min, voltage: 400 V, current: 15 mA
	4a. Nb + Al evaporation	1.0 nm/s each, tilt: 0°, 3 × 15 nm Nb + 5 nm Al
	4b. Nb + Ag evaporation	1.0 nm/s + (1.0 or 2.5) nm/s, tilt: 0°, 4 nm Nb + 100 nm Ag
5	lift-off	N-Ethyl-2-pyrrolidone (NEP) @ 90 °C, 90 min additional 3 min in ultrasonic bath rinsing in IPA and ethanol

Table 2: Fabrication steps for optical lithography of ground planes. The process includes resist spinning, UV exposure with hard mask, plasma cleaning, and a Nb + Al deposition for the first optically defined layer of superconducting ground plane, and a Nb + Ag deposition for the second optically defined layer of normal metal ground plane. Some parameters were varied over different samples, for details see Table 3.

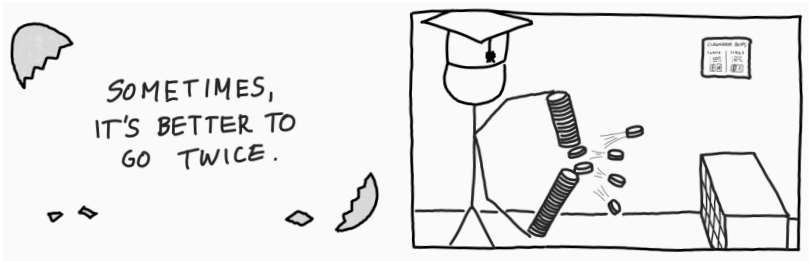

D Overview of Fabricated Wafers

#	label	G	fabrication details			resistance tests	
			EBL	OL_1	OL_2	$R_{\square,\mathrm{grAl}}$ (Ω)	$R_{\mathrm{JJ}}A_{\mathrm{JJ}}$ (Ω µm²)
12	**KC1507**	1	20/30 nm Al (±31°) 6 min @ 20 mbar 40 nm grAl (0°, 5.2 sccm)			-	-
14	KC1501	1	20/30 nm Al (±31°) 6 min @ 25 mbar 40 nm grAl (0°, 5.1 sccm)	-	-	-	728 ± 78
19	KC1311	1	20/30 nm Al (±32°) 6 min @ 25 mbar 40 nm grAl (0°, 4.3 sccm)	15 nm Nb (before EBL)	70 nm Ag	48 ± 4	-
26	KC1309	1	20/30 nm Al (±32°) 6 min @ 25 mbar 40 nm grAl (0°, 4.4 sccm)	15 nm Nb (before EBL)	-	66 ± 16	-
31	KC1548	1	20/30 nm Al (±32°) 6 min @ 25 mbar 40 nm grAl (0°, 4.6 sccm)	100 nm Al	5 nm Ti 200 nm Ag	124 ± 28	764 ± 152
32	KC1547	1	20/30 nm Al (±32°) 6 min @ 25 mbar 40 nm grAl (0°, 4.8 sccm)	100 nm Al	5 nm Ti 200 nm Ag	168 ± 18	589 ± 54
33	KC1549	1	20/30 nm Al (±32°) 6 min @ 25 mbar 40 nm grAl (0°, 5.0 sccm)	60 nm Al	5 nm Ti 100 nm Ag	245 ± 21	825 ± 200
34	**KC1550**[*)]	1	20/30 nm Al (±31°) 6 min @ 25 mbar 40 nm grAl (0°, 4.9 sccm)	60 nm Al	5 nm Ti 100 nm Ag	205 ± 38	775 ± 209
			⋮				

[*)] wafer broken during spin coating optical resist; some chips still usable

Table 3: Overview of selected wafers and corresponding fabrication parameters. Shown are wafer labels (for internal reference), the design generation (G), fabrication details for the electron beam lithography (EBL) and the first and second optical lithography steps ($OL_{1/2}$), as well as measured resistance values from test structures patterned with the EBL step. Details about the EBL step include layer thicknesses, deposition angles, static oxidation parameters, and oxygen flow during the three-angle evaporation. For the $OL_{1/2}$ steps, materials and layer thicknesses are listed. The resistance tests yield values for the room-temperature sheet resistance per square of grAl, $R_{\square,\mathrm{grAl}}$, as well as the junction resistance R_{JJ}. Multiplication of the latter by the junction area A_{JJ} results in an area-independent quantity that should depend only on the oxidation parameters. Wafers with measured samples are highlighted with bold labels.

#	label	G	fabrication details			resistance tests	
			EBL	OL_1	OL_2	$R_{\square,\mathrm{grAl}}$ (Ω)	$R_{\mathrm{JJ}}A_{\mathrm{JJ}}$ (Ω µm^2)
			⋮				
37	CR001	1	20/30 nm Al (±31°) 6 min @ 25 mbar 40 nm grAl (0°, 4.9 sccm)	60 nm Al	5 nm Ti 100 nm Ag	315 ± 98	765 ± 65
39	**CR003**[**)]	1	20/30 nm Al (±31°) 6 min @ 25 mbar 40 nm grAl (0°, 4.9 sccm)	60 nm Al	5 nm Ti 100 nm Ag	355 ± 25	873 ± 95
42	**CR025**	1	20/30 nm Al (∓31°) 6 min @ 25 mbar 41 nm grAl (0°, 4.9 sccm)	60 nm Al	5 nm Ti 200 nm Ag	-	951 ± 96
44	**CR027**[***)]	1	20/25 nm Al (∓31°) 6 min @ 25 mbar 31 nm grAl (0°, 4.9 sccm)	50 nm Al	5 nm Ti 200 nm Ag	284 ± 66	1310 ± 241
51	**CR061**	2	20/30 nm Al (±31°) 4 min @ 20 mbar 40 nm grAl (0°, 5.0 sccm)	50 nm Al	5 nm Ti 200 nm Ag	317 ± 82	1226 ± 193
53	**CR066**	2	20/30 nm Al (∓31°) 4 min @ 20 mbar 40 nm grAl (0°, 4.9 sccm)	3×15 nm Nb 5 nm Al	4 nm Nb 100 nm Ag	189 ± 35	988 ± 113
56	**CR303**	2 (P)	20/30 nm Al (∓31°) 4 min @ 20 mbar 40 nm grAl (0°, 5.0 sccm)	3×15 nm Nb 5 nm Al	4 nm Nb 100 nm Ag	127 ± 10	1078 ± 213
57	**CR304**	2 (P)	20/30 nm Al (∓31°) 4 min @ 20 mbar 40 nm grAl (0°, 5.0 sccm)	3×15 nm Nb 5 nm Al	4 nm Nb 100 nm Ag	400 ± 26	876 ± 54

**) wafer fell in Lugol solution; optical layer rotated by 180°

***) optical resist first on other side; qubits not harmed, but dirt on Al ground plane

Table 4: Continuation of Table 3. '2 (P)' refers to the second design generation with Purcell filters.

E Overview of Measured Samples

cooldown	wafer	chip		f_r (GHz)	$\chi_{ge}/2\pi$ (MHz)	f_q^{HF} (GHz)	f_q^{ZF} (GHz)	L_q (nH)	C_q (fF)	E_J (GHz)	T_1 (µs)	T_2^R (µs)	T_2^E (µs)
2020-02-10 (BF)	?	? (F)	L	8.415	-40.7	2.68	13.88	120	3.99	8.57	9.7	1.5	-
2020-02-28 (BF)	?	?	L	5.140	-	5.60	6.80	180	3.70	1.00	-	-	-
	?	?	R	5.680	-	5.30	6.80	180	3.85	1.10	-	-	-
2020-04-22 (BF)	KC1507	1-1 (F)	R	4.469	-	-	-	-	-	-	-	-	-
2020-07-08 (BF)	KC1550	3-3 (F)	R	6.785	-	-	-	-	-	-	-	-	-
	KC1550	3-5	L	6.558	-	-	-	-	-	-	-	-	-
	KC1550	3-5	R	5.984	-	-	-	-	-	-	-	-	-
2020-08-27 (BF)	CR003	3-5 (F)	R	5.040	-	-	-	-	-	-	-	-	-
	CR003	1-2	L	4.576	-6.9	1.26	7.55	353	4.80	7.42	-	-	-
	CR003	1-2	R	4.928	-12.5	1.33	7.42	356	4.71	7.20	25.0	3.0	-
2020-09-20 (BF)	?	? (F)	L	4.450	-	4.87	5.64	586	1.51	4.88	-	-	-
	?	? (F)	R	4.925	-	4.58	5.81	240	3.90	1.00	-	-	-
2020-10-24 (BF)	CR003	1-2	R	4.923	-	-	-	-	-	-	20.7	4.1	4.0
2020-11-06 (BF)	CR027	1-2 (F)	L	5.301	-8	1.98	8.07	293	4.19	6.35	-	-	-
	CR027	3-3 (F)	L	5.503	-16.5	2.33	8.69	223	4.57	5.42	-	-	-
2020-11-18 (BF)	CR027	1-2 (F)	L	5.299	-	3.09	7.26	288	3.55	4.45	-	-	-
	CR027	1-2 (F)	R	5.782	-	3.12	7.22	-	-	-	-	-	-
	CR027	3-3 (F)	L	5.498	-13.7	2.40	8.71	243	4.09	5.87	22.2	3.6	6.6
	CR027	3-3 (F)	R	6.033	-	2.61	8.32	262	3.75	5.74	-	-	-
2020-12-14 (BF)	CR027	4-5	L	5.644	-	-	-	-	-	-	-	-	-
	CR027	4-5	R	6.179	-	3.63	8.10	185	4.24	3.61	14.7	3.0	5.3
2021-01-26 (BF)	CR061	4-5	L	5.625	-12	-	-	-	-	-	-	-	-
	CR061	4-5	R	5.945	-12	1.73	8.00	355	3.16	10.80	-	-	-
2021-01-30 (BF)	CR061	4-5	R	5.942	-12	1.73	-	-	-	-	11.3	1.2	3.5
2021-02-13 (BF)	CR061	4-1 (F)	L	5.578	-	-	-	-	-	-	-	-	-
	CR066	2-2 (F)	L	6.942	-7.2	0.88	12.66	193	5.64	10.64	37.9	10.1	12
	CR066	2-2 (F)	R	7.398	-6.6	0.70	13.00	191	5.84	10.99	15.0	6.9	7.8
	...												

Table 5: Overview of selected measured samples over various cooldowns. Samples were cooled down either in a *Bluefors LD400* (BF) or a *Qinu Sionludi XL* ($SL_{1/2}$) dilution refrigerator. Resonator-fluxoniums are identified via the wafer label, the chip number ('(F)' denoting the integration of a fast flux line) as well as their position on the chip (left (L) or right (R)). Shown are the resonator frequency f_r, the dispersive shift χ_{ge}, the qubit frequencies f_q^{HF} (f_q^{ZF}) at half flux (zero flux), qubit inductance L_q, capacitance C_q and Josephson energy E_J, as well as measured rates for energy relaxation (T_1), Ramsey decoherence (T_2^R) and echo decoherence (T_2^E) at half flux. Samples without fast flux line, which are plotted in Fig. 2.14, are highlighted with gold background.

cooldown	wafer	chip		f_r (GHz)	$\chi_{ge}/2\pi$ (MHz)	f_q^{HF} (GHz)	f_q^{ZF} (GHz)	L_q (nH)	C_q (fF)	E_J (GHz)	T_1 (µs)	T_2^R (µs)	T_2^E (µs)
⋮													
2021-02-26 (BF)	CR066	4-5	L	7.181	-6.5	0.97	11.84	219	4.96	10.20	40.7	8.0	11.6
	CR066	2-2 (F)	L	6.946	-7	0.88	11.87	-	-	-	13.7	6.9	-
2021-03-23 (BF)	CR066	3-4 (F)	L	6.880	-4.3	0.64	13.02	197	5.76	11.14	13.7	6.9	-
2022-01-17 (SL_1)	CR303	4-1 (F)	L	8.842	-10	0.87	-	-	-	-	-	-	-
	CR303	4-1 (F)	R	8.837	-	0.95	-	-	-	-	-	-	-
	CR304	2-3 (F)	L	4.367	-3.6	0.41	6.92	453	3.74	20.92	-	-	-
	CR304	2-3 (F)	R	4.322	-5.2	0.46	6.80	458	3.57	20.94	-	-	-
2022-08-23 (BF)	?	? (F)	L	4.689	-	0.57	7.01	422	5.75	9.65	8.0	-	-
2023-01-06 (SL_2)	CR304	3-4 (F)	L	4.392	-1.6	0.25	7.09	432	6.60	12.25	2.6	0.3	0.1
	CR304	3-4 (F)	R	4.410	-1.8	0.25	6.99	436	7.15	11.06	2.4	-	-
2023-02-18 (SL_2)	CR304	3-4 (F)	L	4.404	-1.5	0.25	7.09	440	5.19	17.36	2.3	-	-
	CR304	3-4*) (F)	R	4.884	-2.5	0.25	6.98	444	5.75	14.93	-	-	-
2024-02-07 (SL_1)	CR066	2-2 (F)	R	7.455	-2.7	0.28	16.51	176	6.48	14.60	2.2	3.6	4.3
	CR304	3-4 (F)	L	4.388	-1.7	0.24	7.11	424	8.13	9.60	-	-	-
	CR304	3-4*) (F)	R	4.843	-2.2	0.24	6.99	446	5.42	16.59	1.5	0.8	1.7
2024-07-03 (SL_1)	CR304	1-3 (F)	L	4.480	-	0.18	6.74	470	4.93	24.24	-	-	-

*) resonator capacitance was laser trimmed

Table 6: Continuation of Table 5. Samples 1 (pink), 2 (magenta) and 3 (red) from Section 2.5 are highlighted with a respectively colored background.

F Cooldown Performance of Magnetic Shields

This final appendix section is dedicated to the results of a side project investigating the cooldown dynamics of magnetic shields. The usefulness of such shields was discussed in detail in Section 2.2. The shields should have a minimum layer thickness to attenuate external magnetic fields, which, however, introduces significant additional heat capacity that must be cooled down. The cooldown of the shields is further complicated by the fact that mu-metal has very low thermal conductivity at low temperatures, comparable to stainless steel. Therefore, proper mechanical and thermal anchoring of the shields is crucial.

The first goal of this project was to characterize the cooldown performance of two magnetic shields used in the research group: first, a commercial *QCage* magnetic shield [291], as illustrated in Fig. 1A, and second, a custom-made magnetic shield as in Fig. 1B. The latter was first introduced in Ref. [123] and used for all experiments with grAl fluxoniums conducted in this work. Both shields consist of an outer mu-metal shield and an inner Cu/Al shield, as described in Section 2.2 for the custom-made shield. The mu-metal shields are made from 1 mm thick mu-metal sheets and formed into cylinders, before they are annealed at over 1000 °C and then cooled in a slow and controlled manner to achieve high relative permeability $\mu_\mathrm{r} \sim 500000$. The mu-metal volumes are approximately equal at $7 \times 10^{-5}\,\mathrm{m}^3$ for both shields. Under equally good mounting conditions, similar cooldown performance of both shields would be expected. However, a significant difference of the custom-made shield compared to the *QCage* shield is that it consists of two mu-metal parts, one of which is only connected to the central copper rod via the other part. In this regard, a slower cooldown of the custom-made shield may be expected.

The temperature profiles of both shields are shown in Fig. 1C and D, along with a comparison cooldown of the empty cryostat. It can be seen that the cryostat without a magnetic shield reached its base temperature in less than 5 hours. Adding the *QCage* shield (Fig. 1C) roughly doubled this cooldown time to over 10 hours. In the case of the custom shield (Fig. 1D), this time was even longer, at over 12 hours. The mu-metal cools in both cases significantly slower than the mixing chamber (MC) stage, and it is therefore the limiting factor for a fast cooldown. Furthermore, generally slow cooldown dynamics of the mu-metal shields over several hours are observed at low temperatures ($T < 1\,\mathrm{K}$), which is significantly slower than the MC stage particularly in the case of the custom-made shield. In the case of the *QCage* shield, the MC stage initially also has a slower cooling rate. This may be due to better thermal coupling of the shield to the MC plate. Since the cooldowns were terminated after the times shown, the final temperature of the shields cannot be conclusively stated. However, in further cooldowns not shown here, it was found that both shields decouple from the MC plate at a temperature elevated by a few 10 mK. This final temperature is determined by the balance between the Kapitza resistance between different materials and their thermal conductivity, and it can be improved by stronger thermal coupling (e.g., tighter screwing, larger number of screws).

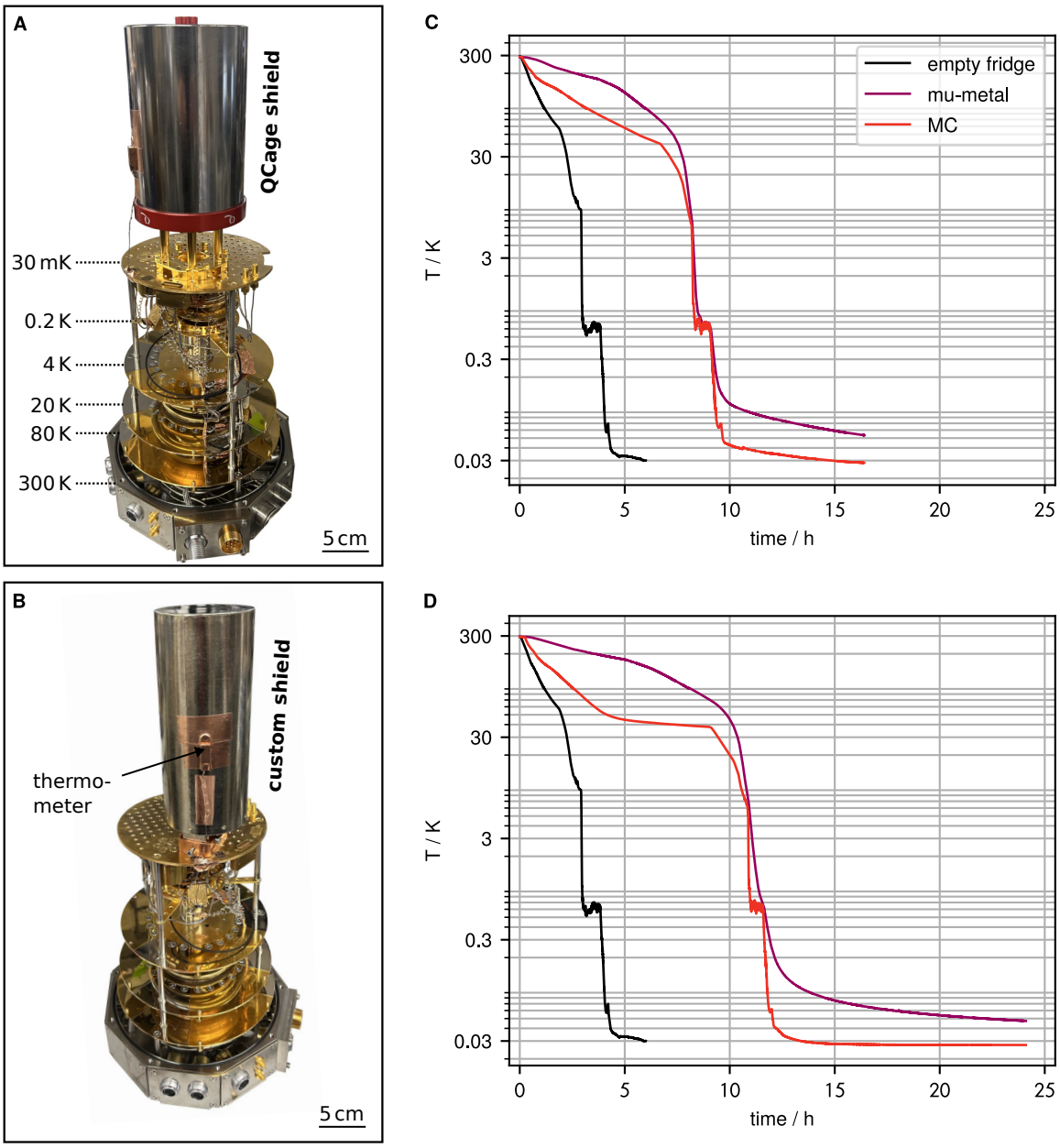

Figure 1: Comparison of magnetic shield cooldowns. **(A)** Photograph of the *QCage* magnetic shield anchored on the 30 mK mixing chamber (MC) stage. An additional thermometer was installed on the mu-metal shield with copper adhesive tape. Temperature stages of the *Sionludi L Eco* table-top dilution refrigerator are indicated by the dashed lines. The empty cryostat has a base temperature of 30 mK. **(B)** Photograph of the custom-made magnetic shielding, similar as in Ref. [123], and as used for the grAl fluxonium throughout this work. Not visible in panels A and B are the inner copper-sleeved superconducting Al cans. **(C)** Temperature profiles of the thermometers on the mu-metal magnetic shield and the MC stage from room temperature down to 30 mK for the *QCage* magnetic shield setup and **(D)** the custom-made magnetic shield setup. For comparison, the temperature profile of the MC stage of an empty fridge is shown in black.

Conclusion and Outlook

These initial characterization measurements showed that the used mu-metal shields are the limiting factor for the cooldown speed of a *Sionludi L Eco* cryostat, extending the cooldown time by at least double. The custom-made shield, compared to the commercial *QCage* shield, has a 20 % longer cooldown time. The different cooldown dynamics of the MC stage in both cases indicate that the *QCage* shield indeed has more efficient thermalization. This is consistent with the fact that the custom-made shield consists of two mu-metal parts that are cooled in series.

Increasing the thermal conductivity could definitely improve the cooldown performance and close the temperature gap between the MC stage and the mu-metal shield during cooldown. Therefore, a planned next step to achieve this is to electroplate the mu-metal shields with a sufficiently thick layer of silver (Ag). At room temperature, mu-metal and Ag have thermal conductivities of $\lambda_\mu \sim 20\,\mathrm{W/m \cdot K}$ and $\lambda_{\mathrm{Ag}} \sim 400\,\mathrm{W/m \cdot K}$, respectively. Under the simplified assumption that the ratio of these two values remains constant down to low temperatures, it can be estimated that a layer thickness of $d_{\mathrm{Ag}} = (\lambda_{\mathrm{Ag}}/\lambda_\mu) d_\mu/2 \sim 25\,\mu\mathrm{m}$ would be sufficient to double the cooling performance of the shield.[1] A final capping layer of gold would also be useful to prevent the Ag from oxidizing.

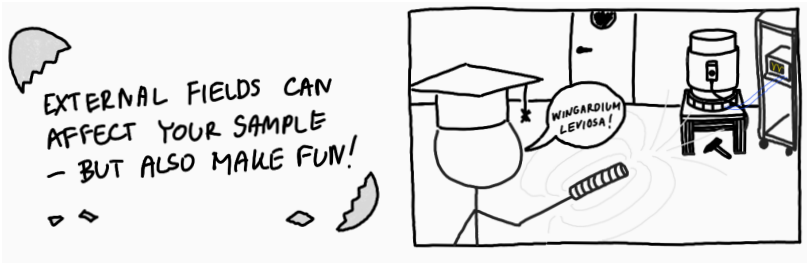

[1] The factor of two arises because the Ag layer is applied both inside and outside the shield.

Bibliography

Note that large language models were employed during the preparation of this manuscript for AI assisted copyediting, including for example improvements to readability, grammar, and style. Their use was limited to refining human-written text generated by the author and did not involve autonomous content generation.

[1] F. Valenti, A. Murani, P. Paluch, R. Gartmann, L. Scheller, R. Weller, R. Kruk, T. Reisinger, L. Ardila-Perez, and I. M. Pop, "Seismometry of radiation-induced quasiparticle bursts in superconducting devices", Phys. Rev. B **113**, 174504 (2026).

[2] D. Bénâtre, M. Féchant, N. Zapata, N. Gosling, P. Paluch, T. Reisinger, and I. M. Pop, "Simultaneous sweet-spot locking of gradiometric fluxonium qubits", Phys. Rev. Appl. **24**, 054031 (2025) (cit. on pp. 65, 66).

[3] M. Khorramshahi, M. Spiecker, P. Paluch, S. Geisert, N. Gosling, N. Zapata, L. Brauch, C. Kübel, S. Dehm, R. Krupke, W. Wernsdorfer, I. M. Pop, and T. Reisinger, "High-impedance granular-aluminum ring resonators", Phys. Rev. Appl. **24**, 024066 (2025) (cit. on p. 47).

[4] S. Ihssen, S. Geisert, G. Jauma, P. Winkel, M. Spiecker, N. Zapata, N. Gosling, P. Paluch, M. Pino, T. Reisinger, W. Wernsdorfer, J. J. Garcia-Ripoll, and I. M. Pop, "Low crosstalk modular flip-chip architecture for coupled superconducting qubits", Appl. Phys. Lett. **126**, 10.1063/5.0245667 (2025) (cit. on p. 48).

[5] P. Paluch, M. Spiecker, N. Gosling, V. Adam, J. Kammhuber, K. Vermeulen, D. Bouman, W. Wernsdorfer, and I. M. Pop, "Thermalization of a flexible microwave stripline measured by a superconducting qubit", Appl. Phys. Lett. **126**, 10.1063/5.0243116 (2025) (cit. on pp. 67, 74).

[6] S. Geisert, S. Ihssen, P. Winkel, M. Spiecker, M. Fechant, P. Paluch, N. Gosling, N. Zapata, S. Günzler, D. Rieger, D. Bénâtre, T. Reisinger, W. Wernsdorfer, and I. M. Pop, "Pure kinetic inductance coupling for cQED with flux qubits", Appl. Phys. Lett. **125**, 064002 (2024) (cit. on pp. 45, 64, 65).

[7] D. Willsch, D. Rieger, P. Winkel, M. Willsch, C. Dickel, J. Krause, Y. Ando, R. Lescanne, Z. Leghtas, N. T. Bronn, P. Deb, O. Lanes, Z. K. Minev, B. Dennig, S. Geisert, S. Günzler, S. Ihssen, P. Paluch, T. Reisinger, R. Hanna, J. H. Bae, P. Schüffelgen, D. Grützmacher, L. Buimaga-Iarinca, C. Morari, W. Wernsdorfer, D. P. DiVincenzo, K. Michielsen, G. Catelani, and I. M. Pop, "Observation of Josephson harmonics in tunnel junctions", Nat. Phys. **20**, 815–821 (2024).

[8] M. Spiecker, P. Paluch, N. Gosling, N. Drucker, S. Matityahu, D. Gusenkova, S. Günzler, D. Rieger, I. Takmakov, F. Valenti, P. Winkel, R. Gebauer, O. Sander, G. Catelani, A. Shnirman, A. V. Ustinov, W. Wernsdorfer, Y. Cohen, and I. M. Pop, "Two-level system hyperpolarization using a quantum Szilard engine", Nat. Phys. **19**, 1–6 (2023) (cit. on pp. 45, 46, 75, 93, 96).

[9] D. Rieger, S. Günzler, M. Spiecker, P. Paluch, P. Winkel, L. Hahn, J. K. Hohmann, A. Bacher, W. Wernsdorfer, and I. M. Pop, "Granular aluminium nanojunction fluxonium qubit", Nat. Mater. **22**, 194–199 (2023) (cit. on pp. 16, 42, 45, 64, 65, 68, 75, 78, 94).

[10] D. Gusenkova, F. Valenti, M. Spiecker, S. Günzler, P. Paluch, D. Rieger, L.-M. Pioraş-Ţimbolmaş, L. P. Zârbo, N. Casali, I. Colantoni, A. Cruciani, S. Pirro, L. Cardani, A. Petrescu, W. Wernsdorfer, P. Winkel, and I. M. Pop, "Operating in a deep underground facility improves the locking of gradiometric fluxonium qubits at the sweet spots", Appl. Phys. Lett. **120**, 054001 (2022) (cit. on p. 45).

[11] I. Newton, *Philosophiae Naturalis Principia Mathematica.* (1687) (cit. on p. 1).

[12] L. Boltzmann, *Über die Beziehung zwischen dem zweiten Hauptsatze der mechanischen Wärmetheorie und der Wahrscheinlichkeitsrechnung, respective den Sätzen über das Wärmegleichgewicht* (K.k. Hof- und Staatsdruckerei, 1877) (cit. on p. 1).

[13] M. Planck, "Ueber irreversible Strahlungsvorgänge", Ann. Phys. **311**, 818–831 (1901) (cit. on p. 1).

[14] A. Einstein, "Über einen die Erzeugung und Verwandlung des Lichtes betreffenden heuristischen Gesichtspunkt", Ann. Phys. **322**, 132–148 (1905) (cit. on p. 1).

[15] R. P. Feynman, "Simulating physics with computers", Int. J. Theor. Phys. **21**, 467–488 (1982) (cit. on p. 2).

[16] A. Aspuru-Guzik, A. D. Dutoi, P. J. Love, and M. Head-Gordon, "Simulated Quantum Computation of Molecular Energies", Science **309**, 1704–1707 (2005) (cit. on p. 2).

[17] P. W. Shor, "Polynomial-Time Algorithms for Prime Factorization and Discrete Logarithms on a Quantum Computer", SIAM Review **41**, 303–332 (1999) (cit. on p. 2).

[18] S. Lloyd, "Universal Quantum Simulators", Science **273**, 1073–1078 (1996) (cit. on p. 2).

[19] E. Farhi, J. Goldstone, S. Gutmann, J. Lapan, A. Lundgren, and D. Preda, "A Quantum Adiabatic Evolution Algorithm Applied to Random Instances of an NP-Complete Problem", Science **292**, 472–475 (2001) (cit. on p. 2).

[20] Google Quantum A. I. and Collaborators, "Quantum error correction below the surface code threshold", Nature **638**, 920–926 (2025) (cit. on pp. 2, 3, 14).

[21] O. V. Ivakhnenko, S. N. Shevchenko, and F. Nori, "Simulating quantum dynamical phenomena using classical oscillators: Landau-Zener-Stückelberg-Majorana interferometry, latching modulation, and motional averaging", Sci. Rep. **8**, 1–11 (2018) (cit. on p. 2).

[22] D. P. DiVincenzo, "The Physical Implementation of Quantum Computation", Fortschr. Phys. **48**, 771–783 (2000) (cit. on p. 3).

[23] I. Georgescu, "The DiVincenzo criteria 20 years on", Nat. Rev. Phys. **2**, 666 (2020) (cit. on p. 3).

[24] C. D. Bruzewicz, J. Chiaverini, R. McConnell, and J. M. Sage, "Trapped-ion quantum computing: Progress and challenges", Appl. Phys. Rev. **6**, 10.1063/1.5088164 (2019) (cit. on p. 3).

[25] J. C. Bardin, D. H. Slichter, and D. J. Reilly, "Microwaves in Quantum Computing", IEEE Journal of Microwaves **1**, 403–427 (2021) (cit. on p. 3).

[26] M. Saffman, T. G. Walker, and K. Mølmer, "Quantum information with Rydberg atoms", Rev. Mod. Phys. **82**, 2313–2363 (2010) (cit. on p. 3).

[27] T. M. Graham, Y. Song, J. Scott, C. Poole, L. Phuttitarn, K. Jooya, P. Eichler, X. Jiang, A. Marra, B. Grinkemeyer, M. Kwon, M. Ebert, J. Cherek, M. T. Lichtman, M. Gillette, J. Gilbert, D. Bowman, T. Ballance, C. Campbell, E. D. Dahl, O. Crawford, N. S. Blunt, B. Rogers, T. Noel, and M. Saffman, "Multi-qubit entanglement and algorithms on a neutral-atom quantum computer", Nature **604**, 457–462 (2022) (cit. on p. 3).

[28] D. S. Weiss and M. Saffman, "Quantum computing with neutral atoms", Phys. Today **70**, 44–50 (2017) (cit. on p. 3).

[29] S. Pezzagna and J. Meijer, "Quantum computer based on color centers in diamond", Appl. Phys. Rev. **8**, 10.1063/5.0007444 (2021) (cit. on p. 3).

[30] G. Burkard, M. J. Gullans, X. Mi, and J. R. Petta, "Superconductor–semiconductor hybrid-circuit quantum electrodynamics", Nat. Rev. Phys. **2**, 129–140 (2020) (cit. on p. 3).

[31] A. Krasnok, P. Dhakal, A. Fedorov, P. Frigola, M. Kelly, and S. Kutsaev, "Superconducting microwave cavities and qubits for quantum information systems", Appl. Phys. Rev. **11**, 011302 (2024) (cit. on p. 3).

[32] Y. Nakamura, Y. A. Pashkin, and J. S. Tsai, "Coherent control of macroscopic quantum states in a single-Cooper-pair box", Nature **398**, 786–788 (1999) (cit. on pp. 3, 11).

[33] S. Krinner, N. Lacroix, A. Remm, et al., "Realizing repeated quantum error correction in a distance-three surface code", Nature **605**, 669–674 (2022) (cit. on pp. 3, 67, 68).

[34] V. V. Sivak, A. Eickbusch, B. Royer, S. Singh, I. Tsioutsios, S. Ganjam, A. Miano, B. L. Brock, A. Z. Ding, L. Frunzio, S. M. Girvin, R. J. Schoelkopf, and M. H. Devoret, "Real-time quantum error correction beyond break-even", Nature **616**, 50–55 (2023) (cit. on p. 3).

[35] P. Krantz, M. Kjaergaard, F. Yan, T. P. Orlando, S. Gustavsson, and W. D. Oliver, "A quantum engineer's guide to superconducting qubits", Appl. Phys. Rev. **6**, 10.1063/1.5089550 (2019) (cit. on pp. 3, 14).

[36] C. H. van der Wal, A. C. J. ter Haar, F. K. Wilhelm, R. N. Schouten, C. J. P. M. Harmans, T. P. Orlando, S. Lloyd, and J. E. Mooij, "Quantum Superposition of Macroscopic Persistent-Current States", Science **290**, 773–777 (2000) (cit. on p. 3).

[37] J. Koch, T. M. Yu, J. Gambetta, A. A. Houck, D. I. Schuster, J. Majer, A. Blais, M. H. Devoret, S. M. Girvin, and R. J. Schoelkopf, "Charge-insensitive qubit design derived from the Cooper pair box", Phys. Rev. A **76**, 042319 (2007) (cit. on pp. 3, 11, 14, 30, 32–34, 36, 93, 99).

[38] V. E. Manucharyan, J. Koch, L. I. Glazman, and M. H. Devoret, "Fluxonium: Single Cooper-Pair Circuit Free of Charge Offsets", Science **326**, 113–116 (2009) (cit. on pp. 3, 11, 14, 46).

[39] P. Brooks, A. Kitaev, and J. Preskill, "Protected gates for superconducting qubits", Phys. Rev. A **87**, 052306 (2013) (cit. on p. 3).

[40] G. Wendin, "Quantum information processing with superconducting circuits: a review", Rep. Prog. Phys. **80**, 106001 (2017) (cit. on p. 3).

[41] P. Winkel, I. Takmakov, D. Rieger, L. Planat, W. Hasch-Guichard, L. Grünhaupt, N. Maleeva, F. Foroughi, F. Henriques, K. Borisov, J. Ferrero, A. V. Ustinov, W. Wernsdorfer, N. Roch, and I. M. Pop, "Nondegenerate Parametric Amplifiers Based on Dispersion-Engineered Josephson-Junction Arrays", Phys. Rev. Appl. **13**, 024015 (2020) (cit. on pp. 3, 44, 52).

[42] M. Esposito, A. Ranadive, L. Planat, and N. Roch, "Perspective on traveling wave microwave parametric amplifiers", Appl. Phys. Lett. **119**, 10.1063/5.0064892 (2021) (cit. on pp. 3, 44).

[43] N. Zapata, I. Takmakov, S. Günzler, S. Geisert, S. Ihssen, M. Field, A. Nambisan, D. Rieger, T. Reisinger, W. Wernsdorfer, and I. M. Pop, "Granular Aluminum Parametric Amplifier for Low-Noise Measurements in Tesla Fields", Phys. Rev. Lett. **133**, 260604 (2024) (cit. on pp. 3, 16, 44).

[44] A. Somoroff, Q. Ficheux, R. A. Mencia, et al., "Millisecond Coherence in a Superconducting Qubit", Phys. Rev. Lett. **130**, 267001 (2023) (cit. on pp. 3, 15, 25, 68).

[45] M. Kjaergaard, M. E. Schwartz, J. Braumüller, et al., "Superconducting Qubits: Current State of Play", Annu. Rev. Condens. Matter Phys., 369–395 (2020) (cit. on pp. 3, 68).

[46] M. Bal, A. A. Murthy, S. Zhu, et al., "Systematic improvements in transmon qubit coherence enabled by niobium surface encapsulation", npj Quantum Inf. **10**, 1–8 (2024) (cit. on pp. 3, 68).

[47] I. Newton, *Letter to Robert Hooke, 1675 :: Library Catalog*, [Online; accessed 4. Mar. 2025], (Feb. 1675) https://discover.hsp.org/Record/dc-9792/Description#tabnav (cit. on p. 4).

[48] F. Pobell, *Matter and Methods at Low Temperatures* (Springer, Berlin, Germany, 1996) (cit. on pp. 4, 80, 82).

[49] H. K. Onnes, "The discovery of superconductivity", Commun. Phys. Lab **12**, 120 (1911) (cit. on p. 4).

[50] P. Mangin and R. Kahn, *Superconductivity. An Introduction* (2017) (cit. on pp. 4, 5, 7, 8, 10).

[51] D. J. Quinn and W. B. Ittner, “Resistance in a Superconductor”, J. Appl. Phys. **33**, 748–749 (1962) (cit. on p. 4).

[52] W. Meissner and R. Ochsenfeld, “Ein neuer Effekt bei Eintritt der Supraleitfähigkeit”, Naturwissenschaften **21**, 787–788 (1933) (cit. on p. 4).

[53] W. Tuyn and H. K. Onnes, “The disturbance of supra-conductivity by magnetic fields and currents. The hypothesis of silsbee”, J. Franklin Inst. **201**, 379–410 (1926) (cit. on p. 4).

[54] D. López-Núñez, Q. P. Montserrat, G. Rius, E. Bertoldo, A. Torras-Coloma, M. Martínez, and P. Forn-Díaz, “Magnetic penetration depth of Aluminum thin films”, arXiv, 10.48550/arXiv.2311.14119 (2023) (cit. on pp. 5, 9).

[55] C. Enss and S. Hunklinger, *Low-Temperature Physics* (2005) (cit. on pp. 5–8).

[56] J. Bardeen, L. N. Cooper, and J. R. Schrieffer, “Theory of Superconductivity”, Phys. Rev. **108**, 1175–1204 (1957) (cit. on p. 5).

[57] H. Fröhlich, “Isotope Effect in Superconductivity”, Proc. Phys. Soc. A **63**, 778 (1950) (cit. on p. 5).

[58] E. Maxwell, “Superconductivity of the Isotopes of Tin”, Phys. Rev. **86**, 235–242 (1952) (cit. on pp. 5, 6).

[59] J. M. Lock, A. B. Pippard, and D. Shoenberg, “Superconductivity of tin isotopes”, Math. Proc. Cambridge Philos. Soc. **47**, 811–819 (1951) (cit. on pp. 5, 6).

[60] B. Serin, C. A. Reynolds, and C. Lohman, “The Isotope Effect in Superconductivity. II. Tin and Lead”, Phys. Rev. **86**, 162–164 (1952) (cit. on pp. 5, 6).

[61] H. Fröhlich, “Theory of the Superconducting State. I. The Ground State at the Absolute Zero of Temperature”, Phys. Rev. **79**, 845–856 (1950) (cit. on p. 5).

[62] H. Fröhlich, “Interaction of electrons with lattice vibrations”, Proc. R. Soc. London A - Math. Phys. Sci. **215**, 291–298 (1952) (cit. on p. 5).

[63] H. Fröhlich, “Electrons in lattice fields”, Adv. Phys. (1954) (cit. on p. 5).

[64] J. Bardeen, “Wave Functions for Superconducting Electrons”, Phys. Rev. **80**, 567–574 (1950) (cit. on p. 5).

[65] L. N. Cooper, “Bound Electron Pairs in a Degenerate Fermi Gas”, Phys. Rev. **104**, 1189–1190 (1956) (cit. on p. 5).

[66] F. Levy-Bertrand, T. Klein, T. Grenet, O. Dupré, A. Benoît, A. Bideaud, O. Bourrion, M. Calvo, A. Catalano, A. Gomez, J. Goupy, L. Grünhaupt, U. v. Luepke, N. Maleeva, F. Valenti, I. M. Pop, and A. Monfardini, “Electrodynamics of granular aluminum from superconductor to insulator: Observation of collective superconducting modes”, Phys. Rev. B **99**, 094506 (2019) (cit. on pp. 7, 16).

[67] R. E. Glover and M. Tinkham, “Conductivity of Superconducting Films for Photon Energies between 0.3 and $40kT_c$”, Phys. Rev. **108**, 243–256 (1957) (cit. on p. 7).

[68] D. C. Mattis and J. Bardeen, “Theory of the Anomalous Skin Effect in Normal and Superconducting Metals”, Phys. Rev. **111**, 412–417 (1958) (cit. on p. 7).

[69] J. Gao, "The Physics of Superconducting Microwave Resonators", PhD thesis (2008) (cit. on pp. 7, 62).

[70] M. v. Laue, F. London, and L. H., "Zur Theorie der Supraleitung", Z. Phys. **96**, 359 (1935) (cit. on p. 8).

[71] A. B. Pippard and W. L. Bragg, "An experimental and theoretical study of the relation between magnetic field and current in a superconductor", Proc. R. Soc. London A - Math. Phys. Sci. **216**, 547–568 (1953) (cit. on p. 8).

[72] U. S. Pracht, N. Bachar, L. Benfatto, G. Deutscher, E. Farber, M. Dressel, and M. Scheffler, "Enhanced Cooper pairing versus suppressed phase coherence shaping the superconducting dome in coupled aluminum nanograins", Phys. Rev. B **93**, 100503 (2016) (cit. on pp. 8, 16).

[73] F. R. Fickett, "Aluminum—1. A review of resistive mechanisms in aluminum", Cryogenics **11**, 349–367 (1971) (cit. on p. 8).

[74] J. W. Ekin, "Critical currents in granular superconductors", Phys. Rev. B **12**, 2676–2681 (1975) (cit. on p. 8).

[75] M. Tinkham, *Introduction to Superconductivity. 2nd edition* (1996) (cit. on p. 9).

[76] R. Holm and W. Meissner, "Messungen mit Hilfe von flüssigem Helium. XIII", Z. Phys. **74**, 715–735 (1932) (cit. on p. 9).

[77] A. F. Andreev, "Thermal conductivity of the intermediate state of superconductors", Zh. Eksperim. i Teor. Fiz **Vol: 46** (1964) (cit. on p. 9).

[78] P. G. de Gennes and D. Saint-James, "Elementary excitations in the vicinity of a normal metal-superconducting metal contact", Physics Letters **4**, 151–152 (1963) (cit. on p. 9).

[79] L. D. Landau and V. L. Ginzburg, "On the theory of superconductivity", Zh. Eksp. Teor. Fiz **20**, 1064 (1950) (cit. on p. 9).

[80] P. Müller, A. Ustinov, and V. Shmidt, *The physics of superconductors : introduction to fundamentals and applications* (1997) (cit. on p. 9).

[81] G. Deutscher and P. G. de Gennes, "Proximity Effects", in *Superconductivity* (Routledge, New York, NY, USA, Mar. 1969), pp. 1005–1034 (cit. on p. 9).

[82] R. Gross and A. Marx, *Applied Superconductivity: Josephson Effect and Superconducitng Electronics. Manuscript to the Lectures*, [Online; accessed 5. Mar. 2025], (Oct. 2005) `https://www.wmi.badw.de/teaching/lecture-notes` (cit. on p. 10).

[83] B. D. Josephson, "Possible new effects in superconductive tunnelling", Physics Letters **1**, 251–253 (1962) (cit. on pp. 10, 11).

[84] I. Giaever, "Detection of the ac Josephson Effect", Phys. Rev. Lett. **14**, 904–906 (1965) (cit. on p. 10).

[85] B. D. Josephson, "Coupled Superconductors", Rev. Mod. Phys. **36**, 216–220 (1964) (cit. on p. 10).

[86] V. Ambegaokar and A. Baratoff, "Tunneling Between Superconductors", Phys. Rev. Lett. **10**, 486–489 (1963) (cit. on p. 10).

[87] J. L. Hall, "Nobel Lecture: Defining and measuring optical frequencies", Rev. Mod. Phys. **78**, 1279–1295 (2006) (cit. on p. 11).

[88] T. W. Hänsch, "Nobel Lecture: Passion for precision", Rev. Mod. Phys. **78**, 1297–1309 (2006) (cit. on p. 11).

[89] J. Kohlmann, R. Behr, J. Kohlmann, and R. Behr, "Development of Josephson voltage standards", in *Superconductivity - Theory and Applications* (IntechOpen, Croatia, July 2011) (cit. on p. 11).

[90] J. Clarke and A. I. Braginski, *The SQUID Handbook* (May 2004) (cit. on p. 11).

[91] P. Seidel, "Josephson-Effekte", in *Effekte der Physik und ihre Anwendungen* (Verlag Harri Deutsch, Frankfurt am Main, 2005), pp. 1060–1062 (cit. on p. 11).

[92] Physikalisch-Technische Bundesanstalt, *Primary thermometry*, [Online; accessed 10. Mar. 2025], (Oct. 2018) `https://www.ptb.de/cms/en/ptb/fachabteilungen/abt7/fb-74/ag-744/primary-thermometry.html` (cit. on p. 11).

[93] M. H. Devoret, "Quantum Fluctuations in Electrical Circuits", in Fluctuations quantiques/quantum fluctuations, edited by S. Reynaud, E. Giacobino, and J. Zinn-Justin (Jan. 1997), p. 351 (cit. on pp. 12, 17, 25).

[94] U. Vool and M. Devoret, "Introduction to quantum electromagnetic circuits", Int. J. Circuit Theory Appl. **45**, 897–934 (2017) (cit. on p. 12).

[95] M. Spiecker, "Two-level system hyperpolarization with a quantum szilard engine", 47.12.01; LK 01, PhD thesis (Karlsruher Institut für Technologie (KIT), 2024) (cit. on pp. 12, 16, 18, 19, 22, 45, 48–50).

[96] C. Cohen-Tannoudji, B. Diu, and F. Laloë, *Quantum Mechanics, Volume 1: Basic Concepts, Tools, and Applications, 2nd Edition* (Wiley, Weinheim, Germany, June 2020) (cit. on p. 12).

[97] M. Dupont, B. Evert, M. J. Hodson, et al., "Quantum-enhanced greedy combinatorial optimization solver", Sci. Adv. **9**, `10.1126/sciadv.adi0487` (2023) (cit. on pp. 14, 67, 68).

[98] Y. Kim, A. Eddins, S. Anand, et al., "Evidence for the utility of quantum computing before fault tolerance", Nature **618**, 500–505 (2023) (cit. on pp. 14, 67, 68).

[99] Q. Zhu, S. Cao, F. Chen, et al., "Quantum computational advantage via 60-qubit 24-cycle random circuit sampling", Science Bulletin **67**, 240–245 (2022) (cit. on pp. 14, 67, 68).

[100] N. A. Masluk, I. M. Pop, A. Kamal, Z. K. Minev, and M. H. Devoret, "Microwave Characterization of Josephson Junction Arrays: Implementing a Low Loss Superinductance", Phys. Rev. Lett. **109**, 137002 (2012) (cit. on pp. 14, 15).

[101] V. E. Manucharyan, "Superinductance", PhD thesis (Yale University, Yale, May 2012) (cit. on p. 14).

[102] L. B. Nguyen, Y.-H. Lin, A. Somoroff, R. Mencia, N. Grabon, and V. E. Manucharyan, "High-Coherence Fluxonium Qubit", Phys. Rev. X **9**, 041041 (2019) (cit. on pp. 15, 25, 26, 46, 64, 65).

[103] L. B. Nguyen, G. Koolstra, Y. Kim, A. Morvan, T. Chistolini, S. Singh, K. N. Nesterov, C. Jünger, L. Chen, Z. Pedramrazi, B. K. Mitchell, J. M. Kreikebaum, S. Puri, D. I. Santiago, and I. Siddiqi, "Blueprint for a High-Performance Fluxonium Quantum Processor", PRX Quantum **3**, 037001 (2022) (cit. on p. 15).

[104] G. J. Grabovskij, L. J. Swenson, O. Buisson, C. Hoffmann, A. Monfardini, and J.-C. Villégier, "In situ measurement of the permittivity of helium using microwave NbN resonators", Appl. Phys. Lett. **93**, 134102 (2008) (cit. on p. 16).

[105] J. Luomahaara, V. Vesterinen, L. Grönberg, and J. Hassel, "Kinetic inductance magnetometer", Nat. Commun. **5**, 1–7 (2014) (cit. on p. 16).

[106] D. Niepce, J. Burnett, and J. Bylander, "High Kinetic Inductance NbN Nanowire Superinductors", Phys. Rev. Appl. **11**, 044014 (2019) (cit. on p. 16).

[107] C. W. Zollitsch, J. O'Sullivan, O. Kennedy, G. Dold, and J. J. L. Morton, "Tuning high-Q superconducting resonators by magnetic field reorientation", AIP Adv. **9**, 10.1063/1.5129032 (2019) (cit. on p. 16).

[108] R. Barends, N. Vercruyssen, A. Endo, P. J. de Visser, T. Zijlstra, T. M. Klapwijk, and J. J. A. Baselmans, "Reduced frequency noise in superconducting resonators", Appl. Phys. Lett. **97**, 033507 (2010) (cit. on p. 16).

[109] N. Samkharadze, A. Bruno, P. Scarlino, G. Zheng, D. P. DiVincenzo, L. DiCarlo, and L. M. K. Vandersypen, "High-Kinetic-Inductance Superconducting Nanowire Resonators for Circuit QED in a Magnetic Field", Phys. Rev. Appl. **5**, 044004 (2016) (cit. on p. 16).

[110] T. M. Hazard, A. Gyenis, A. Di Paolo, A. T. Asfaw, S. A. Lyon, A. Blais, and A. A. Houck, "Nanowire Superinductance Fluxonium Qubit", Phys. Rev. Lett. **122**, 010504 (2019) (cit. on pp. 16, 46).

[111] J. G. Kroll, F. Borsoi, K. L. van der Enden, W. Uilhoorn, D. de Jong, M. Quintero-Pérez, D. J. van Woerkom, A. Bruno, S. R. Plissard, D. Car, E. P. A. M. Bakkers, M. C. Cassidy, and L. P. Kouwenhoven, "Magnetic-Field-Resilient Superconducting Coplanar-Waveguide Resonators for Hybrid Circuit Quantum Electrodynamics Experiments", Phys. Rev. Appl. **11**, 064053 (2019) (cit. on p. 16).

[112] H. G. Leduc, B. Bumble, P. K. Day, B. H. Eom, J. Gao, S. Golwala, B. A. Mazin, S. McHugh, A. Merrill, D. C. Moore, O. Noroozian, A. D. Turner, and J. Zmuidzinas, "Titanium nitride films for ultrasensitive microresonator detectors", Appl. Phys. Lett. **97**, 102509 (2010) (cit. on p. 16).

[113] M. R. Vissers, J. Gao, D. S. Wisbey, D. A. Hite, C. C. Tsuei, A. D. Corcoles, M. Steffen, and D. P. Pappas, "Low loss superconducting titanium nitride coplanar waveguide resonators", Appl. Phys. Lett. **97**, 232509 (2010) (cit. on p. 16).

[114] L. J. Swenson, P. K. Day, B. H. Eom, H. G. Leduc, N. Llombart, C. M. McKenney, O. Noroozian, and J. Zmuidzinas, "Operation of a titanium nitride superconducting microresonator detector in the nonlinear regime", J. Appl. Phys. **113**, 104501 (2013) (cit. on p. 16).

[115] A. Shearrow, G. Koolstra, S. J. Whiteley, N. Earnest, P. S. Barry, F. J. Heremans, D. D. Awschalom, E. Shirokoff, and D. I. Schuster, "Atomic layer deposition of titanium nitride for quantum circuits", Appl. Phys. Lett. **113**, 10.1063/1.5053461 (2018) (cit. on p. 16).

[116] O. Dupré, A. Benoît, M. Calvo, A. Catalano, J. Goupy, C. Hoarau, T. Klein, K. Le Calvez, B. Sacépé, A. Monfardini, and F. Levy-Bertrand, "Tunable sub-gap radiation detection with superconducting resonators", Supercond. Sci. Technol. **30**, 045007 (2017) (cit. on p. 16).

[117] T. Charpentier, D. Perconte, S. Léger, K. R. Amin, F. Blondelle, F. Gay, O. Buisson, L. Ioffe, A. Khvalyuk, I. Poboiko, M. Feigel'man, N. Roch, and B. Sacépé, "First-order quantum breakdown of superconductivity in an amorphous superconductor", Nat. Phys. **21**, 104–109 (2025) (cit. on p. 16).

[118] R. W. Cohen and B. Abeles, "Superconductivity in Granular Aluminum Films", Phys. Rev. **168**, 444–450 (1968) (cit. on p. 16).

[119] G. Deutscher, H. Fenichel, M. Gershenson, E. Grünbaum, and Z. Ovadyahu, "Transition to zero dimensionality in granular aluminum superconducting films", J. Low Temp. Phys. **10**, 231–243 (1973) (cit. on p. 16).

[120] N. Maleeva, L. Grünhaupt, T. Klein, F. Levy-Bertrand, O. Dupre, M. Calvo, F. Valenti, P. Winkel, F. Friedrich, W. Wernsdorfer, A. V. Ustinov, H. Rotzinger, A. Monfardini, M. V. Fistul, and I. M. Pop, "Circuit quantum electrodynamics of granular aluminum resonators", Nat. Commun. **9**, 1–7 (2018) (cit. on pp. 16, 45, 95).

[121] A. Deshpande, J. Pusskeiler, C. Prange, U. Rogge, M. Dressel, and M. Scheffler, "Tuning the superconducting dome in granular aluminum thin films", J. Appl. Phys. **137**, 10.1063/5.0250146 (2025) (cit. on p. 16).

[122] H. Rotzinger, S. T. Skacel, M. Pfirrmann, J. N. Voss, J. Münzberg, S. Probst, P. Bushev, M. P. Weides, A. V. Ustinov, and J. E. Mooij, "Aluminium-oxide wires for superconducting high kinetic inductance circuits", Supercond. Sci. Technol. **30**, 025002 (2016) (cit. on p. 16).

[123] L. Grünhaupt, N. Maleeva, S. T. Skacel, et al., "Loss Mechanisms and Quasiparticle Dynamics in Superconducting Microwave Resonators Made of Thin-Film Granular Aluminum", Phys. Rev. Lett. **121**, 117001 (2018) (cit. on pp. 16, 37, 45, 50, 51, 63, 69, 94, 95, 107, 108).

[124] W. Zhang, K. Kalashnikov, W.-S. Lu, P. Kamenov, T. DiNapoli, and M. E. Gershenson, "Microresonators Fabricated from High-Kinetic-Inductance Aluminum Films", Phys. Rev. Appl. **11**, 011003 (2019) (cit. on p. 16).

[125] D. G. Atanasova, I. Yang, T. Hönigl-Decrinis, D. Gusenkova, I. M. Pop, and G. Kirchmair, "In-situ tunable interaction with an invertible sign between a fluxonium and a post cavity", arXiv, 10.48550/arXiv.2409.07612 (2024) (cit. on pp. 16, 25, 26, 35, 45, 62, 64, 65).

[126] P. Winkel, K. Borisov, L. Grünhaupt, D. Rieger, M. Spiecker, F. Valenti, A. V. Ustinov, W. Wernsdorfer, and I. M. Pop, "Implementation of a Transmon Qubit Using Superconducting Granular Aluminum", Phys. Rev. X **10**, 031032 (2020) (cit. on p. 16).

[127] N. Bachar and A. G. Moshe, "From a superconductor to a Mott insulator: The case of granular aluminum", Phys. C **614**, 1354359 (2023) (cit. on p. 17).

[128] C. M. Caves, K. S. Thorne, R. W. P. Drever, V. D. Sandberg, and M. Zimmermann, "On the measurement of a weak classical force coupled to a quantum-mechanical oscillator. I. Issues of principle", Rev. Mod. Phys. **52**, 341–392 (1980) (cit. on p. 17).

[129] J. M. Raimond, M. Brune, and S. Haroche, "Manipulating quantum entanglement with atoms and photons in a cavity", Rev. Mod. Phys. **73**, 565–582 (2001) (cit. on p. 17).

[130] R. Miller, T. E. Northup, K. M. Birnbaum, A. Boca, A. D. Boozer, and H. J. Kimble, "Trapped atoms in cavity QED: coupling quantized light and matter", J. Phys. B: At. Mol. Opt. Phys. **38**, S551 (2005) (cit. on p. 17).

[131] H. Walther, B. T. H. Varcoe, B.-G. Englert, and T. Becker, "Cavity quantum electrodynamics", Rep. Prog. Phys. **69**, 1325 (2006) (cit. on p. 17).

[132] A. Blais, R.-S. Huang, A. Wallraff, S. M. Girvin, and R. J. Schoelkopf, "Cavity quantum electrodynamics for superconducting electrical circuits: An architecture for quantum computation", Phys. Rev. A **69**, 062320 (2004) (cit. on pp. 17, 29).

[133] Q. Xie, H. Zhong, M. T. Batchelor, and C. Lee, "The quantum Rabi model: solution and dynamics", J. Phys. A: Math. Theor. **50**, 113001 (2017) (cit. on p. 17).

[134] A. Petrescu, M. Malekakhlagh, and H. E. Türeci, "Lifetime renormalization of driven weakly anharmonic superconducting qubits. II. The readout problem", Phys. Rev. B **101**, 134510 (2020) (cit. on pp. 17, 20).

[135] R. Shillito, A. Petrescu, J. Cohen, J. Beall, M. Hauru, M. Ganahl, A. G. M. Lewis, G. Vidal, and A. Blais, "Dynamics of Transmon Ionization", Phys. Rev. Appl. **18**, 034031 (2022) (cit. on pp. 17, 20).

[136] J. Cohen, A. Petrescu, R. Shillito, and A. Blais, "Reminiscence of Classical Chaos in Driven Transmons", PRX Quantum **4**, 020312 (2023) (cit. on pp. 17, 20).

[137] E. T. Jaynes and F. W. Cummings, "Comparison of quantum and semiclassical radiation theories with application to the beam maser", Proc. IEEE **51**, 89–109 (1963) (cit. on p. 17).

[138] S. Haroche and J.-M. Raimond, *Exploring the Quantum: Atoms, Cavities, and Photons*, Vol. 17, 3 (Oxford University Press, Oxford, England, UK, Sept. 1995) (cit. on p. 17).

[139] D. Zueco, G. M. Reuther, S. Kohler, and P. Hänggi, "Qubit-oscillator dynamics in the dispersive regime: Analytical theory beyond the rotating-wave approximation", Phys. Rev. A **80**, 033846 (2009) (cit. on p. 18).

[140] M. Spiecker, *bfqcircuits: Black Forest Quantum Circuits (Version v0.2.1) [Software]*, (2024) `https://github.com/MartinSpiecker/bfqcircuits` (cit. on pp. 19, 58).

[141] E. Jeffrey, D. Sank, J. Y. Mutus, T. C. White, J. Kelly, R. Barends, Y. Chen, Z. Chen, B. Chiaro, A. Dunsworth, A. Megrant, P. J. J. O'Malley, C. Neill, P. Roushan, A. Vainsencher, J. Wenner, A. N. Cleland, and J. M. Martinis, "Fast Accurate State Measurement with Superconducting Qubits", Phys. Rev. Lett. **112**, 190504 (2014) (cit. on p. 20).

[142] P. Krantz, A. Bengtsson, M. Simoen, S. Gustavsson, V. Shumeiko, W. D. Oliver, C. M. Wilson, P. Delsing, and J. Bylander, "Single-shot read-out of a superconducting qubit using a Josephson parametric oscillator", Nat. Commun. **7**, 1–8 (2016) (cit. on p. 20).

[143] T. Walter, P. Kurpiers, S. Gasparinetti, P. Magnard, A. Potočnik, Y. Salathé, M. Pechal, M. Mondal, M. Oppliger, C. Eichler, and A. Wallraff, "Rapid High-Fidelity Single-Shot Dispersive Readout of Superconducting Qubits", Phys. Rev. Appl. **7**, 054020 (2017) (cit. on p. 20).

[144] R. Gebauer, N. Karcher, D. Gusenkova, M. Spiecker, L. Grünhaupt, I. Takmakov, P. Winkel, L. Planat, N. Roch, W. Wernsdorfer, A. V. Ustinov, M. Weber, M. Weides, I. M. Pop, and O. Sander, "State preparation of a fluxonium qubit with feedback from a custom FPGA-based platform", AIP Conf. Proc. **2241**, `10.1063/5.0011721` (2020) (cit. on p. 20).

[145] D. Gusenkova, M. Spiecker, R. Gebauer, et al., "Quantum Nondemolition Dispersive Readout of a Superconducting Artificial Atom Using Large Photon Numbers", Phys. Rev. Appl. **15**, 064030 (2021) (cit. on pp. 20, 45, 75, 77).

[146] I. Takmakov, P. Winkel, F. Foroughi, L. Planat, D. Gusenkova, M. Spiecker, D. Rieger, L. Grünhaupt, A. V. Ustinov, W. Wernsdorfer, I. M. Pop, and N. Roch, "Minimizing the Discrimination Time for Quantum States of an Artificial Atom", Phys. Rev. Appl. **15**, 064029 (2021) (cit. on p. 20).

[147] L. Chen, H.-X. Li, Y. Lu, C. W. Warren, C. J. Križan, S. Kosen, M. Rommel, S. Ahmed, A. Osman, J. Biznárová, A. Fadavi Roudsari, B. Lienhard, M. Caputo, K. Grigoras, L. Grönberg, J. Govenius, A. F. Kockum, P. Delsing, J. Bylander, and G. Tancredi, "Transmon qubit readout fidelity at the threshold for quantum error correction without a quantum-limited amplifier", npj Quantum Inf. **9**, 1–7 (2023) (cit. on p. 20).

[148] L. Ding, M. Hays, Y. Sung, B. Kannan, J. An, A. Di Paolo, A. H. Karamlou, T. M. Hazard, K. Azar, D. K. Kim, B. M. Niedzielski, A. Melville, M. E. Schwartz, J. L. Yoder, T. P. Orlando, S. Gustavsson, J. A. Grover, K. Serniak, and W. D. Oliver, "High-Fidelity, Frequency-Flexible Two-Qubit Fluxonium Gates with a Transmon Coupler", Phys. Rev. X **13**, 031035 (2023) (cit. on p. 20).

[149] M. Boissonneault, J. M. Gambetta, and A. Blais, "Dispersive regime of circuit QED: Photon-dependent qubit dephasing and relaxation rates", Phys. Rev. A **79**, 013819 (2009) (cit. on p. 20).

[150] M. J. Peterer, S. J. Bader, X. Jin, F. Yan, A. Kamal, T. J. Gudmundsen, P. J. Leek, T. P. Orlando, W. D. Oliver, and S. Gustavsson, "Coherence and Decay of Higher Energy Levels of a Superconducting Transmon Qubit", Phys. Rev. Lett. **114**, 010501 (2015) (cit. on p. 20).

[151] M. F. Dumas, B. Groleau-Paré, A. McDonald, M. H. Muñoz-Arias, C. Lledó, B. D'Anjou, and A. Blais, "Measurement-Induced Transmon Ionization", Phys. Rev. X **14**, 041023 (2024) (cit. on p. 20).

[152] K. N. Nesterov and I. V. Pechenezhskiy, "Measurement-induced state transitions in dispersive qubit-readout schemes", Phys. Rev. Appl. **22**, 064038 (2024) (cit. on p. 20).

[153] S. Hazra, W. Dai, T. Connolly, P. D. Kurilovich, Z. Wang, L. Frunzio, and M. H. Devoret, "Benchmarking the readout of a superconducting qubit for repeated measurements", arXiv, 10.48550/arXiv.2407.10934 (2024) (cit. on p. 20).

[154] N. Lacroix, L. Hofele, A. Remm, O. Benhayoune-Khadraoui, A. McDonald, R. Shillito, S. Lazar, C. Hellings, F. Swiadek, D. Colao-Zanuz, A. Flasby, M. B. Panah, M. Kerschbaum, G. J. Norris, A. Blais, A. Wallraff, and S. Krinner, "Fast Flux-Activated Leakage Reduction for Superconducting Quantum Circuits", Phys. Rev. Lett. **134**, 120601 (2025) (cit. on p. 20).

[155] S. Nakajima, "On Quantum Theory of Transport Phenomena: Steady Diffusion", Prog. Theor. Phys. **20**, 948–959 (1958) (cit. on p. 22).

[156] R. Zwanzig, "Ensemble Method in the Theory of Irreversibility", J. Chem. Phys. **33**, 1338–1341 (1960) (cit. on p. 22).

[157] G. Lindblad, "On the generators of quantum dynamical semigroups", Commun. Math. Phys. **48**, 119–130 (1976) (cit. on p. 22).

[158] T. Albash, S. Boixo, D. A. Lidar, and P. Zanardi, "Quantum adiabatic Markovian master equations", New J. Phys. **14**, 123016 (2012) (cit. on p. 22).

[159] G. Schaller, *Lecture notes in theory of quantum transport*, (Oct. 2019) (cit. on pp. 22, 23, 25).

[160] M. Schlosshauer, "Quantum decoherence", Phys. Rep. **831**, 1–57 (2019) (cit. on pp. 22, 23).

[161] A. G. Redfield, "On the Theory of Relaxation Processes", IBM J. Res. Dev. **1**, 19–31 (1957) (cit. on pp. 22, 23).

[162] K. W. Murch, S. J. Weber, C. Macklin, and I. Siddiqi, "Observing single quantum trajectories of a superconducting quantum bit", Nature **502**, 211–214 (2013) (cit. on p. 24).

[163] I. M. Pop, K. Geerlings, G. Catelani, R. J. Schoelkopf, L. I. Glazman, and M. H. Devoret, "Coherent suppression of electromagnetic dissipation due to superconducting quasiparticles", Nature **508**, 369–372 (2014) (cit. on pp. 25–27, 29, 37, 46, 62, 64, 65, 94).

[164] W. C. Smith, A. Kou, X. Xiao, U. Vool, and M. H. Devoret, "Superconducting circuit protected by two-Cooper-pair tunneling", npj Quantum Inf. **6**, 1–9 (2020) (cit. on pp. 25, 27–29).

[165] H. Sun, F. Wu, H.-S. Ku, X. Ma, J. Qin, Z. Song, T. Wang, G. Zhang, J. Zhou, Y. Shi, H.-H. Zhao, and C. Deng, "Characterization of Loss Mechanisms in a Fluxonium Qubit", Phys. Rev. Appl. **20**, 034016 (2023) (cit. on pp. 25, 27, 36, 61, 62).

[166] A. O. Caldeira and A. J. Leggett, "Quantum tunnelling in a dissipative system", Ann. Phys. **149**, 374–456 (1983) (cit. on p. 25).

[167] R. Kubo, "The fluctuation-dissipation theorem", Rep. Prog. Phys. **29**, 255 (1966) (cit. on p. 25).

[168] J. Jackson, *Classical Electrodynamics. (1st ed.)* (John Wiley & Sons, Inc., New York, London, 1962) (cit. on pp. 26, 29).

[169] C. Müller, J. H. Cole, and J. Lisenfeld, "Towards understanding two-level-systems in amorphous solids: insights from quantum circuits", Rep. Prog. Phys. **82**, 124501 (2019) (cit. on p. 26).

[170] D. M. Pozar, *Microwave Engineering, 4th Edition* (Wiley, Hoboken, NJ, USA, Nov. 2011) (cit. on pp. 26, 28, 86).

[171] H. Zhang, S. Chakram, T. Roy, N. Earnest, Y. Lu, Z. Huang, D. K. Weiss, J. Koch, and D. I. Schuster, "Universal Fast-Flux Control of a Coherent, Low-Frequency Qubit", Phys. Rev. X **11**, 011010 (2021) (cit. on pp. 27, 29, 30, 32–34, 46, 64, 65, 93–95, 99, 100).

[172] J. M. Martinis, K. B. Cooper, R. McDermott, M. Steffen, M. Ansmann, K. D. Osborn, K. Cicak, S. Oh, D. P. Pappas, R. W. Simmonds, and C. C. Yu, "Decoherence in Josephson Qubits from Dielectric Loss", Phys. Rev. Lett. **95**, 210503 (2005) (cit. on p. 27).

[173] W. G. Farr, D. L. Creedon, M. Goryachev, K. Benmessai, and M. E. Tobar, "Ultrasensitive microwave spectroscopy of paramagnetic impurities in sapphire crystals at millikelvin temperatures", Phys. Rev. B **88**, 224426 (2013) (cit. on p. 28).

[174] S. Günzler, J. Beck, D. Rieger, N. Gosling, N. Zapata, M. Field, S. Geisert, A. Bacher, J. K. Hohmann, M. Spiecker, W. Wernsdorfer, and I. M. Pop, "Spin Environment of a Superconducting Qubit in High Magnetic Fields", arXiv, `10.48550/arXiv.2501.03661` (2025) (cit. on pp. 28, 36, 38, 56, 57, 96).

[175] R. Gao, F. Wu, H. Sun, J. Chen, H. Deng, X. Ma, X. Miao, Z. Song, X. Wan, F. Wang, T. Xia, M. Ying, C. Zhang, Y. Shi, H.-H. Zhao, and C. Deng, "The effects of disorder in superconducting materials on qubit coherence", Nat. Commun. **16**, 1–8 (2025) (cit. on pp. 28, 36, 64–66).

[176] E. M. Purcell, "Spontaneous emission probabilities at radio frequencies", Phys. Rev. **69** (1946) (cit. on p. 29).

[177] A. A. Houck, J. A. Schreier, B. R. Johnson, J. M. Chow, J. Koch, J. M. Gambetta, D. I. Schuster, L. Frunzio, M. H. Devoret, S. M. Girvin, and R. J. Schoelkopf, "Controlling the Spontaneous Emission of a Superconducting Transmon Qubit", Phys. Rev. Lett. **101**, 080502 (2008) (cit. on p. 29).

[178] S. E. Nigg, H. Paik, B. Vlastakis, G. Kirchmair, S. Shankar, L. Frunzio, M. H. Devoret, R. J. Schoelkopf, and S. M. Girvin, "Black-Box Superconducting Circuit Quantization", Phys. Rev. Lett. **108**, 240502 (2012) (cit. on p. 30).

[179] F. Solgun, D. W. Abraham, and D. P. DiVincenzo, "Blackbox quantization of superconducting circuits using exact impedance synthesis", Phys. Rev. B **90**, 134504 (2014) (cit. on p. 30).

[180] P. Groszkowski, A. Di Paolo, A. L. Grimsmo, A. Blais, D. I. Schuster, A. A. Houck, and J. Koch, "Coherence properties of the 0-π qubit", New J. Phys. **20**, 043053 (2018) (cit. on pp. 30, 32–34, 93, 99, 100).

[181] C. W. Gardiner and M. J. Collett, "Input and output in damped quantum systems: Quantum stochastic differential equations and the master equation", Phys. Rev. A **31**, 3761–3774 (1985) (cit. on p. 33).

[182] J. Schirk, F. Wallner, L. Huang, I. Tsitsilin, N. Bruckmoser, L. Koch, D. Bunch, N. J. Glaser, G. B. P. Huber, M. Knudsen, G. Krylov, A. Marx, F. Pfeiffer, L. Richard, F. A. Roy, J. H. Romeiro, M. Singh, L. Södergren, E. Dionis, D. Sugny, M. Werninghaus, K. Liegener, C. M. F. Schneider, and S. Filipp, "Protected Fluxonium Control with Sub-harmonic Parametric Driving", arXiv, 10.48550/arXiv.2410.00495 (2024) (cit. on p. 36).

[183] D. A. Rower, L. Ateshian, L. H. Li, M. Hays, D. Bluvstein, L. Ding, B. Kannan, A. Almanakly, J. Braumüller, D. K. Kim, A. Melville, B. M. Niedzielski, M. E. Schwartz, J. L. Yoder, T. P. Orlando, J. I.-J. Wang, S. Gustavsson, J. A. Grover, K. Serniak, R. Comin, and W. D. Oliver, "Evolution of $1/f$ Flux Noise in Superconducting Qubits with Weak Magnetic Fields", Phys. Rev. Lett. **130**, 220602 (2023) (cit. on pp. 36, 38).

[184] M. D. Hutchings, J. B. Hertzberg, Y. Liu, N. T. Bronn, G. A. Keefe, M. Brink, J. M. Chow, and B. L. T. Plourde, "Tunable Superconducting Qubits with Flux-Independent Coherence", Phys. Rev. Appl. **8**, 044003 (2017) (cit. on pp. 36, 38).

[185] P. Kumar, S. Sendelbach, M. A. Beck, J. W. Freeland, Z. Wang, H. Wang, C. C. Yu, R. Q. Wu, D. P. Pappas, and R. McDermott, "Origin and Reduction of $1/f$ Magnetic Flux Noise in Superconducting Devices", Phys. Rev. Appl. **6**, 041001 (2016) (cit. on pp. 36, 38, 56).

[186] S. Sendelbach, D. Hover, A. Kittel, M. Mück, J. M. Martinis, and R. McDermott, "Magnetism in SQUIDs at Millikelvin Temperatures", Phys. Rev. Lett. **100**, 227006 (2008) (cit. on pp. 36, 38, 56, 57).

[187] F. C. Wellstood, C. Urbina, and J. Clarke, "Low-frequency noise in dc superconducting quantum interference devices below 1 K", Appl. Phys. Lett. **50**, 772–774 (1987) (cit. on pp. 36, 38, 68).

[188] D. H. Slichter, R. Vijay, S. J. Weber, S. Boutin, M. Boissonneault, J. M. Gambetta, A. Blais, and I. Siddiqi, "Measurement-Induced Qubit State Mixing in Circuit QED from Up-Converted Dephasing Noise", Phys. Rev. Lett. **109**, 153601 (2012) (cit. on pp. 36, 38).

[189] J. Bylander, S. Gustavsson, F. Yan, F. Yoshihara, K. Harrabi, G. Fitch, D. G. Cory, Y. Nakamura, J.-S. Tsai, and W. D. Oliver, "Noise spectroscopy through dynamical decoupling with a superconducting flux qubit", Nat. Phys. **7**, 565–570 (2011) (cit. on pp. 36–38).

[190] F. Yan, J. Bylander, S. Gustavsson, F. Yoshihara, K. Harrabi, D. G. Cory, T. P. Orlando, Y. Nakamura, J.-S. Tsai, and W. D. Oliver, "Spectroscopy of low-frequency noise and its temperature dependence in a superconducting qubit", Phys. Rev. B **85**, 174521 (2012) (cit. on pp. 36, 38).

[191] F. Yan, S. Gustavsson, J. Bylander, X. Jin, F. Yoshihara, D. G. Cory, Y. Nakamura, T. P. Orlando, and W. D. Oliver, "Rotating-frame relaxation as a noise spectrum analyser of a superconducting qubit undergoing driven evolution", Nat. Commun. **4**, 1–8 (2013) (cit. on pp. 36, 38).

[192] F. Yan, S. Gustavsson, A. Kamal, J. Birenbaum, A. P. Sears, D. Hover, T. J. Gudmundsen, D. Rosenberg, G. Samach, S. Weber, J. L. Yoder, T. P. Orlando, J. Clarke, A. J. Kerman, and W. D. Oliver, "The flux qubit revisited to enhance coherence and reproducibility", Nat. Commun. **7**, 1–9 (2016) (cit. on pp. 36, 38, 39, 42, 68, 78, 94).

[193] J. M. Martinis, M. Ansmann, and J. Aumentado, "Energy Decay in Superconducting Josephson-Junction Qubits from Nonequilibrium Quasiparticle Excitations", Phys. Rev. Lett. **103**, 097002 (2009) (cit. on pp. 37, 94).

[194] G. Catelani, R. J. Schoelkopf, M. H. Devoret, and L. I. Glazman, "Relaxation and frequency shifts induced by quasiparticles in superconducting qubits", Phys. Rev. B **84**, 064517 (2011) (cit. on p. 37).

[195] L. Grünhaupt, "Granular aluminium superinductors", [Online; accessed 24. Apr. 2025], PhD thesis (Karlsruher Institut für Technologie (KIT), 2019) (cit. on p. 37).

[196] J. Aumentado, M. W. Keller, J. M. Martinis, and M. H. Devoret, "Nonequilibrium Quasiparticles and $2e$ Periodicity in Single-Cooper-Pair Transistors", Phys. Rev. Lett. **92**, 066802 (2004) (cit. on pp. 37, 94).

[197] A. J. Ferguson, N. A. Court, F. E. Hudson, and R. G. Clark, "Microsecond Resolution of Quasiparticle Tunneling in the Single-Cooper-Pair Transistor", Phys. Rev. Lett. **97**, 106603 (2006) (cit. on pp. 37, 94).

[198] M. D. Shaw, R. M. Lutchyn, P. Delsing, and P. M. Echternach, "Kinetics of nonequilibrium quasiparticle tunneling in superconducting charge qubits", Phys. Rev. B **78**, 024503 (2008) (cit. on pp. 37, 94).

[199] L. J. Swenson, A. Cruciani, A. Benoît, M. Roesch, C. S. Yung, A. Bideaud, and A. Monfardini, "High-speed phonon imaging using frequency-multiplexed kinetic inductance detectors", Appl. Phys. Lett. **96**, 263511 (2010) (cit. on pp. 37, 94).

[200] L. Sun, L. DiCarlo, M. D. Reed, G. Catelani, L. S. Bishop, D. I. Schuster, B. R. Johnson, G. A. Yang, L. Frunzio, L. Glazman, M. H. Devoret, and R. J. Schoelkopf, "Measurements of Quasiparticle Tunneling Dynamics in a Band-Gap-Engineered Transmon Qubit", Phys. Rev. Lett. **108**, 230509 (2012) (cit. on pp. 37, 94).

[201] D. Ristè, C. C. Bultink, M. J. Tiggelman, R. N. Schouten, K. W. Lehnert, and L. DiCarlo, "Millisecond charge-parity fluctuations and induced decoherence in a superconducting transmon qubit", Nat. Commun. **4**, 1–6 (2013) (cit. on pp. 37, 94).

[202] K. Karatsu, A. Endo, J. Bueno, P. J. de Visser, R. Barends, D. J. Thoen, V. Murugesan, N. Tomita, and J. J. A. Baselmans, "Mitigation of cosmic ray effect on microwave kinetic inductance detector arrays", Appl. Phys. Lett. **114**, 10.1063/1.5052419 (2019) (cit. on pp. 37, 47, 94).

[203] A. P. Vepsäläinen, A. H. Karamlou, J. L. Orrell, et al., "Impact of ionizing radiation on superconducting qubit coherence", Nature **584**, 551–556 (2020) (cit. on pp. 37, 75, 94).

[204] M. McEwen, L. Faoro, K. Arya, A. Dunsworth, T. Huang, S. Kim, B. Burkett, A. Fowler, F. Arute, J. C. Bardin, A. Bengtsson, A. Bilmes, B. B. Buckley, N. Bushnell, Z. Chen, R. Collins, S. Demura, A. R. Derk, C. Erickson, M. Giustina, S. D. Harrington, S. Hong, E. Jeffrey, J. Kelly, P. V. Klimov, F. Kostritsa, P. Laptev, A. Locharla, X. Mi, K. C. Miao, S. Montazeri, J. Mutus, O. Naaman, M. Neeley, C. Neill, A. Opremcak, C. Quintana, N. Redd, P. Roushan, D. Sank, K. J. Satzinger, V. Shvarts, T. White, Z. J. Yao, P. Yeh, J. Yoo, Y. Chen, V. Smelyanskiy, J. M. Martinis, H. Neven, A. Megrant, L. Ioffe, and R. Barends, "Resolving catastrophic error bursts from cosmic rays in large arrays of superconducting qubits", Nat. Phys. **18**, 107–111 (2022) (cit. on pp. 37, 94).

[205] F. Henriques, F. Valenti, T. Charpentier, M. Lagoin, C. Gouriou, M. Martínez, L. Cardani, M. Vignati, L. Grünhaupt, D. Gusenkova, J. Ferrero, S. T. Skacel, W. Wernsdorfer, A. V. Ustinov, G. Catelani, O. Sander, and I. M. Pop, "Phonon traps reduce the quasiparticle density in superconducting circuits", Appl. Phys. Lett. **115**, 212601 (2019) (cit. on pp. 37, 47).

[206] L. Cardani, F. Valenti, N. Casali, G. Catelani, T. Charpentier, M. Clemenza, I. Colantoni, A. Cruciani, G. D'Imperio, L. Gironi, L. Grünhaupt, D. Gusenkova, F. Henriques, M. Lagoin, M. Martinez, G. Pettinari, C. Rusconi, O. Sander, C. Tomei, A. V. Ustinov, M. Weber, W. Wernsdorfer, M. Vignati, S. Pirro, and I. M. Pop, "Reducing the impact of radioactivity on quantum circuits in a deep-underground facility", Nat. Commun. **12**, 1–6 (2021) (cit. on pp. 37, 47).

[207] J. M. Martinis, "Saving superconducting quantum processors from decay and correlated errors generated by gamma and cosmic rays", npj Quantum Inf. **7**, 1–9 (2021) (cit. on pp. 37, 47).

[208] R.-P. Riwar, A. Hosseinkhani, L. D. Burkhart, Y. Y. Gao, R. J. Schoelkopf, L. I. Glazman, and G. Catelani, "Normal-metal quasiparticle traps for superconducting qubits", Phys. Rev. B **94**, 104516 (2016) (cit. on pp. 37, 47).

[209] F. Valenti, F. Henriques, G. Catelani, N. Maleeva, L. Grünhaupt, U. von Lüpke, S. T. Skacel, P. Winkel, A. Bilmes, A. V. Ustinov, J. Goupy, M. Calvo, A. Benoît, F. Levy-Bertrand, A. Monfardini, and I. M. Pop, "Interplay Between Kinetic Inductance, Nonlinearity, and Quasiparticle Dynamics in Granular Aluminum Microwave Kinetic Inductance Detectors", Phys. Rev. Appl. **11**, 054087 (2019) (cit. on p. 37).

[210] A. Bargerbos, L. J. Splitthoff, M. Pita-Vidal, J. J. Wesdorp, Y. Liu, P. Krogstrup, L. P. Kouwenhoven, C. K. Andersen, and L. Grünhaupt, "Mitigation of Quasiparticle Loss in Superconducting Qubits by Phonon Scattering", Phys. Rev. Appl. **19**, 024014 (2023) (cit. on pp. 37, 47).

[211] E. L. Hahn, "Spin Echoes", Phys. Rev. **80**, 580–594 (1950) (cit. on p. 37).

[212] H. Y. Carr and E. M. Purcell, "Effects of Diffusion on Free Precession in Nuclear Magnetic Resonance Experiments", Phys. Rev. **94**, 630–638 (1954) (cit. on p. 37).

[213] S. Meiboom and D. Gill, "Modified Spin-Echo Method for Measuring Nuclear Relaxation Times", Rev. Sci. Instrum. **29**, 688–691 (1958) (cit. on p. 37).

[214] A. Cottet, "Implementation of a quantum bit in a superconducting circuit", PhD thesis (Sept. 2002) (cit. on pp. 38, 40).

[215] G. Ithier, E. Collin, P. Joyez, P. J. Meeson, D. Vion, D. Esteve, F. Chiarello, A. Shnirman, Y. Makhlin, J. Schriefl, and G. Schön, "Decoherence in a superconducting quantum bit circuit", Phys. Rev. B **72**, 134519 (2005) (cit. on pp. 38, 40).

[216] D. J. Van Harlingen, T. L. Robertson, B. L. T. Plourde, et al., "Decoherence in Josephson-junction qubits due to critical-current fluctuations", Phys. Rev. B **70**, 064517 (2004) (cit. on pp. 38, 68).

[217] G. Rastelli, I. M. Pop, and F. W. J. Hekking, "Quantum phase slips in Josephson junction rings", Phys. Rev. B **87**, 174513 (2013) (cit. on p. 38).

[218] A. A. Houck, J. Koch, M. H. Devoret, S. M. Girvin, and R. J. Schoelkopf, "Life after charge noise: recent results with transmon qubits", Quantum Inf. Process. **8**, 105–115 (2009) (cit. on p. 39).

[219] R. W. Heeres, P. Reinhold, N. Ofek, L. Frunzio, L. Jiang, M. H. Devoret, and R. J. Schoelkopf, "Implementing a universal gate set on a logical qubit encoded in an oscillator", Nat. Commun. **8**, 1–7 (2017) (cit. on p. 39).

[220] J. Gambetta, A. Blais, D. I. Schuster, et al., "Qubit-photon interactions in a cavity: Measurement-induced dephasing and number splitting", Phys. Rev. A **74**, 042318 (2006) (cit. on pp. 39, 40, 68).

[221] D. I. Schuster, A. A. Houck, J. A. Schreier, A. Wallraff, J. M. Gambetta, A. Blais, L. Frunzio, J. Majer, B. Johnson, M. H. Devoret, S. M. Girvin, and R. J. Schoelkopf, "Resolving photon number states in a superconducting circuit", Nature **445**, 515–518 (2007) (cit. on p. 39).

[222] A. A. Clerk and D. W. Utami, "Using a qubit to measure photon-number statistics of a driven thermal oscillator", Phys. Rev. A **75**, 042302 (2007) (cit. on p. 40).

[223] C. Rigetti, J. M. Gambetta, S. Poletto, et al., "Superconducting qubit in a waveguide cavity with a coherence time approaching 0.1 ms", Phys. Rev. B **86**, 100506 (2012) (cit. on pp. 40, 42, 68, 78, 94).

[224] Z. Wang, S. Shankar, Z. K. Minev, et al., "Cavity Attenuators for Superconducting Qubits", Phys. Rev. Appl. **11**, 014031 (2019) (cit. on pp. 42, 68, 69, 78, 94).

[225] J.-H. Yeh, J. LeFebvre, S. Premaratne, et al., "Microwave attenuators for use with quantum devices below 100 mK", J. Appl. Phys. **121**, 224501 (2017) (cit. on pp. 42, 68–70, 78, 94).

[226] F. Yan, D. Campbell, P. Krantz, et al., "Distinguishing Coherent and Thermal Photon Noise in a Circuit Quantum Electrodynamical System", Phys. Rev. Lett. **120**, 260504 (2018) (cit. on pp. 42, 68, 78, 94).

[227] B. Suri, Z. K. Keane, R. Ruskov, et al., "Observation of Autler–Townes effect in a dispersively dressed Jaynes–Cummings system", New J. Phys. **15**, 125007 (2013) (cit. on pp. 42, 68, 78, 94).

[228] J. Goetz, S. Pogorzalek, F. Deppe, et al., "Photon Statistics of Propagating Thermal Microwaves", Phys. Rev. Lett. **118**, 103602 (2017) (cit. on pp. 42, 68, 78, 94).

[229] G. Zhang, Y. Liu, J. J. Raftery, et al., "Suppression of photon shot noise dephasing in a tunable coupling superconducting qubit", npj Quantum Inf. **3**, 1–4 (2017) (cit. on pp. 42, 68, 78, 94).

[230] S. Krinner, S. Storz, P. Kurpiers, et al., "Engineering cryogenic setups for 100-qubit scale superconducting circuit systems", EPJ Quantum Technol. **6**, 1–29 (2019) (cit. on pp. 42, 43, 67, 82, 83).

[231] Bluefors Oy, *Dilution Refrigerator Measurement Systems*, [Online; accessed 17. Apr. 2025], (Mar. 2025) `https://bluefors.com/products/dilution-refrigerator-measurement-systems` (cit. on p. 43).

[232] V. Gupta, P. Winkel, N. Thakur, P. van Vlaanderen, Y. Wang, S. Ganjam, L. Frunzio, and R. J. Schoelkopf, "Low loss lumped-element inductors made from granular aluminum", arXiv, `10.48550/arXiv.2411.12611` (2024) (cit. on pp. 45, 63, 94, 95).

[233] L. Grünhaupt, M. Spiecker, D. Gusenkova, N. Maleeva, S. T. Skacel, I. Takmakov, F. Valenti, P. Winkel, H. Rotzinger, W. Wernsdorfer, A. V. Ustinov, and I. M. Pop, "Granular aluminium as a superconducting material for high-impedance quantum circuits", Nat. Mater. **18**, 816–819 (2019) (cit. on pp. 45, 46).

[234] A. Kou, W. C. Smith, U. Vool, I. M. Pop, K. M. Sliwa, M. Hatridge, L. Frunzio, and M. H. Devoret, "Simultaneous Monitoring of Fluxonium Qubits in a Waveguide", Phys. Rev. Appl. **9**, 064022 (2018) (cit. on p. 46).

[235] M. D. Reed, B. R. Johnson, A. A. Houck, L. DiCarlo, J. M. Chow, D. I. Schuster, L. Frunzio, and R. J. Schoelkopf, "Fast reset and suppressing spontaneous emission of a superconducting qubit", Appl. Phys. Lett. **96**, 203110 (2010) (cit. on p. 46).

[236] P. S. Mundada, A. Gyenis, Z. Huang, J. Koch, and A. A. Houck, "Floquet-Engineered Enhancement of Coherence Times in a Driven Fluxonium Qubit", Phys. Rev. Appl. **14**, 054033 (2020) (cit. on p. 46).

[237] V. Iaia, J. Ku, A. Ballard, C. P. Larson, E. Yelton, C. H. Liu, S. Patel, R. McDermott, and B. L. T. Plourde, "Phonon downconversion to suppress correlated errors in superconducting qubits", Nat. Commun. **13**, 1–7 (2022) (cit. on p. 47).

[238] A. D'Addabbo, "Applications of Kinetic Inductance Detectors to Astronomy and Particle Physics", PhD thesis (Université de Grenoble ; Università degli studi La Sapienza (Rome), Grenoble, France, Oct. 2014) (cit. on p. 47).

[239] Ansys, Inc, *Ansys HFSS | 3D High Frequency Simulation Software*, [Online; accessed 29. Apr. 2025], (Feb. 2025) https://www.ansys.com/de-de/products/electronics/ansys-hfss (cit. on p. 48).

[240] S. Zhu, F. Crisa, M. Bal, A. A. Murthy, J. Lee, Z. Sung, A. Lunin, D. Frolov, R. Pilipenko, D. Bafia, A. Mitra, A. Romanenko, and A. Grassellino, "High quality superconducting Nb co-planar resonators on sapphire substrate", arXiv, 10.48550/arXiv.2207.13024 (2022) (cit. on p. 48).

[241] G. J. Dolan, "Offset masks for lift-off photoprocessing", Appl. Phys. Lett. **31**, 337–339 (1977) (cit. on p. 48).

[242] M. Spiecker and P. Paluch, *Fluxonium robots*, (Apr. 2025) https://doi.org/10.5281/zenodo.15211399 (cit. on p. 51).

[243] D. P. Schroller, *Design and Characterization of a Tunable Band-Pass Filter in the GHz Regime (Bachelor Thesis)*, (2017) https://www.phi.kit.edu/bachelorarbeiten.php (cit. on p. 53).

[244] Quantum Machines, *OPX+: Ultra-Fast Quantum Control Hardware - Quantum Machines*, [Online; accessed 30. Apr. 2025], (Apr. 2025) https://www.quantum-machines.co/products/opx (cit. on p. 53).

[245] Quantum Machines, *Octave: Seamless Up/Down-Conversion for Quantum Computing*, [Online; accessed 30. Apr. 2025], (Apr. 2025) https://www.quantum-machines.co/products/octave (cit. on p. 53).

[246] C. Hellings, N. Lacroix, A. Remm, R. Boell, J. Herrmann, S. Lazăr, S. Krinner, F. Swiadek, C. K. Andersen, C. Eichler, and A. Wallraff, "Calibrating Magnetic Flux Control in Superconducting Circuits by Compensating Distortions on Time Scales from Nanoseconds up to Tens of Microseconds", arXiv, 10.48550/arXiv.2503.04610 (2025) (cit. on p. 59).

[247] Quantum Machines, *Quantum Orchestration for Superconducting Qubits*, (2022) https://videos.quantum-machines.co/wp-content/uploads/2022/07/12152313/Use-Cases-Superconducting-Qubits.pdf (cit. on p. 61).

[248] Google Quantum AI, "Suppressing quantum errors by scaling a surface code logical qubit.", Nature **614**, 676–681 (2023) (cit. on pp. 67, 68).

[249] E. E. Wollman, V. B. Verma, A. E. Lita, et al., "Kilopixel array of superconducting nanowire single-photon detectors", Opt. Express **27**, 35279–35289 (2019) (cit. on p. 67).

[250] A. Catalano, R. Adam, P. A. R. Ade, et al., "The NIKA2 Instrument at 30-m IRAM Telescope: Performance and Results", J. Low Temp. Phys. **193**, 916–922 (2018) (cit. on p. 67).

[251] L. Gottardi and K. Nagayashi, "A Review of X-ray Microcalorimeters Based on Superconducting Transition Edge Sensors for Astrophysics and Particle Physics", Appl. Sci. **11**, 3793 (2021) (cit. on p. 67).

[252] L. Gastaldo, K. Blaum, K. Chrysalidis, et al., "The electron capture in 163Ho experiment – ECHo", Eur. Phys. J. Spec. Top. **226**, 1623–1694 (2017) (cit. on p. 67).

[253] S. Kempf, M. Wegner, A. Fleischmann, et al., "Demonstration of a scalable frequency-domain readout of metallic magnetic calorimeters by means of a microwave SQUID multiplexer", AIP Adv. **7**, 10.1063/1.4973872 (2017) (cit. on p. 67).

[254] B. Dober, Z. Ahmed, K. Arnold, et al., "A microwave SQUID multiplexer optimized for bolometric applications", Appl. Phys. Lett. **118**, 10.1063/5.0033416 (2021) (cit. on p. 67).

[255] M. Durkin, J. S. Adams, S. R. Bandler, et al., "Mitigation of Finite Bandwidth Effects in Time-Division-Multiplexed SQUID Readout of TES Arrays", IEEE Trans. Appl. Supercond. **31**, ArticleSequenceNumber:1600905 (2021) (cit. on p. 67).

[256] Y. Chen, D. Sank, P. O'Malley, et al., "Multiplexed dispersive readout of superconducting phase qubits", Appl. Phys. Lett. **101**, 182601 (2012) (cit. on p. 67).

[257] J. Heinsoo, C. K. Andersen, A. Remm, et al., "Rapid High-fidelity Multiplexed Readout of Superconducting Qubits", Phys. Rev. Appl. **10**, 034040 (2018) (cit. on p. 67).

[258] F. Lecocq, F. Quinlan, K. Cicak, et al., "Control and readout of a superconducting qubit using a photonic link", Nature **591**, 575–579 (2021) (cit. on p. 67).

[259] A. Youssefi, I. Shomroni, Y. J. Joshi, et al., "A cryogenic electro-optic interconnect for superconducting devices", Nat. Electron. **4**, 326–332 (2021) (cit. on p. 67).

[260] M. Shen, J. Xie, Y. Xu, et al., "Photonic link from single-flux-quantum circuits to room temperature", Nat. Photonics **18**, 371–378 (2024) (cit. on p. 67).

[261] C. G. Pappas, J. Austermann, J. A. Beall, et al., "High-Density Superconducting Cables for Advanced ACTPol", J. Low Temp. Phys. **184**, 473–479 (2016) (cit. on p. 67).

[262] D. B. Tuckerman, M. C. Hamilton, D. J. Reilly, et al., "Flexible superconducting Nb transmission lines on thin film polyimide for quantum computing applications", Supercond. Sci. Technol. **29**, 084007 (2016) (cit. on p. 67).

[263] A. B. Walter, C. Bockstiegel, B. A. Mazin, et al., "Laminated NbTi-on-Kapton Microstrip Cables for Flexible Sub-Kelvin RF Electronics", IEEE Trans. Appl. Supercond. **28**, ArticleSequenceNumber:2500105 (2017) (cit. on p. 67).

[264] V. Gupta, B. Yelamanchili, S. Zou, et al., "Thin-Film Nb/Polyimide Superconducting Stripline Flexible Cables", IEEE Trans. Appl. Supercond. **29**, ArticleSequenceNumber:1501605 (2019) (cit. on p. 67).

[265] S. Zou, B. Yelamanchili, V. Gupta, et al., "Low-loss cable-to-cable parallel connection method for thin-film superconducting flexible microwave transmission lines", Supercond. Sci. Technol. **32**, 075006 (2019) (cit. on p. 67).

[266] J. P. Smith, B. A. Mazin, A. B. Walter, et al., "Flexible Coaxial Ribbon Cable for High-Density Superconducting Microwave Device Arrays", IEEE Trans. Appl. Supercond. **31**, ArticleSequenceNumber:2500105 (2020) (cit. on p. 67).

[267] V. Y. Monarkha, S. Simbierowicz, M. Borrelli, et al., "Equivalence of flexible stripline and coaxial cables for superconducting qubit control and readout pulses", Appl. Phys. Lett. **124**, 10.1063/5.0203101 (2024) (cit. on pp. 67, 70).

[268] G. Zimmerli, T. M. Eiles, R. L. Kautz, et al., "Noise in the Coulomb blockade electrometer", Appl. Phys. Lett. **61**, 237–239 (1992) (cit. on p. 68).

[269] A. Blais, A. L. Grimsmo, S. M. Girvin, et al., "Circuit quantum electrodynamics", Rev. Mod. Phys. **93**, 025005 (2021) (cit. on p. 68).

[270] P. Bertet, I. Chiorescu, G. Burkard, et al., "Dephasing of a Superconducting Qubit Induced by Photon Noise", Phys. Rev. Lett. **95**, 257002 (2005) (cit. on p. 68).

[271] D. I. Schuster, A. Wallraff, A. Blais, et al., "ac Stark Shift and Dephasing of a Superconducting Qubit Strongly Coupled to a Cavity Field", Phys. Rev. Lett. **94**, 123602 (2005) (cit. on p. 68).

[272] A. P. Sears, A. Petrenko, G. Catelani, et al., "Photon shot noise dephasing in the strong-dispersive limit of circuit QED", Phys. Rev. B **86**, 180504 (2012) (cit. on p. 68).

[273] Qinu GmbH, *Sionludi xl table-top dilution cryostats*, (2025) https://qinu.de/version-xl/ (visited on 01/22/2025) (cit. on p. 69).

[274] Delft Circuits BV, *Cri/oFlex® cryogenic RF cable technology*, (2025) https://delft-circuits.com/cri-oflex-technology/core-technology-cryogenic-rf-cable/ (visited on 01/22/2025) (cit. on p. 69).

[275] COAX CO., LTD., *SC-119/50-CN-CN |*, [Online; accessed 18. Apr. 2025], (Apr. 2025) https://www.coax.co.jp/en/product/sc/119-50-cn-cn.html (cit. on p. 69).

[276] U. Vool, I. M. Pop, K. Sliwa, et al., "Non-Poissonian Quantum Jumps of a Fluxonium Qubit due to Quasiparticle Excitations", Phys. Rev. Lett. **113**, 247001 (2014) (cit. on p. 75).

[277] B.-L. Najera-Santos, R. Rousseau, K. Gerashchenko, et al., "High-Sensitivity ac-Charge Detection with a MHz-Frequency Fluxonium Qubit", Phys. Rev. X **14**, 011007 (2024) (cit. on p. 75).

[278] X. Y. Jin, A. Kamal, A. P. Sears, et al., "Thermal and Residual Excited-State Population in a 3D Transmon Qubit", Phys. Rev. Lett. **114**, 240501 (2015) (cit. on p. 75).

[279] I. Takmakov, "Minimizing the discrimination time for quantum states of an artificial atom", 47.12.01; LK 01, PhD thesis (Karlsruher Institut für Technologie (KIT), 2022), 94 pp. (cit. on p. 76).

[280] M. L. Roukes, M. R. Freeman, R. S. Germain, et al., "Hot electrons and energy transport in metals at millikelvin temperatures", Phys. Rev. Lett. **55**, 422–425 (1985) (cit. on pp. 80, 87, 96).

[281] F. C. Wellstood, C. Urbina, and J. Clarke, "Hot-electron effects in metals", Phys. Rev. B **49**, 5942–5955 (1994) (cit. on pp. 80, 87, 96).

[282] W. A. Little, "The Transport of Heat between Dissimilar Solids at Low Temperatures", Can. J. Phys., 10.1139/p59-037 (1959) (cit. on pp. 80, 87, 96).

[283] J. K. Hulm, "The Thermal Conductivity of a Copper-Nickel Alloy at Low Temperatures", Proc. Phys. Soc. B **64**, 207 (1951) (cit. on pp. 85, 86).

[284] Mat Web, *Copper nickel 20%, UNS C71000*, (2025) https://www.matweb.com/search/datasheet.aspx?MatGUID=86c31a4ca1d64f65a8eab9abdeb5c6dd (visited on 01/22/2025) (cit. on p. 85).

[285] D. R. Smith and F. R. Fickett, "Low-Temperature Properties of Silver", J. Res. Nat. Inst. Stand. Technol. **100**, 119 (1995) (cit. on pp. 85, 86).

[286] N. Earnest, S. Chakram, Y. Lu, N. Irons, R. K. Naik, N. Leung, L. Ocola, D. A. Czaplewski, B. Baker, J. Lawrence, J. Koch, and D. I. Schuster, "Realization of a Λ System with Metastable States of a Capacitively Shunted Fluxonium", Phys. Rev. Lett. **120**, 150504 (2018) (cit. on p. 95).

[287] Y.-H. Lin, L. B. Nguyen, N. Grabon, J. San Miguel, N. Pankratova, and V. E. Manucharyan, "Demonstration of Protection of a Superconducting Qubit from Energy Decay", Phys. Rev. Lett. **120**, 150503 (2018) (cit. on p. 95).

[288] K. Borisov, D. Rieger, P. Winkel, F. Henriques, F. Valenti, A. Ionita, M. Wessbecher, M. Spiecker, D. Gusenkova, I. M. Pop, and W. Wernsdorfer, "Superconducting granular aluminum resonators resilient to magnetic fields up to 1 Tesla", Appl. Phys. Lett. **117**, 10.1063/5.0018012 (2020) (cit. on p. 95).

[289] Delft Circuits, *Cri/oSuite™– electrical & thermal analysis (Software & Calibration)*, [Online; accessed 4. May 2025], (June 2024) https://delft-circuits.com/product-overview/software-calibration (cit. on p. 96).

[290] R. Kubo, "Statistical-Mechanical Theory of Irreversible Processes. I. General Theory and Simple Applications to Magnetic and Conduction Problems", J. Phys. Soc. Jpn. **12**, 570–586 (1957) (cit. on p. 98).

[291] Bluefors Oy, *QCage*, [Online; accessed 12. May 2025], (Aug. 2024) https://bluefors.com/products/measurement-infrastructure/qcage (cit. on p. 107).